THÈSE DE DOCTORAT

de l'Université de recherche Paris Sciences et Lettres
PSL Research University

Préparée à l'École Normale Supérieure de Paris
au Laboratoire de Physique Statistique

Large Scale Effects in Turbulence

Effets de grande échelle en turbulence

École doctorale n°564
PHYSIQUE EN ÎLE-DE-FRANCE

Spécialité : Physique

COMPOSITION DU JURY :

M^me Hélène POLITANO
Université de Nice Sophia-Antipolis, Rapporteuse

M. Alain PUMIR
ENS de Lyon, Rapporteur

M. Jérémie BEC
Université de Nice Sophia-Antipolis, Examinateur

M. Sergey NAZARENKO
Warwick University, Examinateur

M. Alexandros ALEXAKIS
ENS de Paris, Co-Directeur de thèse

M. Marc-Étienne BRACHET
ENS de Paris, Directeur de thèse

Soutenue par Alexandre CAMERON
le 7 Juillet 2017

Dirigée par Marc-Étienne BRACHET
et Alexandros ALEXAKIS

Contents

All chapters with a title starting with *Elements of context* review elements of well-documented theories. New results are presented in the chapters with a title finishing with the indication *published* or *submitted*.

Part A

Preamble

Table of Contents

Chapitre 0

Présentation

> "Conformément à la loi, le mémoire de thèse est rédigé en français. [...] En cas de rédaction en anglais, il est nécessaire de fournir un résumé en français de 15 à 20 pages."
>
> https://www.edpif.org/fr/parcours/soutenance/

0.1 Cadre d'étude

L'équation de Navier-Stokes est une brique importante de la physiques qui est utilisée pour modéliser des écoulements dans des domaines allant de la physique expérimentale à l'aéronautique en passant par l'astrophysique. Pourtant, depuis sa première utilisation au milieu du XIX$^{\text{ème}}$ siècle, aucune solution générale n'a pu être exprimée de façon explicite. La résolution de l'équation est si difficile que l'Institut Clay de mathématiques considère que le seul problème de la régularité des solutions de l'équation est l'un des sept problèmes du millénaire que l'Institut Clay récompense par un prix d'un million de dollar.

D'un point de vue plus physique, l'équation de Navier-Stokes a été établie pour décrire l'évolution du mouvement d'un fluide visqueux. L'équation provient de l'utilisation de l'expression linéarisée du tenseur des contraintes avec le principe fondamental de la dynamique. Dans l'espace physique, l'équation de Navier-Stokes peut s'exprimer pour un fluide incompressible comme

$$\partial_t \boldsymbol{u} + (\boldsymbol{u}\cdot\boldsymbol{\nabla})\boldsymbol{u} = -\boldsymbol{\nabla}P + \nu\Delta\boldsymbol{u} + \boldsymbol{F} \quad \text{avec} \quad \boldsymbol{\nabla}\cdot\boldsymbol{u} = 0 \quad \text{où} \quad P = p/\rho\,, \tag{0.1}$$

où $\boldsymbol{u}$, P, ν et $\boldsymbol{F}$ représentent respectivement le champ de vitesse, le champ de pression, la viscosité cinématique du fluide et le champ de force. Dans les écoulements considérés, la viscosité est une grandeur stationnaire (indépendante du temps) et uniforme (indépendante de l'espace). Elle est fixée par l'opérateur soit dans les paramètres d'une simulation, soit en changeant le fluide dans une expérience. Le champ de force peut dépendre du temps et de l'espace et est lui aussi fixé par l'opérateur. Le champ de vitesse et le champ de pression sont les variables du problème. Elles dépendent de l'espace et du temps et ne sont pas fixées directement par l'opérateur. Pour trouver une solution au problème différentiel, il est aussi nécessaire d'imposer des conditions initiales et des conditions aux bords sur la vitesse. Le champ de pression quant à lui est directement

relié au champ de vitesse via la condition solénoïdale du champ de vitesse $\boldsymbol{\nabla} \cdot \boldsymbol{u} = 0$. Il peut être établi en résolvant l'équation de Poisson

$$\Delta P = -\boldsymbol{\nabla} \cdot ((\boldsymbol{u} \cdot \boldsymbol{\nabla})\boldsymbol{u}) \, . \tag{0.2}$$

La dénomination de champ de pression pour la variable P est abusive étant donné que la pression p, définie par le système international d'unités et mesurée par un manomètre, est reliée à P via $\boldsymbol{\nabla} P = \rho^{-1} \boldsymbol{\nabla} p$ où ρ représente la masse volumique du fluide. Quand la densité est uniforme, les deux pressions sont proportionnelles. Dans le cas d'écoulements solénoïdaux, si la densité du fluide est initialement uniforme, elle reste constante (uniforme et stationnaire) car elle suit l'équation de continuité

$$-\partial_t \rho = \boldsymbol{\nabla} \cdot (\rho \boldsymbol{u}) = (\boldsymbol{u} \cdot \boldsymbol{\nabla})\rho + (\boldsymbol{\nabla} \cdot \boldsymbol{u})\rho = 0 \, . \tag{0.3}$$

En effet, $(\boldsymbol{\nabla} \cdot \boldsymbol{u})\rho = 0$ car l'écoulement est solénoïdal et $(\boldsymbol{u} \cdot \boldsymbol{\nabla})\rho = 0$ car la densité du fluide est initialement uniforme. Réciproquement, si le fluide est incompressible, *i.e.* si la densité est constante, l'écoulement doit être solénoïdal. La condition d'incompressibilité d'un fluide est donc équivalente au caractère solénoïdal de l'écoulement.

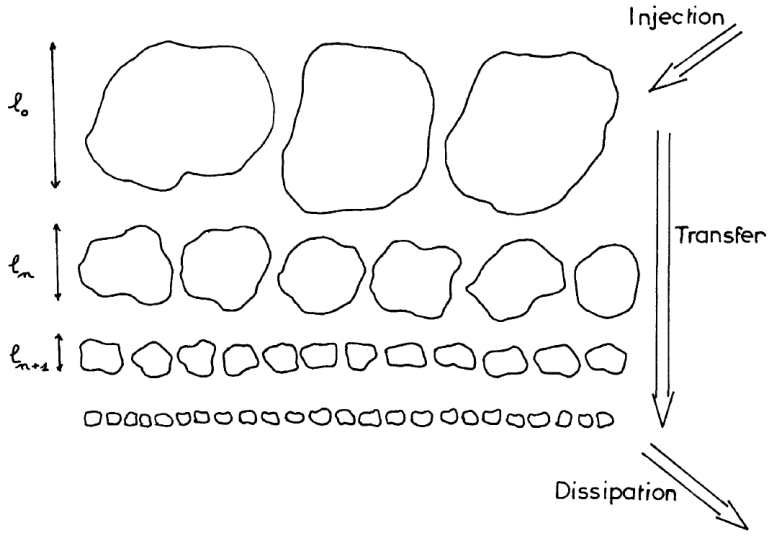

FIGURE 0.1 – Schéma représentant la cascade de Richardson où les tourbillons sont brisés en tourbillons de plus petite taille jusqu'à ce qu'ils atteignent une échelle assez petite pour être dissipés. Cette figure est tirée de l'article de Rose et Sulem (1978) [1].

Dans l'équation de Navier-Stokes, le terme $(\boldsymbol{u} \cdot \boldsymbol{\nabla})\boldsymbol{u}$ est à associer aux effets de convection qui sont aussi appelés effet inertiels, alors que le terme $\nu \Delta \boldsymbol{u}$ est à associer aux effets de diffusion. Le nombre de Reynolds, Re, est le nombre sans dimension utilisé pour caractériser le régime de l'écoulement. Il est défini par

$$Re = \frac{[[(\boldsymbol{u} \cdot \boldsymbol{\nabla})\boldsymbol{u}]]}{[[\nu \Delta \boldsymbol{u}]]} = \frac{U_{rms}}{\nu \ell} \, , \tag{0.4}$$

où $[[\dots]]$ correspond à l'ordre de la quantité se trouvant entre des doubles crochets, U_{rms} et ℓ représentent respectivement la vitesse quadratique moyenne de l'écoulement et la longueur caractéristique de l'écoulement. A faible nombre de Reynolds, $Re \ll 1$, les effets visqueux dominent alors que les effets convectifs dominent à grand nombre de Reynolds $1 \ll Re$. A grand nombre de Reynolds, l'écoulement devient turbulent, la dynamique du fluide est souvent décrite à l'aide de l'image de la cascade de Richardson [2, 3]. Dans la description de cascade de Richardson, l'écoulement est composé de grands tourbillons qui se brisent en plus petits tourbillons qui se brisent eux-même en plus petits tourbillons et ainsi de suite jusqu'à ce que la taille des tourbillons soit assez faible pour que les effets diffusifs soient assez importants pour disperser les tourbillons. La fig. 0.1 représente le schéma fait pour illustrer le phénomène de cascade de Richardon par Rose et Sulem dans [1]. Ce mécanisme de cascade est en accord avec la théorie de Kolgomorov sur la turbulence [4, 3]. En montrant que seul i) le taux d'énergie injectée ϵ et ii) le coefficient de viscosité sont les uniques paramètres indépendants à fixer dans le problème pour décrire le système, Kolmogorov a prouvé que le spectre d'énergie du système, $E(k)$, suit la loi de puissance

$$E(k) \propto \epsilon^{2/3} k^{-5/3} \quad \text{où} \quad E = \int E(k) dk \,, \tag{0.5}$$

où k et E représentent respectivement le nombre d'onde et l'énergie totale du système. La fig.0.2 représente le spectre d'énergie d'un fluide incompressible selon la prédiction de la théorie de Kolmogorov.

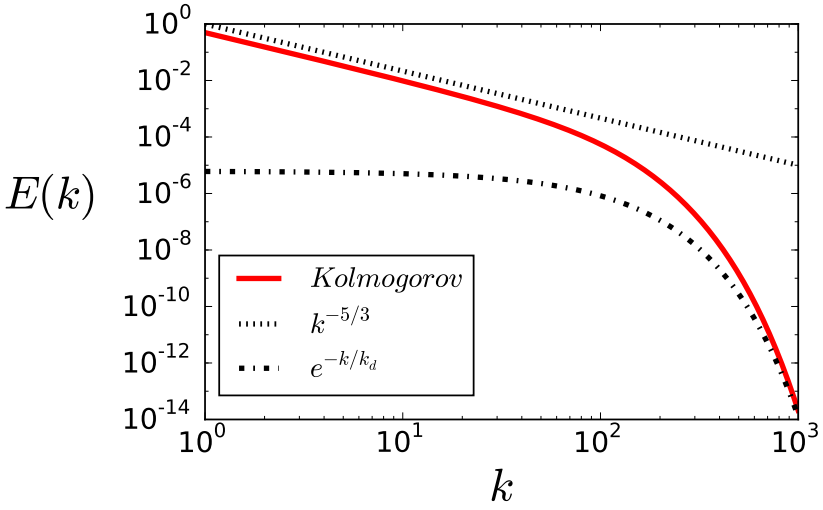

FIGURE 0.2 – Spectre d'énergie prédit par Kolmogorov en échelle logarithmique. La ligne rouge représente la prédiction de Kolmogorov. Les pointillés représentent la loi de puissance en $k^{-5/3}$. La courbe formée de points et de tirets représente la décroissance exponentielle dans la zone visqueuse. Le variable k_d représente la longueur d'onde associée à la dissipation.

De nombreuses études numériques aussi bien qu'expérimentales [5, 6] ont vérifié la validité de la théorie de Kolmogorov. La loi des 4/5 de Kolmogorov-Monin [7] – qui est une résultat en accord avec la théorie de Kolmogorov utilisant les relations de

Kàrmàn and Howarth [8] sur la fonction de corrélation d'ordre trois – a même pu être validée jusqu'à la valeur de son pré-facteur numérique [9]. La théorie de Kolmogorov est en mesure de prédire le comportement des modes dans des échelles plus petites que celles de forçage ; elle ne fait en revanche aucune prédiction en ce qui concerne les modes dans des échelles plus larges que l'échelle de forçage. Par ailleurs, la cascade de Richardson ne permet pas non plus d'avoir une intuition de la dynamique des grands tourbillons. La dynamique des modes présents à des échelles plus grandes que celle du forçage ne peut donc pas être décrite par les même mécanismes que ceux utilisés pour décrire la dynamique qui a lieu dans les petites échelles.

L'objet de ce mémoire est de s'intéresser aux propriétés des écoulements pour des échelles plus grandes que l'échelle du forçage. Le problème étudié est résumé brièvement dans la fig. 0.3. Puisque la théorie de Kolmogorov a été validée en aval du forçage, le spectre d'énergie doit suivre la prédiction de la théorie de Kolmogorov pour des échelles plus petites que l'échelle de forçage. Le comportement du spectre d'énergie avant l'échelle de forçage est quant à lui inconnu et est représenté par des points d'interrogations verts sur la fig. 0.3.

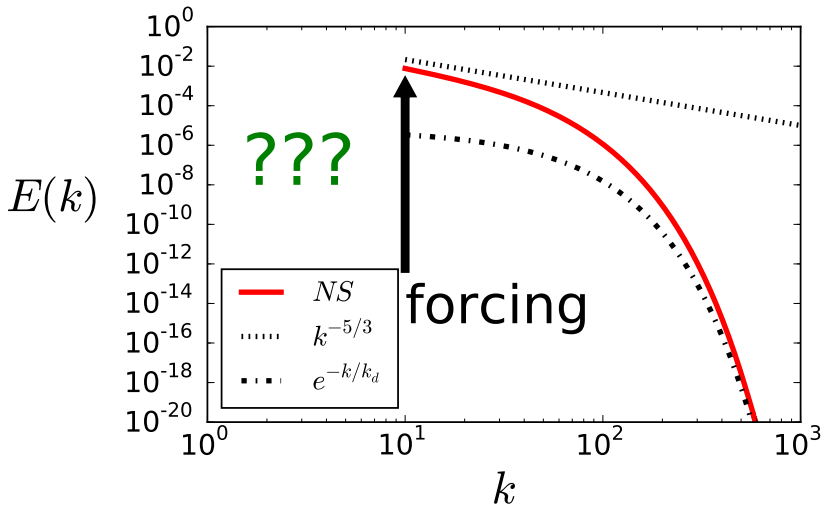

FIGURE 0.3 – Spectre d'énergie d'un champ de vitesse forcé au mode $k = 10^1$. La ligne rouge représente le comportement connue de la vitesse dans les petites échelles et prédit la théorie de Kolmogorov. Les lignes noires représentent les comportements asymptotiques du spectre d'énergie. Les points d'interrogation verts représentent la partie du spectre dont les propriétés sont encore inconnues.

Certaines théories ont postulé des prédictions concernant le comportement des modes dans les échelles plus grandes que celle du forçage. Dans [3], U. Frisch rapporte la conjecture selon laquelle le spectre d'énergie des solutions de l'équation de Navier-Stokes devrait avoir un comportement similaire aux équilibres absolus solutions de l'équation d'Euler tronquée :

> "Absolute equilibrium solutions seem highly unphysical in view of the approximately $k^{-5/3}$ spectrum of the three-dimensional turbulence. Actu-

> ally, they are appropriate at the very smallest wavenumbers of turbulent flows maintained by forcing at intermediate wavenumbers (Forster, Nelson and Stephen 1977)."
>
> — Uriel FRISCH, *Turbulence: The Legacy of A. N. Kolmogorov*, p. 209

L'article de Forster *et al.* [10], évoqué dans la citation, utilise le groupe de renormalisation pour étudier les phénomènes turbulents. Dans un des modèles de cet article, les auteurs sont capables de montrer que la dynamique des modes avant l'échelle de forçage est proche des solutions de l'équation d'Euler tronquée. L'équivalent du nombre d'onde de troncature dans le cadre des modes de grande échelle de l'équation de Navier-Stokes est la longueur d'onde de forçage.

L'équation d'Euler décrit le comportement de fluides idéaux, *i.e.* sans viscosité. Elle peut être obtenue à partir de l'équation de Navier-Stokes en mettant le coefficient de viscosité ν à zero. Kraichnan a étudié le spectre moyen en régime établi des solutions de l'équation d'Euler tronquée dans [11], qu'il a appelé équilibre absolu. L'équation d'Euler tronquée est une version filtrée spectralement de l'équation d'Euler où les modes au-delà d'un nombre d'onde maximal k_M, appelé le nombre d'onde troncature, ont été mis à zéro. Plus précisément, si les modes de Fourier du champ de vitesse sont désignés par $\boldsymbol{u_k}$, où $\boldsymbol{k}$ représente le vecteur d'onde, $\boldsymbol{u_k}$ est égal à zéro si $|\boldsymbol{k}| > k_M$ et $\boldsymbol{u_k}$ suit l'équation d'Euler si $k_M \geq |\boldsymbol{k}|$.

La fig. 0.4 représente l'aspect général du spectre d'énergie d'équilibres absolus solutions de l'équation Euler tronquée. Loin du nombre d'onde de troncature, le spectre d'énergie suit une loi de puissance en k^2. Cette loi de puissance est à relier à la conservation de l'énergie par l'équation d'Euler tronquée. Si l'énergie est distribuée équitablement entre les différents modes, à nombre d'onde constant, le spectre d'énergie doit être proportionnel au nombre de modes par coquille. En dimension trois, la densité de modes par coquille est à peu près constante et la surface d'une coquille est proportionnelle à k^2. Si l'énergie est équi-répartie, le spectre d'énergie doit donc suivre une loi de puissance en k^2.

L'équation d'Euler tronquée ne conserve pas uniquement l'énergie. Elle conserve aussi une seconde quantité appelée l'hélicité, représentée par la lettre H et définie comme

$$H = \frac{1}{L^3}\int (\boldsymbol{u}\cdot\boldsymbol{\nabla}\times\boldsymbol{u}) d^3\boldsymbol{r} \quad \text{avec} \quad L^3 = \int d^3\boldsymbol{r}\,. \tag{0.6}$$

où L^3 correspond au volume du fluide.

La conservation d'un second invariant par l'équation d'Euler tronquée modifie l'aspect du spectre d'énergie moyen. La densité de probabilité de chaque mode du champ de vitesse est régie par un poids de Boltzman modifié proportionnel à $e^{-(\alpha(2E)+\beta H)}$ où α et β sont les paramètres introduits par Kraichnan [11]. Le nombre de Kraichnan $\mathcal{K}r = -\frac{\beta k_M}{\alpha}$ est utilisé pour mesurer le niveau relatif d'hélicité par rapport à l'énergie pour un fluide avec une troncature à k_M. Le nombre de Kraichnan, $\mathcal{K}r$, peut donc être introduit pour mesurer le niveau relatif d'hélicité par rapport à l'énergie. Si le nombre de Kraichnan est égal à zero, l'écoulement n'a pas d'hélicité et le spectre d'énergie suit une loi de puissance en k^2. Si le nombre de Kraichnan est différent de zéro, le système a de l'hélicité. Enfin, si le nombre Kraichnan est proche de 1 en valeur absolue, l'énergie

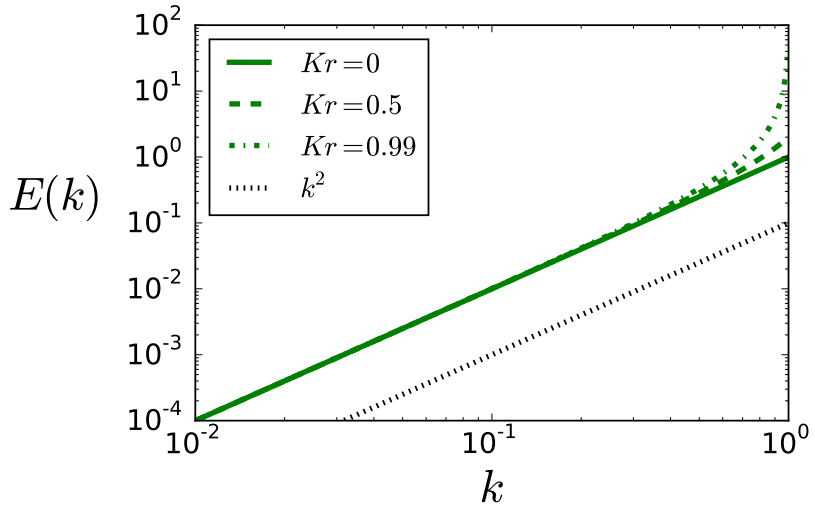

FIGURE 0.4 – Prédiction d'équilibre absolu pour le spectre d'énergie pour des solutions de l'équation d'Euler tronquée à différents nombres de Kraichan.

est concentrée dans les petites échelles et le spectre d'énergie ne suit plus une loi de puissance en k^2.

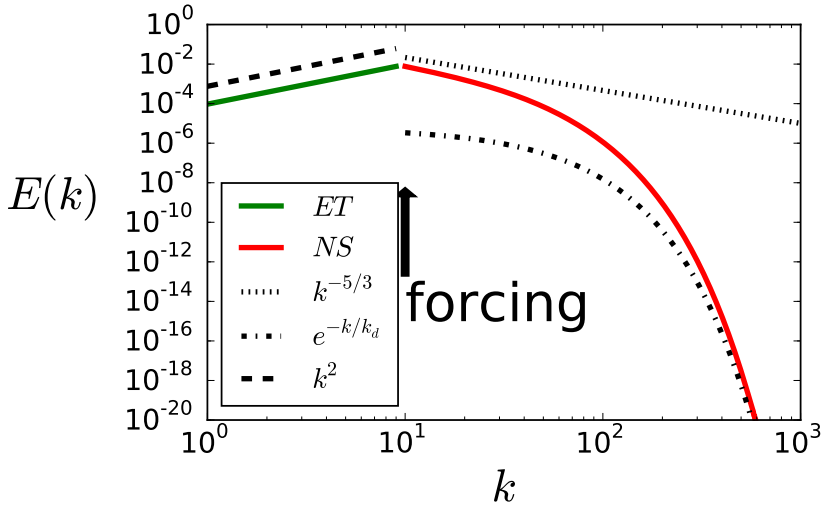

FIGURE 0.5 – Spectre d'énergie tel que décrit par Frisch dans [3]. La ligne rouge représente la prédiction du spectre d'énergie dans les échelles plus petites que l'échelle de forçage. La ligne verte représente la prédiction du spectre d'énergie dans les échelles plus grandes que l'échelle de forçage.

Comme l'ont expliqué Kraichnan et Chen dans [12], les analogies entre la dynamique des modes de grande échelle des solutions de l'équation de Navier-Stokes et les solutions de l'équation d'Euler tronquée peuvent aussi être décrites du point de vue de

l'équation d'Euler tronquée. Leur argument est fondé sur le théorème de fluctuation-dissipation et est expliqué dans la citation présentée à la page xv.

> "The equilibrium equipartition distribution [...] becomes more interesting when the associated fluctuation-dissipation relations are considered. These relations show that the truncated Euler system can imitate a [Navier-Stokes] fluid: the high wavenumber degrees of freedom act like a thermal sink into which the energy of low wavenumber modes excited above equilibrium is dissipated. In the limit where the sink wavenumbers are very large compared with the anomalously excited wavenumbers, this dynamical damping acts precisely like a molecular viscosity. When the wavenumber ratio is not asymptotically large, the dynamical damping is non-local in space and time; it exhibits long-time tails like those obtained from the kinetic theory of a gas."
>
> — Robert H. Kraichnan & Shiyi Chen,
> *Is there a statistical mechanics of turbulence ?*,
> Physica D 37 (1989) 160-172

Un autre argument, qui est utilisé pour donner une prédiction d'équilibre absolu dans les modes de grande échelle des solutions de l'équation de Navier-Stokes, est de considérer comment les modes de grandes échelles sont forcés. Dans les grandes échelles, les harmoniques du mode forcé sont forcées directement par le couplage non-linéaire lié au terme inertiel $(\boldsymbol{u}\cdot\boldsymbol{\nabla})\boldsymbol{u}$. Ce couplage non-linéaire ne permet pas de forcer directement les modes dans les grandes échelles car les nombres d'onde ne sont pas commensurables. Le forçage dans les grandes échelles provient du bruit produit par le battement des modes de petite échelle. Dans les grandes échelles, il est possible que ce bruit contrebalance le terme visqueux dans le régime turbulent, donnant ainsi lieu à une dynamique proche des équilibres absolus.

La fig. 0.5 illustre la prédiction faite à la citation de la page xiii par Frisch concernant le spectre d'énergie des modes dont l'échelle est plus grande que l'échelle de forçage pour des solutions de l'équation de Navier-Stokes. Les modes dans les échelles plus petites que l'échelle de forçage devraient suivre la loi de Kolmogorov, alors que dans les échelles plus grandes que le forçage les modes devraient avoir une dynamique similaire aux équilibres absolus solutions de l'équation Euler tronquée.

Avant d'étudier le comportement des modes de grande échelle dans des écoulements turbulents, il est important de comprendre comment ces modes se comportent à petit nombre de Reynolds. En effet, les propriétés d'écoulements laminaires et turbulents ne sont pas totalement déconnectées puisqu'elles décrivent le même fluide mais à des nombres de Reynolds différents. Même s'il est très improbable que toutes les propriétés d'un écoulement laminaire restent inchangées lorsque le nombre de Reynolds augmente, certains mécanismes peuvent encore influencer dans une moindre mesure la dynamique d'un écoulement. La connaissance de ces mécanismes et leur évolution avec l'augmentation du nombre de Reynolds peut donner une intuition sur le comportement de l'écoulement à grand nombre de Reynolds.

• **Dans la partie B**, nous étudierons le comportement grande échelle d'écoulements solutions de l'équation de Navier-Stokes forcée par des écoulements hélicitaires

à petit nombre de Reynolds. En utilisant l'analyse de Floquet, nous quantifierons comment les instabilités grandes échelles peuvent être engendrées. Nous commencerons par reproduire l'instabilité anisotropique cinétique de type alpha (AKA) produite dans [13, 14] à petit nombre de Reynolds avec une version linéarisée de l'équation de Navier-Stokes. Nous montrerons aussi que le mécanisme responsable de l'instabilité AKA est toujours en vigueur à des nombres de Reynolds modérés. Nous poursuivrons notre étude en étudiant l'instabilité grande échelle engendrée par l'écoulement hélicitaire ABC [15]. Nous montrerons que la première instabilité qui déstabilise l'écoulement est une instabilité grande échelle. En utilisant des simulations numériques directes de la version non-linéaire de l'équation de Navier-Stokes, nous montrerons que l'instabilité grande échelle peut aussi être observée mais qu'elle finit par saturer.

Nous utiliserons la méthodologie introduite pour étudier les fluides pour étudier les propriétés des champs magnétiques de fluides conducteurs. Étant donné que les équations d'évolutions du champ de vitesse dans un fluides visqueux et du champ magnétique d'un fluide conducteur partagent de nombreux points communs, leurs solutions comportent de nombreuses ressemblances. Par exemple, l'instabilité AKA a été introduite comme le pendant cinétique de l'effet alpha magnétique [16, 17]. En utilisant la méthodologie de Floquet, nous montrerons que, tout comme le champ de vitesse, le champ magnétique peut avoir une concentration d'énergie dans les grandes échelles s'il n'a pas encore atteint de régime où il est déstabilisé dans les petites échelles. Nous étayerons notre affirmation à l'aide des trois exemples suivants : un écoulement hélicitaire, un écoulement non-hélicitaire et un écoulement aléatoire en temps.

En ce qui concerne le comportement des modes de grande échelle des écoulements solutions de l'équation de Navier-Stokes, le spectre d'énergie contient beaucoup d'informations sur un écoulement, mais la description d'un champ de vitesse ne peut se limiter à son spectre d'énergie. En particulier, le spectre d'énergie ne donne pas d'information sur la dynamique temporelle de l'écoulement. La fonction de corrélation est l'outil statistique qui est généralement utilisé pour mesurer les corrélations temporelles d'une grandeur physique. Si le comportement des modes dont l'échelle est plus grande que l'échelle de forçage doit ressembler au comportement de l'équation d'Euler tronquée, leurs corrélations temporelles devraient aussi se ressembler.

Des résultats sont déjà connus sur les corrélations temporelles des modes du champ de vitesse. Comme décrit dans [18, 19], au sein de la cascade de Kolmogorov, les corrélations temporelles eulériennes des modes du champ de vitesse sont régies par la vitesse quadratique moyenne du mode de forçage. Étant donné que la majeure partie de l'énergie est concentrée dans le mode de forçage, la vitesse quadratique moyenne est comparable à la racine carrée de l'énergie moyenne de l'écoulement. La seule échelle de temps pouvant être construite à l'aide de la vitesse quadratique moyenne, U_{rms}, et le nombre d'onde, k, est $(kU_{rms})^{-1}$. Des études [20, 6] ont proposé qu'il y ait un impact de l'hélicité sur le temps de corrélation, mais aucune expression exacte n'a été établie concernant le temps de corrélation des équilibres absolus.

• **Dans la partie C**, nous utiliserons une approximation parabolique pour calculer le temps de corrélation d'équilibres absolus solutions de l'équation d'Euler tronquée. Nous montrerons que les écoulements avec une quantité d'hélicité modérée ont un temps de corrélation qui suit la même loi d'échelle que celle associée à l'effet de balayage dans la cascade de Kolmogorov. En revanche, pour les écoulements très hélici-

taires, nous montrerons que le temps de corrélation semble suivre une autre loi d'échelle proportionnelle à $k^{-\frac{1}{2}}$. Cette loi d'échelle est compatible avec un temps caractéristique basé sur l'hélicité. Pour confirmer l'existence de cette nouvelle loi d'échelle, nous montrerons, à l'aide de simulations numériques directes, que les séries temporelles des modes du champ de vitesse ont bien un temps de corrélation qui suit une loi d'échelle en $k^{-\frac{1}{2}}$ pour de grands nombres de Kraichnan. Nous utiliserons la même procédure pour analyser le temps de corrélation des modes de grande échelle de champs de vitesse solutions de l'équation de Navier-Stokes. Nous montrerons que le temps de corrélation d'écoulements sans hélicité suit la même loi d'échelle que celle des équilibres absolus sans hélicité. En revanche, le temps de corrélation des écoulements fortement hélicitaires testés ne montre pas de comportement en loi d'échelle en $k^{-\frac{1}{2}}$.

Nous présenterons aussi des résultats sur des méthodes numériques dans la partie E qui sont totalement indépendants de la thématique principale de ce manuscrit. Enfin, dans la suite de ce chapitre de présentation, nous résumerons les résultats principaux de ce manuscrit en langue française.

Les chapitres dont le titre commence par *Elements of context* **présentent des éléments de théories déjà établies. Les nouveaux résultats sont présentés dans les chapitres dont le titre finit par la mention** *published* **ou** *submitted*.

0.2 Résultats sur les instabilités grande échelle

L'objectif de cette section est de présenter succinctement les résultats principaux obtenus lors de l'étude d'instabilité grande échelle pour des nombres de Reynolds modérés. Nous commencerons tout d'abord par rappeler les équations régissant l'évolution des instabilités de grande échelle dans le cas de l'effet alpha magnétique. Nous utiliserons ensuite la théorie établie à faible nombre de Reynolds magnétique pour avoir une extrapolation du comportement à des nombres de Reynolds magnétiques modérés. Nous présenterons aussi des résultats associés aux instabilités grande échelle dans le cas hydrodynamique.

0.2.1 Équation d'évolution des instabilités de type alpha

Dans les fluides conducteurs se déplaçant selon le champ de vitesse $\boldsymbol{u}$, le champ magnétique $\boldsymbol{B}$ suit l'équation d'induction donnée par

$$\partial_t \boldsymbol{B} = \boldsymbol{\nabla} \times (\boldsymbol{u} \times \boldsymbol{B}) + \eta \Delta \boldsymbol{B} \quad \text{avec} \quad \boldsymbol{\nabla} \cdot \boldsymbol{B} = 0\,. \tag{0.7}$$

où η correspond à la viscosité magnétique du milieu. Comme l'ont montré Steenbeck *et al.* [16], il est possible d'engendrer dans des fluides conducteurs un champ magnétique de grande échelle à partir de certains écoulements de petite échelle. Ce phénomène est désigné comme une instabilité de type alpha et est souvent utilisé pour expliquer l'apparition de champs magnétiques astrophysiques. Dans [17], Childress a réussi à caractériser à l'aide d'une approche multi-échelle les instabilités de type alpha à faible nombre de Reynolds magnétique $Rm = \ll 1$ où $Rm = \frac{U}{\eta k_f}$ où U correspond à la vitesse caractéristique de l'écoulement et k_f correspond au nombre d'onde caractéristique de l'écoulement. L'approche multi-échelle n'est en revanche pas valide pour décrire

le comportement grand échelle du champ magnétique à grand nombre de Reynolds magnétique.

Un phénomène d'instabilité grande échelle, l'effet AKA [13, 14], est aussi présent pour les perturbations du champ de vitesse dans le cas de fluides suivant l'équation de Navier-Stokes. En effet, lorsqu'on écrit l'évolution d'un fluide visqueux en fonction de sa vorticité, on obtient l'équation d'évolution suivante

$$\partial_t \boldsymbol{\omega} = \boldsymbol{\nabla}\times(\boldsymbol{u}\times\boldsymbol{\omega}) + \nu\Delta\boldsymbol{\omega} + \boldsymbol{\nabla}\times\boldsymbol{F} \quad \text{avec} \quad \boldsymbol{\nabla}\cdot\boldsymbol{u} = 0 \quad \text{et} \quad \boldsymbol{\omega} = \boldsymbol{\nabla}\times\boldsymbol{u}\,. \tag{0.8}$$

où $\boldsymbol{F}$ correspond au forçage volumique imposé sur le fluide. Mis à part le terme de forçage, l'équation d'évolution de la vorticité a une expression proche de celle du champ magnétique. Il est tout de même important de noter que le champ de vorticité est relié au champ de vitesse par $\boldsymbol{\omega} = \boldsymbol{\nabla}\times\boldsymbol{u}$, ce qui n'est pas le cas du champ magnétique. Cette relation supplémentaire conduit à des conditions nécessaires différentes pour engendrer une perturbation de grande échelle.

Étant donné que les effets alpha et AKA ont des mécanismes d'action proches, nous rappellerons uniquement les équations permettant de calculer l'effet alpha. Pour établir les caractéristiques de l'effet alpha, le champ magnétique est séparé en une composante petite échelle $\boldsymbol{b}$ et une composante grande échelle $\langle\boldsymbol{B}\rangle_{V_\ell}$ et peut s'exprimer comme $\boldsymbol{B} = \langle\boldsymbol{B}\rangle_{V_\ell} + \boldsymbol{b}$. Les équations d'évolution de ces composantes sont données par

$$\partial_t \boldsymbol{b} = \boldsymbol{\nabla}\times(\boldsymbol{u}\times\langle\boldsymbol{B}\rangle_{V_\ell}) + \boldsymbol{\nabla}\times\boldsymbol{\mathcal{G}} + \eta\Delta\boldsymbol{b} \quad \text{avec} \quad \boldsymbol{\nabla}\cdot\boldsymbol{b} = 0\,, \tag{0.9}$$

$$\partial_t \langle\boldsymbol{B}\rangle_{V_\ell} = \boldsymbol{\nabla}\times\boldsymbol{\mathcal{E}} + \eta\Delta\boldsymbol{B} \quad \text{avec} \quad \boldsymbol{\nabla}\cdot\boldsymbol{B} = 0\,, \tag{0.10}$$

$$\text{où} \quad \boldsymbol{\mathcal{G}} = (\boldsymbol{u}\times\boldsymbol{b} - \langle\boldsymbol{u}\times\boldsymbol{b}\rangle_{V_\ell}) \quad \text{et} \quad \boldsymbol{\mathcal{E}} = \langle\boldsymbol{u}\times\boldsymbol{b}\rangle_{V_\ell}\,. \tag{0.11}$$

où $\langle\ldots\rangle_{V_\ell}$ désigne la valeur moyennée sur les petites échelles. Dans le cas où le terme $\mathcal{G}$ est négligé dans l'éq. 0.9 (par example quand $Rm \to 0$ ou quand le temps de correlation du champ de vitesse est très faible devant uk_f) et où le champ vitesse conduit à un effet alpha, l'amplitude des composantes du champ magnétique peut être décrite par le modèle simplifié décrit par le système d'équations différentielles suivant

$$\frac{\partial}{\partial t}\begin{bmatrix}\langle B\rangle_{V_\ell}\\ b\end{bmatrix} = M\begin{bmatrix}\langle B\rangle_{V_\ell}\\ b\end{bmatrix} \quad \text{avec} \quad M = \begin{bmatrix}-\eta q^2 & qU\\ kU & \gamma_{SSD}\end{bmatrix}, \tag{0.12}$$

$$\text{d'où} \quad \gamma = \frac{1}{2}\left(\gamma_{SSD} - \eta q^2 + \sqrt{4qkU^2 + (\gamma_{SSD} + \eta q^2)^2}\right)\,. \tag{0.13}$$

où γ correspond au taux de croissance du champ magnétique ayant la plus grande valeur propre, γ_{SSD} correspond au taux de croissance du champ magnétique en l'absence de composante grande échelle, q correspond au nombre d'onde de la composante grande échelle du champ magnétique et k correspond au nombre d'onde associé au champ de vitesse. Le système d'équations exactes régissant l'évolution des amplitudes des composantes du champ magnétique nécessite de connaitre l'expression précise du champ de vitesse. L'éq. (0.12) correspond à un modèle jouet où l'amplitude des champs est prise en compte mais où leur géométrie n'est pas considérée. Certains écoulements, notamment ceux qui ne conduisent pas à des effets alpha, ne peuvent pas être décrits par ces équations. Ce modèle jouet n'est donc valable qu'à petits nombres de Reynolds magnétiques. En plus de donner une expression pour le taux de croissance,

le modèle jouet nous donne aussi le rapport entre la composante petite échelle et la composante grande échelle du champ magnétique ayant la plus grande valeur propre. Avec les paramètres de la matrice M, on a

$$\frac{\langle B\rangle_{V_\ell}}{b} = -\frac{\gamma_{SSD} + q^2\eta - \sqrt{4kqU^2 + \left(\gamma_{SSD} + \eta q^2\right)^2}}{2kU}\,. \tag{0.14}$$

Seuil d'instabilité petite échelle	Avant	Après
Taux de croissance :	$\frac{\gamma}{kU} \simeq Rm\left(\frac{q}{k}\right) - \frac{1}{Rm}\left(\frac{q}{k}\right)^2$	$\gamma \simeq \gamma_k$
Rapport d'amplitude :	$\langle B\rangle_{V_\ell}/b \simeq \frac{1}{Rm}$	$\langle B\rangle_{V_\ell}/b \simeq q\frac{U}{\gamma_k}$
Rapport d'énergie :	$\frac{E_0}{E_{tot}} \underset{Rm \ll 1}{\simeq} 1 - Rm^2$	$\frac{E_0}{E_{tot}} \simeq \left(q\frac{U}{\gamma_k}\right)^2$

TABLE 0.1 – Propriétés du champ magnétique de grande échelle pour un écoulement conduisant à un effet alpha avant et après le seuil d'instabilité petite échelle $q \ll k$. Les résultats sont exprimés en fonction du nombre de Reynolds magnétique $Rm = \frac{U}{\eta k}$.

A l'aide des éq. (0.13) et (0.14), nous pouvons trouver le comportement du champ magnétique avant le seuil d'instabilité petite échelle, *i.e.* dans la limite de petits nombres Reynolds magnétiques ; dans ce cas, $\gamma_{SSD} \simeq -\eta k^2$. Même si le développement analytique de l'effet alpha n'est plus valide après l'apparition d'instabilités grande échelle, on peut tout de même calculer le taux de croissance de l'instabilité et le rapport d'amplitude de l'instabilité avec ce modèle en posant $\gamma_{SSD} > 0$. Les propriétés associées à ce modèle sont rassemblées dans tableau 0.1. Elles indiquent qu'après le seuil d'instabilité petite échelle, l'évolution du champ magnétique est déterminée principalement par la dynamique dans les petites échelles.

0.2.2 Méthode de Floquet

Pour analyser les instabilités grande échelle magnétiques et cinétiques, nous allons employer une méthode de Floquet numérique. Dans le cas de l'équation d'induction, la méthode de Floquet correspond à utiliser le changement de variable $\boldsymbol{b} = e^{\imath \boldsymbol{q}\cdot\boldsymbol{r}}\tilde{\boldsymbol{b}} + c.c.$ qui conduit à l'équation d'évolution suivante pour l'amplitude de Floquet du champ magnétique

$$\partial_t \tilde{\boldsymbol{b}} = \imath\boldsymbol{q}\times(\boldsymbol{u}\times\tilde{\boldsymbol{b}}) + \boldsymbol{\nabla}\times(\boldsymbol{u}\times\tilde{\boldsymbol{b}}) + \eta\left(\boldsymbol{\nabla} + \imath\boldsymbol{q}\right)^2\tilde{\boldsymbol{b}} \quad \text{et} \quad (\imath\boldsymbol{q}\cdot + \boldsymbol{\nabla}\cdot)\tilde{\boldsymbol{b}} = 0\,. \tag{0.15}$$

où les champs $\boldsymbol{u}$ et $\tilde{\boldsymbol{b}}$ ont la même périodicité. En utilisant le changement de variable de Floquet, on a introduit un nouveau paramètre $\boldsymbol{q}$ qui est le vecteur d'onde de Floquet. Suivant la valeur de $\boldsymbol{q}$, on peut moduler la séparation d'échelle entre $\boldsymbol{b}$ et $\boldsymbol{u}$. Ces équations permettent de tester le modèle jouet présenté précédemment en modélisant une seule période de l'écoulement. Elles peuvent être intégrées numériquement en utilisant une méthode pseudo-spectrale. On peut ainsi atteindre des séparations d'échelle

de plusieurs ordres de grandeur qui ne sont pas possibles en intégrant directement les équations sans effectuer le changement de variable de Floquet.

La même méthode peut être utilisée pour étudier l'équation de Navier-Stokes linéarisée. Le champ de vitesse peut être décomposé en un champ principal $\boldsymbol{U}$ et une perturbation $\boldsymbol{v}$ de sorte que $\boldsymbol{u} = \boldsymbol{U} + \boldsymbol{v}$. La méthode de Floquet correspond à utiliser ensuite le changement de variable $\boldsymbol{v} = e^{\imath \boldsymbol{q}\cdot\boldsymbol{r}}\tilde{\boldsymbol{v}} + c.c.$ qui conduit à l'équation d'évolution suivante pour l'amplitude de Floquet de la perturbation du champ de vitesse

$$\partial_t \tilde{\boldsymbol{v}} = \tilde{\boldsymbol{v}} \times (\boldsymbol{\nabla} \times \boldsymbol{U}) + \boldsymbol{U} \times (\imath \boldsymbol{q} + \boldsymbol{\nabla} \times \boldsymbol{v}) - (\imath \boldsymbol{q} + \boldsymbol{\nabla})\tilde{p} + \nu \left(\boldsymbol{\nabla} + \imath \boldsymbol{q}\right)^2 \tilde{\boldsymbol{v}} \,. \tag{0.16}$$

Tout comme dans le cas magnétique, les champs U et $\tilde{\boldsymbol{v}}$ ont la même périodicité.

0.2.3 Instabilités magnétiques

Afin de tester le modèle à deux modes décrivant les instabilités grandes échelles, nous allons utiliser une variante du champ de ABC [15] qui prend la forme suivante

$$\boldsymbol{u} = U \begin{bmatrix} \sin(ky + \phi_2) & + & \cos(kz + \psi_3) \\ \sin(kz + \phi_3) & + & \cos(kx + \psi_1) \\ \sin(kx + \phi_1) & + & \cos(ky + \psi_2) \end{bmatrix}. \tag{0.17}$$

où U est l'intensité du champ de vitesse, k est le module du nombre d'onde et les ϕ_i et ψ_i sont des phases qui peuvent être modulées afin de décrire différents écoulements. Nous allons étudier dans le cas (A) un écoulement hélicitaire avec $\phi_i = \psi_i = 0$ pour $i \in \{1; 2; 3\}$, dans le cas (B) un écoulement non-hélicitaire avec $\phi_i = \psi_i - \pi/2 = 0$ pour $i \in \{1; 2; 3\}$ et dans le cas (C) un écoulement hélicitaire avec les phases delta-corrélées en temps mais vérifiant aussi $\phi_i = \psi_i$ pour $i \in \{1; 2; 3\}$.

Les résultats numériques obtenus sont présentés à la fig. 0.6. Sur le panneau de gauche, les résultats obtenus sans la méthode de Floquet sont représentés par une ligne verte continue et ceux obtenus avec la méthode de Floquet sont représentés par des croix. On remarque qu'en accord avec le modèle à deux modes, avant le seuil de transition de l'instabilité petite échelle, les résultats obtenus avec la méthode de Floquet conduisent à un taux de croissance nul alors que ceux obtenus sans la méthode de Floquet conduisent à un taux de croissance négatif. Après le seuil de transition de l'instabilité, les deux méthodes conduisent au même taux de croissance, ce qui est aussi prévu par le modèle à deux modes.

L'analyse du taux de croissance de l'instabilité présenté dans le panneau central est aussi en accord avec le modèle à deux modes. Avant le seuil d'instabilité petite échelle, le taux de croissance dans les écoulements (A) et (C) est proportionnel à q, ce qui est en accord avec un effet de type alpha. Ce taux de croissance devient indépendant de q après l'apparition de l'instabilité de petite échelle. Dans le cas de l'écoulement (B) le taux de croissance est proportionnel à q^2, ce qui correspond à un effet de type beta. En effet, l'écoulement (B) n'est pas propice à la création d'un effet alpha car il n'est pas hélicitaire. On observe pourtant la disparition de la loi d'échelle en q^2 après le seuil d'apparition de l'instabilité petite échelle comme dans le cas de l'effet alpha.

Le changement de loi d'échelle du champ magnétique lors de l'apparition de l'instabilité petite échelle peut aussi être observé sur le rapport entre l'énergie présente

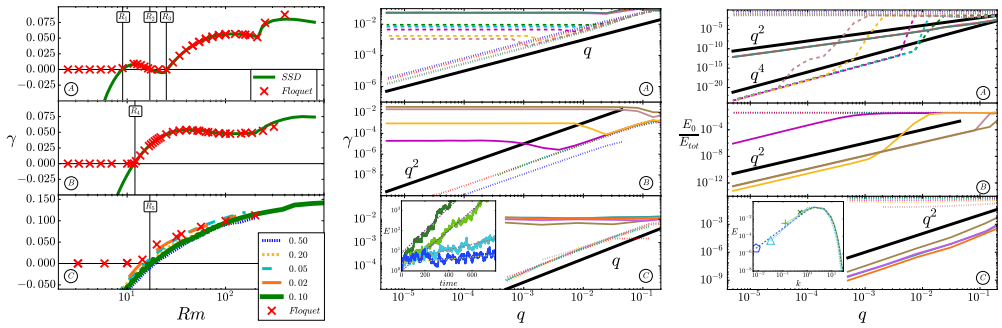

FIGURE 0.6 – Gauche) Taux de croissance en fonction du Reynolds magnétique Rm pour les différents écoulements. Les taux de croissance des instabilités de petite échelle sont représentés par des lignes. Les taux de croissance calculés avec la méthode de Floquet sont représentés par des croix. Centre) Taux de croissance en fonction de q pour différentes valeurs de Rm. La légende des encarts est la suivante : encart (A) : pointillés pour $Rm < R_1$ et $R_2 < Rm < R_3$, tirets pour $R_1 < Rm < R_2$, lignes pour $R_3 < Rm$; encart (B) : pointillés pour $Rm < R_4$, lignes pour $R_4 < Rm$; encart (C) : pointillés pour $Rm < R_5$, lignes pour $R_5 < Rm$. L'encart (D) représente un signal typique pour l'évolution de l'énergie pour des écoulements de type (C) dans le cas où $Rm < R_5$. Droite) Rapport d'énergie E_0/E_{tot}. La légende des écarts est la même qu'au panneau central. L'encart (D) représente le spectre d'énergie typique pour des écoulements de type (C) au plus grand Rm.

dans les modes de grande échelle et l'énergie totale. Les lois d'échelles observées avec les simulations numériques effectuées avec la méthode de Floquet sont en accord avec les expressions obtenues par le modèle à deux modes et rappelées dans le tab. 0.1.

Même si les méthodes de développement multi-échelle ne sont plus valides à grand nombre de Reynolds magnétique, le modèle à deux modes est en mesure de décrire les comportements généraux de l'instabilité du champ magnétique. Les résultats présentés montrent que pour les différents écoulement étudiés, même dans un cadre purement cinématique, la dynamique du champ magnétique est régie par le comportement des petites échelles une fois que le seuil d'instabilité petite échelle est franchi.

0.2.4 Instabilité hydrodynamiques

Les comportements grande échelle des perturbations du champ de vitesse peuvent aussi être étudiés en utilisant des simulations numériques avec la méthode de Floquet. On peut ainsi quantifier l'instabilité AKA de l'écoulement présenté dans [13]. Le mécanisme conduisant à l'effet AKA peut aussi être observé à des nombres de Reynolds modérés. Certains écoulements hélicitaires qui ne produisent pas d'effet AKA peuvent aussi donner lieu à des instabilités comparables à une viscosité négative. Dans le cas de l'écoulement ABC [15], l'effet de viscosité négative conduit à une instabilité grande échelle dont le seuil se trouve avant l'instabilité petite échelle. Elle peut être observée en mesurant l'énergie totale de l'écoulement en fonction du nombre de Reynolds pour différentes séparations d'échelles. On peut ainsi observer sur la fig. 0.7 que pour des grandes séparations d'échelle $KL \in \{5; 10; 20\}$, l'énergie de l'écoulement diminue pour un nombre de Reynolds critique proche de 3, alors que l'énergie de l'écoulement ne diminue qu'à partir d'un nombre de Reynolds proche de 13.5 dans le cas d'une sépa-

ration d'échelle de 1. Par ailleurs, la valeur du seuil de l'instabilité grande échelle est prédite par les simulations numériques utilisant la méthode de Floquet.

La méthode de Floquet permet donc de repérer les instabilités de grande échelle engendrées par un écoulement si elles ont lieux avant le seuil des instabilités de petite échelle. A l'aide de simulations numériques avec la méthode Floquet, on peut quantifier les instabilités grandes échelles et trouver les seuils d'instabilités liés à des effets de viscosité négative.

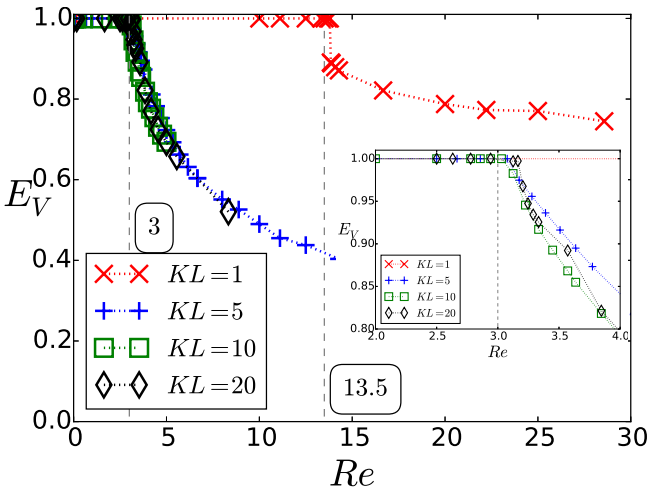

FIGURE 0.7 – Bifurcation : énergie totale de l'écoulement en fonction du nombre de Reynolds pour différentes séparations d'échelle $KL \in \{1; 5; 10; 20\}$. L'encart montre un agrandissement du graphique au niveau du seuil de l'instabilité grande échelle pour $Re \in [2; 5]$.

0.3 Résultats sur les temps de corrélation

L'objectif de cette section est de présenter succinctement quelques résultats concernant les points communs entre les modes de grande échelle d'écoulements solutions de Navier-Stokes et les solutions de l'équation d'Euler tronquée. Pour ce faire, deux caractéristiques principales des écoulements seront analysées, le spectre d'énergie et le temps de corrélation des modes du champ de vitesse. Nous commencerons par développer un modèle thermodynamique permettant d'avoir un résultat analytique sur le temps de corrélation, puis nous détaillerons la procédure numérique utilisée pour mesurer les corrélations dans des simulations numériques. Nous présenterons ensuite quelques caractéristiques de solutions numériques de l'équation d'Euler tronquée et de l'équation de Navier-Stokes forcée.

0.3.1 Modèle thermodynamique

Un fluide idéal tronqué spectralement suit l'équation d'Euler tronquée et conserve donc son énergie et son hélicité. Comme l'a montré Kraichnan [11], les statistiques des modes de Fourier du champ de vitesse suivent une généralisation des poids de Boltzmann qui prend en compte la conservation de l'hélicité. En fonction des conditions initiales du système, l'écoulement peut être décrit par deux paramètres α et β qui définissent la

densité de probabilité du système de se trouver dans un état donné. En effet, proche de l'équilibre, la densité de probabilité du système est proportionnelle à

$$e^{-\alpha(2E-\frac{\mathcal{K}r}{k_M}H)} \quad \text{avec} \quad \mathcal{K}r = -\frac{\beta k_M}{\alpha}\,. \tag{0.18}$$

Ce modèle a permis à Kraichnan de calculer le spectre d'énergie moyen des équilibres absolus. Il peut aussi être utilisé pour calculer le temps de corrélation des équilibres absolus à l'aide d'une approximation parabolique de la fonction de corrélation $\Gamma_k(t)$ des modes de la vitesses. En effet, aux temps courts, la fonction de corrélation du champ de vitesse peut être écrite comme

$$\Gamma_{\boldsymbol{k}}(t) = \frac{\overline{\boldsymbol{u}_{\boldsymbol{k}}^*(s)\boldsymbol{u}_{\boldsymbol{k}}(s+t)}}{\overline{|\boldsymbol{u}_{\boldsymbol{k}}(s)|^2}} = \frac{\overline{\boldsymbol{u}_{\boldsymbol{k}}^*(s)\boldsymbol{u}_{\boldsymbol{k}}(s)}}{\overline{|\boldsymbol{u}_{\boldsymbol{k}}(s)|^2}} + \frac{t^2}{2}\frac{\overline{\boldsymbol{u}_{\boldsymbol{k}}^*(s)\partial_t^2\boldsymbol{u}_{\boldsymbol{k}}(s)}}{\overline{|\boldsymbol{u}_{\boldsymbol{k}}(s)|^2}} + \mathcal{O}(t^4)\,. \tag{0.19}$$

où $\overline{G(s)}$ correspond à la moyenne d'une observable générique G sur la variable s qui correspond au temps, et $\boldsymbol{u}_{\boldsymbol{k}}(s)$ correspond au mode du champ de vitesse. En supposant que le système est ergodique, on peut échanger les moyennes temporelles par des moyennes sur des ensembles thermodynamiques $\langle \ldots \rangle$ et calculer le temps de corrélation provenant de l'approximation parabolique

$$\tau_k = \sqrt{\frac{\langle|\partial_t \boldsymbol{u}_{\boldsymbol{k}}|^2\rangle}{\langle|\boldsymbol{u}_{\boldsymbol{k}}|^2\rangle}}\,. \tag{0.20}$$

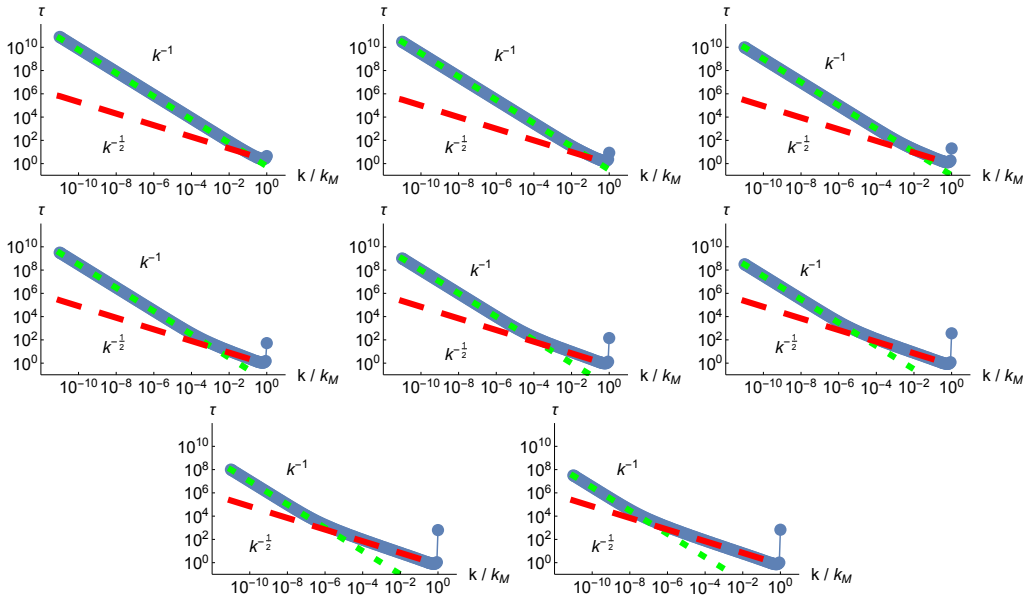

FIGURE 0.8 – Temps de corrélation calculé avec l'approximation parabolique en fonction du nombre d'onde pour $1-\mathcal{K}r \in \{10^{-1}, 10^{-2}, 10^{-3}, 10^{-4}, 10^{-5}, 10^{-6}, 10^{-7}, 10^{-8}\}$. La ligne pleine représente les résultats obtenus avec Mathematica, les tirets représentent la loi de puissance en $k^{-\frac{1}{2}}$ et les pointillés représentent la loi de puissance en k^{-1}.

Le calcul du temps de corrélation ne peut pas être effectué de manière analytique jusqu'à son terme. Il est nécessaire de calculer une intégrale de manière numérique. Le temps de corrélation obtenu via Mathematica est présenté à la fig. 0.8.

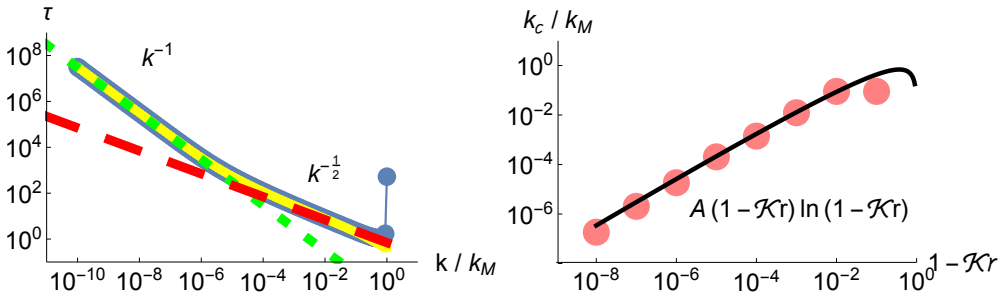

FIGURE 0.9 – Gauche) Temps de corrélation en fonction du nombre d'onde pour $1-\mathcal{K}r = 10^{-6}$. Les résultats semi-analytiques du temps de corrélation sont représentés par la ligne avec les points foncés. Les points clairs représentent le temps de corrélation de la composante d'hélicité négative du champ de vitesse. La loi d'échelle en $k^{-1/2}$ est représentée par des tirets. La loi d'échelle en k^{-1} est représentée par des pointillés. Droite) Nombre d'onde critique en fonction de $1 - \mathcal{K}r$, les résultats semi-analytiques sont représentés par des points et la loi de puissance $A(1 - \mathcal{K}r)\ln(1 - \mathcal{K}r)$ est représentée par une ligne.

On peut observer que lorsque l'écoulement devient très hélicitaire $\mathcal{K}r \to 1$, le temps de corrélation des modes du champ de vitesse suit deux lois de puissance. La première loi de puissance est proportionnelle à k^{-1} qui est compatible avec un temps de corrélation formé à partir de l'énergie. La seconde loi d'échelle en $k^{-\frac{1}{2}}$ est compatible avec un temps de corrélation formé à partir de l'hélicité. Le nombre d'onde critique où le temps de corrélation change de loi d'échelle est représenté à la fig. 0.9. Même s'il n'est pas aisé de calculer le temps de corrélation pour tous les nombres d'onde, on peut calculer le comportement asymptotique des temps de corrélation en fonction du nombre de Kraichnan et trouver le lieu de coexistence des deux lois d'échelle des temps de corrélation. La ligne noire sur le panneau de droite de la fig. 0.9 montre la loi d'échelle obtenue à l'aide du calcul asymptotique.

Le calcul thermodynamique du temps de corrélation du champ vitesse indique qu'il est possible d'avoir deux régimes pour le temps de corrélation. Le premier régime est régi par l'énergie et le second régime est régi par l'hélicité. La prochaine section s'attardera à expliquer comment le temps de corrélation des modes de la vitesse peut être mesuré dans le cas de simulations numériques.

0.3.2 Procédure d'évaluation numérique

Le calcul de corrélations temporelles n'est pas chose aisée à mesurer dans le cas de simulations numériques car il nécessite de produire et de conserver de longues séries temporelles. Pour limiter le nombre de données à conserver sans pour autant perdre trop d'information sur les corrélations temporelles des différents modes, nous avons uniquement conservé les séries temporelles des modes qui se trouvent sur les plans à $k_x = 0$, $k_y = 0$ et $k_z = 0$. Pour évaluer le temps de corrélation, nous avons d'abord calculé le spectre de puissance de l'écoulement $S(k, \omega)$ avant de calculer les fonctions de corrélation $\Gamma(k, t)$. Nous avons ensuite utilisé le temps pour lequel la fonction de corrélation atteint la mi-hauteur pour calculer le temps de corrélation.

La fig.0.10 représente le spectre de puissance et les fonctions de corrélation d'un équilibre absolu solution de l'équation d'Euler tronquée avec les symétries de Taylor-

Green. On remarque bien que les nombres d'onde où le spectre de puissance est resserré au niveau des petites pulsations correspondent aux nombres d'onde qui ont la fonction de corrélation la plus étalée.

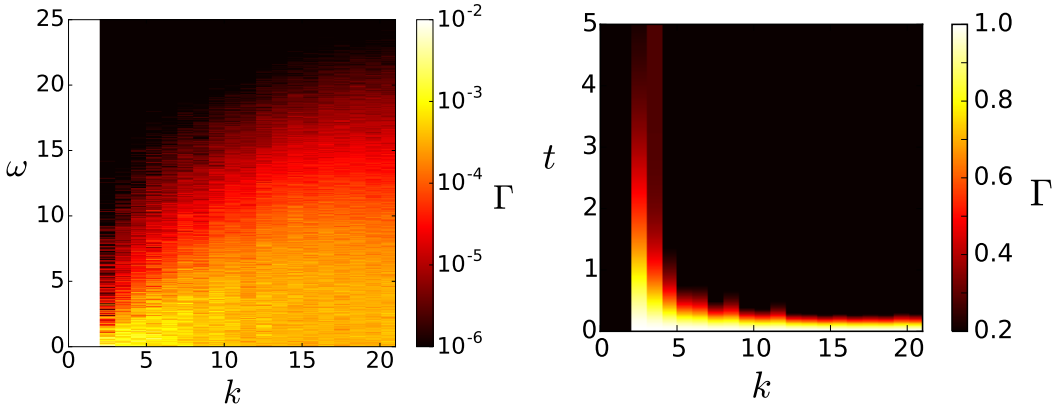

FIGURE 0.10 – Spectre spatio-temporel de simulations numériques de l'équation d'Euler tronquée avec les symétries Taylor-Green. Gauche) Spectre de puissance $S(k,\omega)$. Droite) Fonction de corrélation $\Gamma(k,t)$.

0.3.3 Résultats de simulations numériques

Avec la procédure de calcul du temps de corrélation, il est maintenant possible de tester la théorie thermodynamique établie pour les équilibres absolus. La même procédure peut aussi être utilisée pour évaluer si les modes en amont du forçage des solutions de l'équation de Navier-Stokes forcée ont une dynamique temporelle proche de celle des équilibres absolus.

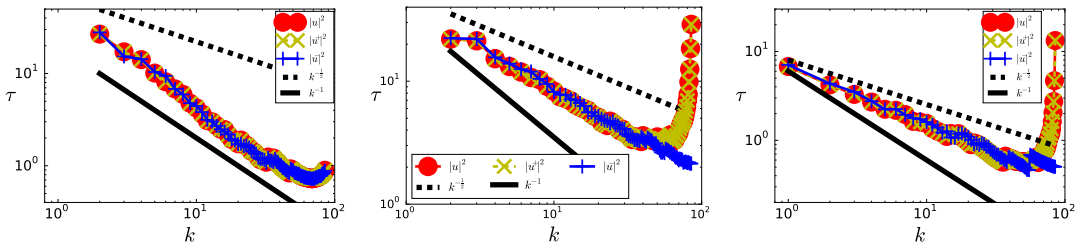

FIGURE 0.11 – Temps de corrélation pour des simulations de l'équation d'Euler tronquée. Gauche) Écoulement non-hélicitaire $\mathcal{K}r = 0$. Centre) Écoulement avec de l'hélicité $\mathcal{K}r = 0.85$. Droite) Écoulement très hélicitaire $\mathcal{K}r = 0.9$.

La fig. 0.11 montre les résultats obtenus par l'analyse du temps de corrélation de simulations de l'équation d'Euler tronquée pour différentes valeurs du nombre de Kraichnan. On peut voir qu'à petit nombre de Kraichnan, le temps de corrélation suit une loi d'échelle en k^{-1} alors que pour des nombres de Kraichnan proches de 1, la loi d'échelle du temps de corrélation change de pente et finit par suivre une loi de puissance en $k^{-\frac{1}{2}}$. Ce changement de loi d'échelle est en parfait accord avec le calcul thermodynamique du temps de corrélation mais la résolution des simulations

numériques ne permet pas d'observer le changement de pente aussi nettement que dans le cas du calcul thermodynamique.

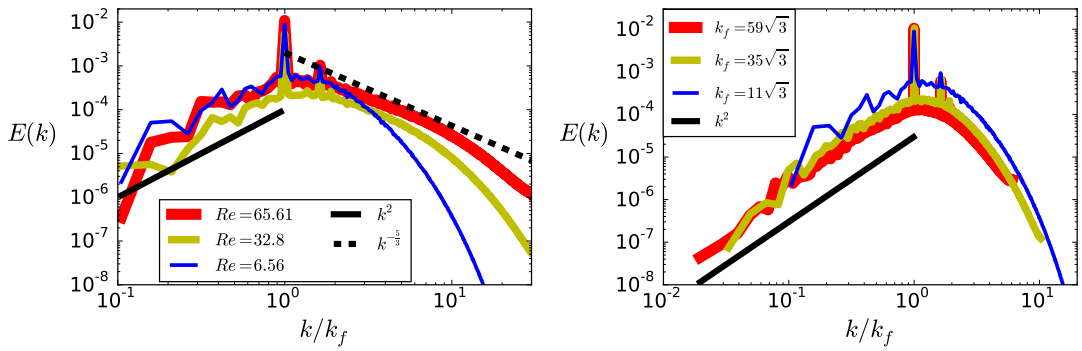

FIGURE 0.12 – Spectre d'énergie de simulations numériques de l'équation de Navier-Stokes forcée avec les symétries Taylor-Green. Gauche) Nombre d'onde de forçage fixé à $k_f = 19$ pour différents nombres de Reynolds $Re \in \{204; 1021; 2041\}$. Droite) Produit viscosité-nombre d'onde de forçage fixé à $\nu k_f = 2 \cdot 10^{-2}$ pour différent nombre d'onde de forçage $k_f \in \{19; 60; 102\}$.

Les fig. 0.12 et 0.13 présentent quelques résultats sur les modes de grande échelle de solutions de l'équation de Navier-Stokes forcée pour des écoulements respectant les symétries d'écoulement de type Taylor-Green. La fig. 0.12 montre que, dans les grandes échelles, le spectre d'énergie de l'écoulement correspond bien au spectre d'équipartition de l'énergie avec $E(k) \propto k^2$. Sur le panneau de gauche, on peut observer au plus grand nombre de Reynolds que le spectre d'énergie suit aussi la loi d'échelle de Kolmogorov en $k^{-\frac{5}{3}}$ pour des nombres d'onde dans le régime inertiel. Les spectres d'énergie provenant d'écoulements à des nombres de Reynolds plus petits montrent que la loi d'échelle d'équipartition d'énergie des modes en amont du forçage peut être observée avant d'observer la loi d'échelle de Kolmogorov. On peut ainsi étudier l'équivalence entre les équilibres absolus et les solutions de l'équation de Navier-Stokes forcée à de plus petits nombres de Reynolds. Le panneau de droite présente le spectre d'énergie d'écoulement avec différentes séparations d'échelle avec des produits viscosité sur nombre d'onde de forçage identiques à la simulation avec le plus petit nombre de Reynolds présentée dans le panneau de droite. Cette étude de convergence permet de mettre clairement en évidence la loi d'échelle en k^2 caractéristique de l'équipartition en énergie.

La fig. 0.13 présente les résultats sur les corrélations temporelles des modes du champ de vitesse d'écoulement respectant les symétries Taylor-Green. Tout comme le spectre d'énergie, on peut observer que sur le panneau de gauche, le temps de corrélation converge plus rapidement vers un régime indépendant du nombre de Reynolds dans les grandes échelles que dans les petites échelles. Sur le panneau de droite, on observe que le temps de corrélation des modes du champ de vitesse suit une loi de puissance en k^{-1} qui est compatible avec le temps de corrélation observé dans le cas d'équilibres absolus.

Dans le cas d'écoulements respectant les symétries Taylor-Green, les simulations numériques directes ont mis en évidence des comportements comparables du spectre d'énergie et du temps de corrélation des modes du champ de vitesse de solutions de l'équation d'Euler tronquée et des modes en amont du forçage pour des écoulements

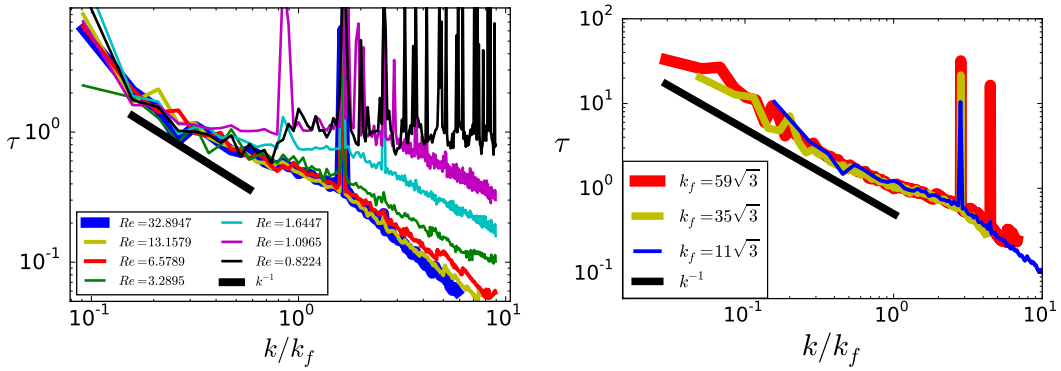

FIGURE 0.13 – Temps de corrélation de simulations numériques de l'équation de Navier-Stokes forcée pour des écoulements avec les symétries Taylor-Green. Gauche) Nombre d'onde de forçage fixé à $k_f = 19$ et viscosité variable. Droite) Produit viscosité-nombre d'onde de forçage fixé à $\nu k_f = 2 \cdot 10^{-2}$ pour des nombres d'onde variables $k_f \in \{19; 60; 102\}$.

solutions de l'équation de Navier-Stokes forcée.

Chapter 1

Introduction

The Navier-Stokes equation is commonly used in astrophysics, physics and engineering to model flows. But since the first use of the equation in the middle of the nineteenth century, no general exact solutions have been found. Proving that the solutions of the Navier-Stokes equation exist and are smooth was even deemed by the Clay Mathematics Institute to be one the seven Millennium Prize Problems with a one million dollar reward [21].

On a more physical point of view, the Navier-Stokes equation was established to describe the evolution of the motion of viscous fluids. The equation comes from the combination of the linear expansion of stresses in a continuous medium with Newton's second law. In physical space, the Navier-Stokes equation can be expressed for incompressible flows as

$$\partial_t \boldsymbol{u} + (\boldsymbol{u}\cdot\boldsymbol{\nabla})\boldsymbol{u} = -\boldsymbol{\nabla}P + \nu\Delta\boldsymbol{u} + \boldsymbol{F} \quad \text{with} \quad \boldsymbol{\nabla}\cdot\boldsymbol{u} = 0\,, \tag{1.1}$$

where $\boldsymbol{u}$, P, ν, $\boldsymbol{F}$ denote the velocity field, the pressure field, the viscosity and the force field respectively. In the flows considered in this manuscript, the viscosity is a stationary (independent of time) and uniform (independent of space) parameter fixed by the operator either by changing the parameter of the simulation or changing the fluid in an experiment. The forcing field can depend on space and time and is also fixed by the operator. The velocity and pressure fields are the variables of the problem. They depend on space and time and are not directly fixed by the operator since they are solution of the differential eq. (1.1). Hence, to find a solution to the differential problem, initial and boundary conditions have also to be set on the velocity field. The pressure field is directly related to the velocity field via the solenoidal condition $\boldsymbol{\nabla}\cdot\boldsymbol{u} = 0$. It can be derived by solving the Poisson equation

$$\Delta P = -\boldsymbol{\nabla}\cdot\Big((\boldsymbol{u}\cdot\boldsymbol{\nabla})\boldsymbol{u}\Big)\,. \tag{1.2}$$

Calling P a pressure field is in fact an improper use of the world pressure since the pressure p, defined by the International System of Units and measured by a manometer, is related to P via $\boldsymbol{\nabla}P = \rho^{-1}\boldsymbol{\nabla}p$ where ρ denotes the density of the fluid. When the density is uniform, the two pressures are simply proportional. In the case of solenoidal flows, if the density is initially uniform, it will remain constant (uniform and stationary)

because it follows the continuity equation

$$-\partial_t \rho = \boldsymbol{\nabla} \cdot (\rho \boldsymbol{u}) = (\boldsymbol{u} \cdot \boldsymbol{\nabla})\rho + (\boldsymbol{\nabla} \cdot \boldsymbol{u})\rho = 0\,. \tag{1.3}$$

Indeed, $(\boldsymbol{\nabla}\cdot\boldsymbol{u})\rho = 0$ because the flow is solenoidal and $(\boldsymbol{u}\cdot\boldsymbol{\nabla})\rho = 0$ because the density is initially uniform. Reciprocally, if the fluid is incompressible, *i.e.* if the density is constant, the flow has to be solenoidal, *i.e.* the velocity field has zero divergence. The solenoidal condition on the flow is equivalent to the incompressible condition on the fluid.

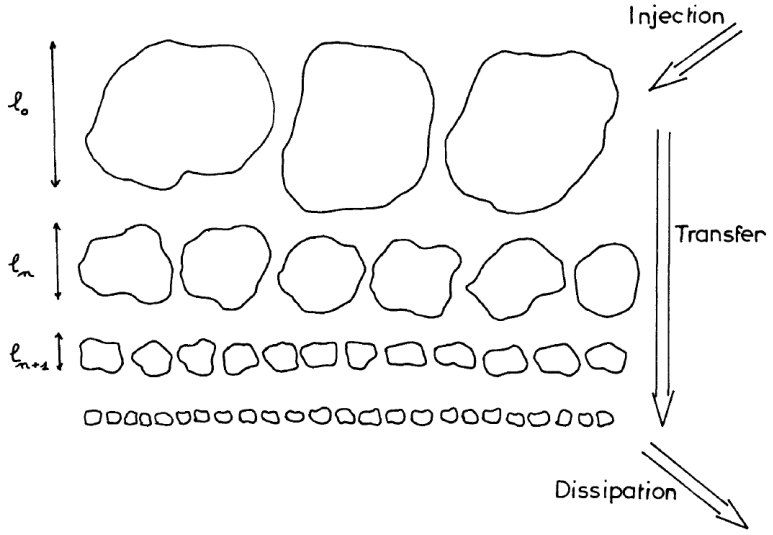

Figure 1.1 – Scheme for representing the Richardson cascade where eddies are broken into smaller eddies until their size is small enough to be dissipated. The figure is extracted from Rose and Sulem (1978) [1].

In the Navier-Stokes equation, the $(\boldsymbol{u} \cdot \boldsymbol{\nabla})\boldsymbol{u}$ term is associated to convective or inertial effects whereas the $\nu\Delta\boldsymbol{u}$ term is associated to diffusive effects. The Reynolds number, Re, is the dimensionless number which characterizes whether the regime is dominated by convection or diffusion. It is defined by

$$Re = \frac{[[(\boldsymbol{u} \cdot \boldsymbol{\nabla})\boldsymbol{u}]]}{[[\nu\Delta\boldsymbol{u}]]} = \frac{U_{rms}}{\nu\ell}\,, \tag{1.4}$$

where $[[\dots]]$ corresponds to the order of magnitude of the quantity within the double square brackets, U_{rms} and ℓ denote the root mean square velocity and the characteristic length-scale of the flow respectively. At low Reynolds number $Re \ll 1$, viscous effects dominate, whereas convective effects dominate at large Reynolds number $1 \ll Re$. At large Reynolds number, the flow becomes turbulent, the dynamic of the flow is often described using the image of the Richarson cascade [2, 3]. In the cascade description, large eddies are broken into smaller eddies which are themselves broken into even smaller eddies and so on and so forth until the size of the eddies is sufficiently small to dissipate the eddies because of viscous effects. Fig. 1.1 reproduces the scheme from Rose and Sulem (1978) [1]. This mechanism is in agreement with Kolmogorov's theory

[4, 3]. By proving that the energy injection rate ϵ and the viscosity are the only two fixed quantities in the problem, Kolmogorov showed that the energy spectrum of the system, $E(k)$, followed the power law

$$E(k) \propto \epsilon^{2/3} k^{-5/3} \quad \text{where} \quad E = \int E(k) dk = \frac{1}{2} \int \boldsymbol{u}^2 d^3\boldsymbol{r}\,, \tag{1.5}$$

where k and E denote the wavenumber and the total energy respectively. Fig.1.2 represents the energy spectrum for an incompressible fluid as predicted by Kolmogorov's theory with an exponential decay corresponding to the dissipation zone $k_d < k$ where k_d denotes the dissipation wavenumber. With Kolmogorov's theory, the dissipative wavenumber k_d can be related to the forcing wavenumber k_f via $k_d \simeq k_f Re^{3/4}$.

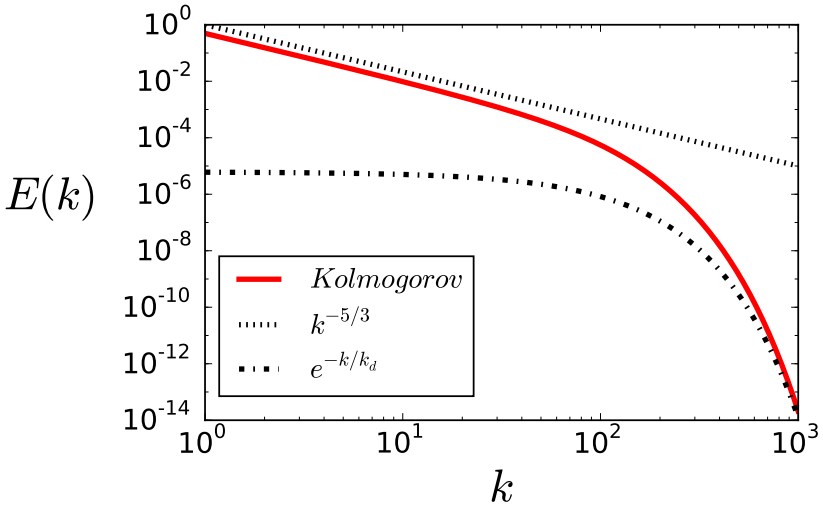

Figure 1.2 – Energy spectrum predicted by Kolmogorov in logarithmic scale. The red line represents Kolmogorov's prediction, the dotted line represents the $k^{-5/3}$-power law and the dash-dotted line represents the exponential decay in the viscous range where k_d denotes the dissipation wavenumber.

Many numerical and experimental studies [5, 6] have checked the validity of Kolmogorov's theory. The Kolmogorov-Monin 4/5-law [7] – which is an exact result consistent with Kolmogorov's theory applying the theory of Kàrmàn and Howarth [8] on third order correlation functions – has even been proven to be valid in experiements [9]. Kolmogorov's theory may be able to predict how the modes in scales smaller than the forcing scale behave, it does not give any information on the behavior of the modes larger than the forcing scale. In addition, the Richardson cascade does not give any intuition on the dynamic of formation of large eddies. The dynamic of the modes larger the forcing scale cannot be explained with the same arguments as those used to describe the small scale dynamic. Furthermore, let us recall that Kolmogorov's theory does not describe the so-called 'intermitency' corrections [3]. We shall not consider intermitency in the rest of this manuscript.

The aim of this manuscript is to investigate the properties of the flow for wavenumbers smaller than the forcing wavenumber. The problem is summed up in fig. 1.3. Since

Kolmogorov's theory has already been validated, the energy spectrum should follow Kolmogorov's prediction for wavenumbers above the forcing wavenumber. However, the aspect of the spectrum below the forcing scale is unknown and is denoted by green question marks in fig. 1.3.

A few theories have attempted to give a description of what should happen below the forcing. In [3], U. Frisch reported the conjecture that the energy spectrum of solution of the Navier-Stokes equation should follow absolute equilibrium solutions:

> "Absolute equilibrium solutions seem highly unphysical in view of the approximately $k^{-5/3}$ spectrum of the three-dimensional turbulence. Actually, they are appropriate at the very smallest wavenumbers of turbulent flows maintained by forcing at intermediate wavenumbers (Forster, Nelson and Stephen 1977)."
>
> — Uriel FRISCH, *Turbulence: The Legacy of A. N. Kolmogorov*, p. 209

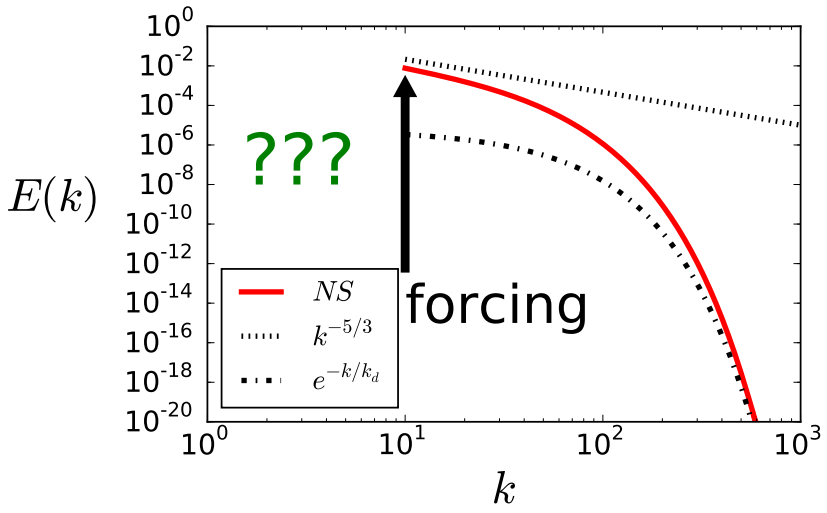

Figure 1.3 – Energy spectrum of a velocity field forced at $k = 10^1$. The red line represents the known trend of the velocity which has been shown to satisfies Kolmogorov's prediction. The dark lines represent the asymptotic behaviors of the energy spectrum. The green question marks represent the part of the spectrum whose properties are still unknown.

The article by Forster *et al.* [10] mentioned in the quote used renormalisation group theory to study turbulence. In one of the models described in the article, the authors were able to show that the behavior of the modes below the forcing wavenumber should have a dynamic similar to that of solution of the truncated Euler equation. The equivalent of the truncation wavenumber for the large scale modes solution of the Navier-Stokes equation is the forcing wavenumber. Let us give a few details on the Euler equation to understand the comparison.

The Euler equation describes ideal fluids without any viscosity. It can be obtained from the Navier-Stokes equation by setting the viscosity coefficient ν to zero. Kraichnan studied in [11] the average spectrum of the solutions of a truncated Euler equation

in their statistically stationary regime. The associated solutions are called absolute equilibrium solutions. The truncated Euler equation is a spectrally-filtered version of the Euler equation where the modes above a cut-off wavenumber k_M are set to zero. More precisely, if the Fourier modes of the velocity are denoted by $\boldsymbol{u_k}$ where $\boldsymbol{k}$ is the wavevector, $\boldsymbol{u_k}$ is set to zero if $k_M < |\boldsymbol{k}|$ and $\boldsymbol{u_k}$ follows the Euler equation if $|\boldsymbol{k}| \leq k_M$.

The equivalence between the truncated Euler equation and the Navier-Stokes equation is valid in the case of forced turbulence. In the case of decaying tubulence where k^2-spectrum (Saffman turbulence) [22] and k^4-spectrum (Batchelor turbulence) [23] can be observed, the equivalence between the two equations is not as clear because the maximum of the energy spectrum drifts to the large scales as time elapses.

Fig. 1.4 represents the global aspect of the energy spectrum of absolute equilibrium solutions of the truncated Euler equation. Far below the truncation wavenumber, the spectrum follows a k^2-power law. This power law is related to the energy conservation of the truncated Euler equation. If the energy is evenly spread out in every mode, the energy spectrum should be proportional to the number of modes per shell. In three dimensions, the density of modes per shell is roughly constant and the area of shell is proportional to k^2, the energy spectrum should therefore follow a k^2-power law.

The truncated Euler equation does not only conserve energy, it also conserves a second quantity called helicity, denoted with the letter H and defined by

$$H = \frac{1}{L^3}\int (\boldsymbol{u}\cdot\boldsymbol{\nabla}\times\boldsymbol{u})d^3\boldsymbol{r} \quad \text{and} \quad L^3 = \int d^3\boldsymbol{r}\,. \tag{1.6}$$

where L^3 is the volume of the fluid.

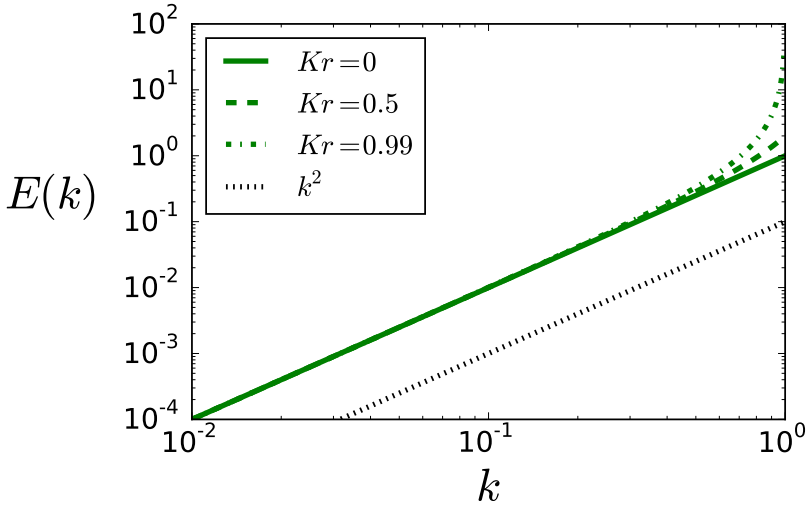

Figure 1.4 – Absolute equilibrium prediction for the energy spectrum of solutions of the truncated Euler equation for different Kraichnan numbers.

The conservation of a second invariant by the truncated Euler equation modifies the aspect of the average energy spectrum. The probability distribution of each mode of the velocity field is governed by a modified Boltzman weight proportional to $e^{-(\alpha(2E)+\beta H)}$

where α and β are parameters introduced by Kraichnan in [11]. The Kraichnan number $\mathcal{K}r = -\frac{\beta k_M}{\alpha}$ can be used to measure the relative level of helicity compared with energy for a flow truncated at k_M. If the Kraichnan number is equal to zero, the system does not have any helicity and the energy spectrum follows a k^2-power law. If the Kraichnan number is different from zero, the system has some helicity. Finally, if the Kraichnan number is near one in absolute value, the energy is concentrated in the small scales and the k^2-power law cannot be observed in the small scales.

As described by Kraichnan and Chen in [12], the apparent similarity between the dynamic of the large scale modes of the solutions of the Navier-Stokes equation and the solutions of the truncated Euler equation can also be considered from the truncated Euler perspective. Their argument is based on the fluctuation-dissipation theorem and is explained in the quotation presented on page 6.

> "The equilibrium equipartition distribution [...] becomes more interesting when the associated fluctuation-dissipation relations are considered. These relations show that the truncated Euler system can imitate a [Navier-Stokes] fluid: the high wavenumber degrees of freedom act like a thermal sink into which the energy of low wavenumber modes excited above equilibrium is dissipated. In the limit where the sink wavenumbers are very large compared with the anomalously excited wavenumbers, this dynamical damping acts precisely like a molecular viscosity. When the wavenumber ratio is not asymptotically large, the dynamical damping is non-local in space and time; it exhibits long-time tails like those obtained from the kinetic theory of a gas."
>
> — Robert H. KRAICHNAN & Shiyi CHEN,
> *Is there a statistical mechanics of turbulence ?*,
> Physica D 37 (1989) 160-172

Another argument used to predict an absolute equilibrium behavior of the large scale mode for solution of the Navier-Stokes equation is to consider how energy flows to the modes. In the small scales, the harmonics of the forcing mode can directly transmit energy in the small scale modes via the non-linear interaction term. However, in the large scales, the energy is transmitted by the sum of the non-linear interactions resulting from the beating of all the modes. The resulting effect acts as a thermal bath forcing all large scale modes independently and leaves the same amount of energy in every mode.

Fig. 1.5 illustrates the prediction made by Frisch (see the quote on page 4) on the energy spectrum of solutions of the forced Navier-Stokes equation. The modes in scales smaller than the forcing scale should follow Kolmogorov's scaling whereas the mode in scales larger than the forcing scale should have absolute equilibrium behavior similar to that of solutions of the truncated Euler equation.

As a prelude to the study of the large scale behavior of turbulent flows, it is important to understand how the large scale modes behave at smaller Reynolds number. Indeed the properties of laminar and turbulent flows are not totally disconnected since they correspond to the same system but with a different Reynolds number. Even though it is highly unlikely that all the laminar properties of the flow will remain

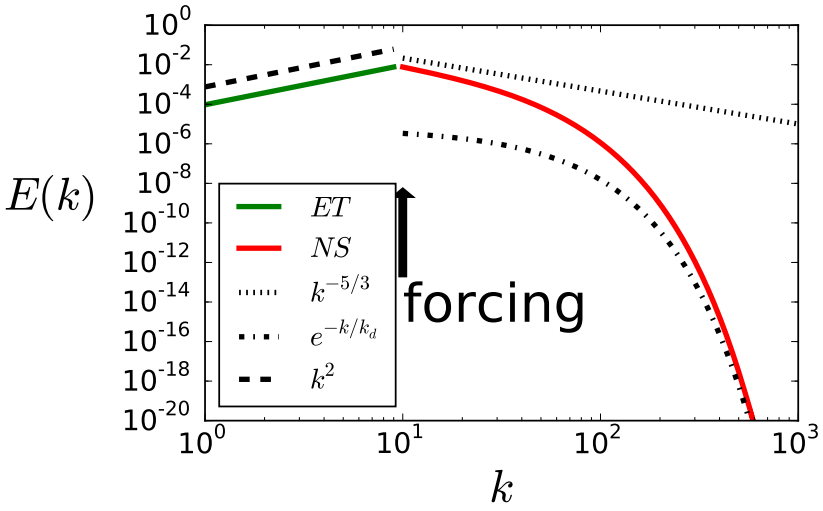

Figure 1.5 – Energy spectrum as described by Frisch in [3]. The red line represents the energy spectrum in scales smaller than the forcing scale. The green line represents the energy in the scales larger than the forcing scale.

unaltered as the Reynolds number increases, some mechanisms may still impact some modes for a wide range of Reynolds number. Knowing how these mechanisms evolve as the Reynolds number increases can give an intuition on their turbulent behavior.

The manuscript is organized as follows:

• **In part B**, we will study the large scale behavior of helically-forced Navier-Stoke problems at small Reynolds numbers. Using Floquet analysis, we will quantify how large scale perturbation can be generated. We will first reproduce the anisotropic kinetic alpha (AKA) instability reported in [13, 14] at low Reynolds number with a linearized version of the Navier-Stokes equation. We will also show that the mechanism governing the AKA instability still holds at moderate Reynolds number. We will proceed by studying the large scale instability generated by the helical ABC flow [15]. We will show that the flow is first destabilized by a large scale instability before being destabilized in the small scales. Using direct numeric simulations of the fully non-linear version of the Navier-Stokes equation, we will show that the large scale instability can be observed and eventually saturates.

We will also investigate properties of the magnetic field in kinematic magneto-hydrodynamic (MHD). Since the evolution equation of the velocity field of a viscous fluid and that of the magnetic field in conductive fluid share many similarities, their solution also have common properties. For instance, the AKA instability was introduced in fluid dynamics as the counterpart of the magnetic alpha-effect [16, 17]. Using the Floquet methodology, we will show that, similarly to the velocity field, the magnetic field can have a concentration of energy in the large scales as long as it has not crossed the small scale instability threshold. We will support our claim with three examples: a helical flow, a non-helical flow and a random flow in time.

Concerning the issue of the behavior of large scale modes of flows solutions of the

Navier-Stokes equation, the energy spectrum may carry a lot of information on a flow, but the description of a velocity field cannot be limited to its energy spectrum. The energy spectrum does not give any information on the temporal behavior of the flow. The correlation function is a general statistical tool used to measure the time dependence of an observable. If the behavior of the modes before the forcing scale of flows solutions of the Navier-Stokes equation are supposed to resemble that of the truncated Euler equation, their temporal correlations should also have the same properties.

A few results are already known on the correlation time of the modes of velocity. As described in [18, 19], in the Kolmogorov cascade, the correlation time is governed by the sweeping effect of the root mean square velocity of the forcing mode. Since most of the energy is concentrated in the forcing mode, the correlation time is proportional to the only time scale that can be built using the root mean square velocity, U_{rms}, and a wavenumber, k, *i.e.* $(kU_{rms})^{-1}$. Some studies [20, 6] have proposed an influence of helicity on the correlation time, but no direct expression of the correlation time has been derived for absolute equilibrium.

• **In part C**, we will use a short-time parabolic approximation to evaluate the correlation time of absolute equilibrium solutions of the truncated Euler equation. We will show that flows with a moderate level of helicity follow the same correlation time scaling law as that generated by the sweeping effect in the Kolmogorov cascade. However, in highly helical flows, another power law appears where the correlation time is proportional to $k^{-\frac{1}{2}}$ which is compatible with a time-scale based on helicity. To confirm this new scaling, we will use direct numeric simulations of the truncated Euler equation to produce time series of the modes of velocity which we will then analyze to compute the correlation time. We will use the same procedure to analyze the large scale modes of solutions of the forced Navier-Stokes equation. We will show that the large scale modes of flows without helicity follow the same scaling for their correlation time as the absolute equilibrium. However, the correlation time in large scale modes of highly helical flows are not able to exibit a $k^{-\frac{1}{2}}$-power law.

We will also present some results on numeric methods in part E that are independent of the core problem of this manuscript.

All chapters with a title starting with *Elements of context* **review elements of well-documented theories. New results are presented in the chapters with a title finishing with the indication***published* **or** *submitted***.**

Chapter 2

Elements of context: Hydrodynamics

The aim of this chapter is to give details on some of the properties presented in chap. 1. We will (i) derive some properties of the evolution equation of ideal fluids, (ii) give the equivalence between the evolution equation of viscous fluids and magnetic fields in conductive fluids and (iii) explain how the helicity and the energy are conserved. More information on how to integrate the equation numerically are presented in part E. Most of the properties presented in this chapter are explained in greater depth in [3, 24]. A general description of the pseudo-spectral numeric method used is presented in chap. 10.

This chapter reviews elements of well-documented theories.

2.1 Ideal fluids (review)

The Navier-Stokes equation may already be an approximation of a real fluid, further approximations are required to derive analytic results. Some results can be derived on a simplified version of the equations where the viscosity is set to zero. This simplified equation is called the Euler equations and satisfies

$$\partial_t \boldsymbol{u} + (\boldsymbol{u}\cdot\boldsymbol{\nabla})\boldsymbol{u} = -\boldsymbol{\nabla} P \quad \text{and} \quad \boldsymbol{\nabla}\cdot\boldsymbol{u} = 0 \quad \text{with} \quad P = p/\rho\,. \tag{2.1}$$

In the case of the Euler equation, the viscosity has been set to zero thus making the viscous term $\nu\boldsymbol{\Delta u}$ vanish. The forcing field has also been set to zero. The absence of viscosity in the Euler equation leads to solutions which differ a lot from the solutions of the Navier-Stokes equation. D'Alembert's paradox gives a good example of the limitation of the Euler equation. In the inviscid framework, there is no friction, drag is thus not possible, which is in contradiction with experimental results showing that drag goes to a constant value at large Reynolds numbers. As a general rule, the Euler equation is not well adapted to describe real fluids near solid boundaries. D'Alembert paradox is the reason which led Stokes to use Navier's theory of viscosity to compute the drag of a sphere. The dynamic of the flow is totally changed by adding a small amount of viscosity, thus the invisicid limit in fluid mechanics is a singular limit.

Another difference between the solutions of the Navier-Stokes equation and those of the Euler equation concerns their behavior at large wavenumber. Fourier space is better suited to understand what is at hand. In Fourier space, the Navier-Stokes equation can be written as

$$\partial_t u^\alpha_{\boldsymbol{k}} = F^\alpha_{\boldsymbol{k}} - k^2 \nu u^\alpha_{\boldsymbol{k}} - \frac{\imath}{2} \mathcal{P}^{\alpha\beta\gamma}_{\boldsymbol{k}} \sum_{\boldsymbol{p}} u^\beta_{\boldsymbol{p}} u^\gamma_{\boldsymbol{k}-\boldsymbol{p}} \quad \text{where} \quad \mathcal{P}^{\alpha\beta\gamma}_{\boldsymbol{k}} = k^\beta P^{\alpha\gamma}_{\boldsymbol{k}} + k^\gamma P^{\alpha\beta}_{\boldsymbol{k}}\,, \tag{2.2}$$

$$\text{with} \quad P^{\alpha\beta}_{\boldsymbol{k}} = \delta^{\alpha\beta} - \frac{k^\alpha k^\beta}{k^2} \quad \text{and} \quad \delta^{\alpha\beta} = \begin{cases} 1 & \text{if } \alpha{=}\beta \\ 0 & \text{otherwise} \end{cases}. \tag{2.3}$$

where $u^\alpha_{\boldsymbol{k}}$, $F^\alpha_{\boldsymbol{k}}$, $\mathcal{P}^{\alpha\beta}_{\boldsymbol{k}}$, $P^{\alpha\beta}_{\boldsymbol{k}}$, $\delta^{\alpha\beta}$ denote the Fourier component of the velocity field, the Fourier component of the forcing, the solenoidal transport tensor, the tensor enforcing incompressibility and Kronecker's delta tensor respectively. The Greek exponents indicate the Cartesian directions and the index $\boldsymbol{k}$ indicates the wavevector. The equation has been written with Einstein's implicit summation convention over repeated Greek variables, the sum on Latin variables are denoted with the capital sigma symbol. The Fourier formulation may seem more difficult but the temporal evolution of every mode can clearly be identified and the pressure term enforcing the incompressibility condition is now included in the solenoidal transport tensor.

With the formulation of eq. (2.3), the diffusive scale of the Richardson cascade can be identified. Since the solenoidal transport tensor is of order k and the viscous term is of order k^2, at large wavenumber, the viscous term becomes dominant even if the forcing is strong. If the forcing is not applied, the mode of the velocity field would decay exponentially similarly to solutions of the heat equation. However, the $e^{-\kappa k^2 t}$ decay of the heat equation and the e^{-k/k_d} spectral decay of turbulent Navier-Stokes solution are not directly related. On the other hand, in the inviscid limit, the viscous term is absent. Hence, in the small scales, velocity modes are not damped. Some solutions of the Euler equation can even have average values in the small scales larger than those in the large scales. Similarly to the Navier-Stokes equation, the regularity of the solutions of the Euler equation is still an open question. In order to carry out numeric analysis, the Navier-Stokes equation is often truncated spectrally which only leads to a small error on the numeric solution if the truncation is done below the dissipative scale. The truncated Euler equation is useful to understand the large scale behavior of Navier-Stokes solutions. However, truncating the Euler equation changes a lot more the solutions. Indeed, when the spectral truncation is applied, all modes of wavenumber greater than the maximal wavenumber k_M are set to zero. The truncated Euler equation can be written as

$$\partial_t u^\alpha_{\boldsymbol{k}} = -\frac{\imath}{2} \mathcal{P}^{\alpha\beta\gamma}_{\boldsymbol{k}} \sum_{\boldsymbol{p}} u^\beta_{\boldsymbol{p}} u^\gamma_{\boldsymbol{k}-\boldsymbol{p}} \quad \text{with} \quad \boldsymbol{u}_{k>k_M} = 0\,. \tag{2.4}$$

Even though solutions of the Euler equation and truncated Euler equation have many discrepancies with real fluids, they still yield interesting properties that can be used to understand the properties of real fluids, especially concerning large scale thermalization and conserved quantities.

2.2 Magnetic equivalences (review)

Using the Fourier formalism to express the Navier-Stokes equation, the pressure fields can be removed from the equation by imposing directly the solenoidal condition on the tensor used in the evolution equation of the flow. In physical space, the Navier-Stokes equation can also be rewritten in an expression where the pressure field has disappeared. The properties of this expression are close to those of the magnetic field which is also a solenoidal field. To derive this formalism, the standard version of the Navier-Stokes equation (eq.(1.1)) can be rewritten using the following vectorial formula for generic $\boldsymbol{U}$ and $\boldsymbol{V}$ fields

$$\boldsymbol{\nabla}(\boldsymbol{U}\cdot\boldsymbol{V}) = (\boldsymbol{U}\cdot\boldsymbol{\nabla})\boldsymbol{V} + \boldsymbol{U}\times(\boldsymbol{\nabla}\times\boldsymbol{V}) + (\boldsymbol{V}\cdot\boldsymbol{\nabla})\boldsymbol{U} + \boldsymbol{V}\times(\boldsymbol{\nabla}\times\boldsymbol{U})\,, \tag{2.5}$$

$$(\boldsymbol{U}\cdot\boldsymbol{\nabla})\boldsymbol{U} = -\boldsymbol{U}\times(\boldsymbol{\nabla}\times\boldsymbol{U}) + \tfrac{1}{2}\boldsymbol{\nabla}(\boldsymbol{U}^2)\,. \tag{2.6}$$

With this modification, the Navier-Stokes equation can be expressed as

$$\partial_t\boldsymbol{u} = \boldsymbol{u}\times\boldsymbol{\omega} - \boldsymbol{\nabla}\Big(P + \tfrac{\boldsymbol{u}^2}{2}\Big) + \nu\Delta\boldsymbol{u} + \boldsymbol{F} \quad \text{with} \quad \boldsymbol{\nabla}\cdot\boldsymbol{u} = 0 \quad \text{and} \quad \boldsymbol{\omega} = \boldsymbol{\nabla}\times\boldsymbol{u}\,. \tag{2.7}$$

where $\boldsymbol{\omega}$ is the vorticity field. Taking the curl of the equation, the evolution of the vorticity fields follows

$$\partial_t\boldsymbol{\omega} = \boldsymbol{\nabla}\times(\boldsymbol{u}\times\boldsymbol{\omega}) + \nu\Delta\boldsymbol{\omega} + \boldsymbol{\nabla}\times\boldsymbol{F} \quad \text{with} \quad \boldsymbol{\nabla}\cdot\boldsymbol{u} = 0 \quad \text{and} \quad \boldsymbol{\omega} = \boldsymbol{\nabla}\times\boldsymbol{u}\,. \tag{2.8}$$

In the vorticity equation, the pressure term has disappeared in the right hand side. By construction of the nabla operator, the transport term $\boldsymbol{\nabla}\times(\boldsymbol{u}\times\boldsymbol{\omega})$ always satisfies the solenoidal condition. This simplification comes at a cost: the velocity field has to be computed by uncurling the vorticity. Similarly to the pressure field in the case of the Navier-Stokes equation, the velocity field is solution of a Poisson equation in the case of the vorticity equation

$$\Delta\boldsymbol{u} = -\boldsymbol{\nabla}\times\boldsymbol{\omega} \quad \text{with} \quad \boldsymbol{\nabla}\cdot\boldsymbol{u} = 0\,. \tag{2.9}$$

With the formulation of the Navier-Stokes equation in terms of vorticity, it appears that flows satisfying $\boldsymbol{u}\times\boldsymbol{\nabla}\times\boldsymbol{u} = 0$ are exact solutions of the Euler equation. These flows are often referred to as Beltrami flows and have the main property of being highly helical.

At this stage, all these reordering of terms may seem insignificant but having the correct formulation of the evolution of the flow greatly simplifies derivations, particularly when investigating large scale instabilities. The temporal evolution of the vorticity equation corresponds to the general transport and diffusion of a vector field with a solenoidal constraint. The definition of the vorticity field as the curl of velocity appears independently when solving the Poisson equation.

Similarly to the vorticity field, the magnetic field in a conductive fluid is a vector field governed by diffusive and transport processes with the Maxwell-Gauss solenoidal constraint $\boldsymbol{\nabla}\cdot\boldsymbol{B} = 0$. Finding the evolution of the magnetic field requires to solve the Maxwell-Faraday equation and the stationary Maxwell-Ampere equation with Ohm's law in a moving frame

$$\partial_t\boldsymbol{B} = -\boldsymbol{\nabla}\times\boldsymbol{E} \quad , \quad \boldsymbol{\nabla}\times B = \mu_0\boldsymbol{J} \quad \text{and} \quad \boldsymbol{J} = \sigma(\boldsymbol{E} + \boldsymbol{u}\times\boldsymbol{B})\,, \tag{2.10}$$

where $\boldsymbol{E}$, $\boldsymbol{B}$, $\boldsymbol{J}$, μ_0, σ denote the electric field, the magnetic field, the current field, the permeability and the electric conductivity respectively. Combining the equations, the magnetic field follows the induction equation

$$\partial_t \boldsymbol{B} = \boldsymbol{\nabla}\times(\boldsymbol{u}\times\boldsymbol{B}) + \eta\Delta\boldsymbol{B} \quad , \quad \boldsymbol{\nabla}\cdot\boldsymbol{B} = 0\,. \tag{2.11}$$

where $\eta = 1/(\mu_0\sigma)$ denotes the magnetic diffusivity. Besides the forcing, the equation is similar to the vorticity equation. Because of their similarities, magnetic effects often have a kinetic counterpart. For instance the alpha-effect was first discovered in the magnetic case and then found in the kinetic case.

Similarly to the kinetic case, the magnetic Reynolds number, Rm, is the dimensionless number which characterizes whether the evolution of the magnetic field is dominated by convection or diffusion. It is defined by

$$Rm = \frac{[[\boldsymbol{\nabla}\times(\boldsymbol{u}\times\boldsymbol{B})]]}{[[\eta\Delta\boldsymbol{B}]]} = \frac{U_{rms}}{\eta\ell}\,. \tag{2.12}$$

When magnetic fields become important, the Laplace force $\boldsymbol{J}\times\boldsymbol{B}$ generated on the fluid has to be taken into account in the Navier-Stokes equation. The evolution of the magnetic field follows a non-linear set of equation and the magnetic field can follow dynamics where it undergoes reversals.

2.3 Conserved quantities (review)

Conserved quantities are some of the most general properties of ideal fluids that can easily be transcribed for real flows. To derive the evolution equation of the energy for solutions of the Navier-Stokes equation, the following relations for generic G, $\boldsymbol{U}$ and $\boldsymbol{V}$ fields are very useful

$$\boldsymbol{\nabla}\cdot(\boldsymbol{U}\times\boldsymbol{V}) = \boldsymbol{V}\cdot\boldsymbol{\nabla}\times\boldsymbol{U} - \boldsymbol{U}\cdot\boldsymbol{\nabla}\times\boldsymbol{V}\,, \tag{2.13}$$

$$\boldsymbol{\nabla}\cdot(G\boldsymbol{U}) = G\boldsymbol{\nabla}\cdot\boldsymbol{U} + \boldsymbol{U}\cdot\boldsymbol{\nabla}G\,. \tag{2.14}$$

Neglecting the boundary terms, which are equal to zero in periodic domains, the temporal derivative of the evolution of energy leads to

$$\partial_t\left\langle\frac{|\boldsymbol{u}|^2}{2}\right\rangle_{L^3} = \left\langle\boldsymbol{u}\cdot\left(\boldsymbol{u}\times\boldsymbol{\omega} - \boldsymbol{\nabla}\left(P+\tfrac{\boldsymbol{u}^2}{2}\right) + \nu\Delta\boldsymbol{u} + \boldsymbol{F}\right)\right\rangle_{L^3} = -\nu\left\langle|\boldsymbol{\omega}|^2\right\rangle_{L^3} + \langle\boldsymbol{u}\cdot\boldsymbol{F}\rangle_{L^3} \tag{2.15}$$

$$\text{where}\quad \langle\ldots\rangle_{L^3} = \frac{1}{L^3}\int\ldots d^3\boldsymbol{r} \quad \text{with} \quad L^3 = \int d^3\boldsymbol{r}\,. \tag{2.16}$$

The angle brackets, $\langle\ldots\rangle_{L^3}$, denote the average over space. This notation is not common to describe an average, but the standard notations will be taken by other averages. The thermodynamic ensemble average will be denoted by the angle brackets $\langle\ldots\rangle_{ens}$, and temporal average will be denoted by a super-scripted line $\overline{\ldots}$. The equation of evolution of the energy indicates that energy can be added to the system via the forcing term $\langle\boldsymbol{u}\cdot\boldsymbol{F}\rangle_{L^3}$. With non-zero viscosity, the enstrophy $\left\langle|\boldsymbol{\omega}|^2\right\rangle_{L^3}$ always leads to energy

dissipation. However, the system conserves energy in the ideal case corresponding to the Euler equation. The other possible option to cancel out the average dissipation would be to have $\boldsymbol{\omega} = 0$. But since the problem has fixed boundaries, the only solution is for the fluid to be at rest without any motion. The conservation of energy is not simply restricted to the average quantity. Let us assume that only three velocity modes of wavevector $\boldsymbol{k}$, $\boldsymbol{p}$ and $\boldsymbol{q}$ forming a triad, *i.e.* $\boldsymbol{k}+\boldsymbol{q}+\boldsymbol{p}=0$, are different from zero, using eq.(2.15), the evolution of energy at the wavenumber $\boldsymbol{k}$ is given by

$$\frac{1}{2}\partial_t|\boldsymbol{u_k}|^2 = -\frac{\imath}{2}\left(k^\beta(u_{\boldsymbol{k}}^\gamma)^* u_{\boldsymbol{p}}^\beta u_{\boldsymbol{q}}^\gamma + k^\gamma(u_{\boldsymbol{k}}^\beta)^* u_{\boldsymbol{p}}^\beta u_{\boldsymbol{q}}^\gamma\right) \quad \text{with} \quad k^\alpha(u_{\boldsymbol{k}}^\alpha)^* = 0\,, \tag{2.17}$$

where $(\ldots)^*$ corresponds to the complex conjugation of the quatity in between the parenthesis. Bearing in mind that the three wavevectors form a triad and that the modes are solenoidal, the energy on a triad, $\frac{1}{2}\left(|\boldsymbol{u_k}|^2+|\boldsymbol{u_p}|^2+|\boldsymbol{u_q}|^2\right)$, is conserved. For the moment, the truncation condition has not yet been used, therefore the demonstration is valid in a general case. The energy flux, $(u_{\boldsymbol{k}}^\gamma)^* u_{\boldsymbol{p}}^\beta u_{\boldsymbol{q}}^\gamma$, depends on the three modes of the triad. When one of the mode is equal to zero, no energy can be transferred within the triad. Consequently, the truncated Euler equation conserves energy without any specific condition on the truncation condition.

As noted by Moffat in [25], similarly to magnetic fields, ideal flows also conserve the total helicity, H. Indeed

$$\partial_t H = 2\nu\left\langle(\boldsymbol{\omega}\cdot\Delta\boldsymbol{u})\right\rangle_{L^3} + 2\left\langle(\boldsymbol{\omega}\cdot\boldsymbol{F})\right\rangle_{L^3} \quad \text{with} \quad H = \left\langle\boldsymbol{u}\cdot\boldsymbol{\omega}\right\rangle_{L^3}\,. \tag{2.18}$$

When the fluid is inviscid, the helicity is conserved. The evolution of helicity is quite different from the evolution of energy. The viscous term in the evolution equation is not always negative. Unlike energy, helicity does not have to be positive, it can also be negative. With the current framework, it is hard to go beyond the global conservation of helicity. The Craya-Herring helical decomposition [26, 27] is more adapted to look at how helicity evolves on a triad. The helical decomposition relies on the fact that all velocity fields can be decomposed into a positive, $\boldsymbol{u}^+$, and a negative, $\boldsymbol{u}^-$, helical components using

$$\boldsymbol{u}_{\boldsymbol{k}}^\pm = \boldsymbol{u_k} \pm k^{-1}\boldsymbol{\nabla}\times\boldsymbol{u_k} = u_{\boldsymbol{k}}^\pm \boldsymbol{h}_{\boldsymbol{k}}^\pm \quad \text{where} \quad \boldsymbol{\nabla}\times\boldsymbol{h}_{\boldsymbol{k}}^\pm = \pm k\boldsymbol{h}_{\boldsymbol{k}}^\pm \quad \text{and} \quad |\boldsymbol{h}_{\boldsymbol{k}}^\pm|^2 = 1\,, \tag{2.19}$$

where $\boldsymbol{h}_{\boldsymbol{k}}^+$ denotes a complex positively helical unitary vector at mode $\boldsymbol{k}$. $\boldsymbol{h}_{\boldsymbol{k}}^\pm$ are unique up to a complex phase. In the inviscid case, with this decomposition and eq. (2.7), the evolution of a mode [28] is given by

$$\partial_t(u_{\boldsymbol{k}}^{s_{\boldsymbol{k}}})^* = \sum_{\substack{\boldsymbol{k}+\boldsymbol{p}+\boldsymbol{q}=0\\ s_{\boldsymbol{p}},s_{\boldsymbol{q}}}} C_{\boldsymbol{kpq}}^{s_{\boldsymbol{k}}s_{\boldsymbol{p}}s_{\boldsymbol{q}}} u_{\boldsymbol{p}}^{s_{\boldsymbol{p}}} u_{\boldsymbol{q}}^{s_{\boldsymbol{q}}} \quad \text{where} \quad C_{\boldsymbol{kpq}}^{s_{\boldsymbol{k}}s_{\boldsymbol{p}}s_{\boldsymbol{q}}} = \frac{-1}{4}(s_{\boldsymbol{p}}p - s_{\boldsymbol{q}}q)(\boldsymbol{h}_{\boldsymbol{k}}^{s_{\boldsymbol{k}}}\cdot\boldsymbol{h}_{\boldsymbol{p}}^{s_{\boldsymbol{p}}}\times\boldsymbol{h}_{\boldsymbol{q}}^{s_{\boldsymbol{q}}})\,. \tag{2.20}$$

$C_{\boldsymbol{kpq}}^{s_{\boldsymbol{k}}s_{\boldsymbol{p}}s_{\boldsymbol{q}}}$ denotes the Craya-Herring tensor. It is symmetric on its last two variables: $C_{\boldsymbol{kpq}}^{s_{\boldsymbol{k}}s_{\boldsymbol{p}}s_{\boldsymbol{q}}} = C_{\boldsymbol{kqp}}^{s_{\boldsymbol{k}}s_{\boldsymbol{q}}s_{\boldsymbol{p}}}$. Because of the triple product, the Craya-Herring tensor is equal to zero when at least two of the three helical modes in the triad and identical : $C_{\boldsymbol{kkq}}^{s_{\boldsymbol{k}}s_{\boldsymbol{k}}s_{\boldsymbol{q}}} = 0$, $C_{\boldsymbol{kpk}}^{s_{\boldsymbol{k}}s_{\boldsymbol{p}}s_{\boldsymbol{k}}} = 0$ and $C_{\boldsymbol{kpp}}^{s_{\boldsymbol{k}}s_{\boldsymbol{p}}s_{\boldsymbol{p}}} = 0$.

The evolution of helicity can also be analyzed on a triad. Similarly to the conservation of energy on a triad, let us assume that only three helical velocity modes of

wavevector $\boldsymbol{k}$, $\boldsymbol{p}$ and $\boldsymbol{q}$ forming a triad, *i.e.* $\boldsymbol{k}+\boldsymbol{q}+\boldsymbol{p}=0$, are different from zero. Using eq.(2.20), the evolution of helicity at the wavenumber $\boldsymbol{k}$ is given by

$$s_{\boldsymbol{k}} k \partial_t |\boldsymbol{u}_{\boldsymbol{k}}^{s_{\boldsymbol{k}}}|^2 = -\frac{1}{4} s_{\boldsymbol{k}} k (s_{\boldsymbol{p}} p - s_{\boldsymbol{q}} q) \left(\boldsymbol{h}_{\boldsymbol{k}}^{s_{\boldsymbol{k}}} \cdot \boldsymbol{h}_{\boldsymbol{p}}^{s_{\boldsymbol{p}}} \times \boldsymbol{h}_{\boldsymbol{q}}^{s_{\boldsymbol{q}}}\right) u_{\boldsymbol{k}}^{s_{\boldsymbol{k}}} u_{\boldsymbol{p}}^{s_{\boldsymbol{p}}} u_{\boldsymbol{q}}^{s_{\boldsymbol{q}}} . \tag{2.21}$$

The additional $s_{\boldsymbol{k}} k$ coefficient comes from the curl operator applied on the helical vector $h_{\boldsymbol{k}}^{s_{\boldsymbol{k}}}$. The derivative of the helicity of the three modes of the triad is equal to zero. Helicity is thus conserved on a triad. The conservation of energy on a triad can also be derived using the Craya-Herring helical decomposition. This decomposition describe with more details the conservation of energy since the Craya-Herring helical decomposition separates positive and negative helical components. The argument made about the truncation condition in the case of the conservation of energy on a triad can also be made for the conservation of helicity on a helical triad. Since the helicity flux is proportional to $u_{\boldsymbol{k}}^{s_{\boldsymbol{k}}} u_{\boldsymbol{p}}^{s_{\boldsymbol{p}}} u_{\boldsymbol{q}}^{s_{\boldsymbol{q}}}$, it depends on the three modes of the triad. When one of the modes is equal to zero, no helicity can be transferred within the triad. Consequently, the truncated Euler equation conserves helicity without any condition on the truncation method.

When $\boldsymbol{F}=0$, the helical decomposition gives another insight on the evolution of the total helicity written in eq. (2.18)

$$\partial_t \sum_{\boldsymbol{k}} (H_{\boldsymbol{k}}^+ + H_{\boldsymbol{k}}^-) = -2\nu \sum_{\boldsymbol{k}} k^2 \left(H_{\boldsymbol{k}}^+ + H_{\boldsymbol{k}}^-\right) \quad \text{where} \quad H_{\boldsymbol{k}}^{\pm} = \pm k |u_{\boldsymbol{k}}^{\pm}|^2 . \tag{2.22}$$

Because of the non-linear interaction of the modes, the evolution of the helicity is quite complex. However, if the flow is not forced, the energy at every mode will eventually decrease which will in turn results in a decrease of helicity at every mode.

In the inviscid limit, the magnetic evolution equation also conserves a quantity called the magnetic helicity. The magnetic helicity, H_M, can be expressed as

$$H_M = \langle \boldsymbol{A} \cdot \boldsymbol{B} \rangle_{L^3} \quad \text{with} \quad \boldsymbol{\nabla} \times \boldsymbol{A} = \boldsymbol{B} \quad \text{and} \quad \boldsymbol{\nabla} \cdot \boldsymbol{A} = 0 . \tag{2.23}$$

where $\boldsymbol{A}$ denotes the magnetic potential vector associated to the magnetic field with the Coulomb gauge. The magnetic potential follows the evolution equation

$$\partial_t \boldsymbol{A} = \boldsymbol{u} \times \boldsymbol{\nabla} \times \boldsymbol{A} + \eta \Delta \boldsymbol{A} . \tag{2.24}$$

Adding the Laplace force to the hydrodynamic force, it can also be shown that the sum of the kinetic and magnetic energies and the cross helicity, $\langle \boldsymbol{u} \cdot \boldsymbol{B} \rangle_{L^3}$, are conserved in the ideal case.

Part B

Large scale instabilities

Table of Contents

Chapter 3

Elements of context: Large scale effects

This aim of this chapter is to present some large scale effects that can occur in magnetic fields and velocity fields. Even though the magnetic effect is not directly linked with the study of absolute equilibrium, we will start by considering the alpha-effect before considering its kinetic counterpart, the anisotropic kinetic alpha (AKA) effect.

Subsec. 3.1 and 3.2 review elements of well-documented theories. Subsec. 3.3 presents a new model used in sec. 5 and 6 to report new results.

3.1 Alpha-effect (review)

As introduced in chap. 2, the evolution of the magnetic field in a conductive fluid is governed by the induction equation

$$\partial_t \boldsymbol{B} = \boldsymbol{\nabla} \times (\boldsymbol{u} \times \boldsymbol{B}) + \eta \Delta \boldsymbol{B} \quad \text{where} \quad \boldsymbol{\nabla} \cdot \boldsymbol{B} = 0\,, \tag{3.1}$$

where $\boldsymbol{B}$, $\boldsymbol{u}$ and η denote the magnetic field, the velocity field and the magnetic diffusivity respectively. Similarly to the kinetic case, the magnetic Reynolds number, Rm, is the dimensionless number which characterizes whether the evolution of the magnetic field is dominated by convection or diffusion. It reads

$$Rm = \frac{[[\boldsymbol{\nabla} \times (\boldsymbol{u} \times \boldsymbol{B})]]}{[[\eta \Delta \boldsymbol{B}]]} = \frac{U_{rms}}{\eta \ell}\,. \tag{3.2}$$

where U_{rms} and ℓ denote the root mean square velocity and the length-scale of the velocity field respectively. The double square brackets represent the order of magnitude of the observable within it. At low Rm, for specific flows, the induction equation has the surprising feature of being able to generate a large scale instability [16]. This instability can be understood with a heuristic argument.

To quantify this phenomenon more precisely, let us consider the specific problem where the velocity field is of length-scale ℓ and the magnetic field evolving in a domain of size L with $\ell \ll L$. Let us define the averaging procedure for generic field G as

$$\langle G \rangle_{V_\ell} (\boldsymbol{R}) = \frac{1}{V_\ell} \int_{V_\ell} G(\boldsymbol{R} + \boldsymbol{r}) d^3\boldsymbol{r}\,, \tag{3.3}$$

where V_ℓ is an isotropic volume centered on $\boldsymbol{R}$ with $\ell^3 \ll V_\ell \ll L^3$. By definition of the length-scale, the velocity field has an average equal to zero $\langle \boldsymbol{u} \rangle_{V_\ell} = 0$. The magnetic field can be decomposed as $\boldsymbol{B} = \langle \boldsymbol{B} \rangle_{V_\ell} + \boldsymbol{b}$, where $\langle \boldsymbol{B} \rangle_{V_\ell}$ is the large scale component of the magnetic field and $\boldsymbol{b}$ is the small scale component satisfying $\langle \boldsymbol{b} \rangle_{V_\ell} = 0$. The evolution equations of the two components of the magnetic field are given by

$$\partial_t \boldsymbol{b} = \boldsymbol{\nabla} \times (\boldsymbol{u} \times \langle \boldsymbol{B} \rangle_{V_\ell}) + \boldsymbol{\nabla} \times \boldsymbol{\mathcal{G}} + \eta \Delta \boldsymbol{b} \quad \text{with} \quad \boldsymbol{\nabla} \cdot \boldsymbol{b} = 0\,, \tag{3.4}$$

$$\partial_t \langle \boldsymbol{B} \rangle_{V_\ell} = \boldsymbol{\nabla} \times \boldsymbol{\mathcal{E}} + \eta \Delta \boldsymbol{B} \quad \text{with} \quad \boldsymbol{\nabla} \cdot \boldsymbol{B} = 0\,, \tag{3.5}$$

$$\text{where} \quad \boldsymbol{\mathcal{G}} = (\boldsymbol{u} \times \boldsymbol{b} - \langle \boldsymbol{u} \times \boldsymbol{b} \rangle_{V_\ell}) \quad \text{and} \quad \boldsymbol{\mathcal{E}} = \langle \boldsymbol{u} \times \boldsymbol{b} \rangle_{V_\ell}\,. \tag{3.6}$$

For small Reynolds numbers, $Rm \ll 1$, the term $\mathcal{G}$ can be neglected. In this situation, the small scale component, $\boldsymbol{b}$, has a much smaller evolution time-scale than the large scale component, $\langle \boldsymbol{B} \rangle_{V_\ell}$. $\partial_t \boldsymbol{b}$ can can thus be neglected in front of $\eta \Delta \boldsymbol{b}$ in eq. 3.4. Solving the coupled system of equations can therefore be done by solving the equation in the small scales and deriving an expression of $\boldsymbol{b}$ as a function of $\langle \boldsymbol{B} \rangle_{V_\ell}$. Once $\boldsymbol{b}$ is known, $\boldsymbol{\mathcal{E}}$ can be computed and the large scale component of the magnetic field can be derived. Since $\boldsymbol{\mathcal{E}}$ is a function of $\langle \boldsymbol{B} \rangle_{V_\ell}$, it can be expanded in gradients of $\langle \boldsymbol{B} \rangle_{V_\ell}$ using

$$\mathcal{E}^\delta = \alpha^{\delta\mu} \langle \boldsymbol{B} \rangle^\mu_{V_\ell} + \beta^{\delta\mu\nu} \nabla^\mu \langle \boldsymbol{B} \rangle^\nu_{V_\ell} + \mathcal{O}(\nabla^\delta \nabla^\mu \langle \boldsymbol{B} \rangle^\nu_{V_\ell})\,. \tag{3.7}$$

where $\alpha^{\delta\mu}$ and $\beta^{\delta\mu\nu}$ are tensors whose components only depend on the velocity field. In eq. (3.7), Einstein's summation convention is used on repeated Greek exponents. The $\mathcal{O}(\nabla^\delta \nabla^\mu \langle \boldsymbol{B} \rangle^\nu_{V_\ell})$ term represents higher order terms which are negligible compared to diffusion.

At small magnetic Reynolds number, for isotropic flows, the large scale magnetic evolution equation becomes

$$\partial_t \langle \boldsymbol{B} \rangle_{V_\ell} = \alpha \boldsymbol{\nabla} \times \langle \boldsymbol{B} \rangle_{V_\ell} + (\eta + \beta) \Delta \langle \boldsymbol{B} \rangle_{V_\ell} + \mathcal{O}((\boldsymbol{\nabla}\times)^3 \langle \boldsymbol{B} \rangle_{V_\ell})\,. \tag{3.8}$$

In spatio-temporal Fourier space, for a magnetic field satisfying $\boldsymbol{\nabla} \times \boldsymbol{B} = k\boldsymbol{B}$, the growth rate γ of the instability can be expressed as

$$\gamma = \alpha k - (Rm^{-1} + \beta) k^2 + \mathcal{O}(k^3)\,, \tag{3.9}$$

where k denotes the wavenumber. A large scale instability can be generated at $\alpha = 0$, if the coefficient β satisfies $Rm^{-1} + \beta < 0$.

The instability can also be derived [17] using the following multiscale expansion in power of Rm

$$\partial_t = Rm^{-1} \partial_\tau + Rm^3 \partial_T \quad , \quad \boldsymbol{\nabla} = \boldsymbol{\nabla}_{\boldsymbol{r}} + Rm \boldsymbol{\nabla}_{\boldsymbol{R}} \quad \text{and} \quad \boldsymbol{B} = \sum_{p=0}^{\infty} Rm^p \boldsymbol{B}_p\,, \tag{3.10}$$

where τ and $\boldsymbol{r}$ denote the fast variables and T and $\boldsymbol{R}$ denote the slow variables. The multiscale expansion gives the evolution equation of the fast variables at every order of the expansion. It also gives evolution equation of slow variables via the solvability condition. The equations derived with this method for $\boldsymbol{B}_0$ and $\boldsymbol{B}_1$ are identical to those

derived with the averaging procedure for $\langle \boldsymbol{B} \rangle_{V_\ell}$ and $\boldsymbol{b}$ respectively. It is important to stress that the multiscale derivation is only valid in the limit of small magnetic Reynolds numbers for the alpha-effect. Consequently, the multiscale expansion can neither be used to justify an alpha-effect at moderate or large Rm, nor can it be used to explain a beta-effect at low Rm.

For the moment, the different methods have only shown that the possibility of a large scale magnetic instability cannot been ruled out. They also gave properties on the growth rate of the instability. Using the Roberts velocity field [29], $\boldsymbol{u}^{\text{Ro70}}$, defined at eq. (3.11), let us exhibit a system that does indeed generate an alpha-instability

$$\boldsymbol{u}^{\text{Ro70}} = [U \sin ky \ ; \ U \cos kx \ ; \ V(\sin kx + \cos ky)] \,. \tag{3.11}$$

Let us initialize the problem with a large scale magnetic field

$$\langle \boldsymbol{B} \rangle_{V_\ell} = [\langle B_x \rangle_{V_\ell} \ ; \ \langle B_y \rangle_{V_\ell} \ ; \ \langle B_z \rangle_{V_\ell}] \,. \tag{3.12}$$

After the transient, the first harmonic of the small scale magnetic field $\boldsymbol{b}_1$ can be computed using eq. (3.4) and setting the $\mathcal{G}$-coupling to zero. It satisfies

$$\boldsymbol{b}_1 = \frac{-1}{\eta} \Delta^{-1} \boldsymbol{\nabla} \times (\boldsymbol{u}^{\text{Ro70}} \times \langle \boldsymbol{B} \rangle_{V_\ell}) = \frac{-1}{\eta k^2} (\langle \boldsymbol{B} \rangle_{V_\ell} \cdot \boldsymbol{\nabla}) \boldsymbol{u}^{\text{Ro70}} \tag{3.13}$$

$$\boldsymbol{b}_1 = \frac{1}{\eta k} \begin{bmatrix} U \langle B_y \rangle_{V_\ell} \cos ky \\ -U \langle B_x \rangle_{V_\ell} \sin kx \\ V \langle B_x \rangle_{V_\ell} \cos kx - V \langle B_y \rangle_{V_\ell} \sin ky \end{bmatrix} . \tag{3.14}$$

The α-tensor can then be computed

$$\langle \boldsymbol{u}^{\text{Ro70}} \times \boldsymbol{b}_1 \rangle_{V_\ell} = \alpha \begin{bmatrix} 1 & 0 & 0 \\ 0 & 1 & 0 \\ 0 & 0 & 0 \end{bmatrix} \langle \boldsymbol{B} \rangle_{V_\ell} \quad \text{with} \quad \alpha = \frac{UV}{\eta k} \,. \tag{3.15}$$

The large scale magnetic field depends on the slow variables Z and T, since only its x- and y-components are forced by the alpha-tensor. The evolution equation of the large scale magnetic filed $\langle B \rangle_{V_\ell}$ is given by

$$\partial_T \langle B_x \rangle_{V_\ell} = -\alpha \partial_Z \langle B_y \rangle_{V_\ell} + \eta \partial^2_{ZZ} \langle B_x \rangle_{V_\ell} \tag{3.16}$$

$$\partial_T \langle B_y \rangle_{V_\ell} = \alpha \partial_Z \langle B_x \rangle_{V_\ell} + \eta \partial^2_{ZZ} \langle B_y \rangle_{V_\ell} \,. \tag{3.17}$$

Since some coefficients of the alpha-tensor are equal to zero, the third component of the large scale magnetic field does not influence the evolution of the most unstable mode. The evolution equation of the most unstable large scale magnetic field $\boldsymbol{B}$ can be solved efficiently by introducing $\mathcal{B} = \langle B_x \rangle_{V_\ell} + \imath \langle B_y \rangle_{V_\ell}$. The variable $\mathcal{B}$ follows

$$\partial_t \mathcal{B} = \imath \alpha \partial_Z \mathcal{B} + \eta \partial^2_{ZZ} \mathcal{B} \quad \text{thus} \quad \mathcal{B} = \mathcal{B}_0 e^{(\pm \alpha q - \eta q^2) T \pm \imath q Z} \,, \tag{3.18}$$

where q is the wavenumber associated to the large scale variable Z. A stationary small scale flow can therefore give rise to an alpha-instability. It is important to stress that all the derivation above has been carried out at low magnetic Reynolds number. Even though the arguments presented do not forbid the existence of alpha-instability at larger Rm, they cannot be used to justify the presence of an alpha-instability at an arbitrarily high magnetic Reynolds number.

3.2 Anisotropic kinetic alpha (AKA) effect (review)

Using the similarity between the magnetic field and the velocity field, Frisch *et al.* (1987) were able to show in [13, 14] that the perturbation of the velocity field can also have an alpha-type instability. The differences between the evolution equations of the magnetic field and the velocity field have major implications. The conditions required for the basic flow to generate a kinetic instability turn out to be more restrictive than those for the magnetic instability. The following extract gives the general conditions required to generate an anisotropic kinetic alpha (AKA) effect.

> There are many important instances where the [kinetic] α-tensor vanishes. When the basic flow is parity-invariant, this vanishing occurs because [the tensor] has an odd number of velocities. When the basic flow is random isotropic (that is invariant under genuine rotations, not including parity), vanishing occurs because the tensor $\alpha_{\delta\mu\nu}$ is by construction symmetrical in δ and μ and there exists no non-vanishing third order isotropic tensor with such symmetry. When the basic flow is time-independent, the alpha-tensor, calculated perturbatively in powers of the Reynolds number, vanishes to leading order. Vanishing also occurs when the basic flow is random and delta-correlated in time. Finally, vanishing occurs for the ABC flows. It must be stressed that in MHD, none of the above assumptions, excepting parity-invariance, implies the vanishing of the alpha-effect.
>
> — Frisch *et al.*, *Large-scale flow driven by the anisotropic kinetic alpha-effect*, Physica D: Nonlinear Phenomena, October 1st, 1987

In order to prove the existence of the AKA instability, Frisch *et al.* (1987) applied the time-dependent anisotropic forcing, $\boldsymbol{F}^{\text{Fr87}}$, to the Navier-Stokes equation in a $[0;2\pi]^3$-periodic box

$$\boldsymbol{F}^{\text{Fr87}} = \frac{\nu V_0\sqrt{2}}{\ell_0^2}\left[\cos\left(\frac{y}{\ell_0}+\frac{\nu t}{\ell_0^2}\right)\ ;\ \cos\left(\frac{x}{\ell_0}-\frac{\nu t}{\ell_0^2}\right)\ ;\ \cos\left(\frac{y}{\ell_0}+\frac{\nu t}{\ell_0^2}\right)+\cos\left(\frac{x}{\ell_0}-\frac{\nu t}{\ell_0^2}\right)\right], \quad (3.19)$$

$$\text{with}\quad \partial_t\boldsymbol{u}+(\boldsymbol{u}\cdot\boldsymbol{\nabla})\boldsymbol{u}=-\boldsymbol{\nabla}P+\nu\Delta\boldsymbol{u}+\boldsymbol{F}^{Fr87}\quad\text{and}\quad\boldsymbol{\nabla}\cdot\boldsymbol{u}=0\,, \quad (3.20)$$

where V_0, ℓ_0 denote the velocity and length-scale of the flow respectively. To quantify the evolution of the kinetic instability, the velocity field is decomposed into a large scale component, $\langle\boldsymbol{u}\rangle_{V_\ell}$, and a small scale component, $\boldsymbol{v}$, such that $\boldsymbol{u}=\langle\boldsymbol{u}\rangle_{V_\ell}+\boldsymbol{v}$ with $\langle\boldsymbol{v}\rangle_{V_\ell}=0$. The Navier-Stokes equation is then linearized into two coupled differential equations

$$\partial_t\boldsymbol{v}+(\langle\boldsymbol{u}\rangle_{V_\ell}\cdot\boldsymbol{\nabla})\boldsymbol{v}=\nu\Delta\boldsymbol{v}+\boldsymbol{F}\quad\text{and}\quad\partial_t\langle\boldsymbol{u}\rangle_{V_\ell}+\langle(\boldsymbol{v}\cdot\boldsymbol{\nabla})\boldsymbol{v}\rangle_{V_\ell}=\nu\Delta\langle\boldsymbol{u}\rangle_{V_\ell}\,. \quad (3.21)$$

The term quadratic in $\boldsymbol{v}$ in the evolution equation of $\boldsymbol{v}$ and the term quadratic in $\langle\boldsymbol{u}\rangle_{V_\ell}$ in the evolution equation of $\langle\boldsymbol{u}\rangle_{V_\ell}$ are not kept because they do not force the correct wavenumber. Even though there is no pressure term, the velocity fields are still incompressible. Indeed, since the equation does not have any non-linearity generating a compressible flow, the pressure gradient is equal to zero. Since $\langle\boldsymbol{u}\rangle_{V_\ell}$ varies slowly and $V_0\ell_0/\nu$, the gradients of $\langle\boldsymbol{u}\rangle_{V_\ell}$ are always negligible in front of the gradients of $\boldsymbol{v}$

except in the viscous term $\nu\Delta\langle\boldsymbol{u}\rangle_{V_\ell}$. The evolution equation of the components of the field $\boldsymbol{v}$ can thus be computed analytically using spatio-temporal Fourier transform

$$\boldsymbol{v}_{\boldsymbol{k}\omega} = \frac{\boldsymbol{F}_{\boldsymbol{k}\omega}}{\imath(\omega + \boldsymbol{k}\cdot\boldsymbol{u}) - \nu k^2}\,. \tag{3.22}$$

Using the Parceval-Plancherel theorem on the Fourier transform of the velocity field $\boldsymbol{v}$, the $\langle\boldsymbol{v}_\delta\boldsymbol{v}_\mu\rangle_{V_\ell}$-tensor can be computed. At the first order in $\langle\boldsymbol{u}\rangle_{V_\ell}$, the $\langle\boldsymbol{v}_\delta\boldsymbol{v}_\mu\rangle_{V_\ell}$-tensor is equal to

$$\langle\boldsymbol{v}_\delta\boldsymbol{v}_\mu\rangle_{V_\ell} = \frac{V_0^2}{2}\begin{bmatrix}1&0&1\\0&1&1\\1&1&2\end{bmatrix} + \alpha_{\text{AKA}}\begin{bmatrix}-\langle u_y\rangle_{V_\ell} & 0 & -\langle u_y\rangle_{V_\ell}\\ 0 & \langle u_x\rangle_{V_\ell} & \langle u_x\rangle_{V_\ell}\\ -\langle u_y\rangle_{V_\ell} & \langle u_x\rangle_{V_\ell} & \langle u_x\rangle_{V_\ell} - \langle u_y\rangle_{V_\ell}\end{bmatrix} + \mathcal{O}(U^2) \tag{3.23}$$

$$\text{with}\quad \alpha_{AKA} = \frac{V_0^2\ell_0}{2\nu}\,. \tag{3.24}$$

Since the velocity field $\boldsymbol{v}$ is incompressible, the $\langle\boldsymbol{v}_\delta\boldsymbol{v}_\mu\rangle_{V_\ell}$-tensor is related to the $\langle(\boldsymbol{v}\cdot\boldsymbol{\nabla})\boldsymbol{v}\rangle_{V_\ell}$-tensor via $\partial_\delta(\langle\boldsymbol{v}_\delta\boldsymbol{v}_\mu\rangle_{V_\ell}) = \langle(\partial_\delta\boldsymbol{v}_\delta)\boldsymbol{v}_\mu\rangle_{V_\ell} + \langle\boldsymbol{v}_\delta(\partial_\delta\boldsymbol{v}_\mu)\rangle_{V_\ell} = \langle(\boldsymbol{v}\cdot\boldsymbol{\nabla})\boldsymbol{v}_\mu\rangle_{V_\ell}$. The large scale perturbations depending only on Z are the most unstable mode. Similarly to the magnetic alpha-instability, the x- and y-components of the large scale component of the velocity field are differentially coupled via

$$\partial_T\langle u_x\rangle_{V_\ell} = -\alpha_V\partial_Z\langle u_y\rangle_{V_\ell} + \nu\partial^2_{ZZ}\langle u_x\rangle_{V_\ell} \tag{3.25}$$

$$\partial_T\langle u_y\rangle_{V_\ell} = \alpha_V\partial_Z\langle u_x\rangle_{V_\ell} + \nu\partial^2_{ZZ}\langle u_y\rangle_{V_\ell}\,. \tag{3.26}$$

The set of coupled equations in eq. (3.25)-(3.26) are strictly equivalent to those written in eq. (3.16)-(3.17) if the variables U and B are exchanged. The $\boldsymbol{F}^{\text{Fr87}}$ is able to generate a kinetic instability similar to the magnetic α-instability. Similarly to the magnetic case, the kinetic Reynolds number has to be small for the instability to occur. However, in the case of the kinetic instability, the perturbation of the velocity field also needs to be small, otherwise the non-linear term cannot be neglected. Frisch *et al.* (1987) have shown that after an initial exponential increase of the perturbation, it saturates and gives rise to a new flow which does seem to be AKA-stable.

The AKA-instability presented in Frisch *et al.* (1987) was considered as the unstable response of a flow to a forcing. It can also be viewed as the instability of a fixed velocity field. Instead of fixing the forcing, the basic flow can be fixed. Since the basic flow is the solution of the Navier-Stokes equation in the viscous limit which is a linear problem, both points of view are equivalent.

In order to carry out this analysis, the velocity field is decomposed into a basic flow $\boldsymbol{U}$ and a perturbation $\boldsymbol{v}$ such that $\boldsymbol{u} = \boldsymbol{U} + \boldsymbol{v}$, with $\|\boldsymbol{v}\| \ll \|\boldsymbol{U}\|$. To enforce incompressibility both on the basic flow and on the perturbation, the pressure field is also decomposed into a basic component $P_{\boldsymbol{U}}$ and a perturbation $P_{\boldsymbol{v}}$ such that $P = P_{\boldsymbol{U}} + P_{\boldsymbol{v}}$. The Navier-Stokes equation can then be linearized using eq. (2.7) as

$$\partial_t\boldsymbol{U} = \boldsymbol{U}\times\boldsymbol{\nabla}\times\boldsymbol{U} - \boldsymbol{\nabla}P_U + \nu\Delta\boldsymbol{U} + \boldsymbol{F} \qquad \text{with}\quad \boldsymbol{\nabla}\cdot\boldsymbol{U} = 0\,, \tag{3.27}$$

$$\partial_t\boldsymbol{v} = \boldsymbol{U}\times\boldsymbol{\nabla}\times\boldsymbol{v} + \boldsymbol{v}\times\boldsymbol{\nabla}\times\boldsymbol{U} - \boldsymbol{\nabla}P_{\boldsymbol{v}} + \nu\Delta\boldsymbol{v} \qquad \text{with}\quad \boldsymbol{\nabla}\cdot\boldsymbol{v} = 0\,. \tag{3.28}$$

where the term quadratic in $\boldsymbol{v}$ is neglected. At low Reynolds number, the term $\boldsymbol{U}\times\boldsymbol{\nabla}\times\boldsymbol{U}$, quadratic in $\boldsymbol{U}$ in the evolution equation of $\boldsymbol{U}$, is negligible in front of the diffusive

term. This term can modify the basic flow especially in its small scales but it will not generate an instability since it does not depend explicitly on $\boldsymbol{v}$.

Taking the curl of the evolution equation of $\boldsymbol{v}$, the evolution equation of the vorticity perturbation can be derived

$$\partial_t \boldsymbol{\omega} = \boldsymbol{\nabla}\times(\boldsymbol{U}\times\boldsymbol{\omega}) + \boldsymbol{\nabla}\times(\boldsymbol{v}\times\boldsymbol{\nabla}\times\boldsymbol{U}) + \nu\Delta\boldsymbol{\omega} \quad \text{where} \quad \boldsymbol{\omega} = \boldsymbol{\nabla}\times\boldsymbol{v}\,. \tag{3.29}$$

Besides the additional $\boldsymbol{\nabla}\times(\boldsymbol{v}\times\boldsymbol{\nabla}\times\boldsymbol{U})$ term, the evolution equation of the vorticity perturbation is very similar to the induction equation (see eq. (3.1)) where $\boldsymbol{B}$ and $\boldsymbol{u}$ are replaced by $\boldsymbol{\omega}$ and $\boldsymbol{U}$ respectively. The similarity between the equations explains the equivalence between the magnetic alpha-effect and the AKA-effect. The additional $\boldsymbol{\nabla}\times(\boldsymbol{v}\times\boldsymbol{\nabla}\times\boldsymbol{U})$ term is at the origin of the differences in the conditions needed to generate an instability as described in the quote at page 22.

In addition to the small Reynolds number hypothesis, the AKA-effect has another constraint related to the amplitude of the basic flow. The exponential growth of the velocity perturbation will eventually lead to a modification of the basic flow and produces the saturation observed in [13] when studying Navier-Stokes equation. The saturation does not occur in eq. (3.29) because the Navier-Stokes equation has been linearized. Even though the absence of saturation in eq. (3.29) is highly unphysical, it is very useful to measure numerically the growth rate of the perturbation.

3.3 Distribution of energy (description of a new model)

In the previous section, it has been shown that the alpha- and AKA-effects can generate large scale magnetic and velocity perturbations fields respectively. The growth rate of this instability was determined but the energy distribution was not detailed. If the instability is described as happening in the large scale, the energy of the instability should be located in the largest scale. To get more details on the energy distribution, let us come back to the Roberts example of the alpha-instability. In the magnetic case for the Roberts flows, eq. (3.14) can be used to get the order of magnitude of the ratio of the large scale magnetic field to the small scale magnetic field

$$\left\langle \boldsymbol{b}_1^2 \right\rangle_{V_\ell} = \frac{(U^2+V^2)\frac{(\langle B_x\rangle_{V_\ell}^2+\langle B_y\rangle_{V_\ell}^2)}{2}}{(\eta k)^2} = \frac{\left\langle (\boldsymbol{u}^{\mathrm{Ro70}})^2\right\rangle_{V_\ell}\langle \boldsymbol{B}\rangle_{V_\ell}^2}{(\eta k)^2} \tag{3.30}$$

$$\text{thus} \quad \frac{\|\langle \boldsymbol{B}\rangle_{V_\ell}\|}{\sqrt{\langle \boldsymbol{b}_1^2\rangle_{V_\ell}}} = \frac{\eta k}{\sqrt{\langle (\boldsymbol{u}^{\mathrm{Ro70}})^2\rangle_{V_\ell}}} = \frac{1}{Rm}\,. \tag{3.31}$$

If the magnetic Reynolds number is small, the instability has most of its energy located in the large scales, which is in agreement with the approximation used to derive the alpha-effect. However, when the magnetic Reynolds number becomes of order one, eq. (3.31) indicates that the energy in the large scales becomes as important as that in the small scale. The magnetic field cannot be described as being a large scale field, even using the alpha-description out of its range of validity. Additionally, at large magnetic Reynolds number, the magnetic field can become unstable in the large scale, which makes the alpha-description problematic.

The alpha-description can be adapted to derive a toy model describing the evolution of magnetic field in a regime with large scale instabilities. The AKA-instability has close properties since its evolution equation is similar to the evolution equation of the alpha-effect. To describe the evolution of magnetic field with the toy model, eq. (3.4)&(3.5) are used to write a set of coupled equations on the Fourier amplitude of the magnetic field

$$\partial_t \langle B\rangle_{V_\ell} = qUb - \eta q^2 \langle B\rangle_{V_\ell} \quad \text{and} \quad \partial_t b = kU \langle B\rangle_{V_\ell} + \gamma_{SSD} b\,, \tag{3.32}$$

where $\langle B\rangle_{V_\ell}$, b, U, q and η denote the amplitude of the large scale magnetic field, the amplitude of the small scale magnetic field, the amplitude of the velocity field, the large scale wavenumber and the magnetic diffusivity respectively. γ_{SSD} denotes the growth rate of the small scale magnetic field in the absence of large scale magnetic field. Eq. (3.4) indicates that γ_{SSD} depends on $\mathcal{G}$ and $\eta\Delta b$. At low magnetic Reynolds number, γ_{SSD} is governed by diffusion and can be approximated by $-\eta k^2$ where k is the wavenumber of the small scale magnetic field. At high Reynolds number, γ_{SSD} is governed by the $\mathcal{G}$-term and will be denoted as $\gamma_{\mathcal{G}}$. If the magnetic field is unstable in the small scale, $\gamma_{\mathcal{G}}$ is positive.

If the system of equations presented in eq. (3.32) is unstable, the growth rate of the instability is given by the largest eigenvalue γ of the matrix M defined by

$$\frac{\partial}{\partial t}\begin{bmatrix} \langle B\rangle_{V_\ell} \\ b \end{bmatrix} = M \begin{bmatrix} \langle B\rangle_{V_\ell} \\ b \end{bmatrix} \quad \text{with} \quad M = \begin{bmatrix} -\eta q^2 & qU \\ kU & \gamma_{SSD} \end{bmatrix}, \tag{3.33}$$

$$\text{therefore} \quad \gamma = \frac{1}{2}\left(\gamma_{SSD} - \eta q^2 + \sqrt{4qkU^2 + (\gamma_{SSD} + \eta q^2)^2}\right). \tag{3.34}$$

The eigenvector associated to the eigenvalue has an amplitude ratio given by

$$\frac{\langle B\rangle_{V_\ell}}{b} = -\frac{\gamma_{SSD} + q^2\eta - \sqrt{4kqU^2 + (\gamma_{SSD} + \eta q^2)^2}}{2kU}\,. \tag{3.35}$$

The large scale energy to total energy ratio can be related to the amplitude ratio via

$$\frac{E_0}{E_{tot}} = \frac{\langle B\rangle_{V_\ell}^2}{\langle B\rangle_{V_\ell}^2 + b^2} = \frac{1}{1 + \left(\frac{b}{\langle B\rangle_{V_\ell}}\right)^2}\,. \tag{3.36}$$

In the small magnetic Reynolds number limit, the small scale growth rate satisfies $\gamma_{SSD} \simeq -\eta k^2 < 0$. For large scale separations $q \ll k$, the growth rate can be approximated by $\gamma \simeq \frac{qkU^2}{\eta k^2} = qURm$, and the amplitude ratio can be approximated by $\langle B\rangle_{V_\ell}/b \simeq \frac{\eta k^2}{kU} = \frac{1}{Rm}$. Both scaling laws are in agreement with the alpha-instability generated by the Roberts flow.

Let us now use the toy model to describe the magnetic field at large magnetic Reynolds number. For $q \ll k$, after the small scale instability threshold, the growth rate in the small scales is supposed to follow $\gamma_{SSD} \simeq \gamma_{\mathcal{G}} > 0$. In this limit the growth rate of the instability can be approximated by $\gamma \simeq \gamma_{\mathcal{G}}$ and the amplitude ratio can be approximated by $\langle B\rangle_{V_\ell}/b \simeq \frac{kqU^2}{\gamma_{\mathcal{G}} kU} = q\frac{U}{\gamma_{\mathcal{G}}}$. These relations indicate that after the

instability threshold, the properties of the magnetic field change. The magnetic field is located in the small scales and the growth rate of the instability is independent of the scale separation. As the growth rate γ_k of the small scale instability increases, the amount of energy in the large scales decreases. Tab. 3.1 briefly recapitulates the main relations concerning the growth rate and the large scale energy ratio for a magnetic field with an alpha-effect before and after the small scale instability threshold.

Small scale instability threshold	Before	After
Growth rate:	$\frac{\gamma}{kU} \simeq Rm\left(\frac{q}{k}\right) - \frac{1}{Rm}\left(\frac{q}{k}\right)^2$	$\gamma \simeq \gamma_{\mathcal{G}}$
Amplitude ratio:	$\langle B\rangle_{V_\ell}/b \simeq \frac{1}{Rm}$	$\langle B\rangle_{V_\ell}/b \simeq q\frac{U}{\gamma_{\mathcal{G}}}$
Energy ratio:	$\frac{E_0}{E_{tot}} \underset{Rm \ll 1}{\simeq} 1 - Rm^2$	$\frac{E_0}{E_{tot}} \simeq \left(q\frac{U}{\gamma_{\mathcal{G}}}\right)^2$

Table 3.1 – Properties of the large scale magnetic fields in the presence of an alpha-effect before and after the small scale instability threshold for $q \ll k$.

At fixed velocity, the decrease of energy in the large scales can be explained heuristically by comparing the order of magnitude of the diffusive term and the convective term in Fourier space as the diffusivity varies. Indeed, an increase in diffusivity will lead to an increase in the dampening of all the modes of the magnetic mode. This dampening will be more important in the small scale modes than in large scale modes since the viscous term is expressed as $-\eta k^2$ in Fourier space. As the diffusivity increases, the energy is therefore more concentrated in the large scales. Consequently, if the magnetic Reynolds number increases, the relative energy of large scale modes should increase. Once the magnetic Reynolds number is large enough for the generation of large scale instabilities, large scale instabilities should hinder the alpha-mechanism, limiting the energy to the large scales.

The scaling laws derived from the toy model are used to analyzed the magnetic instabilities in chap. 6 and the kinetic instabilities in chap. 5. In order to quantify properly the large scale behavior of the instability, the instabilities are studied using the Floquet method described in chap. 4. The equations have also been integrated directly in the magnetic case in [30]. But Floquet methods are able to study magnetic fields at scale separations which are greater by several orders of magnitude than those achieved with a direct integration of the equation.

Chapter 4

Elements of context: Floquet analysis

The aim of this chapter is to recapitulate some elements of Floquet theory [31], the application made by Bloch [32] in solid state physics and the method used to analyze the large scale instabilities. Extensive descriptions of Floquet theory and of the Mathieu equation are given in [33, 34]. Bloch theory is broadly described in [35].

This chapter reviews elements of well-documented theories.

4.1 Floquet theory (review)

Historically Floquet theory [31, 36] was first used to solve the Mathieu ordinary differential equation (ODE)

$$\frac{d^2x}{dt^2} + (\delta + \epsilon \cos t)\, x = 0\,, \tag{4.1}$$

where δ and ϵ are the two canonical parameters of the problem [33, 34]. The Mathieu equation describes the evolution of a parametric oscillator with a varying pulsation. In the limit of small angle, a pendulum with a varying length is governed by the Mathieu equation. Fig. 4.1 represents a sketch of the parametric pendulum.

Even though the Mathieu equation is a second-order linear differential equation, the time-dependent coefficient makes it difficult to express the solution in terms of elementary functions. In fact, mathematicians defined special functions called Mathieu functions [37] to describe the solution of the Mathieu equation.

Floquet theory is able to give some properties of the solutions of high-order linear differential equations with T-periodic forcing of the form

$$\frac{d}{dt}x^{(\alpha)}(t) = A_{\alpha\beta}(t)\, x^{(\beta)}(t) \quad \text{where} \quad x^{(\beta)}(t) = \frac{d^\beta}{dt^\beta}x(t) \tag{4.2}$$

where $A_{\alpha\beta}(t)$ is T-periodic in the variable t: $A_{\alpha\beta}(t+T) = A_{\alpha\beta}(t)$. In eq. (4.2), Einstein's summation conventions are used on repeated Greek indices and exponents. One of the main properties of Floquet theory is that, at large t, the solution $x(t)$ can

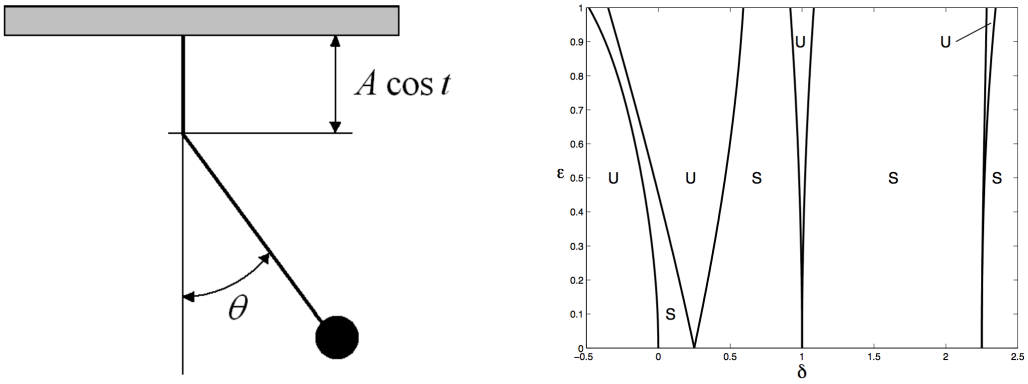

Figure 4.1 – Left) Experimental sketch of parametric oscillator. Right) δ-ϵ stability diagram of the Mathieu equation. S represents stable regions and U represents unstable regions. The figures are extracted from Recktenwald (2006) [33].

be expressed as

$$x(t) = \tilde{x}(t)x^{\ddagger}(t) \quad \text{where} \quad \tilde{x}(t+T) = \tilde{x}(t)\,, \tag{4.3}$$

where $\tilde{x}(t)$ is a T-periodic function and $x^{\ddagger}(t)$ is an exponentially increasing function.

For a first order ODE, the derivation can be carried out exactly. If the differential problem is of first order, it can be rewritten as

$$\frac{d}{dt}x(t) = A(t)x(t) \quad \text{where} \quad A(t+T) = A(t) \quad \text{and} \quad A(t) = \frac{da}{dt}\,. \tag{4.4}$$

The function $\frac{da}{dt}$ is introduced because $A(t)$ has to be integrated in order to solve the ODE. The solution of eq. (4.4) can be found by separating the variables and integrating the ODE. At $s = t + nT$ where $n \in \mathbb{N}$ and $t \in [0;T]$, the solution satisfies $x(s) = x(0)e^{a(s)-a(0)}$, which can be rewritten as

$$\frac{x(t+nT)}{x(0)e^{-a(0)}} = e^{a(t+nT)} = e^{na(T)+a(t)} = e^{\frac{t+nT}{T}a(T)}e^{a(t)-\frac{t}{T}a(T)}\,, \tag{4.5}$$

$$\text{therefore} \quad \tilde{x}(t+nT) = e^{a(t)-\frac{t}{T}a(T)} \quad \text{and} \quad x^{\ddagger}(s) = x(0)e^{\frac{s}{T}a(T)-a(0)}\,, \tag{4.6}$$

where $\tilde{x}$ is a T-periodic function and $x^{\ddagger}$ is exponentially increasing.

To analyze the solutions of eq. (4.2) at higher orders, we can build a fundamental solution matrix $X_{\mu\nu}(t) = x_{\nu}^{(\mu)}(t)$, where the functions $x_{\nu}(t)$ are a basis of solutions of eq. (4.2). Any solution of the eq. (4.2) can be written as a linear combination of the $x_{\nu}(t)$ functions. Since $A_{\alpha\beta}(t)$ is periodic of period T, $X_{\mu\nu}(t+T)$ is also a fundamental solution matrix of eq. (4.2) and it can be related to $X_{\mu\nu}(t)$ by a constant matrix $C_{\mu\nu}$ satisfying

$$\forall t,\ X_{\mu\nu}(t+T) = C_{\mu\alpha}X_{\alpha\nu}(t) \quad \text{thus} \quad C_{\mu\alpha} = X_{\mu\nu}(T)((X(0))^{-1})_{\nu\alpha}\,, \tag{4.7}$$

where $(X(0))^{-1}$ denotes the inverse matrix of $X(0)$. The inverse matrix of $X(0)$ is properly defined since $X(0)$ is constructed with a basis of solutions and has therefore

linearly-independent columns. Since by construction $X_{\mu\nu}(t)$ is non-singular for all t, $C_{\mu\alpha}$ is non-singular.

Eq. (4.7) implies that $C_{\mu\alpha}$ can be found by integrating $X_{\mu\nu}(t)$ for $t \in [0;T]$. The expression of $X_{\mu\nu}(t)$ can then be computed at all time using the eigen-decomposition of $C_{\mu\alpha}$. Supposing that $C_{\mu\alpha}$ is diagonalizable, let us consider one of its eigenvectors $y(t)$ of eigenvalue λ. At $s = t + nT$ where $n \in \mathbb{N}$ and $t \in [0;T]$, the evolution of $y(t)$ is given by

$$y(t+nT) = \lambda^n y(t) = y(t) e^{\frac{nT}{T}\ln\lambda} = \left(y(0) e^{\frac{t+nT}{T}\ln\lambda}\right)\left(\frac{y(t)}{y(0)} e^{-\frac{t}{T}\ln\lambda}\right), \tag{4.8}$$

$$y(t+nT) = \tilde{y}(t) y^{\ddagger}(t+nT) \quad \text{with} \quad y^{\ddagger}(s) = y(0)\lambda^{-\frac{s}{T}} \quad \text{and} \quad \tilde{y}(t) = \frac{y(t)}{y(0)}\lambda^{-\frac{t}{T}}, \tag{4.9}$$

$$\text{with} \quad \tilde{y}(T) = \frac{y(T)}{y(0)}\lambda^{-1} = \frac{1}{\lambda}\frac{\lambda y(0)}{y(0)} = 1 = \tilde{y}(0)\,. \tag{4.10}$$

The solutions of eq. (4.2) can thus be expressed as linear combinations of the modes formed with the product of a T-periodic function with another function. At large t, the function with the greatest eigenvalue in the linear combination dominates the other modes.

4.2 Bloch theory (review)

Floquet theory is also used in solid state physics to describe the wave-function in lattice with a periodic potential. The application of Floquet theory is referred to as Bloch theory in the field of solid state physics. Even though quantum mechanics has little in common with MHD, the geometry in which Bloch theory is applied is similar to the problem described in chap. 5 and 6.

In the general context of quantum mechanics, the wave-function ψ of an electron is described by the Schrödinger equation

$$i\hbar\partial_t\psi = \mathcal{H}\psi = -\frac{\hbar^2}{2m}\Delta\psi + V\psi\,, \tag{4.11}$$

where $\hbar$, $\mathcal{H}$, m and V denote the reduced Planck constant, the Hamiltonian of the system, the mass of the electron and the potential respectively. In quantum mechanics, the term $-\frac{\hbar^2}{2m}\Delta\psi$ is related to the kinetic energy of the electron. The square of the norm of wave-function, $|\psi|^2$, is also equal to the probability density function (PDF) of the electron. Since the PDF is smooth and normalized, the wave-function is assumed to be bounded.

Because of the linear structure of the Schrödinger equation, wave-function solution of eq. (4.11) can be decomposed in a linear combination of eigen-state of energy E_n, where n identifies the energy level. In the stationary case, the wave-function is solution of the eigen-problem

$$-\frac{\hbar^2}{2m}\Delta\psi + V\psi = \mathcal{E}_n\psi\,. \tag{4.12}$$

In one dimension, eq. (4.12) can be written as

$$\frac{d^2}{dx^2}\psi + \frac{2m}{\hbar^2}(\mathcal{E}_n - V)\psi = 0\,. \tag{4.13}$$

If the potential is sinusoidal, switching x with t and $\psi(x)$ with $x(t)$, eq. (4.13) is equivalent to the eq. (4.1). With such an equivalence, it is natural to introduce Floquet theory, or rather Bloch theory, to solve the equation.

In solid state physics, the wave-function describes the probability amplitude of an electron in a crystal. The atoms in the crystal form a finite Bravais lattice [35], *i.e.* one atom is located at every position $\boldsymbol{R} = n_\alpha \boldsymbol{a}_\alpha$ where $n_\alpha \in [\![1; N_\alpha]\!]$ and $\boldsymbol{a}_\alpha$ are the directions of the finite Bravais lattice. To solve the problem, periodic boundary conditions are applied to the finite Bravais lattice. These conditions are referred to as Born-Von Karman conditions in the context of solid state physics. Since the potential is associated to the presence of an atom, the potential is said to have the periodicity associated to the Bravais lattice. On the other hand, the wave-function covers all the lattice and is said to have the periodicity associated to the Born-Von Karman condition.

The problem has two levels of periodicity. The first level of periodicity is associated to the inter-atomic distance in the finite Bravais lattice. The second level of periodicity is associated to the periodic Born-Von Karman boundary condition used to solve the problem. A one-dimensional analogy of the problem can be done by looking at a pearl necklace similar to that presented in fig. 4.2. Every item of the necklace is a pearl. Similarly to the Bravais lattice, starting from a pearl, a translation of the necklace of a pearl diameter will bring another pearl as long as you are not near the clasp of the necklace. But pearls are not exactly the same. If you start from a specific pearl, you have to make a translation of an integer number of necklace length to come back to this specific pearl just like with the Born-Von Karman periodicity.

Figure 4.2 – Photograph of an Akoya pearl necklace.

Let $\boldsymbol{p}$ be the wavevectors associated with the Fourier decomposition with the Born-Von Karman periodicity and let $\boldsymbol{k}$ be the wavevectors associated with the Fourier decomposition with the Bravais lattice periodicity. The wave-function and the potential

can be written as

$$\psi(r) = \sum_{\boldsymbol{p}} \psi_{\boldsymbol{p}} e^{\imath \boldsymbol{p}\cdot\boldsymbol{r}} \quad \text{and} \quad V(r) = \sum_{\boldsymbol{k}} V_{\boldsymbol{k}} e^{\imath \boldsymbol{k}\cdot\boldsymbol{r}} \tag{4.14}$$

With this decomposition, eq. (4.12) can be rewritten as

$$\sum_{\boldsymbol{p}} e^{\imath \boldsymbol{p}\cdot\boldsymbol{r}} \left(\left(\frac{\hbar^2}{2m} p^2 - \mathcal{E}_n \right) \psi_{\boldsymbol{p}} + \sum_{\boldsymbol{k}} V_{\boldsymbol{k}} \psi_{\boldsymbol{p}-\boldsymbol{k}} \right) = 0 \,. \tag{4.15}$$

Since the plane-waves $e^{\imath \boldsymbol{p}\cdot\boldsymbol{r}}$ form an orthogonal set, each term in the sum of eq. (4.15) must be equal to zero. The problem has therefore been transformed into independent equations grouping wavevectors with the Bravais lattice periodicity. More precisely, all wavevectors $\boldsymbol{p}$, differing by a wavevector $\boldsymbol{k}_1$ in the Fourier decomposition associated with the Bravais lattice periodicity, follow

$$\left(\frac{\hbar^2}{2m} (\boldsymbol{p} - \boldsymbol{k}_1)^2 - \mathcal{E}_n \right) \psi_{\boldsymbol{p}-\boldsymbol{k}_1} + \sum_{\boldsymbol{k}} V_{\boldsymbol{k}} \psi_{\boldsymbol{p}-\boldsymbol{k}_1-\boldsymbol{k}} = 0 \,. \tag{4.16}$$

Fixing the wavevector $\boldsymbol{p}$, all the modes associated to the wavevectors of the form $\boldsymbol{p} - \boldsymbol{k}_1$ are coupled together. This coupling links all these modes with as many linear equations as the number of modes. In order to define uniquely the set of wavevectors $\boldsymbol{p} - \boldsymbol{k}_1$, the smallest wavevector in norm, $\boldsymbol{q}$, is chosen. The wavevector $\boldsymbol{q}$ is unique, otherwise it would not be the smallest wavevector of the set. In the solid state physics nomenclature, $\boldsymbol{q}$ is said to belong to the first Brillouin zone. The coefficients of the wave-function in eq. (4.14) can therefore be written as

$$\psi(r) = \sum_{\boldsymbol{q},\boldsymbol{k}} \psi_{\boldsymbol{q}+\boldsymbol{k}} e^{\imath (\boldsymbol{q}+\boldsymbol{k})\cdot\boldsymbol{r}} = \sum_{\boldsymbol{q}} e^{\imath \boldsymbol{q}\cdot\boldsymbol{r}} \widetilde{\psi}_{\boldsymbol{q}}(\boldsymbol{r}) \quad \text{with} \quad \widetilde{\psi}_{\boldsymbol{q}}(\boldsymbol{r}) = \sum_{\boldsymbol{k}} \psi_{\boldsymbol{q}+\boldsymbol{k}} e^{\imath \boldsymbol{k}\cdot\boldsymbol{r}} \,, \tag{4.17}$$

where the $\widetilde{\psi}_{\boldsymbol{q}}(\boldsymbol{r})$ functions have the periodicity of the Bravais lattice. The $\widetilde{\psi}_{\boldsymbol{q}}(\boldsymbol{r})$-functions are not coupled in q-wavenumber. Their expression depends only on the wavevector $\boldsymbol{q}$ and the potential. They are solution of the ODE

$$-\frac{\hbar^2}{2m} \left(\Delta \widetilde{\psi}_{\boldsymbol{q}}(\boldsymbol{r}) + 2\imath (\boldsymbol{q} \cdot \boldsymbol{\nabla}) \widetilde{\psi}_{\boldsymbol{q}}(\boldsymbol{r}) - q^2 \widetilde{\psi}_{\boldsymbol{q}}(\boldsymbol{r}) \right) + V(\boldsymbol{r}) \widetilde{\psi}_{\boldsymbol{q}}(\boldsymbol{r}) = \mathcal{E}_n \widetilde{\psi}_{\boldsymbol{q}}(\boldsymbol{r}) \tag{4.18}$$

In eq. (4.18), the ODE is a second-order linear differential equations, solutions have two free parameters which are usually set by the boundary conditions. Since the modulus square of the wave-function must be normalized, the wave-functions solutions of eq. (4.18) have only one free parameter. The functions $\widetilde{\psi}_{\boldsymbol{q}}(\boldsymbol{r})$ are therefore unique up to one parameter which is associated to the global phase of the wave-function.

The element of Bloch theory to bear in mind for the analysis of MHD instabilities is that, for a given wavenumber $\boldsymbol{q}$, the unique solution of the problem up to a complex phase can be found using the *ansatz* $e^{\imath \boldsymbol{q}\cdot\boldsymbol{r}} \widetilde{\psi}_{\boldsymbol{k}}(\boldsymbol{r})$, where $\widetilde{\psi}_{\boldsymbol{k}}(\boldsymbol{r})$ has the periodicity of the Bravais lattice.

Bloch theorem can also be derived using the quantum mechanic Hermitian formulation by demonstrating that the impulsion operator commutes with the translation operator. However this formulation cannot easily be transcribed to the study of MHD instabilities.

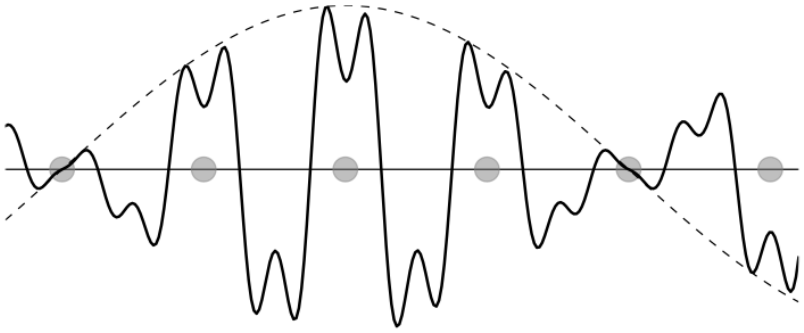

Figure 4.3 – Representation of the real part of a Bloch wave for a one-dimensional Bravais lattice with eight atoms. The gray dots represent the vertex of the lattice. The thick line represents the real part of the wave-function. The dashed line represents the carrier plane wave.

4.3 Floquet Linear Analysis of Spectral MHD (review)

Our objective is to study large scale effects that can happen for two linear MHD phenomena : (i) the induction equation presented in eq.(4.19) and (ii) the linearized Navier-Stokes equation presented in equation eq.(4.20). The induction equation describes the evolution of the magnetic field $\boldsymbol{b}$ in a conductive fluid of velocity $\boldsymbol{u}$ with a magnetic diffusivity η

$$\partial_t \boldsymbol{b} = \boldsymbol{\nabla}\times(\boldsymbol{u}\times\boldsymbol{b}) + \eta\Delta\boldsymbol{b} = \mathcal{L}_m\boldsymbol{b} \quad \text{and} \quad \boldsymbol{\nabla}\cdot\boldsymbol{b} = 0\,. \tag{4.19}$$

The linearized Navier-Stokes equation describes the evolution of the velocity perturbation $\boldsymbol{v}$ in a global flow of velocity $\boldsymbol{U}$ with a kinematic viscosity ν

$$\partial_t \boldsymbol{v} = \boldsymbol{U}\times\boldsymbol{\nabla}\times\boldsymbol{v} + \boldsymbol{v}\times\boldsymbol{\nabla}\times\boldsymbol{U} - \boldsymbol{\nabla}P_{\boldsymbol{v}} + \nu\Delta\boldsymbol{v} = \mathcal{L}_{\text{NS}}\boldsymbol{v} \quad \text{and} \quad \boldsymbol{\nabla}\cdot\boldsymbol{v} = 0\,. \tag{4.20}$$

The linearity of both equations is highlighted with the linear operators $\mathcal{L}_m$ and $\mathcal{L}_{\text{NS}}$. These operators are spatial differential operators but are time-independent.

The analogy between large scale effects of the MHD phenomenon and the Bloch wave is quite straightforward. In the case of $[0;2\pi]^3$-periodic geometries, studying the large scale effect of a flow requires to connect several periodic boxes and enforces a global periodicity to group of boxes. In that sense, large scale MHD systems in periodic box have two levels of periodicity just like Bloch wave-system. The first level of periodicity is due to the presence of the same flow in every cell and the second level of periodicity is related to the periodic boundary condition applied to global system. For the induction equation, the magnetic field $\boldsymbol{b}$ and the velocity field $\boldsymbol{u}$ are the Bloch analogues to the wave-function ψ and to the atomic potential V respectively. For the linearized Navier-Stokes equation, the perturbation $\boldsymbol{v}$ and the flow $\boldsymbol{U}$ are the Bloch analogues to the wave-function ψ and to the atomic potential V respectively.

Applying a Floquet analysis to the linear MHD equation is however different from the Bloch method used to study crystalline lattices. Unlike Bloch waves, MHD problems cannot be solved in the stationary case with the eigen-states of the Hamiltonian.

In addition, the normalization condition on the modulus square of the wave-function does not apply to MHD problem, thus the fields are not bounded. These two elements imply that MHD problems have growth properties that can be related to the standard Floquet method. Because the MHD problems considered are linear, solutions can be decomposed in a basis of eigen-states of the linear operator $\mathcal{L}_m$ and $\mathcal{L}_{\text{NS}}$.

The solution of the evolution equation $\partial_t \boldsymbol{\Psi} = \mathcal{L}(\boldsymbol{\Psi})$ where $\mathcal{L}$ is a linear operator with eigenvalues λ_α and eigenvector $\boldsymbol{y}_\alpha$ can be expressed as

$$\partial_t \boldsymbol{\Psi}(t) = \mathcal{L}(\Psi_\alpha(t)\boldsymbol{y}_\alpha) = \Psi_\alpha(t)\lambda_\alpha \boldsymbol{y}_\alpha \quad \text{thus} \quad \Psi_\alpha(t) = \Psi_\alpha(0)e^{\lambda_\alpha t}\,, \tag{4.21}$$

where the $\Psi_\alpha \boldsymbol{y}_\alpha$ is the decomposition of $\boldsymbol{\Psi}$ on the basis of eigenvector.

Since the operators are linear, the eigenvectors $\boldsymbol{y}_\alpha$ do not couple during the time evolution. Similarly to eq. (4.12), they can be computed by solving the eigenvalue equation $\mathcal{L}\boldsymbol{y} = \lambda \boldsymbol{y}$. Using the properties established for Bloch waves, the solution of eq. (4.21) can be expressed as

$$\boldsymbol{\Psi}(t) = \sum_{\boldsymbol{q}} \left(\Psi_{\boldsymbol{q}}(t) e^{\imath \boldsymbol{q}\cdot\boldsymbol{r}} \tilde{\boldsymbol{y}}_{\boldsymbol{q}}(r) + c.c.\right) \tag{4.22}$$

where *c.c.* denotes the complex conjugate and $\tilde{\boldsymbol{y}}_{\boldsymbol{q}}(r)$ has the periodicity of one $[0;2\pi]^3$-periodic box. The evolution of a field at a given Floquet vector can therefore be found using the *ansatz* $\boldsymbol{\Psi} = e^{\imath \boldsymbol{q}\cdot\boldsymbol{r}} \tilde{\boldsymbol{y}}_{\boldsymbol{\Psi}}(r) + c.c.$. After a transitory regime where the mode of greatest eigenvalue becomes dominant, the field will have an exponential growth with a growth rate equal to the largest eigenvalue. For the induction equation, the Floquet *ansatz* $\boldsymbol{b} = e^{\imath \boldsymbol{q}\cdot\boldsymbol{r}} \tilde{\boldsymbol{b}} + c.c.$ leads to

$$\partial_t \tilde{\boldsymbol{b}} = \imath\boldsymbol{q}\times(\boldsymbol{u}\times\tilde{\boldsymbol{b}}) + \boldsymbol{\nabla}\times(\boldsymbol{u}\times\tilde{\boldsymbol{b}}) + \eta\left(\boldsymbol{\nabla} + \imath\boldsymbol{q}\right)^2 \tilde{\boldsymbol{b}} \quad \text{and} \quad (\imath\boldsymbol{q}\cdot + \boldsymbol{\nabla}\cdot)\tilde{\boldsymbol{b}} = 0\,. \tag{4.23}$$

The fields $\boldsymbol{u}$ and $\tilde{\boldsymbol{b}}$ are both periodic in the $[0;2\pi]^3$-box. In the kinetic case, the Floquet *ansatz* $\boldsymbol{v} = e^{\imath \boldsymbol{q}\cdot\boldsymbol{r}} \tilde{\boldsymbol{v}} + c.c.$ leads to

$$\partial_t \tilde{\boldsymbol{v}} = (\boldsymbol{\nabla}\times\boldsymbol{U})\times\tilde{\boldsymbol{v}} + (\imath\boldsymbol{q} + \boldsymbol{\nabla}\times\boldsymbol{v})\times\boldsymbol{U} - (\imath\boldsymbol{q} + \boldsymbol{\nabla})\tilde{p} + \nu\left(\boldsymbol{\nabla} + \imath\boldsymbol{q}\right)^2 \tilde{\boldsymbol{v}}\,, \tag{4.24}$$

where the Floquet field satisfies the solenoidal condition $(\imath\boldsymbol{q}\cdot + \boldsymbol{\nabla}\cdot)\tilde{\boldsymbol{v}} = 0$. The fields $\boldsymbol{U}$ and $\tilde{\boldsymbol{v}}$ are both periodic in the $[0;2\pi]^3$-box.

The evolution equations eq. (4.23) and (4.24) both have two parameters, the Floquet wavevector $\boldsymbol{q}$ and the dissipation coefficient – η for the magnetic field and ν for the velocity field. These parameters can be changed independently.

Eq. (4.23) and (4.24) can be solved numerically using a pseudo-spectral method similar to that used to solve the Navier-Stokes equation (see chap. 10). The number of variables required to integrate the pseudo-spectral algorithm is doubled compared to the standard Navier-Stokes equation since the Floquet variables $\tilde{\boldsymbol{b}}$ and $\tilde{\boldsymbol{v}}$ are complex.

The Fourier decomposition of the Floquet variables also enables to carry out spectral analysis of the fields. It is especially useful to find in which scale the energy of the field is local. This information can then be used to characterize the large scale effects taking place in the system.

Chapter 5

Large scale instabilities of helical flows (*published* in PRF)

This chapter presents new results.

In the following article, we investigate the large scale hydrodynamic instabilities of periodic helical flows of a given wavenumber K using three dimensional Floquet numerical computations. In the Floquet formalism the unstable field is expanded in modes of different spacial periodicity. This allows (i) to clearly distinguish large from small scale instabilities and (ii) to study modes of wavenumber q of arbitrarily large scale separation $q \ll K$. Different flows are examined including flows that exhibit small scale turbulence. The growth rate σ of the most unstable mode is measured as a function of the scale separation $q/K \ll 1$ and the Reynolds number Re. It is shown that the growth rate follows the scaling $\sigma \propto q$ if an AKA-effect [Frisch *et al.*, Phys. D 1987] is present or a negative eddy-viscosity scaling $\sigma \propto q^2$ in its absence.

This holds both for the $Re \ll 1$ regime where previously derived asymptotic results are verified but also for $Re = \mathcal{O}(1)$, that is beyond their range of validity. Furthermore, for values of Re above a critical value Re_S^c beyond which small scale instabilities are present, the growth rate becomes independent of q and the energy of the perturbation at large scales decreases with scale separation. The non-linear behavior of these large scale instabilities are also examined in the non-linear regime where the largest scales of the system are found to be the most dominant energetically. These results are interpreted by low order models.

5.1 Introduction

Hydrodynamic instabilities are responsible for the frequent encounter of turbulence in nature. Although instabilities are connected to the onset of turbulence and the generation of small scales, in many situation, instabilities are also responsible for the formation of large scale structures. In such situations, flows of a given coherent length-scale are unstable to larger scale perturbations transferring energy to these scales. A classical example of a large scale instability is the alpha-effect [16, 24] in magneto-hydrodynamic (MHD) flows to which the origin of large scale planetary and solar magnetic field is attributed. In alpha-dynamo theory, small scale helical flows self-

organize to generate magnetic fields at the largest scale of the system.

While large scale instabilities have been extensively studied for the dynamo problem, limited attention has been drawn to large scale instabilities of the pure hydrodynamic case. Hence, most direct numeric simulations (DNS) and turbulence experiments are designed so that the energy injection scale ℓ is close to the domain size L. This allows to focus on the forward energy cascade and the formation of the Kolmogorov spectrum [3]. Scales larger that the forcing scale, where no energy cascade is present, are expected [38, 39] to reach a thermal equilibrium with a k^2 spectrum [40, 41, 42, 43]. Recent studies, using (hyper-viscous) simulations of turbulent flows randomly forced at intermediate scales [44], have shown that the energy spectrum at large scales deviates from the thermal equilibrium prediction and forms a strong peak at the largest scale of the system. A possible explanation for this intriguing result is that a large scale instability is present.

In pure hydrodynamic flows, the existence of large scale instabilities has been known for some time. An asymptotic expansion based on scale separation was used in [13, 14] to demonstrate the existence of a mechanism similar to the MHD alpha-dynamo called the anisotropic kinetic alpha (AKA) instability. The AKA instability is present in a certain class of non-parity-invariant, time-dependent and anisotropic flows. It appears for arbitrary small values of the Reynolds number and leads to a growth rate σ proportional to the wavenumber q of the unstable mode: $\sigma \propto q$. However, the necessary conditions for the presence of the AKA instability are stricter than those of the alpha-dynamo. Thus, most archetypal flows studied in the literature do not satisfy the AKA conditions for instability. This, however, does not imply that the large scales are stable since other mechanisms may be present.

In the absence of an AKA-effect higher-order terms in the large scale expansion may lead to a so-called eddy-viscosity effect [19]. This eddy-viscosity can be negative and thus produce a large scale instability [45, 46]. The presence of a negative eddy-viscosity instability appears only above a critical value of the Reynolds number. It results in a weaker growth rate than the AKA-effect, proportional to the square of the wavenumber of the unstable mode $\sigma \propto q^2$. Furthermore, the calculations of the eddy-viscosity coefficient can be much more difficult than those of the AKA alpha-coefficient. This difficulty originates on the order at which the Reynolds number enters the expansion as we explain below.

In the present paper, the Reynolds number is defined as $Re \equiv U_{rms}\ell/\nu$ where U_{rms} is the root mean square value of the velocity and ν is the viscosity. Note that we have chosen to define the Reynolds number based on the energy injection scale ℓ. An alternative choice would be to use the domain length scale L which would lead to the large scale Reynolds number that we will denote as $Re^L = UL/\nu = (L/\ell)Re$. For the AKA effect, the large scale Reynolds number Re^L is large, while the Reynolds number Re, based on the forcing scale ℓ, is small. This allows to explicitly solve for the small scale behavior and obtain analytic results. This is not possible for the eddy-viscosity calculation where there are two regimes to consider. Either the Reynolds numbers is small and the eddy-viscosity only provides a small correction to the regular viscosity, or the Reynolds numbers is large and the inversion of an advection operator is needed. This last case can be obtained analytically only for very simple one dimensional shear flows [45, 46].

To illustrate the basic mechanisms involved in such multi-scale interactions, we depict in fig. 5.1 a toy model demonstrating the main ideas behind these instabilities. This toy model considers a driving flow, $\boldsymbol{U}$ at wavenumber $\mathbf{K} \sim 1/\ell$, that couples to a small amplitude large scale flows, $\boldsymbol{v_q}$ at wavenumber $\mathbf{q} \sim 1/L$ with $|\mathbf{q}| \ll |\mathbf{K}|$. The advection of $\boldsymbol{v_q}$ by $\boldsymbol{U}$ and visa versa will then generate a secondary flow $\boldsymbol{v_Q}$ at wavenumbers $\boldsymbol{Q} = \boldsymbol{K} \pm \boldsymbol{q}$. This small scale perturbation in turn couples to the driving flow and feeds back the large scale flow. If this feedback is constructive enough to overcome viscous dissipation, it will amplify the large scale flow and this process will lead to an exponential increase of $\boldsymbol{v_q}$ and $\boldsymbol{v_Q}$. This toy model has most of the ingredients required for the instabilities to occur.

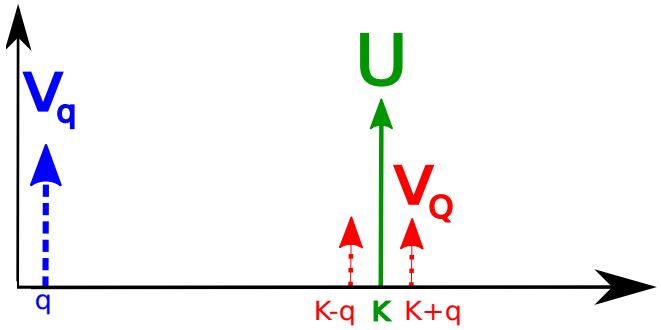

Figure 5.1 – Sketch of the three-mode model. U represents the small scale driving flow of wavenumber K (full arrow), v_q is the large scale perturbation of wavevector q (dashed arrow) and v_Q is the small scale perturbation of wavevector $Q = K \pm q$ (doted arrow).

For the full flow, in order to study independently the large scale instabilities, they must be isolated from other small scale competing instabilities that might coexist. This can be achieved using Floquet theory [31] (also referred as Bloch theory in quantum mechanics [32]). Indeed, Floquet theory decomposes the unstable flow to modes of different spacial periodicity that evolve independently. This enables us to study precisely large and small spatial periodicity separately. In addition the formalism of Floquet theory allows the study of arbitrary large scale separation between the smallest scale of the driving flow and the largest scale of the unstable mode without including the intermediate scales. This minimizes the computational cost and permits us to have a systematic study for a wide range of both scale separation and Reynolds numbers without using any approximations.

In what follows, we use direct numerical simulations (DNS) in the Floquet framework to study large scale instabilities for different flows. Our aim is to go beyond the range of validity of the asymptotic results (obtained rigorously only at the $Re \ll 1$ limit) and measure the values of the alpha-coefficient and eddy-viscosity for arbitrary Re when this description is applicable. In addition we extend our investigation to turbulent flows that respect a given periodicity, that in general cannot be treated analytically. This allows us to quantify the effect of small scale turbulence in the large scales. Finally, we compare the results of Floquet DNS to those of full Navier-Stokes DNS to test non-linear effects on the instabilities.

The remaining sections are structured as follows. Section 5.2 describes in detail the set-up of the problem we are studying and the methods used. Section 5.3 gives the

results for the linear instability of four different flows, as well as the results from the non-linear evolution of the instability. Our conclusions are drawn in the section 5.4.

5.2 Methods (description of new procedures)

5.2.1 Navier-Stokes

Our starting point is the Navier-Stokes equation in the $[0, 2\pi L]^3$-periodic cube:

$$\partial_t \boldsymbol{V} = \boldsymbol{V} \times \boldsymbol{\nabla} \times \boldsymbol{V} - \boldsymbol{\nabla} P + \nu \Delta \boldsymbol{V} + \boldsymbol{F}\,, \tag{5.1}$$

with $\boldsymbol{\nabla} \cdot \boldsymbol{V} = 0$ and where $\boldsymbol{V}$, $\boldsymbol{F}$, P and ν denote the velocity field, the forcing field, the generalized pressure field and the viscosity coefficient, respectively. The geometry imposes that all fields be $2\pi L$-periodic. We further assume that the forcing has a shorter spatial period $2\pi\ell$ with L/ℓ an arbitrary large integer. We denote the wavenumber of this periodic forcing as $\mathbf{K}$, with $K = |\mathbf{K}| = 1/\ell$ for the flows examined. If the initial conditions of $\mathbf{V}$ satisfy the same periodicity as $\boldsymbol{F}$, then this periodicity will be preserved by the solutions of the Navier-Stokes and corresponds to the preservation of the discrete symmetries $x \to x + 2\pi\ell$, $y \to y + 2\pi\ell$ and $z \to z + 2\pi\ell$. However, these solutions can be unstable to arbitrary small perturbations that break this symmetry and grow exponentially. To investigate the stability of the periodic solutions, we decompose the velocity and pressure field in a driving flow and a perturbation component:

$$\boldsymbol{V} = \boldsymbol{U} + \boldsymbol{v} \quad , \quad P = P_{\boldsymbol{U}} + P_{\boldsymbol{v}} \tag{5.2}$$

where $\boldsymbol{U}$ denotes the driving flow that has the same periodicity as the forcing $2\pi\ell$ and $\boldsymbol{v}$ is the velocity perturbation. The linear stability analysis amounts to determining the evolution of small amplitude perturbations so that only the first-order terms in $\boldsymbol{v}$ are kept. The evolution equation of the driving flow is thus:

$$\partial_t \boldsymbol{U} = \boldsymbol{U} \times \boldsymbol{\nabla} \times \boldsymbol{U} - \boldsymbol{\nabla} P_{\boldsymbol{U}} + \nu \Delta \boldsymbol{U} + \boldsymbol{F}\,. \tag{5.3}$$

The remaining terms give the linearized Navier-Stokes equation for the perturbation:

$$\partial_t \boldsymbol{v} = \boldsymbol{U} \times \boldsymbol{\nabla} \times \boldsymbol{v} + \boldsymbol{v} \times \boldsymbol{\nabla} \times \boldsymbol{U} - \boldsymbol{\nabla} p_{\boldsymbol{v}} + \nu \Delta \boldsymbol{v}\,, \tag{5.4}$$

The two pressure terms enforce the incompressibility conditions $\boldsymbol{\nabla} \cdot \boldsymbol{U} = 0$ and $\boldsymbol{\nabla} \cdot \boldsymbol{v} = 0$. The $\mathbf{U}$ flow is not necessarily a laminar flow (but respects $2\pi\ell$-periodicity). In general, the linear perturbation $\boldsymbol{v}$ does not only consist of modes that break the periodicity of the forcing. Linear unstable modes respecting the periodicity may also exist: they correspond to small scale instabilities. We show how these modes can be distinguished from periodicity-breaking large scale modes in the following section devoted to Floquet analysis.

5.2.2 Floquet Analysis

Studying large scale flow perturbations with a code that solves the full Navier-Stokes equation requires considerable computational power as resolution of all scales from domain size L to the smallest viscous scales $\ell_\nu \ll \ell$ must be achieved. This is particularly

difficult in our case where scale separation $\ell \ll L$ is required. In order to overcome this limitation, we adopt the Floquet framework [31]. In Floquet theory, the velocity perturbation can be decomposed into modes that are expressed as the product of a complex harmonic wave, $e^{i\mathbf{q}\cdot\mathbf{r}}$, multiplied by a periodic vector field $\tilde{\boldsymbol{v}}(\boldsymbol{r},t)$ with the same periodicity $2\pi\ell$ as that of the driving flow:

$$\boldsymbol{v}(\boldsymbol{r},t) = \tilde{\boldsymbol{v}}(\boldsymbol{r},t)e^{\imath\boldsymbol{q}\cdot\boldsymbol{r}} + c.c.\,, \tag{5.5}$$

and similar for the pressure,

$$p_{\boldsymbol{v}}(\boldsymbol{r},t) = \tilde{p}(\boldsymbol{r},t)e^{\imath\boldsymbol{q}\cdot\boldsymbol{r}} + c.c.\,, \tag{5.6}$$

where *c.c.* denotes the complex conjugate of the previous term.

Perturbations whose values of $\mathbf{q}$ are such that at least one component is not an integer multiple of $1/\ell$, break the periodicity of the driving flow. The perturbation field $\boldsymbol{v}$ then involves all Fourier wavenumbers of the type $\mathbf{Q} = \mathbf{q}+\mathbf{k}$, where $\mathbf{k}$ is a wavevector corresponding to the $2\pi\ell$-periodic space dependent of $\tilde{\boldsymbol{v}}$. We restrict the study to values of $q = |\mathbf{q}|$ satisfying $0 < q \leq K$. For finite domain sizes $\mathbf{q}$ is a discrete vector with $q \geq 1/L$, while for infinite domain sizes $\boldsymbol{q}$ can take any arbitrarily small value. In the limit $q/K \ll 1$ the perturbation involves scales much larger than ℓ. Therefore, scale separation is achieved without solving intermediate scales as would be required if the full Navier-Stokes equations were used. Furthermore, this framework has the advantage of isolating perturbations that break the forcing periodicity ($\boldsymbol{q}\ell \notin \mathbb{Z}^3$), from other small scale unstable modes with the same periodicity ($\boldsymbol{q}\ell \in \mathbb{Z}^3$) that might also exist in the system.

A drawback of the Floquet decomposition is that some operators have somewhat more complicated expressions than in the simple periodic case. For instance, taking a derivative requires to take into account the variations of both the harmonic and the amplitude. Separating the amplitude in its real and imaginary parts $\tilde{\boldsymbol{v}}(\boldsymbol{r},t) = \tilde{\boldsymbol{v}}^r + \imath\tilde{\boldsymbol{v}}^i$, we obtain

$$\partial_x \boldsymbol{v} = \left[\partial_x\tilde{\boldsymbol{v}}^r - q_x\tilde{\boldsymbol{v}}^i + \imath(q_x\tilde{\boldsymbol{v}}^r + \partial_x\tilde{\boldsymbol{v}}^i)\right] e^{\imath\boldsymbol{q}\cdot\boldsymbol{r}} + c.c.\,, \tag{5.7}$$

where ∂_x denotes the x-derivative and q_x denotes the x-component of the $\boldsymbol{q}$ wavevector.

Using eq. (5.4) and (5.7), the linearized Navier-Stokes equation can be written as a set of $3+1$ complex scalar equations:

$$\begin{aligned}\partial_t\tilde{\boldsymbol{v}} =& (\boldsymbol{\nabla}\times\boldsymbol{U})\times\tilde{\boldsymbol{v}} + (\imath\boldsymbol{q}\times\tilde{\boldsymbol{v}} + \boldsymbol{\nabla}\times\tilde{\boldsymbol{v}})\times\boldsymbol{U} \\ & - (\imath\boldsymbol{q}+\boldsymbol{\nabla})\tilde{p} + \nu(-\boldsymbol{q}^2+\Delta)\tilde{\boldsymbol{v}}\,, \qquad (5.8)\\ \text{with}\quad & \imath\boldsymbol{q}\cdot\tilde{\boldsymbol{v}} + \boldsymbol{\nabla}\cdot\tilde{\boldsymbol{v}} = 0\,. \qquad (5.9)\end{aligned}$$

We use standard pseudo-spectral methods to solve this system of equations in the $2\pi\ell$-periodic cube. The complex velocity field $\tilde{\boldsymbol{v}}$ is decomposed in Fourier space where derivatives are reduced to a multiplication by $\imath\boldsymbol{k}$, where $\boldsymbol{k}$ is the Fourier wavevector. Multiplicative term are computed in real space. These methods have been implemented in the: Floquet Linear Analysis for Spectral Hydrodynamics ($FLASHy$) code and details are given in appx. 5.5.

In order to find the growth rate of the most unstable mode, eq. (5.8),(5.9) are integrated, for a time long enough for a clear exponential behavior to be observed. The growth rate of this most unstable mode can then be measured by linear fitting. Note that this process only leads to the measurement of the fastest growing mode.

5.2.3 Three-mode model

Although the Floquet framework is very convenient to solve equations numerically, it does not easily yield analytic results. Rigorous results must be based on asymptotic expansions and can only be derived in the limit of large Reynolds number [47], small Reynolds number [45], or for simple shear layers [46]. To obtain a basic understanding of the processes involved, we will use the idea represented in the toy model of fig. 5.1. This model also has the major advantage of using a formalism that can easily be related to the physical aspect of the problem.

In our derivation, we only consider the evolution of the two most intense modes of the perturbation and of the driving flow. The velocity perturbation is thus decomposed as a series of velocity fields of different modes:

$$\boldsymbol{v}(\boldsymbol{r},t) = \boldsymbol{v_q}(\boldsymbol{r},t) + \boldsymbol{v_Q}(\boldsymbol{r},t) + \boldsymbol{v}_>(\boldsymbol{r},t)\,, \tag{5.10}$$

$$\boldsymbol{v_q}(\boldsymbol{r},t) = \tilde{\boldsymbol{v}}(\boldsymbol{q},t)e^{\imath \boldsymbol{q}\boldsymbol{r}} + c.c.\,, \tag{5.11}$$

$$\boldsymbol{v_Q}(\boldsymbol{r},t) = \sum_{||\boldsymbol{k}||=1} \tilde{\boldsymbol{v}}(\boldsymbol{q},\boldsymbol{k},t)e^{\imath(\boldsymbol{q}\cdot\boldsymbol{r}+\boldsymbol{k}\cdot\boldsymbol{r})} + c.c.\,, \tag{5.12}$$

$$\boldsymbol{v}_>(\boldsymbol{r},t) = \sum_{||\boldsymbol{k}||>1} \tilde{\boldsymbol{v}}(\boldsymbol{q},\boldsymbol{k},t)e^{\imath(\boldsymbol{q}\cdot\boldsymbol{r}+\boldsymbol{k}\cdot\boldsymbol{r})} + c.c.\,, \tag{5.13}$$

where $\boldsymbol{q}$ denotes the wavenumber of the large scale modes and $\boldsymbol{Q}$ denotes the modes directly coupled to $\boldsymbol{q}$ via the driving flow, since $K = 1$. At wavenumber $\boldsymbol{q}$, the linearized Navier-Stokes equation can be rewritten as:

$$\partial_t \boldsymbol{v_q} = \boldsymbol{U}\times\boldsymbol{\nabla}\times\boldsymbol{v_Q} + \boldsymbol{v_Q}\times\boldsymbol{\nabla}\times\boldsymbol{U} - \boldsymbol{\nabla}p_{\boldsymbol{q}} + \nu\Delta\boldsymbol{v_q}\,. \tag{5.14}$$

Assuming that the coupling with the truncated velocity, $\boldsymbol{v}_>$, is negligible with respect to the coupling with the large scale velocity, $\boldsymbol{v_q}$, the linearized equation at $\boldsymbol{Q}$ reads:

$$\partial_t \boldsymbol{v_Q} = \boldsymbol{U}\times\boldsymbol{\nabla}\times\boldsymbol{v_q} + \boldsymbol{v_q}\times\boldsymbol{\nabla}\times\boldsymbol{U} - \boldsymbol{\nabla}p_{\boldsymbol{Q}} + \nu\Delta\boldsymbol{v_Q}\,, \tag{5.15}$$

where $p_{\boldsymbol{q}}$ and $p_{\boldsymbol{Q}}$ denote the pressure enforcing the incompressible conditions: $\boldsymbol{\nabla}\cdot\boldsymbol{v_q} = 0$ and $\boldsymbol{\nabla}\cdot\boldsymbol{v_Q} = 0$, respectively.

The derivation is restricted to stationary positive helical driving flows, satisfying: $\boldsymbol{U}_{\mathcal{H}}(\boldsymbol{r}) = K^{-1}\boldsymbol{\nabla}\times\boldsymbol{U}_{\mathcal{H}}(\boldsymbol{r})$. The problem can then be solved by making use of the vorticity fields:

$$\boldsymbol{\omega_q} = \boldsymbol{\nabla}\times\boldsymbol{v_q} \quad \text{and} \quad \boldsymbol{\omega_Q} = \boldsymbol{\nabla}\times\boldsymbol{v_Q}\,, \tag{5.16}$$

and the adiabatic approximation: $\partial_t\boldsymbol{v_Q} \ll \nu\Delta\boldsymbol{v_Q}$. The system of equations of the three-mode model is thus:

$$\nu\Delta\boldsymbol{\omega_Q} = -\boldsymbol{\nabla}\times[\boldsymbol{U}_{\mathcal{H}}\times(\boldsymbol{\omega_q} - K\boldsymbol{v_q})]\,, \tag{5.17}$$

$$\partial_t\boldsymbol{\omega_q} = \boldsymbol{\nabla}\times[\boldsymbol{U}_{\mathcal{H}}\times(\boldsymbol{\omega_Q} - K\boldsymbol{v_Q})] + \nu\Delta\boldsymbol{\omega_q}\,. \tag{5.18}$$

The greatest eigenvalue of the system, σ, gives the growth rate of the perturbation. The growth rate can be derived analytically for an ABC large scale flow:

$$U_x^{ABC} = C\sin(Kz) + B\cos(Ky)\,, \tag{5.19}$$
$$U_y^{ABC} = A\sin(Kx) + C\cos(Kz)\,, \tag{5.20}$$
$$U_z^{ABC} = B\sin(Ky) + A\cos(Ky)\,. \tag{5.21}$$

For $A{=}1{:}B{=}1{:}C{=}\lambda$ flows ($\lambda{-}ABC$), one finds:

$$\sigma = \beta q^2 - \nu q^2 \quad \text{with} \quad \beta = bRe^2\nu\,, \tag{5.22}$$
$$b = \frac{1-\lambda^2}{4+2\lambda^2} \quad \text{and} \quad Re = \tfrac{U}{K\nu}\,, \tag{5.23}$$

where Re denotes the small scale Reynolds number defined using the driving flow. The fastest growing mode is found to be fully helical.

This simple model indicates that some driving flows, not satisfying the hypotheses of the AKA-effect, described in [13], can generate a negative eddy-viscosity instability satisfying $\sigma \propto q^2$. The largest growth rate is obtained for $\lambda = 0$, while no q^2 instability is predicted for $\lambda = 1$. For $\lambda \neq 1$ the flow becomes unstable when the β term can overcome the viscosity $\beta > \nu$. This happens when Re is above a critical value: $Re^c = b^{-1/2}$.

5.3 Results (new results)

5.3.1 AKA

We begin by examining a flow that satisfies the conditions for an AKA-instability. Such a flow was proposed in [13] (from now on $Fr87$) and is given by:

$$\begin{aligned} U_x^{Fr87} &= U_0\cos\left(Ky + \nu K^2 t\right)\,, \\ U_y^{Fr87} &= U_0\sin\left(Kx - \nu K^2 t\right)\,, \\ U_z^{Fr87} &= U_x^{Fr87} + U_y^{Fr87}\,. \end{aligned} \tag{5.24}$$

The growth rate of large scale unstable modes can be calculated in the small Reynolds number limit and is given by:

$$\sigma = \alpha q - \nu q^2\,, \tag{5.25}$$

with $\alpha = aReU_0$ and $a = \frac{1}{2}$. The fastest growing mode has negative helicity and $\boldsymbol{q}$ along the z-direction.

Setting $\boldsymbol{q}$ along the z-direction, we integrated eq. (5.8)-(5.9) numerically and measured the growth rate σ. Fig. 5.2 displays the growth rate of the most unstable mode as a function of the wavenumber amplitude $q = |\boldsymbol{q}|$ for three different values of Re measured by the Floquet code and compared to the theoretical prediction. The agreement is good for small values of q and for small values of Re where the asymptotic limit is valid. For q small enough, the flow is unstable and satisfies $\sigma \propto q$. The inset

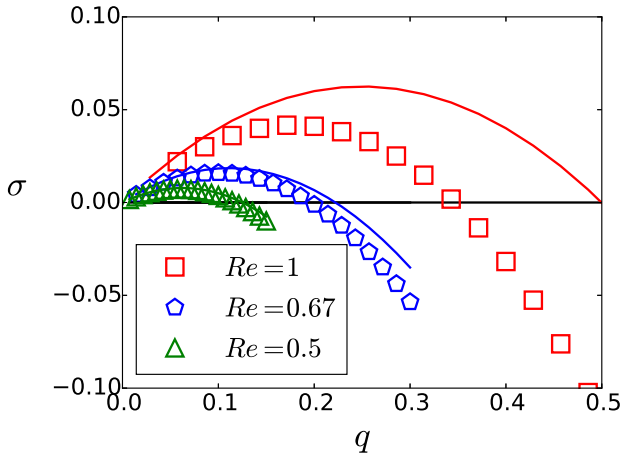

Figure 5.2 – Growth rate of the perturbation plotted as a function of the Floquet wavenumber in log-log scale for a $Fr87$ flow, eq. (5.24). The different markers represent data for different Reynolds number. The solid lines placed above the different sets of markers represent the theoretical prediction.

of fig. 5.3 shows in log-log scale the growth rate of the perturbation as a function of q for different Reynolds numbers. The solid line in the graph indicates the $\sigma \propto q$ scaling which is satisfied for all Re. In fig. 5.3, we compare the theoretical and numerically calculated prefactor a of the alpha coefficient. This coefficient increases linearly with Re and is seen to be in good agreement with the theoretical prediction up to $Re \simeq 10$. For larger values of Re, a deviates from the linear prediction and saturates.

A positive growth rate for a small q mode does not guarantee the dominance of large scales. We should also consider what fraction of the perturbation energy is concentrated in the large scales. Fig. 5.4 shows the energy spectra for different Reynolds numbers. The energy spectrum for the complex Floquet field $\tilde{\boldsymbol{v}}$ is defined as: $E(k) = \sum_{k-\frac{1}{2}\leq|\mathbf{k}|\leq k+\frac{1}{2}} |\tilde{\boldsymbol{v}}|^2$ with $E(k=0)$ the energy at large scales $1/q$. While at small Reynolds numbers, the smallest wavenumber $k = 0$ dominates, as the Reynolds number increases, more energy is concentrated in the wavenumber of the driving flow $K = 1$.

To quantify this behavior, we plot in the inset of fig. 5.5 the fraction of the energy in the zero mode $E_0 = E(0)$ divided by the total energy of the perturbation $E_{tot} = \sum_{k=0}^{\infty} E(k)$, as a function of the wavenumber q for different values of Re. In the small q limit, this ratio reaches an asymptote that depends on the Reynolds number. This asymptotic value is shown as a function of the Re in fig. 5.5. The small scale energy $(E_{tot} - E_0)$ is then shown to follow a power law $1 - \frac{E_0}{E_{tot}} \propto Re^2$ for small values of Re. Therefore, for the AKA-instability, at small Re, the energy is concentrated in the large scales, whereas, at large Re, the most unstable mode has a small projection in the large scales.

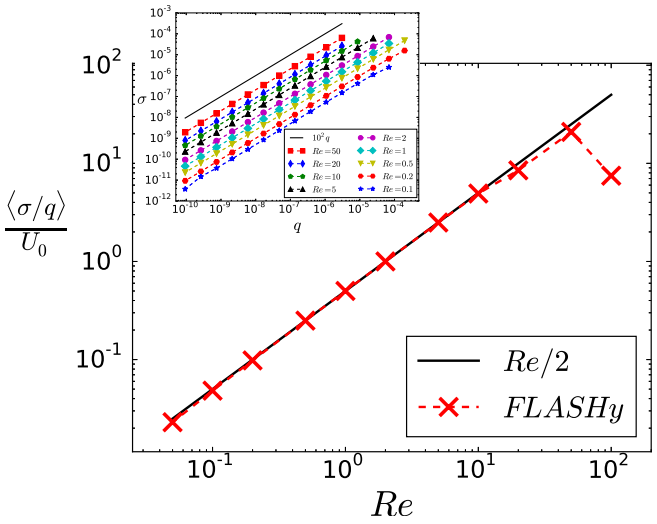

Figure 5.3 – The observable related to the alpha-coefficient ($\langle\sigma/q\rangle/U_0$ using eq. (5.25)) plotted as a function of the Reynolds number in log-log scale for an instability generated by a $Fr87$ flow. The solid line represents the prediction and the crosses the numeric results collected with the $FLASHy$ code.
In the inset, evolution of the growth rate of the perturbation represented as a function of the Floquet wavenumber. The results are plotted in log-log scale at various Reynolds numbers for a $Fr87$ flow, eq. (5.24). The solid line represents the theoretical scaling law.

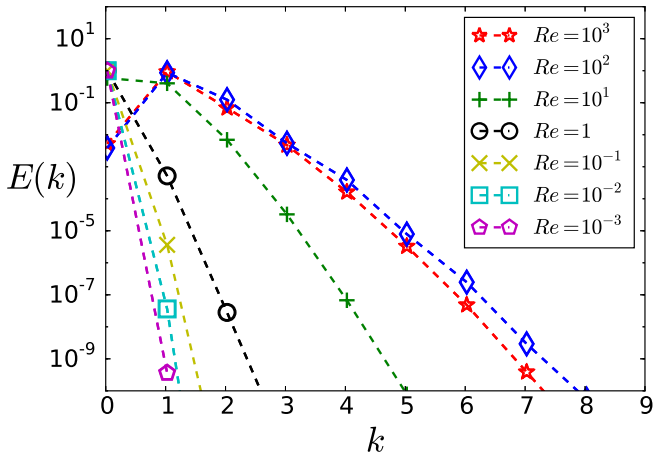

Figure 5.4 – The energy spectrum of the Floquet perturbation of wavenumber $\boldsymbol{q} = (0; 0; 0.025)$ represented as a function of the Fourier wavenumber in semi-log scale. The Floquet perturbation was generated by a $Fr87$ flow, eq. (5.24). Markers of different shapes represent data with different Reynolds number.

5.3.2 Roberts flow: $\lambda = 0$

We now investigate non-AKA-unstable flows. We consider the family of the ABC flow, for which we expect large scale instabilities of the form given in eq. (5.22)-(5.23). The three-mode model predicts that, from the family of ABC flows, the most unstable is the $A = 1 : B = 1 : C = 0$ flow that is commonly referred to as the Roberts flow in

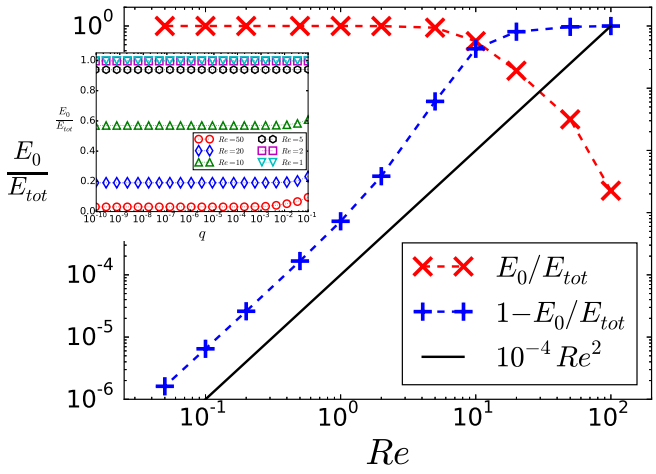

Figure 5.5 – Large scale energy ratio represented as a function the Reynolds number in log-log scale for a $Fr87$ flow, eq. (5.24). The solid line shows the theoretical scaling.
In the inset, evolution of the large scale energy ratio of the perturbation represented as a function of the Floquet wavenumber. The results are plotted in log-log scale for different Reynolds number for a $Fr87$ flow.

the literature [29]. The model predicts a positive growth rate when $Re > 2$. Fig. 5.6 shows the growth rate σ as a function of q for various Reynolds numbers calculated using the Floquet code. For small values of the Reynolds number, all modes q have negative growth rate. Above a critical value $Re^c \simeq 2$, unstable modes appear at small values of q in agreement with the model predictions.

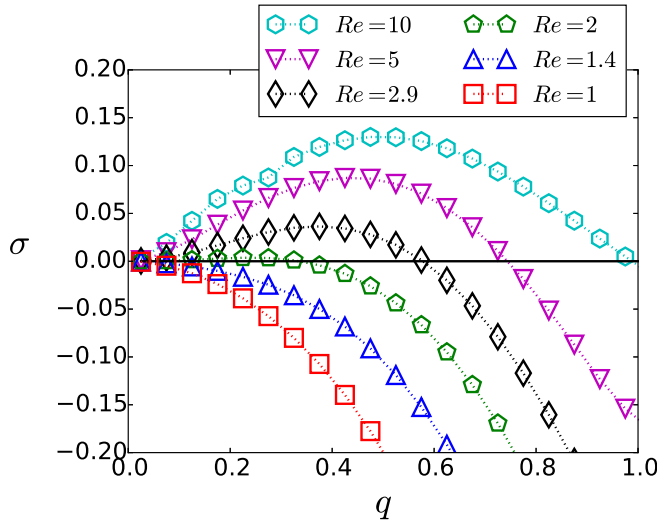

Figure 5.6 – Growth rate plotted as a function of the Floquet wavenumber in log-log scale for a Robert flow. The different markers represent data for different Reynolds numbers.

To investigate the behavior of the instability for small values of q we plot in the inset of fig. 5.7 the absolute value of the growth rate as a function of q, in a logarithmic

scale, for Reynolds numbers ranging from 0.312 to 160. Dashed lines indicate positive growth rates while dotted lines indicate negative growth rates. The solid black line indicates the $\sigma \propto q^2$ scaling followed by all curves. Therefore, the scaling predicted by the model (eq. (5.22),(5.23)) is verified. We will refer to the instabilities that follow this scaling $\sigma \propto q^2$ as negative eddy-viscosity instabilities. To further test the model predictions we measure the proportionality coefficient for the q^2-power law obtained from the Floquet code. Fig. 5.7 compares the b coefficient predicted by the three-mode model with the results of the Floquet code. The figure shows $(\langle\sigma/q^2\rangle + \nu)/\nu$ measured from the data for different values of Re, while the $Re^2/4$ prediction of the model is shown by a solid black line. The two calculations agree on nearly two orders of magnitude. Positive growth rate for the large scale modes implies $\langle\sigma/q^2\rangle/\nu + 1 > 1$. The critical value of the Reynolds number, for which the instability begins, can be obtained graphically at the intersection of the numerically obtained curve with the $\langle\sigma/q^2\rangle/\nu + 1 = 1$ line plotted with a dash-dot green line. The predictions of the model $Re^c = 2$ and the numerically values obtained are in excellent agreement.

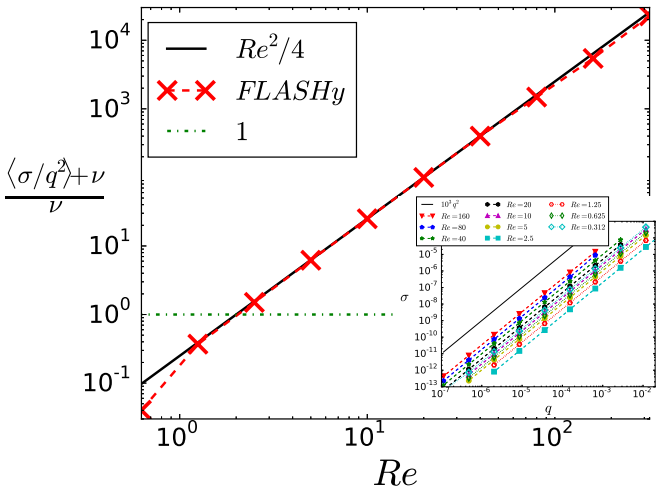

Figure 5.7 – The observable related to the β-coefficient ($\langle\sigma/q^2\rangle/\nu + 1$ using eq. (5.22)) of the Floquet perturbation generated by a Roberts flow is plotted as a function of the Reynolds number in semi-log scale.
In the inset, evolution of the growth rate of the perturbation of a Roberts flow represented as a function of the Floquet wavenumber. The data in presented in log-log scale to highlight the power-law. The different markers on the graph represent different Reynolds numbers. The full markers with dashed lines represent the value of positive growth rates whereas the empty markers with dots represent the absolute value of negative growth rates. The solid line represents the theoretical prediction.

Similarly to the AKA flow, the fraction of energy concentrated in the large scales ($k = 1$) becomes independent of q in the small q limit. This is demonstrated in the inset of fig. 5.8 where the ratio of E_0/E_{tot} is plotted as a function of q. In fig. 5.8, we show the asymptotic value of this ratio as a function of the Reynolds number. As in the case of the AKA instability, the projection to the large scales depends on the Reynolds number, and at large Re, it follows the power law $\frac{E_0}{E_{tot}} \propto Re^{-2}$.

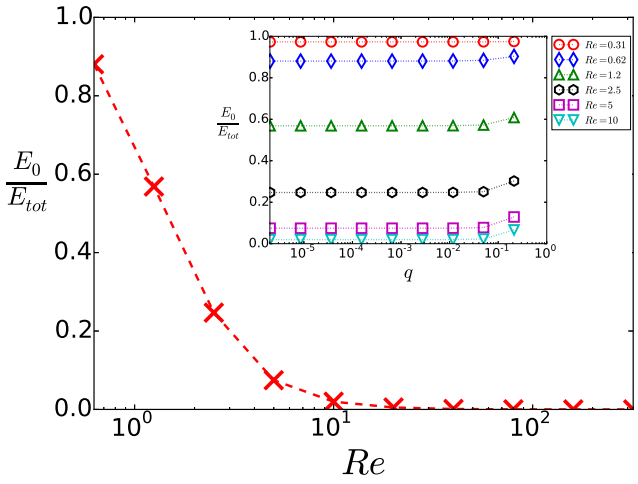

Figure 5.8 – The large scale energy ratio is represented as a function of the Reynolds number for the most unstable Floquet mode of the Roberts flow. In inset, evolution of the large scale energy ratio of the perturbation as a function of the Floquet wavenumber plotted in log-log scale at different Re for a Roberts flow.

5.3.3 Equilateral ABC flow: $\lambda = 1$

For the $A=1:B=1:C=1$ flow, the three-mode model predicts that the b coefficient is zero. Therefore, the model does not predict a negative eddy-viscosity instability with: $\sigma \propto q^2$. Fig. 5.9 shows the growth rate as a function of the wavenumber q calculated using the Floquet code for different values of the Reynolds number. Clearly the small q modes still become unstable but the dependence on Re appears different from the previously examined cases. We thus examine separately the small Re and large Re behaviors.

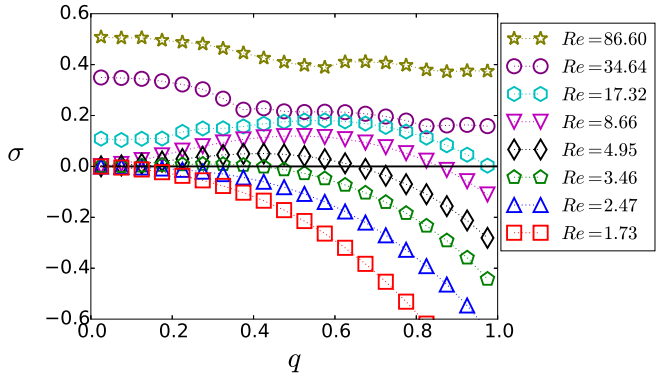

Figure 5.9 – Growth rate evolution of the perturbation represented as a function of the Floquet wavenumber for the equilateral ABC flow. The different markers represent the evolution of the growth rate of data for different Reynolds number.

5.3.3.1 Small values of Re

First, we examine the instability for small values of $Re \leq 10$ for which the growth rate σ tends to zero as $q \to 0$. The inset of fig. 5.10 shows the growth rate of the instability for the equilateral ABC flow as a function of the wavenumber q in logarithmic scale for different values of Re ranging from 0.312 to 10. In this range, the growth rate behaves much like the Roberts flow, and is in contradiction with the three-mode model. The numerically calculated growth rates show a clear negative eddy-viscosity scaling $\sigma \propto q^2$. The growth rate becomes positive above a critical value of Re. In fig. 5.10, the measured value of $\langle \sigma/q^2 \rangle/\nu + 1$ is represented as a function of the Reynolds number. In the inset, the plot lin-log of $\frac{\langle \sigma/q^2 \rangle + \nu}{Re^2 \nu}$ provides a measurement of the b coefficient. This expression becomes larger than one (signifying the instability boundary that is marked by a dash-dot line) for $Re \gtrsim 3$. This value $Re^c \simeq 3$ is slightly higher than the critical Reynolds number of the Roberts flow $Re^c = 2$. At very small Reynolds number, the value of $b = \frac{\langle \sigma/q^2 \rangle + \nu}{Re^2 \nu}$ approaches zero very quickly, which indicates that the model prediction is recovered at $Re \to 0$.

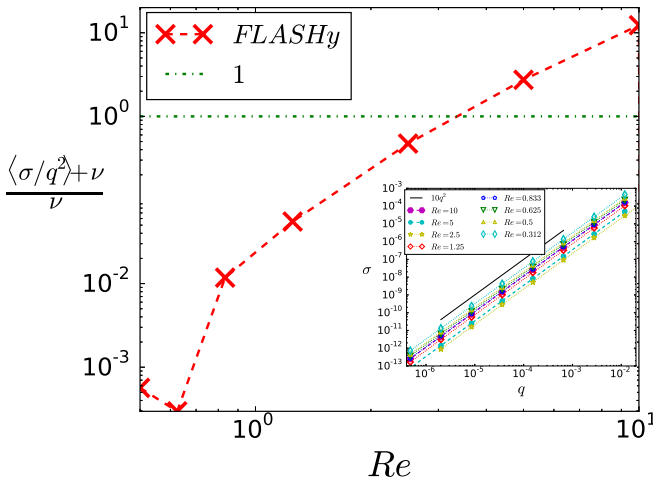

Figure 5.10 – The observable related to the β-coefficient ($\langle \sigma/q^2 \rangle/\nu + 1$ using eq. (5.22)) of the Floquet perturbation generated by a equilateral ABC flow, represented as a function of the Reynolds number in log-log scale.
In inset, evolution of growth rate of the perturbation of a equilateral ABC flow represented as a function of the Floquet wavenumber in log-log scale to highlight the power-law. The different markers on the graph represent different Reynolds number. The full markers with dashed lines represent the value of positive growth rates whereas the empty markers with dots represent the absolute value of negative growth rates.

To investigate further the discrepancy of the Floquet results with the three-mode model. Fig. 5.11 shows the b coefficient (measured as $b = \frac{\langle \sigma/q^2 \rangle + \nu}{Re^2 \nu}$) for different λ parameters from 0 (Roberts flow) to 1 (equilateral ABC flow). All the DNS are carried out at $Re = 10$. The results indicate that the three-mode model and the results from the Floquet code agree for $\lambda \lesssim 0.5$ but deviate as λ becomes larger. To identify where this discrepancy between the model and the DNS occurs, we modified the $FLASHy$ code in order to test the assumptions of the model. This is achieved

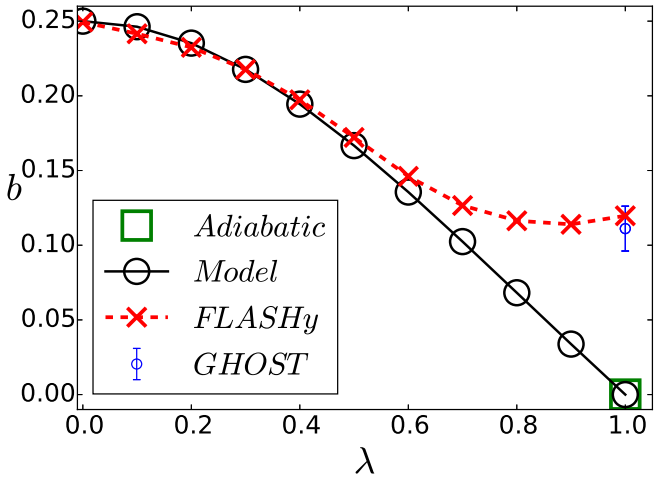

Figure 5.11 – The measured values of the b coefficient represented as a function of the λ-parameter of the flow (ABC flow with $A = 1 : B = 1 : C = \lambda$) for $Re = 10$. The dashed curves with crosses represent the numeric data collected with the $FLASHy$ code. The full line curve with circle represents the prediction given by the three-mode model.

by enforcing the adiabatic approximation in the Floquet code and by controlling the number of modes that play a dynamical role. The latter is performed by using a Fourier truncation of the Floquet perturbation at a value k_{cut} so that only modes with $k < k_{cut}$ are present. Fig.5.12 shows the dependence of the b coefficient on the truncation mode, k_{cut}. For $k_{cut} \geq 3$, the growth rate reaches the asymptotic value that is also observed in the inset of fig. 5.10 for $Re = 10$ obtained from the "untampered" $FLASHy$ code. This confirms the assumption that modes in the smallest scales have little impact on the evolution of the large scale perturbation. However, the b coefficient strongly varies for $k_{cut} \leq 3$. The model predictions are recovered only when $k_{cut} = 1$, which amounts to keeping only the modes used in the model. Therefore, the hypothesis of the model to restrict the interaction of the perturbation to its first two Fourier modes does not seem to hold for the equilateral ABC flow at moderate Reynolds number, $1 \leq Re \leq 10$. The adiabatic hypothesis does not appear to affect the results. Therefore, the discrepancy between the three-mode model and the numeric results is due to the coupling of the truncated velocity $\boldsymbol{v}_>$ that was neglected in the model.

5.3.3.2 Large values of Re

We now turn our focus to large values of the Reynolds number that display a finite growth rate σ at $q \to 0$ (see fig. 5.9). Fig. 5.13 shows the growth rate σ in a lin-log scale for four different values of the Reynolds number. Unlike the small values of Re examined before here it is clearly demonstrated that above a critical value of Re the growth rate σ reaches an asymptotic value independent of q. At first, this finite growth rate seems to violate the momentum conservation. Indeed, momentum conservation enforces modes with $q = 0$, corresponding to uniform flows, not to grow.

The resolution of this conundrum can be obtained by looking at the projection of the unstable modes to the large scales. In fig. 5.14, we plot the ratio E_0/E_{tot} as a

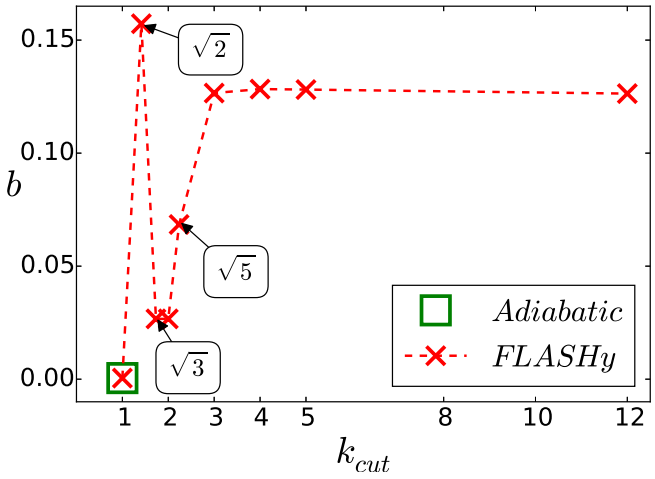

Figure 5.12 – The values of the b coefficient computed by the $FLASHy$ code are represented as a function of the truncation imposed in the code. The perturbation was generated by equilateral ABC flow at $Re = 10$.

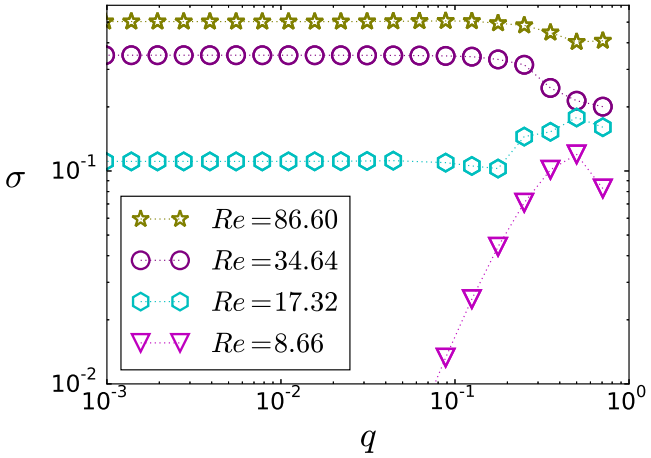

Figure 5.13 – Evolution of growth rate of the perturbation generated by an equilateral ABC flow at large values of Re represented as a function of the Floquet wavenumber. The different markers represent data for different Reynolds numbers.

function of q for the same values of Re as used in fig. 5.13. Unlike the small Re cases examined previously, for large Re, this energy ratio decays to zero at small values of q and appears to follow the power law $E_0/E_{tot} \propto q^4$. Therefore, at $q = 0$, the energy at large scales E_0 is zero and the momentum conservation is not violated in the $q = 0$ limit.

5.3.3.3 Small and large scale instabilities

The results of the previous sections indicate that there are two distinct behaviors: the first one for which $\lim_{q\to 0} \sigma = 0$ and $\lim_{q\to 0} E_0/E_{tot} > 0$ when Re is small and the second one for which $\lim_{q\to 0} \sigma > 0$ and $\lim_{q\to 0} E_0/E_{tot} = 0$ when Re is large. We argue that there is a second critical Reynolds number Re_S^c such that flows for which

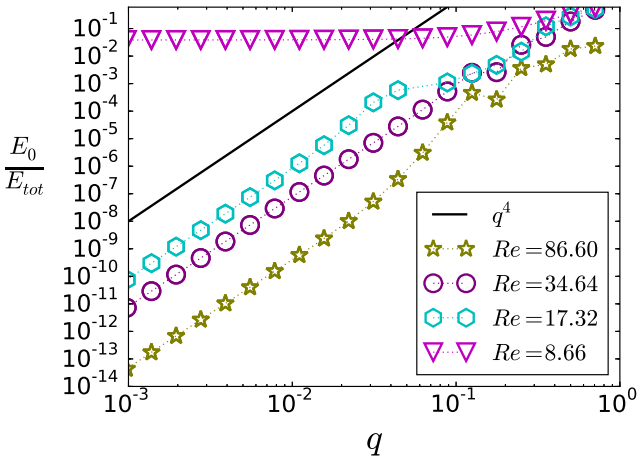

Figure 5.14 – Evolution of the large scale energy ratio of the perturbation generated by an equilateral ABC flow at large values of Re represented as a function of the Floquet wavenumber. The different markers represent data with different Reynolds number.

$Re^c < Re < Re_S^c$ show the first behavior while flows with $Re_S^c < Re$ show the second behavior. This second critical value is related to the onset of small scale instabilities.

To demonstrate this claim, we are going to use a simple model. We consider the evolution of two modes, one at large scales v_q and one at small scales v_Q. These modes are coupled together by an external field U. In the absence of this coupling, the large scale mode v_q decays while the evolution of the small scale mode v_Q depends on the value of the Reynolds number. The simplest model satisfying these constraints, dimensionally correct and leading to an AKA-type $\sigma \propto q$ instability or a negative eddy-viscosity instability $\sigma \propto q^2$, is:

$$\frac{d}{dt}v_q = \quad -\nu q^2 v_q \quad + U q^n Q^{1-n} v_Q \,, \tag{5.26}$$

$$\frac{d}{dt}v_Q = \quad UQ v_q \quad + \sigma_Q v_Q \,. \tag{5.27}$$

The index n takes the values $n = 1$ if an AKA instability is considered and $n = 2$ if an instability of negative eddy-viscosity is considered. Note that for $q = 0$ the growth of v_q is zero, as required by momentum conservation. $\sigma_Q = sUQ - \nu Q^2$ gives the small scale instability growth rate that is positive if $Re = U/(\nu Q) > 1/s = Re_S^c$.

The simplicity of the model allows for an analytic calculation of the growth rate and the eigenmodes. Despite its simplicity, it can reproduce most of the results obtained here in the $q \ll Q$ limit. The general expression for the growth rate is given by $\sigma = \frac{1}{2}\left[(\sigma_Q - \nu q^2 \pm \sqrt{(\sigma_Q + \nu q^2)^2 + 4Q^{2-n}q^n U^2}\right]$ and eigenmode satisfies $v_q/v_Q = Uq^nQ^{1-n}/(\sigma + \nu q^2)$.

First, we focus on large values of ν such that $\sigma_Q = -\nu Q^2 < 0$. For $n = 1$, the growth rate σ and the energy ratio $E_0/E_{tot} = v_q^2/(v_q^2 + v_Q^2)$ are given to the first order in q

$$\sigma \simeq \frac{U^2 q}{\nu Q} \quad \text{and} \quad \frac{E_0}{E_{tot}} \simeq \frac{1}{1 + Re^2}. \tag{5.28}$$

In the same limit for $n = 2$ we obtain:

$$\sigma \simeq \nu(Re^2 - 1)q^2 \quad \text{and} \quad \frac{E_0}{E_{tot}} \simeq \frac{1}{1 + Re^2}. \tag{5.29}$$

The critical Reynolds number for the large scale instability is given by $Re^c = 1$. Both of these results in eqs. (5.28) and (5.29) are in agreement with the results demonstrated in figs. 5.3, 5.5, 5.7, 5.8.

The behavior changes when a small scale instability exists $\sigma_{_Q} > 0$. This occurs when $sUQ > \nu Q^2$ at the critical Reynolds number: $Re^c_S = 1/s$. For large $Re \gg Re^c_S$ we thus expect $\sigma_{_Q} \simeq sUQ > 0$. In this case for $n = 1$ to first order in q, we have:

$$\sigma \simeq \sigma_{_Q} \quad \text{and} \quad \frac{E_0}{E_{tot}} \simeq \frac{q^2}{s^2Q^2} \tag{5.30}$$

while for $n = 2$, we obtain:

$$\sigma \simeq \sigma_{_Q} \quad \text{and} \quad \frac{E_0}{E_{tot}} \simeq \frac{q^4}{s^2Q^4}. \tag{5.31}$$

The model is thus in agreement also with the scalings observed in figs. 5.13 and 5.14. The transition from one behavior to the other occurs at the onset of small scale instability Re^c_S. It is thus worth pointing out that the results of the $FLASHy$ codes showed that the transition from $\lim_{q\to 0}\sigma = 0$ modes to $\lim_{q\to 0}\sigma > 0$ occurs at the value of Re for which small scale instability of the ABC flow starts $Re^c_S \simeq 13$ see [48] and the article of Zheligovsky and Pouquet in [49]. This further verifies that the transition observed is due to the development of small scale instabilities.

We also note here that both the Roberts flow and the $Fr87$ flow given in eq. (5.24) are invariant in translations along the z-direction. This implies that each q_z mode evolves independently without coupling to other k_z modes. The onset of small scale instabilities Re^c_S for $q = 0$ in this case then corresponds to the onset of two-dimensional instabilities. Two-dimensional flows however forced at the largest scale of the system are known to be stable at all Reynolds numbers [50]. This result originates from the fact that two-dimensional flows conserve both energy and enstrophy and small scales cannot be excited without exciting large scales at the same time. This is the reason why no Re^c_S was observed in these flows.

5.3.4 Turbulent equilateral ABC flows

As discussed in the introduction, the driving flow does not need to be laminar to use Floquet theory. It is only required to obey the $2\pi\ell$-periodicity. It is worth thus considering large scale instabilities in a turbulent ABC flow that satisfies the forcing periodicity. This amounts to the turbulent flow forced by an ABC forcing in a periodic cube of the size of the forcing period $2\pi\ell$. Due to the stationarity of the laminar ABC flow, it can be excluded as possible candidate for an AKA-instability. However, this is not true of a turbulent ABC flow since it evolves in time. We cannot thus *a priori* infer that a turbulent ABC flow results in an AKA-instability or not.

To test this possibility, we consider the linear evolution of the large scale perturbations $\boldsymbol{v}$ driven by an equilateral ABC flow above $Re = 50$, that is beyond the onset

of the small scale instability $Re_S^c \simeq 13$. The turbulent equilateral ABC flow $\mathbf{U}$ is obtained solving the Navier-Stokes eq. (5.3) in the domain $(2\pi\ell)^3$ driven by the forcing function $\mathbf{F}^{ABC} = \mathbf{U}^{ABC}$. The code is executed until the flow reaches saturation. The evolution of the large scale perturbations is then examined solving eq. (5.8)-(5.9) with the $FLASHy$ code coupled to the Navier-Stokes eq. (5.3).

The kinetic energy E_U of the turbulent equilateral ABC flow $\mathbf{U}$ is shown in fig. 5.15. The energy E_U strongly fluctuates around a mean value. The evolution of the energy

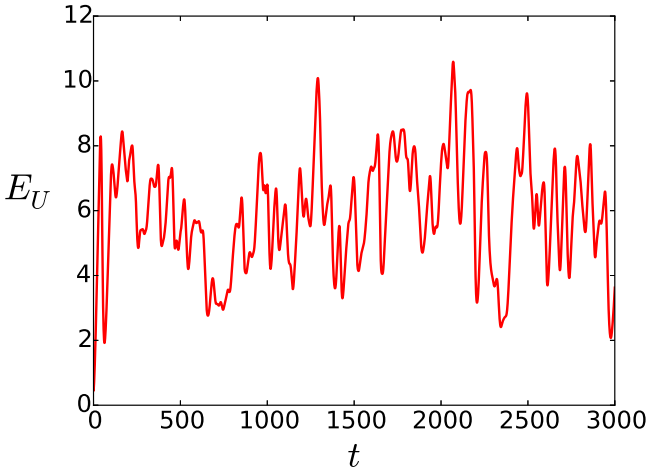

Figure 5.15 – Temporal evolution of the energy of the turbulent equilateral ABC driving flow at $Re = 122$.

E_{tot} of the perturbations $\mathbf{v}$ for different values of q is shown in the inset of 5.16. E_{tot} shows an exponential increase, from which the growth rate can be measured. The growth rate σ as a function of the wavenumber q is shown in fig. 5.16 while the ratio E_0/E_{tot} is shown in fig. 5.17. The growth rate of the large scale instabilities appears to reach a finite value in the limit $q \to 0$ just like laminar ABC flows above the small scale critical Reynolds Re_S^c. However, the ratio E_0/E_{tot} does not scale like q^4 as laminar equilateral ABC flows but like q^2. This indicates that the turbulent equilateral ABC flow has a stronger effect on the large scales than its laminar version. This can have possible implications for the saturated stage of the instability that we examine next.

5.3.5 Non-linear calculations and bifurcation diagram

We further pursue our investigation of large scale instabilities by examining the non-linear behavior of the flow close to the instability onset. We restrict ourselves to the case of the equilateral ABC flow whose non-linear behavior has been extensively studied in the absence however of scale separation [15]. The linear stability of the ABC flow in the minimum domain size has been studied in [48] and more recently in [51]. These studies have shown that the ABC flow destabilizes at $Re_S^c \simeq 13$.

To investigate the non-linear behavior of the flow in the presence of scale separation, we perform a series of DNS of the forced Navier-Stokes equation (eq. (5.1)) in triple periodic cubic boxes of size $2\pi L$ using the GHOST code [52, 53]. The forcing maintaining the flow is $\mathbf{F}^{ABC} = \frac{\sqrt{2}}{\sqrt{3}}\nu|\mathbf{K}|^2\mathbf{U}^{ABC}$ so that the laminar solution of the

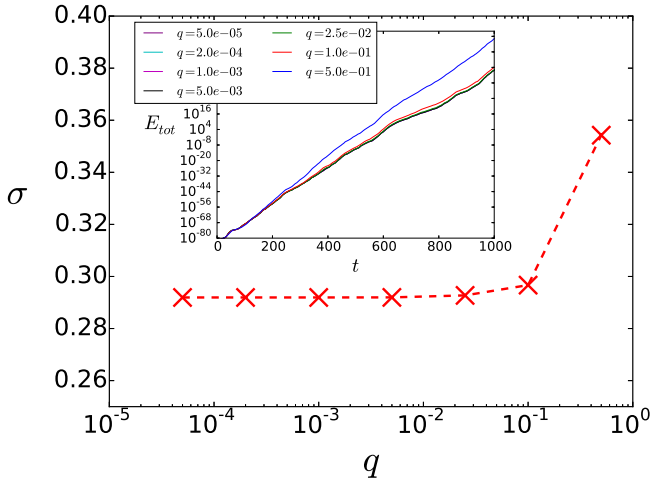

Figure 5.16 – The growth rate of the perturbation generated by the turbulent equilateral ABC driving flow, is represented as a function of the Floquet wavenumber. In inset, the exponential growth of the energy of the large scale perturbations represented as a function of time for various q.

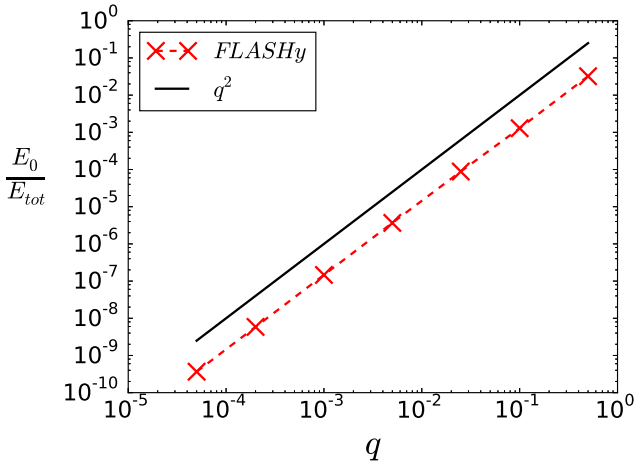

Figure 5.17 – The large scale energy ratio is represented as a function of the Floquet wavenumber for a perturbation forced by a turbulent equilateral ABC flow. The dashed line with the crosses represents the numeric results and the solid line the scaling law.

flow is the ABC flow [15] normalized to have unit energy. Four different box-sizes are considered: $KL = 1, 5, 10$ and 20. For each box size and for each value of Re, the flow is initialized with random initial conditions and evolves until a steady state is reached.

Fig. 5.18 shows the saturation level of the total energy E_V at steady state as a function of Re for the four different values of KL. At low Reynolds number, the laminar solution $\mathbf{V} = \mathbf{U}^{ABC}$ is the only attractor and so the energy is $E_V = 1$. At the onset of the instability the total energy decreases. A striking difference appears between the $KL = 1$ case and the other three cases. For the $KL = 1$ case the first instability appears at $Re_S^c \simeq 13$ in agreement with the previous work [48, 51]. By definition,

only small scale instabilities are present in the $KL = 1$ case (*i.e.* instabilities that do not break the forcing periodicity). For the other three cases, which allow the presence of modes of larger scale than the forcing scale, the flow becomes unstable at a much smaller value: $Re^c \simeq 3$. This value of Re^c is in agreement with the results obtained in section 5.3.3 for large scale instability by a negative eddy-viscosity mechanism. The

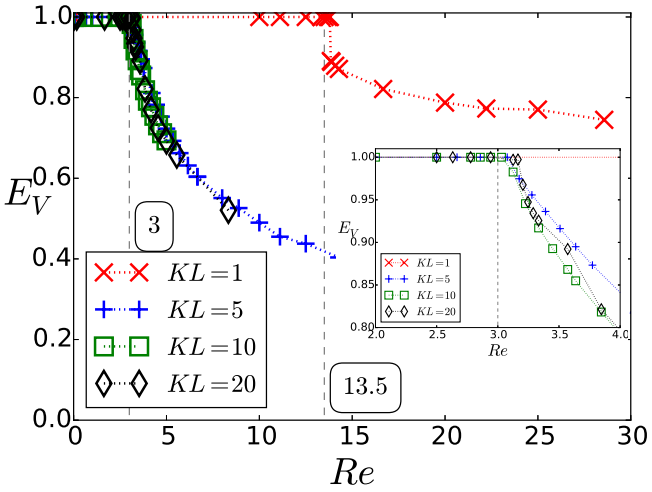

Figure 5.18 – Bifurcation: the total energy of the flow is represented as a function of the Reynolds number for different scale separations $K \in \{1; 5; 10; 20\}$. In inset, zoom of the graph of the total energy near the large scale bifurcation for $Re \in [2; 5]$.

energy curves for the forcing modes $KL \geq 5$ all collapse on the same curve. This indicates that not only the growth rate but also the saturation mechanism for these three simulations are similar.

Further insight on the saturation mechanism can be obtained by looking at the energy spectra. Fig. 5.19 shows the energy spectrum of the velocity field at the steady state of the simulations. Two types of spectra are plotted. In fig. 5.19, spectra plotted using lines and denoted as k-bin display energy spectrum collected in bins where modes $\mathbf{k}$ satisfy $n_1 - 1/2 < |\mathbf{k}|L \leq n_1 + 1/2$, with n_1 a positive integer. $E(k)$ then represents the energy in the bin $n_1 = k$. In fig. 5.19, spectra plotted using red dots and denoted by k^2-bin display the energy spectrum collected in bins where modes $\mathbf{k}$ satisfy $|\mathbf{k}|^2L^2 = n_2$, with n_2 a positive integer. Since $\mathbf{k}L$ is a vector with integer components m_x, m_y and m_z, its norm $k^2L^2 = m_x^2 + m_y^2 + m_z^2$ is also a positive integer. $E(k)$ then represents the energy in the bin $n_2 = k^2L^2$. This type of spectrum provides more precise information about the energy distribution among modes. In our case, they help separate K modes from $K \pm 1/L$ modes and highlight the three-mode interaction. The $k = K \pm 1/L$ modes as well as the largest scale mode $kL = 1$ that were used in the three-mode model are shown by blue circles in the spectra. The drawback of k^2-bin spectra is their memory consumption. They have a number of bins equal to the square of the number of bins of standard k-bin spectra. However, since spectra are not outputted at every time-step, this inconvenience is limited.

The plots of the spectra show that the most energetic modes are the modes close to the forcing scale and the largest scale mode $kL = 1$. This is true even for the largest scale separation examined $KL = 20$. We note that the largest scale mode is not the

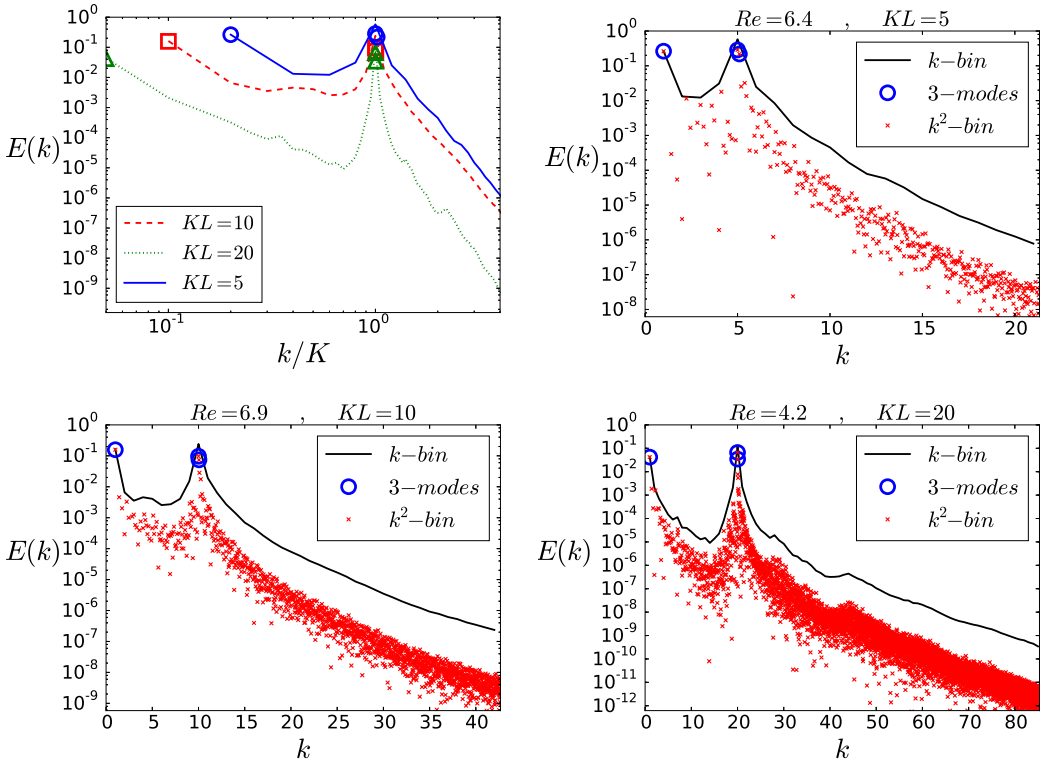

Figure 5.19 – The energy spectra of the flow in the large scale instability bifurcation plotted for different scale separations $K \in \{1; 5; 10; 20\}$.

most unstable one as seen in all the cases examined (see figs. 5.2,5.6,5.9). Despite this fact, it appears that the $kL = 1$ is the dominant mode that controls saturation. The exact saturation mechanism however is beyond the scope of this work.

5.4 Conclusion

In this work, using the Floquet framework as well as simplified models, we examined in detail large scale hydrodynamic instabilities for a variety of flows. The Floquet framework allowed us to distinguish small from large scale instabilities in a rigorous manner, and study the evolution of the latter independently for a wide parameter range. The results depend on the type of flow under study and the value of the Reynolds number.

More precisely it was shown that for the $Fr87$ flow (see eq. (5.24)) and for small values of Re, the instability growth rate scales like: $\sigma \propto q\, Re$, with most of the energy in the large scales $1 - E_0/E_{tot} \propto Re^2$. It is present for any arbitrarily small value of the Reynolds number provided that scale separation is large enough. The linear scaling of the growth rate with q persisted for values of Re beyond the asymptotic regime with the prefactor becoming independent of Re at sufficiently large Re.

Flows without an AKA-instability, like the ABC and Roberts flow, show a negative eddy-viscosity scaling. The instability appears only above a critical value of the

Reynolds number Re^c that was found to be $Re^c \simeq 2$ for the Roberts flow and $Re^c \simeq 3$ for the equilateral ABC flow. The growth rate follows the scaling $\sigma \propto \nu(bRe^2 - 1)q^2$. The value of b can be calculated based on a three mode model for the Roberts flow and was found to be $b = 1/4$. The three-mode model however failed to predict the b coefficient of the equilateral ABC flow because more modes were contributing to the instability.

For the equilateral ABC flow the negative eddy-viscosity scaling $\sigma \propto q^2$ was shown to stop at a second critical Reynolds number Re_S^c, where the flow becomes unstable to small scale perturbations. For values of Re larger than Re_S^c the growth rate remains finite and independent of q ($\sigma \propto q^0$) at the $q \to 0$ limit. On the contrary, the fraction of energy at the largest scale becomes dependent on q decreasing as $E_0/E_{tot} \propto q^4$ as $q \to 0$. This behavior is well described by a two-mode model that is explained in sec. 5.3.3.3.

The scaling of the growth rate $\sigma \propto q^0$ was also observed for the turbulent ABC flow that was also examined in this work. However, the projection on the large scales of the unstable mode was stronger than the laminar flow following the scaling $E_0/E_{tot} \propto q^2$, implying that the turbulent flow is more effective at exciting large scales. We note that a turbulent/chaotic flow is by definition small scale unstable with a growth rate of the unstable modes proportional to the Lyaponov exponent of phase-space trajectories. For this reason, any flow with Re that is large enough for the flow to be turbulent can not display a $\sigma \propto q$ or $\sigma \propto q^2$ scaling. We further note that the observed scaling cannot be expressed in terms of a turbulent alpha-effect or a turbulent viscosity. This can have important implications on sub-grid models commonly used in numerical codes. These models mimic the effect of unresolved turbulent scales on large eddies and typically have only a damping effect. Our work indicates that small scales are also responsible for the excitation of large scales, an effect that needs to be taken into account.

Finally our study was carried out further to the non-linear regime where the saturation of the large scale instabilities was examined for four different box sizes. The presence of scale separation alters the bifurcation diagram, with the large scale modes playing a dominant role in the saturation mechanism. The saturation amplitude of the energy of the large scale instability appears to be independent of the scale separation and of larger amplitude than in the absence of scale separation. This indicates that studying small scale turbulence isolated from any large scale effects could also be misleading. The persistence of this behavior at larger values of Re remains to be examined.

5.5 Appendix: FLASHy (description of a new procedure)

A pseudo-spectral method is adopted to compute numerically eq. (5.8) and (5.9). The linear terms are computed in Fourier space. All the terms involving the driving flow are computed in physical space made incompressible by solving in periodic space the Poisson problem, using:

$$\boldsymbol{\Psi}^{(2)} = -\Delta^{-1}(\boldsymbol{\nabla}\times)^2\boldsymbol{\Psi}^{(1)}\,. \tag{5.32}$$

The main steps of the algorithm are written below. In this algorithm, $\mathcal{F}$ and $\mathcal{F}^{-1}$ denote direct and inverse fast Fourier transforms. $\boldsymbol{AUX}^{(1)}$ and $\boldsymbol{AUX}^{(2)}$ are two

auxiliary vector fields.

Floquet Linear Analysis of Spectral Hydrodynamic ($FLASHy$)

Require: ν, T, dt, $\boldsymbol{q}$, $\boldsymbol{v}^{(0)}$, $\boldsymbol{U}$

1: $\boldsymbol{\Omega} = \boldsymbol{\nabla} \times \boldsymbol{U}$
2: $n = 0$
3: $\boldsymbol{V}^{(n)} = \mathcal{F}(\boldsymbol{v}^{(n)})$
4: **while** $t < T$ **do**
5: $\quad \boldsymbol{AUX}^{(1)} = \boldsymbol{U} \times \mathcal{F}^{-1}(\imath(\boldsymbol{k}+\boldsymbol{q}) \times \boldsymbol{V}^{(n)}) - \boldsymbol{\Omega} \times \mathcal{F}^{-1}(\boldsymbol{V}^{(n)})$
6: $\quad \boldsymbol{AUX}^{(2)} = -||\boldsymbol{k}+\boldsymbol{q}||^{-2}(\boldsymbol{k}+\boldsymbol{q}) \times (\boldsymbol{k}+\boldsymbol{q}) \times \mathcal{F}[\boldsymbol{AUX}^{(1)}]$
7: $\quad \boldsymbol{V}^{(n+1)} = \boldsymbol{V}^{(n)} + dt(\boldsymbol{AUX}^{(2)} - \nu||\boldsymbol{k}+\boldsymbol{q}||^2 \boldsymbol{V}^{(n)})$
8: $\quad n = n+1$, $t = t + dt$
9: **end while**

To carry out the computations with greater precision, a fourth-order Runge-Kutta method is used instead of the simple Euler method at line 7 of the algorithm. The Fourier parallel expansions are also truncated at 1/3 to avoid aliasing error. The code is parallelised with MPI and uses many routine from the GHOST code [52, 53]. Most of the DNS are done at a 32^3 and 64^3 resolution. Convergence tests show that this resolution is sufficient for the range of Reynolds numbers studied.

Chapter 6

Fate of alpha-dynamos at large Rm (*published* in PRL)

This chapter presents new results.

At the heart of today's solar magnetic field evolution models lies the alpha-dynamo description. In the following letter, we investigate the fate of alpha-dynamos as the magnetic Reynolds number Rm is increased. Using Floquet theory, we are able to precisely quantify mean field effects like the alpha- and beta-effects (i) by rigorously distinguishing dynamo modes that involve large scale components from the ones that only involve small scales, and by (ii) providing a way to investigate arbitrary large scale separations with minimal computational cost. We apply this framework to helical and non-helical flows as well as to random flows with short correlation time. Our results determine that the alpha-description is valid for Rm smaller than a critical value Rm_c at which small scale dynamo instability starts. When Rm is above Rm_c the dynamo ceases to follow the mean field description and the growth rate of the large scale modes becomes independent of the scale separation while the energy in the large scale modes is inversely proportional to the square of the scale separation. The results in this second regime do not depend on the presence of helicity. Thus alpha-type modeling for solar and stellar models needs to be reevaluated and new directions for mean field modeling are proposed.

6.1 Introduction

Dynamo instability refers to the spontaneous amplification of magnetic energy due to the stretching and refolding of magnetic field lines by a flow. It explains the presence of magnetic fields throughout the universe from planetary to galactic scales. In many of these cases, dynamo action produces ordered fields at scales L larger than the typical underlying turbulent scales ℓ. A prominent example is the sun whose magnetic field possesses a global time and spatial coherence much larger than the typical turbulent time and length-scales [54, 55, 56]. A mechanism for the generation of such large scale magnetic fields by small scale turbulent eddies was proposed by E. Parker in [57], where he considered the evolution of large scale fields due to the averaged effect of small scale eddies that lack parity invariance. This idea has led to the concept

of mean-field magneto-hydrodynamics [16, 17, 24, 58] where the averaged effect of small scale velocity field is taken into account through the calculation of transport coefficients.

The starting point for these calculations is the magnetic induction equation for the magnetic field $\mathbf{B}$:

$$\partial_t \mathbf{B} = \nabla \times (\mathbf{u} \times \mathbf{B}) + \eta \nabla^2 \mathbf{B} \tag{6.1}$$

that is advected by a small scale velocity $\mathbf{u}$ under the effect of magnetic diffusion η. The magnetic field is then split in a mean part $\langle \mathbf{B} \rangle_{V_\ell}$ (averaged over the small scales) and a fluctuating part $\mathbf{b}$ so that $\mathbf{B} = \langle \mathbf{B} \rangle_{\mathbf{V}_\ell} + \mathbf{b}$ and $\langle \mathbf{b} \rangle_{V_\ell} = 0$. The averaged equation for the large scale magnetic field reads:

$$\partial_t \langle \mathbf{B} \rangle_{\mathbf{V}_\ell} = \nabla \times \mathcal{E} + \eta \nabla^2 \langle \mathbf{B} \rangle_{\mathbf{V}_\ell} \tag{6.2}$$

where the mean electromotive force $\mathcal{E} = \langle \mathbf{u} \times \mathbf{b} \rangle_{V_\ell}$ is a measure of the cross correlation of the small scale velocity $\mathbf{u}$ and magnetic $\mathbf{b}$ fields. It can be found by solving for the evolution of the small scale field $\mathbf{b}$:

$$\partial_t \mathbf{b} - \eta \nabla^2 \mathbf{b} = \nabla \times (\mathbf{u} \times \langle \mathbf{B} \rangle_{\mathbf{V}_\ell}) + \nabla \times \mathbf{G} \tag{6.3}$$

where $\mathbf{G} = \mathbf{u} \times \mathbf{b} - \langle \mathbf{u} \times \mathbf{b} \rangle_{\mathbf{V}_\ell}$. If $\mathbf{G}$ can be neglected (which implies that there is no small scale dynamo), $\mathbf{b}$ has a linear dependence on $\langle \mathbf{B} \rangle_{V_\ell}$ that acts as a source term for the small scale fluctuations. In this case the mean electromotive force can be expanded in a series of the gradients of the large scale magnetic field as:

$$\mathcal{E}^i = \alpha^{ij} \langle B \rangle^j_{V_\ell} + \beta^{ijk} \nabla^j \langle B \rangle^k_{V_\ell} + \dots . \tag{6.4}$$

The tensors $\alpha, \beta, \dots$ are the transport coefficients that depend on the properties of the small scale velocity field. In particular the first tensor α is non-zero if the flow is helical. It can drive large scale magnetic field amplification with a growth rate γ that is proportional to the scale separation $\gamma \propto \ell/L$. These types of dynamos are referred to as alpha-dynamos in the literature. In the absence of helicity, large scale dynamos are also known to exist through an instability related to the second tensor β [59]. This effect leads to a growth rate proportional to the square of the scale separation $(\ell/L)^2$. Both cases are examples of large scale dynamos (LSD).

Given the value of these tensors and inserting eq. (6.4) in eq. (6.2), one obtains a closed equation for the large scale magnetic field. This allows to compute the large scale evolution without knowing the precise details of small scale turbulence. This procedure is commonly used in solar [60, 61, 62] and planetary models [63]. Due to limited computational power, these models only compute the large scale magnetic field while the effect of small scale fluctuations is modeled through the transport coefficients. If these coefficients are properly parametrized, these models reproduce the observed behavior of the solar magnetic field. Global models that solve the full stellar system without parametrization still fall short of reproducing quantitatively the solar cycle despite the great advancement in recent calculations [64, 65, 66, 67, 68, 69].

Calculating the transport coefficients with this hypothesis remains non-trivial. It can be achieved when the magnetic Reynolds number: $Rm = U\ell/\eta$ (where U is the rms value of the velocity field) is much smaller than unity $Rm \ll 1$. In this case, the

small scale induction equation can be simplified to $\eta\nabla^2\mathbf{b} = -\nabla\times(\mathbf{u}\times\langle\mathbf{B}\rangle_{\mathbf{V}_\ell})$ and easily solved by spectral methods. Another frequent approximation consists in assuming that the velocity field has a very short correlation time τ compared to the eddy turnover time. The solution is then approximated to $\mathbf{b} \approx \tau\nabla\times(\mathbf{u}\times\langle\mathbf{B}\rangle_{\mathbf{V}_\ell})$. Both cases lead to a linear dependence of $\mathbf{b}$ on $\langle\mathbf{B}\rangle_{V_\ell}$ in agreement with alpha-modeling, and lead to a non-zero alpha-effect provided that the flow is helical. In particular for the small Rm, the alpha-tensor can be rigorously calculated using multi-scale methods. However, for natural flows, neither of these assumptions hold and different methods have been devised to measure the transport coefficients by 'local' numerical simulations of small scale turbulence [70, 71, 72, 73].

6.2 Results (new results)

For large values of Rm, which correspond to astrophysical regimes, neglecting the $\mathbf{G}$ term is not necessarily a valid assumption. Indeed, at sufficiently large Rm, small scale dynamo (SSD) action is expected to take place and small scale magnetic fields to be self-generated, exponentially amplifying the value of the electromotive force. This is against the basic assumption made above that the electromotive force has a linear dependence on the large scale field $\langle\mathbf{B}\rangle_{V_\ell}$. Indeed, many authors have questioned the validity of alpha-modeling beyond the critical value of Rm_c where SSD takes place [74, 75, 76, 77, 78].

Part of the objections in this work can be elegantly summed up in the following two-mode model. We consider the evolution of a large scale mode b_q at wavenumber $q \propto 1/L$ and a small scale mode b_k at wavenumber $k \propto 1/\ell$, with $q \ll k$, that are coupled by an alpha-effect as follows:

$$\begin{array}{rrrrr} \dot{b}_q = & -\eta q^2 & b_q & +\alpha q & b_k\,, \\ \dot{b}_k = & \alpha k & b_q & +\gamma_{SSD} & b_k \end{array} \tag{6.5}$$

where $\gamma_{SSD} = u_k k - \eta k^2$ is the growth rate of the SSD obtained by setting $\alpha = 0$. It is positive if $Rm = u_k/\eta k > 1$ that marks the SSD onset. Looking for exponential solutions $(b_q, b_k) \propto e^{\gamma t}$ the growth rate γ of the two modes can be explicitly calculated and it is given by $\gamma = \frac{1}{2}\left[\gamma_{SSD} - \eta q^2 \pm \sqrt{\gamma_{SSD}^2 + 4\alpha k q + 2\gamma_{SSD}\eta q^2 + \eta^2 q^4}\right]$. One notices directly that in the $q \ll k$ limit, if $\gamma_{SSD} < 0$, the system has one negative eigenvalue $\gamma \simeq \gamma_{SSD}$ and one positive eigenvalue $\gamma \simeq \alpha^2 kq/|\gamma_{SSD}|$. The growing eigen-mode satisfies $b_q/b_k \simeq (|\gamma_{SSD}|/\alpha k) = \mathcal{O}(1)$. On the other hand, if $\gamma_{SSD} > 0$, the system has one positive eigenvalue $\gamma \simeq \gamma_{SSD}$ and its eigenvector satisfies $b_q/b_k \simeq (\alpha q/|\gamma_{SSD}|) = \mathcal{O}(q/k)$. Thus, beyond the SSD dynamo onset, the growth rate does not satisfy the scaling $\gamma \propto q$ while the projection of the unstable eigen-mode on the large scales decreases with scale separation.

To demonstrate the above arguments and the possible failure of the LSD description, the notion of scale separation needs to be clearly formulated. This has been attempted in the past using direct numerical simulations [79] but only for moderate scale separations. A precise way to quantify the evolution of large scales can be done using Floquet theory [31] also known as Bloch theory in quantum mechanics [32]. Floquet theory can be applied to the linear evolution of the magnetic field $\mathbf{B}(\mathbf{x}, t)$

driven by a spatially periodic flow $\mathbf{u}(\mathbf{x},t)$ of a given spatial period $\ell = 2\pi/k$. Under these assumptions, Floquet theory states that the magnetic field can be decomposed as $\mathbf{B}(\mathbf{x},t) = e^{i\mathbf{q}\cdot\mathbf{x}}\tilde{\mathbf{b}}(\mathbf{x},t) + c.c.$ where $\tilde{\mathbf{b}}(\mathbf{x},t)$ is a complex vector field that satisfies the same spatial periodicity as the velocity field $\mathbf{u}$, and $\mathbf{q}$ is an arbitrary wavenumber. For $q = |\mathbf{q}| \ll k$, the average $\left\langle \tilde{\mathbf{b}} \right\rangle_{V_\ell}$ over one spatial period $2\pi/k$ gives the amplitude of $\tilde{\mathbf{b}}$ at large scales $L \propto 1/q$. Thus, fields with $q = 0$ and $\left\langle \tilde{\mathbf{b}} \right\rangle_{V_\ell} = 0$ correspond to purely small scale fields. If such fields are dynamo-unstable, the system has a SSD instability and we will denote its growth rate as γ_{SSD}. For $0 < q < 1$ the dynamo mode has in general a finite projection to the large scales measured by $\left\langle \tilde{\mathbf{b}} \right\rangle_{V_\ell}$. Substituting in the induction eq. (6.1), we obtain:

$$\partial_t \tilde{\mathbf{b}} = i\mathbf{q} \times (\mathbf{u} \times \tilde{\mathbf{b}}) + \nabla \times (\mathbf{u} \times \tilde{\mathbf{b}}) + \eta(\nabla + i\mathbf{q})^2 \tilde{\mathbf{b}} \tag{6.6}$$

Note that now $\mathbf{q}$ is a control parameter that can be taken to be arbitrarily small. The gain in using the Floquet framework is two-fold: (i) it provides us with a clear way to disentangle dynamos that involve only small scales (for which $\mathbf{q}/k \in \mathbb{Z}^3$) from dynamos that involve large scales ($0 < q/k \ll 1$); (ii) it allows to investigate numerically arbitrary large scale separations $q \ll k$ with no additional numerical cost.

In this work, we consider the velocity fields parametrized as:

$$\mathbf{u} = U \begin{bmatrix} \sin(ky + \phi_2) & + & \cos(kz + \psi_3), \\ \sin(kz + \phi_3) & + & \cos(kx + \psi_1), \\ \sin(kx + \phi_1) & + & \cos(ky + \psi_2) \end{bmatrix}. \tag{6.7}$$

Three cases are examined. In the first case (A), $\phi_i = \psi_i = 0$ for all $i \in (1,2,3)$, the flow corresponds to the well-studied helical ABC flow [80, 81, 82, 83, 84, 85], in the second case (B), $\phi_i = \psi_i - \pi/2 = 0$ is a non-helical flow, and in the last case (C) the phases $\phi_i = \psi_i$ change randomly every time τ and correspond to random helical flows. For the time-independent flows (cases A and B), the magnetic Reynolds number is defined as $Rm = U/k\eta$ and the growth rate is measured in units of Uk. For the random flow (case C), the definition $Rm = (U/k\eta) \times (\tau Uk) = U\tau/\eta$ is used and the growth rate is measured in units of $U^2k^2\tau$. The latter definition takes into account that a fast de-correlation time reduces the rate at which the flow shears the magnetic field lines. As will be shown in fig. 6.1, this scaling makes the results collapse on the same curve small τ. Eq. 6.6 was solved numerically and the dynamo growth rate γ was measured for various values of Rm and $\mathbf{q} = \hat{z}q$ using a pseudo-spectral code in a cubic periodic domain of side 2π with $k = 1$ and spatial resolution ranging from 32^3 to 128^3 depending on Rm. Details on the Floquet code can be found in [86]. The results are compared with the SSD growth rate γ_{SSD} obtained from a tested dynamo code [53].

The calculated growth rates are plotted in fig. 6.1 as a function of the Reynolds number for the three different velocity fields used. Crosses correspond to the results obtained from the Floquet code with $q = 10^{-3}$ while γ_{SSD} is shown with a solid green line. In the first flow (A) the γ_{SSD} reproduces the classical 'two-window' result of the ABC dynamo [80, 81, 82, 83, 84, 85] for which SSD exists for Rm in the range $R_1 < Rm < R_2$ and $R_3 < Rm$. For the non-helical case (B) SSD appears for $Rm > R_4 \simeq 12$. In the case (C), different values of τ were used in the range $(0.02, 0.5)$ as mentioned

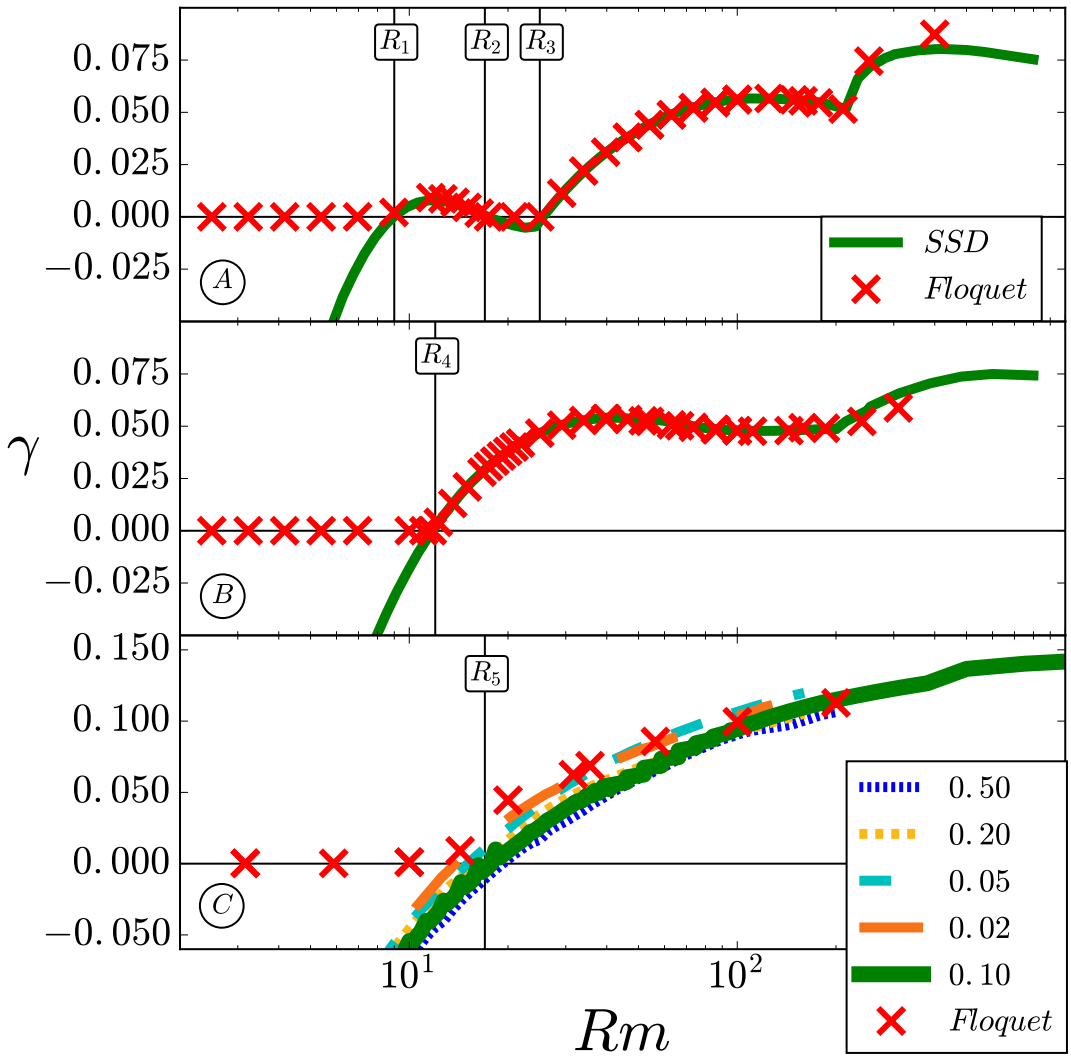

Figure 6.1 – Growth rate as a function of Rm for the different flows considered. The SSD results are given by the solid lines, while the results from the Floquet code with $q = 10^{-3}$ are denoted by crosses. In the bottom panel, the value of $\tau = 0.1$ was used for the Floquet code, and different values of τ were used for the SSD as indicated.

in the legend. For the Floquet results the value of τ used was $\tau = 0.1$. SSD appears above a critical value R_5 that weakly depends on the value of τ. At sufficiently small τ, the critical value of $Rm = R_5$, at which SSD appears, becomes independent of τ with $R_5 \simeq 11$. All three cases show the same feature: when $\gamma_{SSD} > 0$, the Floquet and SSD results have the same growth rate, while, when $\gamma_{SSD} < 0$, the Floquet results have a positive growth rate but of order q (or q^2).

This observation is achieved examining the dependence of the growth rate on q shown in the three panels of fig. 6.2. For each line in these figures, a series of simulations of fixed Rm and varying q was performed. Each line corresponds to a different value of Rm. Panel (A) shows the growth rate for the ABC flow. For the values of $Rm < R_1$

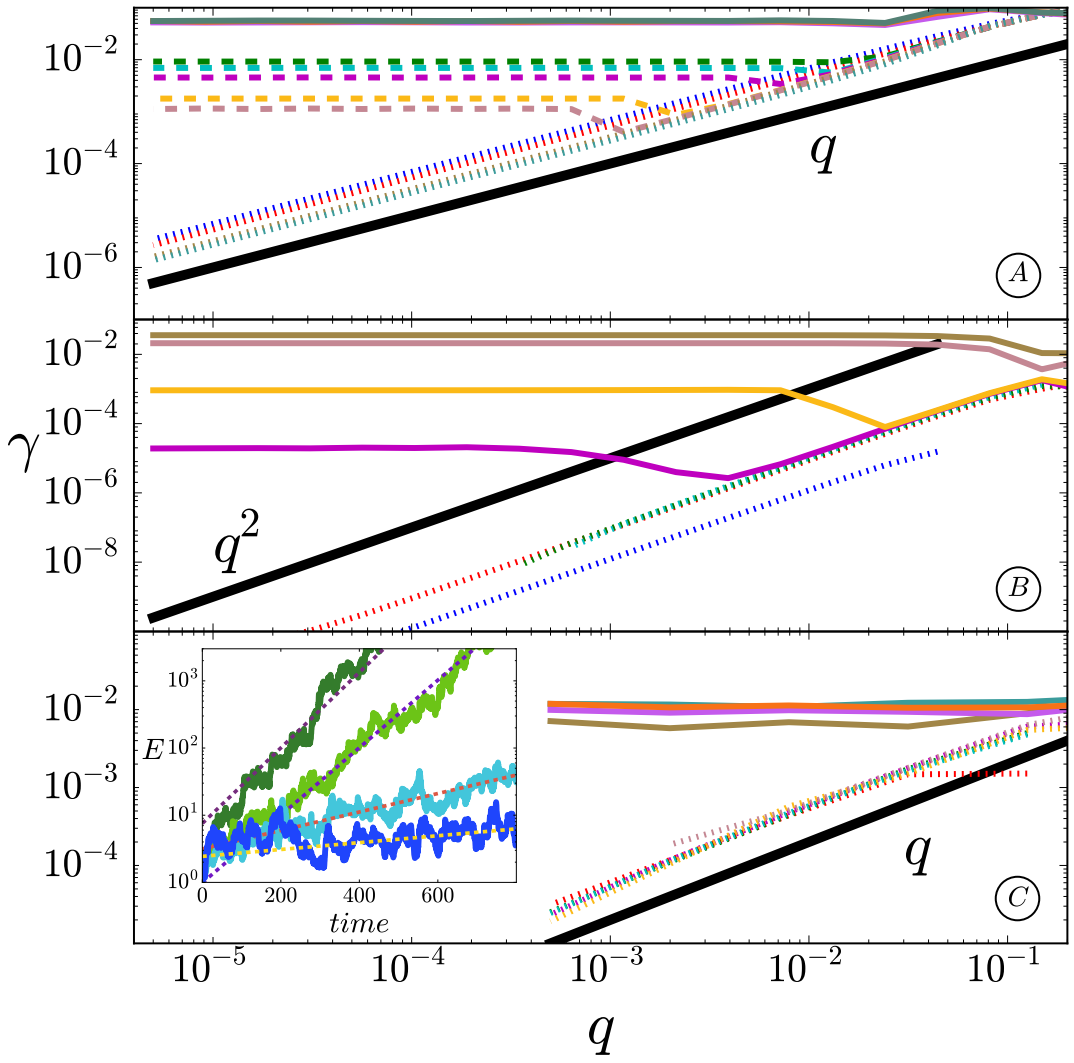

Figure 6.2 – The growth rate as a function of q for different values of Rm. The line types are as follows. Panel (A): For $Rm < R_1$ and $R_2 < Rm < R_3$ (dotted lines), for $R_1 < Rm < R_2$ (dashed lines), for $R_3 < Rm$ (solid lines). Panel (B): For $Rm < R_4$ (dotted lines), for $R_4 < Rm$ (solid lines). Panel (C): For $Rm < R_5$ (dotted lines), for $R_5 < Rm$ (solid lines). The inset (D) shows a typical signal for the evolution of energy from case (C) for $Rm < R_5$.

and $R_2 < Rm < R_3$ (where there is no SSD), the growth rate is plotted with dotted lines; the first dynamo window $R_1 < Rm < R_2$ is plotted using dashed lines; while in the range $R_3 < Rm$ solid lines are used. It is clear that for the no-small-scale-dynamo range, a $\gamma \propto q$ scaling is followed (alpha-dynamos) while in the presence of SSD γ is independent of the value of q. Similarly, for the non-helical runs, in the absence of SSD ($Rm < R_4$ dotted lines), the growth rate follows the scaling $\gamma \propto q^2$, which indicates a β-type dynamo instability, while in the presence of SSD (solid lines) there is no dependence of the growth rate on q. Even in the random flow, the same feature is observed: for $Rm < R_5$ (dotted lines) the results show a $\gamma \propto q$ scaling that suggests

the presence of a random alpha-effect, but for $Rm > R_5$ this behavior transitions to a q-independent growth rate (solid lines). We note that due to the random nature of this flow the accuracy of our measurements is limited and we only examine values of $q > 5 \cdot 10^{-4}$. The inset (D) shows a typical energy time-series from case (C).

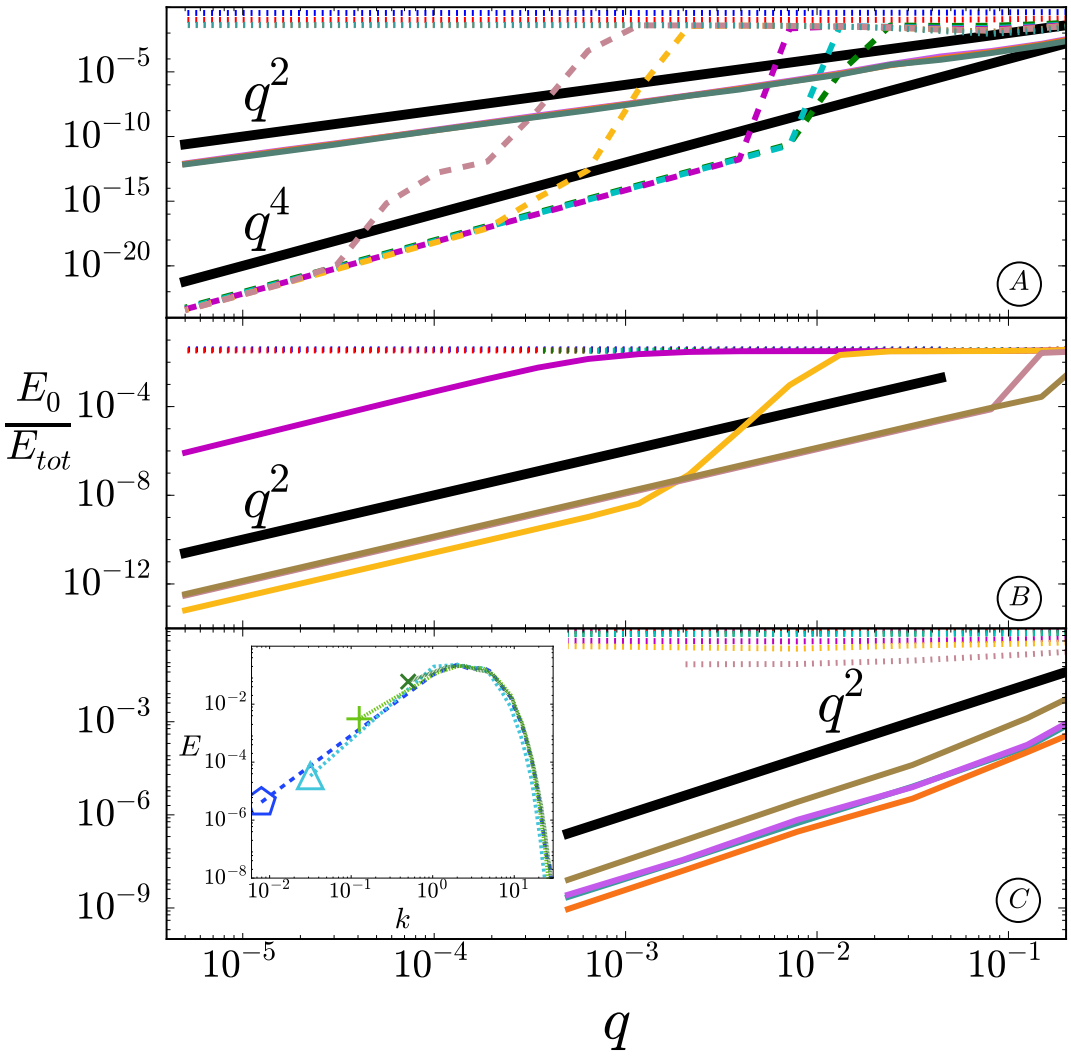

Figure 6.3 – The energy ratio E_0/E_{tot}. The line styles are as in figure 6.2. The inset (D) shows the energy spectra for four different values of q of case (C) at the highest Rm.

At first, a finite growth rate $\gamma > 0$ in the limit of $q \to 0$ seems to violate the flux conservation. Indeed, flux conservation enforces modes with $q = 0$, corresponding to uniform fields, not to grow. The explanation is found by looking at the projection of the unstable modes to the large scales. In fig. 6.3, we plot the ratio of the energy contained in the large scale mode $e^{i\mathbf{q}\cdot\mathbf{x}}$ that is given by $E_0 = \frac{1}{2}|\left\langle \tilde{\mathbf{b}} \right\rangle_{V_\ell}|^2$ to the total energy $E_{tot} = \frac{1}{2}\left\langle |\tilde{\mathbf{b}}|^2 \right\rangle_{V_\ell}$ as a function of q for the same values of Rm as used in fig. 6.2 and the same line types. For LSD (of the type α or β) the projection to the large

scales becomes independent of q for $q \to 0$ (although it still depends on the value of Rm). As Rm approaches the small scale instability onset, this projection decreases. For values of Rm larger than the onset of the SSD, the projection to the large scale modes becomes dependent on q and follows the scaling $\gamma \propto q^2$ in most cases or $\gamma \propto q^4$ for the case of the ABC dynamo in the first dynamo window. This result can be obtained by a regular expansion of eq. (6.6) for small q such that $\gamma = \gamma_0 + q\gamma_1 + \dots$ and $\mathbf{b} = \mathbf{b}_0 + q\mathbf{b}_1 \dots$. At zeroth-order, one obtains $\gamma = \gamma_{SSD}$ and $\langle \mathbf{b}_0 \rangle_{V_\ell} = 0$. At next order, by averaging over space, one obtains $\gamma_0 \langle \mathbf{b}_1 \rangle_{V_\ell} = i\mathbf{q} \times \langle \mathbf{u} \times \mathbf{b}_0 \rangle_{V_\ell}$. This last result shows that the energy in the large scale modes scales like q^2, provided that the mean electromotive force $\langle \mathbf{u} \times \mathbf{b}_0 \rangle_{V_\ell}$ due to the SSD mode is not zero. If it is zero, the next order term leads to a q^4 scaling and so on. Note that this argument does not depend on the presence or absence of helicity in the flow. In fact, as shown in the top panel of fig. 6.3, the same flow results in different scalings of E_0/E_{tot} depending on which dynamo window is examined. Indeed, in the first window $R_1 < Rm < R_2$, the most unstable mode possesses different symmetries than the most unstable mode for $Rm > R_3$ [85].

6.3 Discussion

The results above give a clear description of the transition from SSD to LSD. Below the SSD onset, the mean field predictions are valid and lead to a growth rate proportional to q or q^2 depending whether an α- of β-dynamo is present. Above the SSD onset large scales grow with the γ_{SSD} growth rate but with a projection to the large scales that decreases with a scale separation. This behavior cannot be modeled with terms that are linear in the amplitude of the large scale field as eq. (6.4) implies. On the contrary, the behavior of the large scales mode depends on SSD. Despite its small projection, it has a faster growth rate than mean field dynamos. Therefore, the large scales mode could possibly be modeled as a non-homogeneous term in the mean field dynamo equation. This possibility however requires further investigations.

Part C

Thermalized state

Table of Contents

Chapter 7

Elements of context: Thermodynamics

The aim of this chapter is to recapitulate the absolute equilibrium properties by making analogies with the probability density function (PDF) of an ideal gas. Most of the properties presented are explained in greater depth in [87, 88, 89, 90, 11].

This chapter reviews well-documented theories.

7.1 Ideal gas distribution (review)

To get an intuition of the probability density function of the modes of an ideal fluid, let us start by studying an ideal gas of n indistinguishable particles of negligible size with hard sphere elastic collisions as only interactions without dissipation. The ideal gas has an energy expression close to the energy of ideal fluid and has similar statistical properties. For the ideal gas, the equations of motion can be described using the Hamiltonian $\mathcal{H}$

$$\mathcal{H} = V + \sum_i \frac{p_i^2}{2m} \quad \text{with} \quad \dot{p}_i = -\partial_{q_i}\mathcal{H} = -\partial_{q_i}V \quad \text{and} \quad \dot{q}_i = \partial_{p_i}\mathcal{H} = \frac{p_i}{m}\,, \tag{7.1}$$

where V denotes the interaction potential between particles. The Hamilton is a function of the position $\{q\}$ and impulsion $\{p\}$ of the particles of the gas, and the interaction potential is only a function of the position. Because of the elastic nature of the interactions of the particles in the gas, the interaction potential bans configurations having two particles at the same position. Between two collisions, the system is described by n ballistic trajectories. If the total energy, E_{IG}, of the system is fixed, the system is located on the surface of the $3n$-dimensional unitary hyper-sphere defined by

$$\sum_i X_i^2 = 1 \quad \text{with} \quad X_i = \frac{p_i}{\sqrt{2mE_{IG}}} \quad \text{and} \quad S_d = \frac{2\pi^{d/2}}{\Gamma_{Euler}(d/2)}\,, \tag{7.2}$$

where S_d and Γ_{Euler} denote the surface of a d-dimensional unitary hyper-sphere and Euler's Gamma function respectively. At fixed energy, the total number of configurations, W, is proportional to the surface of the $3n$-dimensional unitary hyper-sphere.

The number of possible configurations, $w(x, \delta x)$, with one coordinate, X, varying in the interval $[x, x+\delta x]$, corresponds to the shell of the $3n-1$-dimensional hyper-sphere of radius $\sin(\phi) = \sqrt{1-X^2}$. It can be computed using Pythagoras theorem and trigonometric relation presented in fig. 7.1

$$w(x, \delta x) = S_{3n-1} \int_{\arccos(x)}^{\arccos(x+\delta x)} \sin^{3n-1}(\phi) d\phi = S_{3n-1} \int_{x}^{x+\delta x} (1-X^2)^{(3n-3)/2} dX \,. \tag{7.3}$$

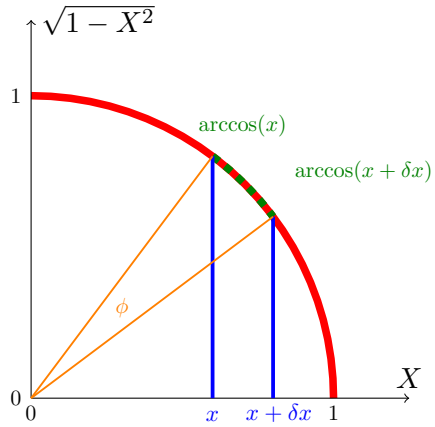

Figure 7.1 – Trigonometric scheme describing the domain of integration of the integral. The red line corresponds to the unit circle, the blue line corresponds to the interval in which the variable X varies. The orange line corresponds to the bound of the domain over which the integral is computed. The green dashed line correspond to the domain of integration

The probability density function $f_1(x)$ of finding one coordinate equal to x can be computed using the ratio of the number of possible configurations to the total number of configurations

$$f_1(x) = \frac{d}{d(\delta x)} \frac{w(x, \delta x)}{W} = \frac{S_{3n-1}}{S_{3n}} (1-x^2)^{\frac{3n-3}{2}} \underset{\substack{x \ll 1 \\ 1 < n}}{\sim} \frac{S_{3n-1}}{S_{3n}} e^{-\frac{x^2}{2}(3n-3)} \,. \tag{7.4}$$

In the thermodynamic limit, $n \to \infty$, the PDF is well approximated by a Gaussian near zero, that is for values of X near the maximum of f_1. In this limit, the normalization of the PDF can also be computed using the Gaussian integral. Fig. 7.2 represents the analytic expression of f_1 in full lines and its Gaussian approximation in dashed lines for gases with different number of particles n. As the number of particles increases, the number of orders of magnitude over which the Gaussian approximation overlaps the analytic PDF increases.

The Gaussian approximation of the PDF can be done analytically for the ideal gas but it is still correct in more general cases thanks to the central limit theorem. Gaussian distributions give a good approximation of the PDF in the vicinity of the maximum, but their predictions can be highly unphysical when pushed outside this domain. In the case of the ideal gas, the Gaussian distribution gives a non-zero probability for $X > 1$, which is in contradiction with the conservation of energy. In the thermodynamic limit, the Gaussian approximation still gives back the equipartition of energy

$$\left\langle \frac{p_1^2}{2m} \right\rangle_{ens} \underset{n \to \infty}{\sim} \frac{E_{IG}}{3n} \quad \text{with} \quad \langle \ldots \rangle_{ens} = \int \ldots f_1(x) dx \tag{7.5}$$

$$\text{since} \quad \int x^2 \frac{e^{\frac{x^2}{2\sigma^2}}}{\sqrt{2\pi\sigma^2}} dx = \sigma^2 \,. \tag{7.6}$$

The triangle brackets denote the ensemble average over all configurations weighted with their probability. At the thermodynamic limit, the average computed with the Gaussian distribution gives the same results as those computed using the analytic expression.

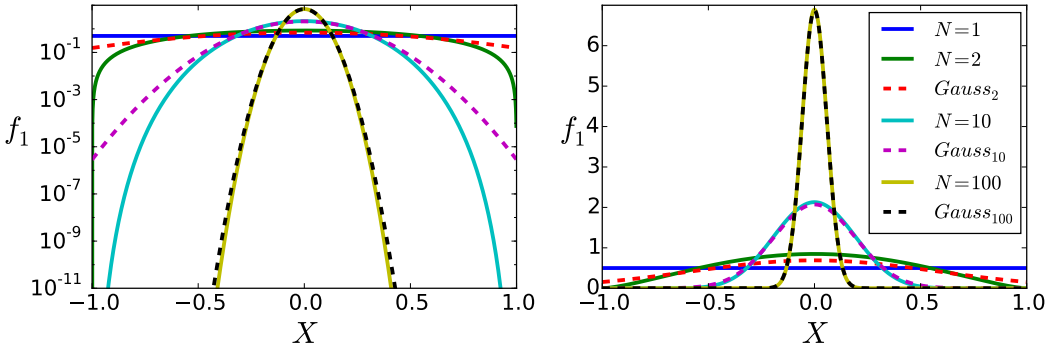

Figure 7.2 – PDF of ideal gas. The full line represents the PDF computed analytically using eq. (7.2) and the dashed line represents the PDF computed using the Gaussian approximation. In the legend, the analytic PDFs are denoted with the label $n = \ldots$, and their Gaussian approximations are denoted with the label $Gauss_{\ldots}$. The value corresponds to the number of particles of the system. In the legend, the value also corresponds to the number of particles. (Left) PDF plotted in logarithmic scale. (Right) PDF plotted in linear scale.

The PDF $f_1(x)$ of having one coordinate equal to x is different from the PDF $f_{3n}(\{x\})$ of having the system in a given configuration $\{x\}$. For independent variables, the two distributions are related via $f_{3n}(\{x\}) = \prod_{k=1}^{3n} f_1(x_k)$, where x_k is the k-th component of $\{x\}$. This is however not the case for an ideal gas because the energy is fixed. This expression is still a good approximation for the PDF, or at least it is the best that can be done with minimal computation.

Before deriving other properties on the PDF, let us sum up the main points of the derivation. The number of possible configurations was computed at fixed energy for a given parameter. The probability density was then derived using the ratio of the number of possible configurations to the total number of configurations. Finally, near its maximum, the PDF was approximated to a Gaussian distribution. Besides the position of the maximum giving the average of the PDF, Gaussian distributions have another free parameter, σ, associated to the standard deviation. For the ideal gas, the standard deviation could be directly computed from the analytic results. In many cases, the derivation cannot be done analytically. The Liouville theorem can help solve this problem. Another way to carry out the derivation is to use the equivalence between micro-canonical and canonical ensembles at the thermodynamic limit.

7.2 The Liouville theorem (review)

For Hamiltonian systems, the Liouville theorem is able to give a constraint on the stationary PDF of the system. This additional constraint can be used to solve the problem raised at the end of the last section. If a system derives from a Hamiltonian, it can be described in the position-impulsion space. The temporal evolution of the

PDF f of its configuration is given by the generalized Lagrangian time-derivative

$$D_t f = \partial_t f + \dot{q}_\alpha \partial_{q_\alpha} f + \dot{p}_\alpha \partial_{p_\alpha} f \,, \tag{7.7}$$

where $\{q\}$ and $\{p\}$ denote the position and the impulsion of the independent components of the system respectively. Einstein's summation convention is used on repeated Greek variables. Additionally, if the system derives from a Hamiltonian, $\mathcal{H}$, the trajectories follow the Hamilton equations

$$\dot{p}_i = -\partial_{q_i}\mathcal{H} \quad \text{and} \quad \dot{q}_i = \partial_{p_i}\mathcal{H} \quad \text{thus} \quad \partial_{p_i}\dot{p}_i = -\partial_{p_i q_i}\mathcal{H} = -\partial_{q_i}\dot{q}_i \,. \tag{7.8}$$

By definition, the PDF is normalized, therefore its integral over phase-space is conserved, which implies that it follows the conservation equation

$$0 = \partial_t f + \partial_{q_\alpha}(\dot{q}_\alpha f) + \partial_{p_\alpha}(\dot{p}_\alpha f) = \partial_t f + f(\partial_{q_\alpha}\dot{q}_\alpha + \partial_{p_\alpha}\dot{p}_\alpha) + \dot{q}_\alpha \partial_{q_\alpha} f + \dot{p}_\alpha \partial_{p_\alpha} f \,. \tag{7.9}$$

Using eq. (7.8) and (7.9), we get that the temporal evolution of the PDF has a Lagrangian time-derivative equal to zero. If we consider the specific case where the density, denoted by f_s, is stationary, we get that

$$0 = D_t f_s = \dot{q}_\alpha \partial_{q_\alpha} f_s + \dot{p}_\alpha \partial_{p_\alpha} f_s \,. \tag{7.10}$$

The invariants of the problem also satisfy eq. (7.10). In fact this relation can be used as the criterion to define an invariant of the system. The stationary distribution can therefore be expressed as a function of the invariants of the system. In the case of the ideal gas, the only invariant is the energy, the standard deviation of the Gaussian distribution should only depend on the energy.

7.3 Absolute equilibrium theory (review)

Even though the total energy of a spectrally-truncated ideal fluid is conserved and has an expression close to the energy of an ideal gas, ideal fluids do not have a Hamiltonian formulation close to that of ideal gas [91, 92]. Instead of describing the system in the position-impulsion phase space, the system will be expressed as a function of its positive and negative Fourier helical components given in eq. (2.19). These components do not following the equations of Hamiltonian given in eq. (7.8). However using these variables simplifies the expression of the helicity which is the other conserved quantity in an ideal fluid (see eq. (2.22)). In order to have consistency between the expression of energy and helicity, they will be written as

$$2E = \mathbb{E} = \mathbb{E}^+ + \mathbb{E}^- \quad \text{where} \quad \mathbb{E}^\pm = \sum_{\boldsymbol{k}} |\boldsymbol{u}^\pm|^2 \,, \tag{7.11}$$

$$H = H^+ + H^- \quad \text{where} \quad H^\pm = \pm \sum_{\boldsymbol{k}} k |\boldsymbol{u}^\pm|^2 \,. \tag{7.12}$$

It may seem to be an overkill to introduce a new variable for a mere factor two, but it helps follow more smoothly the derivation. With this notation, the helicity of the Euler equation truncated at k_M is bounded by

$$|H| \leq H^\pm \leq k_M \sum_{\boldsymbol{k}} |\boldsymbol{u}^\pm|^2 \leq k_M \sum_{\boldsymbol{k}} |\boldsymbol{u}|^2 = k_M \mathbb{E} \,. \tag{7.13}$$

As a consequence of this bound, two independent positive definite constants quadratic in velocity, $\mathcal{C}_+$ and $\mathcal{C}_-$, can be built

$$\mathcal{C}_\pm = \alpha \left(\mathbb{E} \pm \tfrac{\mathcal{K}r}{k_M} H \right) = \sum_{\boldsymbol{k}, s_{\boldsymbol{k}}} \alpha \left(1 \pm s_{\boldsymbol{k}} k \tfrac{\mathcal{K}r}{k_M} \right) |\boldsymbol{u}_{\boldsymbol{k}}^{s_{\boldsymbol{k}}}|^2 , \tag{7.14}$$

α has the dimension of the inverse of an energy and will be assumed to be positive. $\mathcal{K}r$ is a dimensionless number and $|\mathcal{K}r| < 1$. Since the energy and the helicity are two independent invariants, $\mathcal{C}_\pm$ are also two independent invariants and can be used to describe the system. When the energy and the helicity are used to compute the number of possible configurations, it is difficult to derive the maximum number of configurations of the system. Indeed, at fixed helicity, depending on the sign of the helical component, it not clear how w varies with the amplitude of the helical component. Changing the set of invariants from the $\mathbb{E}$-H set to the $\mathcal{C}_\pm$ set proves to help solve the problem.

The space of configurations of fixed energy and helicity has a geometrical description. For the ideal gas, the hyper-surface of constant energy is an hyper-sphere. For an ideal fluid, having two different invariants implies that the hyper-surface of configurations is located at the intersection of two hyper-surfaces. Using the $\mathbb{E}$-H set of invariants, the surface of constant energy and helicity is the intersection of an hyper-sphere with a $3n$-dimensional hyperboloid. Even when $n = 1$, it does not seem intuitive to know how this surface behaves. With the $\mathcal{C}_\pm$-set of invariants, the surface of constant energy and helicity corresponds to the intersection of two ellipsoids. It is still hard to visualize, but the computation is able to give enough information to pursue the derivation.

We tried to compute analytically the distribution associated with the intersection, but were unable to get a simple result. We also carried simulations at low resolution, $N \in \{2; 3; 4\}$, to see if we could get a deviation from the Gaussian statistics but on two orders of magnitude the logarithm of the distribution perfectly matches a Gaussian distribution both for non-helical and highly helical flows.

Let us consider one helical component of the velocity field at a given wavevector, $\boldsymbol{u}_{\boldsymbol{a}}^{s_{\boldsymbol{a}}}$, the number $w(u)$ of possible configurations at fixed energy and helicity is given by the surface satisfying the following two conditions

$$\sum_{\substack{\boldsymbol{k}, s_{\boldsymbol{k}} \\ (\boldsymbol{k}, s_{\boldsymbol{k}}) \neq (\boldsymbol{a}, s_{\boldsymbol{a}})}} \alpha \left(1 \pm s_{\boldsymbol{k}} k \tfrac{\mathcal{K}r}{k_M} \right) |\boldsymbol{u}_{\boldsymbol{k}}^{s_{\boldsymbol{k}}}|^2 = \mathcal{C}_\pm - \alpha \left(1 \pm s_{\boldsymbol{a}} \tfrac{\mathcal{K}ra}{k_M} \right) |\boldsymbol{u}_{\boldsymbol{a}}^{s_{\boldsymbol{a}}}|^2 . \tag{7.15}$$

At fixed $\mathcal{C}_\pm$, when $|\boldsymbol{u}_{\boldsymbol{a}}^{s_{\boldsymbol{a}}}|^2$ increases, the radii of the surfaces decrease, reducing the number of possible configurations as a result. The maximum of $w(u)$ is thus located near zero. The number of possible configurations $w(u)$ can now be expanded near its maximum $u = 0$, to get an approximation of the PDF. Noting W the total number of configurations, the PDF of one mode, $f_1(u)$, can be computed using

$$f_1(u) = \frac{w(u)}{W} \underset{u \to 0}{\sim} \frac{w(0)}{W} \exp \left(-\frac{u^2}{2} \frac{d_{uu}^2 w(0)}{w(0)} \right) . \tag{7.16}$$

Since the approximation is a Gaussian of average zero, the distribution only depends on one parameter, the standard deviation. The pre-factor is related to the standard deviation because the PDF is normalized.

When the system does not have helicity, it is not surprising that the conservation of energy leads once more to PDFs with zero average. However, in highly helical systems, it may seem surprising that this property still holds. The energy is placed preferentially in the largest wavenumbers. These modes still have an average energy equal to zero, since they are coupled together. The energy does not have to be stored in one mode, it can be spread across all the modes of the shell before the truncation.

If ideal fluids had a Hamiltonian description similar to ideal gas, the next step would be to use the Liouville theorem to compute the value of the standard deviation. Since the Hamiltonian version of the Liouville theorem cannot directly be applied to ideal fluids, we will use a more general version and check that the hypothesis can be applied to an ideal fluid. Similarly to ideal gas, the PDF of a configuration of an ideal fluid is normalized and follows therefore a conservation law. Using the Craya-Herring decomposition of the components of the velocity field, the conservation of the PDF can be expressed as

$$-\partial_t f = \partial_{u^+_{\boldsymbol{\alpha}}}(\dot{u}^+_{\boldsymbol{\alpha}} f) + \partial_{u^-_{\boldsymbol{\alpha}}}(\dot{u}^-_{\boldsymbol{\alpha}} f) = f(\partial_{u^+_{\boldsymbol{\alpha}}}\dot{u}^+_{\boldsymbol{\alpha}} + \partial_{u^-_{\boldsymbol{\alpha}}}\dot{u}^-_{\boldsymbol{\alpha}}) + (\dot{u}^+_{\boldsymbol{\alpha}}\partial_{u^+_{\boldsymbol{\alpha}}} + \dot{u}^-_{\boldsymbol{\alpha}}\partial_{u^-_{\boldsymbol{\alpha}}})f\,. \tag{7.17}$$

To have a result similar to the Hamiltonian version of the Liouville theorem, the term $\partial_{u^+_{\boldsymbol{\alpha}}}\dot{u}^+_{\boldsymbol{\alpha}} + \partial_{u^-_{\boldsymbol{\alpha}}}\dot{u}^-_{\boldsymbol{\alpha}}$ should be equal to zero. Using the expression of the Euler equation in the Craya-Herring basis given at eq. (2.20), we get

$$\frac{\partial}{\partial u^{s_{\boldsymbol{k}}}_{\boldsymbol{k}}}(\dot{u}^{s_{\boldsymbol{k}}}_{\boldsymbol{k}})^* = -\frac{1}{4}\sum_{\substack{\boldsymbol{k}+\boldsymbol{p}+\boldsymbol{q}=0\\ s_{\boldsymbol{p}},s_{\boldsymbol{q}}}} (s_{\boldsymbol{p}}p - s_{\boldsymbol{q}}q)\,(\boldsymbol{h}^{s_{\boldsymbol{k}}}_{\boldsymbol{k}}\cdot\boldsymbol{h}^{s_{\boldsymbol{p}}}_{\boldsymbol{p}}\times\boldsymbol{h}^{s_{\boldsymbol{q}}}_{\boldsymbol{q}})\,\frac{\partial}{\partial u^{s_{\boldsymbol{k}}}_{\boldsymbol{k}}}(u^{s_{\boldsymbol{p}}}_{\boldsymbol{p}}u^{s_{\boldsymbol{q}}}_{\boldsymbol{q}}) = 0\,. \tag{7.18}$$

In this last expression, the terms in the sum, where either $(\boldsymbol{p}, s_{\boldsymbol{p}}) = (\boldsymbol{k}, s_{\boldsymbol{k}})$ or $(\boldsymbol{q}, s_{\boldsymbol{q}}) = (\boldsymbol{k}, s_{\boldsymbol{k}})$, are equal to zero because the triple product has two identical vectors. The other terms are also equal to zero since the derivative is equal to zero because the helical components are all assumed to be independent variables.

Similarly to Hamiltonian systems, when the PDF is stationary, ideal fluids have an additional constraint on their PDF

$$0 = (\dot{u}^+_{\boldsymbol{\alpha}}\partial_{u^+_{\boldsymbol{\alpha}}} + \dot{u}^-_{\boldsymbol{\alpha}}\partial_{u^-_{\boldsymbol{\alpha}}})f\,. \tag{7.19}$$

This constraint is satisfied by the invariants of the systems and can even be used to characterize an invariant. Consequently, the PDF of a configuration, f, should be expressed as a function of the invariants of the system. Since the PDF can be approximated by a Gaussian distribution, which is quadratic in velocity, we get that

$$f(\{\boldsymbol{u}\}) \propto e^{-\mathcal{C}(\{\boldsymbol{u}\})} \quad \text{where} \quad \mathcal{C}(\{\boldsymbol{u}\}) = \alpha\mathbb{E}(\{\boldsymbol{u}\}) + \beta H(\{\boldsymbol{u}\})\,, \tag{7.20}$$

where α has the dimension of the inverse of an energy and β has the dimension of the inverse of a helicity. These constants were first introduced by Kraichnan in [11]. The argument of the exponential has an expression very similar to the $\mathcal{C}^-$ introduced in (7.14). Using α, β and k_M, a dimensionless number, $\mathcal{K}r$, can be constructed

$$\mathcal{K}r = -\frac{\beta k_M}{\alpha}\,. \tag{7.21}$$

It will be referred to as the Kraichnan number. Similar to $\mathcal{C}^-$, the convergence of the PDF at infinity requires for the Kraichnan number to be less than one in absolute value, $|\mathcal{K}r| < 1$, and the coefficient α to be positive, $\alpha > 0$.

Before making some comments about the probability distribution, let us recall the main hypothesis required to derive the absolute equilibrium distribution.

- The evolution of the velocity fields is governed by the truncated Euler equation.
- The truncated Euler equation has two invariants: energy and helicity.
- The helical components of the velocity field are independent variables.
- The probability are approximated by a Gaussian near their maximum.

The expression of the probability distribution, given in eq. (7.20), can be compared to a Boltzmann weight in thermodynamics. However, Boltzmann weights described physical systems at equilibrium with a thermostat and not isolated systems. Since the energy and the helicity of the system are supposed to be constant, it is surprising to see a probability distribution that has non-zero values for all energy and helicity. This discrepancy between the constraints of ideal fluids and the properties of the PDF was already observed for the ideal gas. The Gaussian approximation is only valid in the vicinity of the maximum of the functional and give unphysical results outside of this region.

The theory may indicate that the components of the velocity modes should follow Gaussian statistics. It is more difficult to get confirmation of this property from direct numeric simulations (DNS). Indeed going back to the helical decomposition, the helical unitary vector is uniquely defined up to a phase. The amplitude of a helical component of a velocity mode is thus a complex number that is unique up to a phase. The two independent real Gaussian variables within the complex amplitude cannot be separated. Identifying the Gaussian behavior of the complex amplitude of the mode can still be done by looking at the real and imaginary part of the amplitude or by looking at the energy associated to the amplitude. The main advantage of looking at the energy is that it does not depend on the phase of unitary helical vector and therefore is not subject to related errors. Contrary to the amplitude of the velocity, the energy of the modes does not follow a Gaussian statistics.

To describe the statistics followed by the energy associated to the complex amplitude of a velocity mode, let us define X a random variable built with the square of g independent random variables $G_{i\in[\![1;g]\!]}$ following the same centered $\langle G_i\rangle_{ens} = 0$ and reduced $\langle G_i^2\rangle_{ens} = 1$ Gaussian statistics $\mathtt{G}$:

$$X = \sum_i G_i^2 \quad \text{and} \quad \mathtt{G}(G_i) = \frac{e^{-\frac{G_i^2}{2}}}{\sqrt{2\pi}} \,. \tag{7.22}$$

The random variables X follows a χ^2_g-distribution [93] defined by

$$\chi^2_g(X) = \frac{1}{2^g \Gamma_{Euler}(\frac{g}{2})} X^{\frac{g}{2}-1} e^{-\frac{X}{2}} \,. \tag{7.23}$$

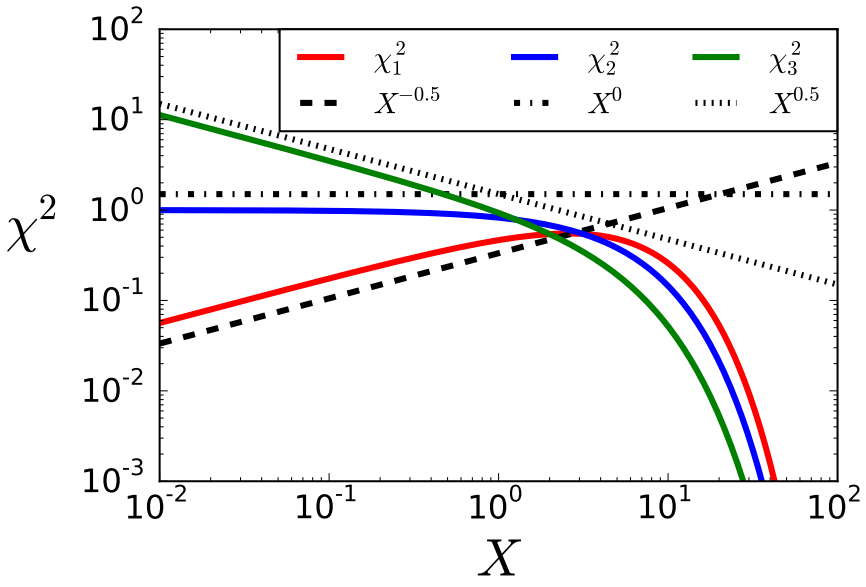

Figure 7.3 – Representation of the χ_g^2-distribution for $g \in \{1;2;3\}$. The black curves represent the asymptotic trends followed by the distribution.

Fig. 7.3 represents χ_g^2-distribution for $g \in \{1;2;3\}$. Consequently, if the real and imaginary parts of the helical components of the velocity modes have Gaussian statistics, their energy should follow a χ_2^2-distribution. Checking the Gaussian property of the helical components of velocity modes can thus be done by checking the PDF of the energy associated to these components.

Using the Gaussian approximation of the PDF, the ensemble averages can be computed using

$$\langle \dots \rangle_{ens} = \frac{1}{\mathcal{Z}} \int \dots e^{-\mathcal{C}(\{\boldsymbol{u}\})} \mathcal{D}\{\boldsymbol{u}\} \quad \text{where} \quad \mathcal{Z} = \int 1 e^{-\mathcal{C}(\{\boldsymbol{u}\})} \mathcal{D}\{\boldsymbol{u}\}\,, \tag{7.24}$$

where $\mathcal{D}\{\boldsymbol{u}\}$ denotes the functional integral over all possible velocity fields. For the truncated Euler equation, the functional integral reduces to a finite number of the integral over the the helical component of the velocity of modes below the truncation. The averages of energy and helicity per mode are given by

$$e_{\boldsymbol{k}}^{\pm} = \left\langle |u_{\boldsymbol{k}}^{\pm}|^2 \right\rangle_{ens} = \frac{\alpha^{-1}}{1 - (\pm \mathcal{K}r)\frac{k}{k_M}} \quad \text{and} \quad h_{\boldsymbol{k}}^{\pm} = \left\langle (u_{\boldsymbol{k}}^{\pm})^* \cdot \omega_{\boldsymbol{k}}^{\pm} \right\rangle_{ens} = \pm k e_{\boldsymbol{k}}^{\pm}\,. \tag{7.25}$$

The minus sign introduced in the definition of the Kraichnan number in eq. (7.21) may have seemed surprising. But, with it, the sign of the helicity of the flow can directly be known. When the Kraichnan number is positive, $0 < \mathcal{K}r$, the energy of the positive helical modes are greater than their negative counterparts $e_{\boldsymbol{k}}^- > e_{\boldsymbol{k}}^+$. Positive Kraichnan number implies that the flow has a positive helicity. Respectively, negative Kraichnan number implies that the flow has a negative helicity.

The average energy and helicity per mode can be summed on a shell of constant wavenumbers to give the energy and helicity spectrum. This can be done for the

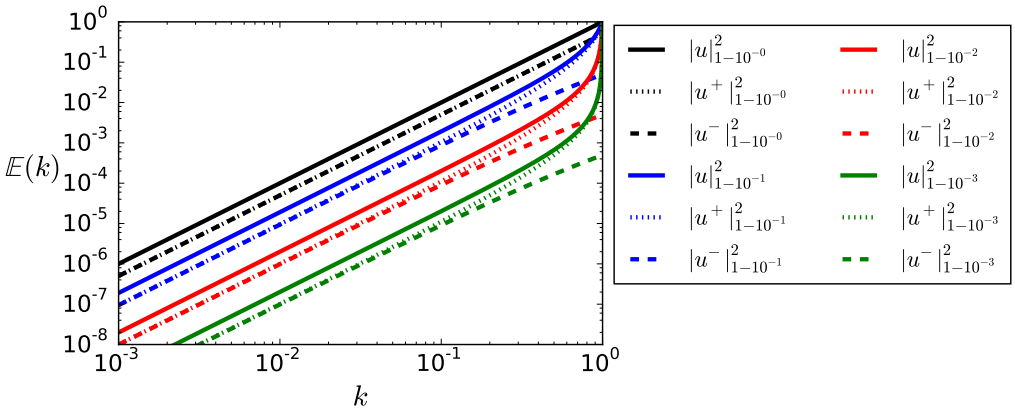

Figure 7.4 – Representation of the spectrum $|u_k|^2$ (full line), $|u_k^+|^2$ (dotted line) and $|u_k^-|^2$ (dashed line) as a function of the wavenumber for different values of Kraichnan number $\mathcal{K}r \in \{0; 1-10^{-1}; 1-10^{-2}; 1-10^{-3}\}$ and $\alpha^{-1} = 1 - \mathcal{K}r^2$.

modulus square of the velocity modes as well as their positive and negative helical components. Since the average quantity only depends on the wavenumber and does not depend on the direction of the wavenumber, the integral of the shell is done by multiplying the averaged quantity by the surface $4\pi k^2$ of the shell. The energy and helicity spectrum are then given by

$$\mathbb{E}_k = 4\pi k^2 \left(e_k^+ + e_k^-\right) = \frac{\frac{8\pi k_M^2}{\alpha}\left(\frac{k}{k_M}\right)^2}{1-\mathcal{K}r^2\left(\frac{k}{k_M}\right)^2} \quad \text{and} \quad H_k = \frac{\frac{8\pi k_M^2}{\alpha}\mathcal{K}r k_M\left(\frac{k}{k_M}\right)^4}{1-\mathcal{K}r^2\left(\frac{k}{k_M}\right)^2}. \tag{7.26}$$

Fig. 7.4 represents the energy of the different helical components integrated on a shell of constant wavenumber. As the Kraichnan number reaches one, the spectrum deviates for the equipartition k^2-power law. The global velocity and positive helical spectrum peak at large wavenumber and the negative helical spectrum has a slight dip.

There is no equivalent for the energy spectrum in the case of an ideal gas. However, in the solid phase, crystalline lattice can be described by Hamiltonian quadratic in impulsion and position. The collective excitation of the lattice can be decomposed in plane-waves associated to acoustic and optic phonons. Each acoustic plane-wave has the same energy. Using the plane-wave decomposition of the excitation, the energy spectrum of the system can be evaluated by averaging over a shell of constant wavenumbers. Since all plane-waves have the same energy, at small wavenumber, the average energy spectrum is proportional to the surface of the shell of constant wavenumber $E(k) \propto k^2$.

For a Kraichnan number equal to zero, the average energy spectrum of ideal fluids follows the k^2-power law observed in acoustic phonons. When the Kraichnan number is different from zero, which corresponds to a system with helicity, the average energy spectrum deviates from the equipartition distribution of acoustic phonon.

Knowing the energy and helicity spectrum, the total energy and helicity of ideal

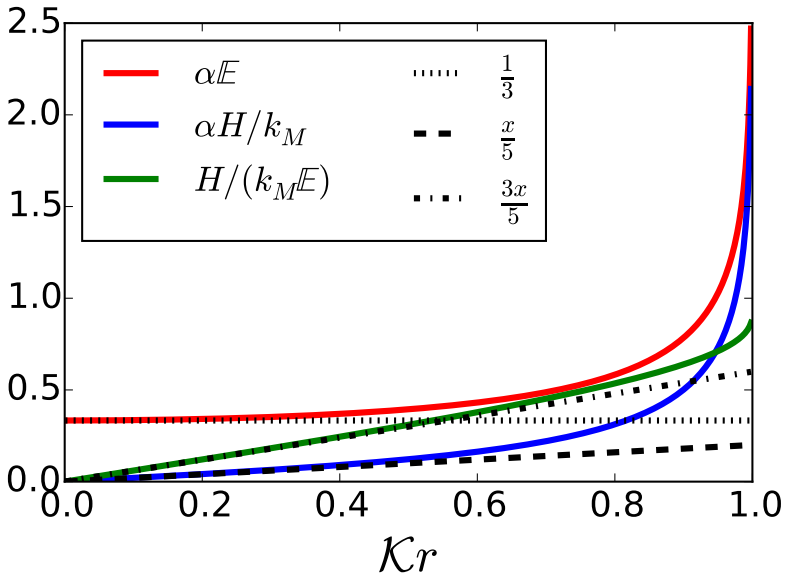

Figure 7.5 – Representation of the $\alpha\mathbb{E}$ (red line), $\alpha H/k_M$ (blue line) and $H/(k_M\mathbb{E})$ (green line) as a function of $\mathcal{K}r$. The black curves represent the different asymptotic trends reached by the functions.

fluids can be computed and expressed as a function of α, $\mathcal{K}r$ and k_M:

$$\mathbb{E} = \frac{8\pi k_M^2}{\alpha \mathcal{K}r^3}\left(\operatorname{argtanh}\mathcal{K}r - \mathcal{K}r\right) \quad \text{and} \quad H = \frac{8\pi k_M^3}{\alpha \mathcal{K}r^4}\left(\operatorname{argtanh}\mathcal{K}r - \mathcal{K}r - \frac{\mathcal{K}r^3}{3}\right). \quad (7.27)$$

The evolution of the total energy and total helicity are represented in fig. 7.5 as a function of the Kraichnan number. The relation between the ($\mathbb{E}$,H) pair of parameters and the (α, $\mathcal{K}r$) pair of parameters is bijective. Fixing one pair of parameters is enough to describe unequivocally the system. At low Kraichnan number, the helicity goes to zero and the energy goes to one third. When the Kraichnan number goes to one, the helicity reaches its upper bound $H = k_M\mathbb{E}$.

Using the same hypotheses as those used in thermodynamics, the absolute equilibrium theory is able to show that the PDF of the helical components of the velocity field can be approximated with Gaussian statistics. Then, with a generalized version of the Liouville theorem valid for ideal flows, the parameters of these Gaussians can be computed. As a consequence, the absolute equilibrium theory gives a prediction on the energy spectrum. At small wavenumber, the energy spectrum follows a k^2-power law similar to the equipartition of acoustic phonons in crystalline lattice. However, at large wavenumber, helical flows deviate from the the k^2-power law.

Chapter 8

Elements of context: Time correlation

In the chapter on absolute equilibrium, we could give predictions on the average energy spectrum of the system and the standard deviation of the velocity modes. But this does not give any information on the temporal evolution of the velocity modes. The absolute equilibrium properties mainly assume that energy and helicity are conserved throughout the evolution. Studying the temporal correlations will give additional information on the evolution of modes. The results will be more specific to ideal fluids since, this time, the derivation requires the detail of the temporal evolution of the system. Some of the properties concerning ideal fluids without helicity can be found in [94] and in chap. 9.

Subsec. 8.1 reviews elements of well documented theories. Subsec. 8.2 and 8.3 present a new model and a new numeric procedure used in chap. 9 which reports new results.

8.1 Definition and examples (review)

In experiments, it is extremely difficult to measure an observable for all the positions of space. However it is much more simple to place a sensor at a given point and record its evolution in time. The time series collected carry more information than the statistical properties (average, moments, PDF) of the system at this given point. The data points of the series are chronologically ordered and can be used to compute correlation functions. We will only consider the correlation of an observable with itself. From now on, the term correlation function will be used for what is in fact the auto-correlation of an observable. The correlation function $\Gamma(t)$ of the observable X can be computed using

$$\Gamma(t) = \mathcal{N}(x)\overline{x^*(s)x(s+t)} \quad \text{with} \quad x(s) = X(s) - \overline{X} \tag{8.1}$$

$$\text{where} \quad \mathcal{N}(x) = \frac{1}{\overline{|x|^2}(s)} \quad \text{and} \quad \overline{G(s)} = \lim_{T\to\infty} \frac{1}{2T}\int_{-T}^{T} G(s)ds\,, \tag{8.2}$$

where x and G denote the fluctuations of X and a generic function respectively. s and t denote the starting time and the time interval of the correlation respectively. x

corresponds to the fluctuation of the observable X around its mean value and $\mathcal{N}(x)$ is the normalization of the correlation function. The normalization $\mathcal{N}(x)$ makes the correlation function dimensionless. The super-scripted line $\overline{\dots}$ denotes the temporal average of an observable recorded on an infinite time series. The function G used in the definition of the time average is a generic dummy observable. To avoid improperly defined integrals, correlation analysis should only be carried out on bounded functions. In the definition of the auto-correlation function, it is important to remove the average of the observable.

An immediate consequence of the definition of the correlation function is that the correlation function is even. When the $T \to \infty$ limit is taken, any finite offset in the bounds of integral used to compute a temporal average can be neglected, therefore

$$\int_{-T}^{T} x^*(s_1)x(s_1+t)ds_1 = \int_{-T+t}^{T+t} x^*(s_2-t)x(s_2)ds_2 \quad \text{thus} \quad \Gamma(t) = \Gamma(-t)\,. \tag{8.3}$$

For all observables, the correlation function is an even function in t, hence all the odd powers of the Taylor expansion of the correlation function are equal to zero.

The correlation function can be computed analytically in a few cases. In the trivial situation where the observable is independent of time, the temporal value of the observable is equal to the average of the observable and the correlation function is always equal to zero. Since polynomial function are not bounded for $t \in [-\infty; +\infty]$, a sinusoidal function is the next simplest function to analyze. Let us compute the correlation of the cosine function of amplitude A

$$\Gamma_{\cos}(t) = \frac{1}{\overline{A^2\cos^2(s)}}\overline{A^2\cos(s)\cos(s+t)} = 2\left(\overline{\tfrac{1}{2}\left(\cos(2s+t)+\cos(t)\right)}\right) = \cos(t)\,. \tag{8.4}$$

Besides making the correlation function dimensionless, the normalization of the correlation function makes the amplitude pre-factor A disappear. Another consequence of the normalization is that the correlation function is bounded below one in absolute value $|\Gamma_{\cos}(t)| \leq 1$. This property is not only valid for the cosine function, it is still true for a generic function because the correlation function has the structure of a dot product. The dot product structure of the correlation function also implies that the correlation must be maximal at $t = 0$. In the case of the cosine function, the correlation function has other local maxima but these are related to the periodic nature of the cosine function.

Since the correlation function is maximal at $t = 0$, it can be approximated by a parabola near $t = 0$. It may not bring any additional information in the case of the cosine function, but the approximation is useful when the correlation function cannot be computed analytically. The parabolic approximation can be used to compute the half-time $\tau_{1/2}$where the correlation reached one half, defined by

$$\Gamma(\tau_{1/2}) = \frac{1}{2}\,. \tag{8.5}$$

In the case of the cosine function, the analytic half-time is $\frac{\pi}{3} \sim 1.057$ and the parabolic approximation of the cosine, $1 - \frac{t^2}{2}$, leads to a half-time equal to 1. The parabolic approximation gives a half-time in agreement with the analytic results.

For solutions of stochastic differential equations, the correlation function can also be computed in a few cases such as the one-dimensional Langevin equation. This equation describes the evolution of the velocity U of a particle mass m undergoing a friction force $-\frac{m}{\tau}U$ and a stochastic force F. It can be solved in the general case using Newton's second law:

$$m\frac{dU}{dt} = -\frac{m}{\tau}U + F \quad \text{thus} \quad U(t) = e^{-\frac{t}{\tau}}\left(U(0) + \frac{1}{m}\int_0^t e^{\frac{s}{\tau}}F(t)ds\right). \tag{8.6}$$

Let us now suppose that the forcing satisfies $\underset{\sim}{F} = 0$ and that for all s, $F(s)F(s+t) = \gamma_{\text{F}}\delta(t)$, where γ_{F} is the correlation coefficient and $\delta(t)$ is the Dirac delta function. Even though the exact solution of eq. (8.6) is still valid, it will be easier to express the Langevin equation in Fourier space to compute the correlation function

$$\hat{U}(\omega) = \frac{\hat{F}(\omega)}{m\left(\frac{1}{\tau} - \imath\omega\right)} \quad \text{and} \quad |\hat{F}|^2 = \iint e^{-i\omega(t_1-t_2)}F(t_1)F(t_2)dt_1dt_2 = \gamma_{\text{F}}\,, \tag{8.7}$$

where $\widehat{\ldots}$ corresponds to the Fourier transform and ω denotes the temporal variable in Fourier space. Convolutions in physical space are products in Fourier space. Consequently, the correlation function, Γ_{lgv}, of a solution of the Langevin equation can be written using

$$\int U(s)U(s+t)ds = \frac{1}{2\pi}\int |\hat{U}|^2 e^{i\omega t}d\omega = \frac{\gamma_{\text{F}}\left(\frac{\tau}{m}\right)^2}{2\pi}\int \frac{e^{i\omega t}}{1+(\omega\tau)^2}d\omega \tag{8.8}$$

$$\text{and} \quad \int \frac{e^{i\omega t}}{1+(\omega\tau)^2}d\omega = \begin{cases} \frac{\pi}{\tau}e^{-\frac{t}{\tau}} & \text{if} \quad 0 \le t \\ \frac{\pi}{\tau}e^{+\frac{t}{\tau}} & \text{if} \quad t \le 0 \end{cases} \quad \text{thus} \quad \Gamma_{lgv}(t) = e^{-\frac{|t|}{\tau}}\,. \tag{8.9}$$

Note that the correlation function of the Langevin equation does not depend on the coefficient γ_{F} of the delta-correlated forcing. The other feature is that the correlation function decays with time and goes to zero at infinity which is characteristic of systems losing the memory of their initial condition. In the case of the Langevin equation, the half-time of the process can be computed analytically and is given by $\tau \ln 2$. However, the parabolic approximation is improperly defined because the correlation function has a cusp at $t = 0$. The behavior of the correlation function near $t = 0$ is specific to the expression of differential equation and the characteristics of the forcing. For the stochastic Langevin equation, the correlation function is not smooth because the forcing is delta-correlated in time.

The example of the Langevin equation is not only interesting because it introduces the idea of memory loss. The method used to derive the correlation function with Fourier transform is also important. This method can be generalized and gives the Wiener-Khinchin theorem which states that the spectrum of the correlation function is equal to the power spectrum. The main consequence of the Wiener-Khinchin theorem is that the computation of the correlation function of a temporal data-set can be done using Fourier transform instead of computing a convolution. For a discrete data-set, the convolution becomes a Cauchy product. The Wiener-Khinchin theorem can then be used to accelerate the computation of correlation functions.

The two simple examples used to present the notion of correlation function and correlation time can guide our intuition of what is expected for the correlation of modes in a spectrally-truncated ideal fluid. Since the modes of an ideal fluid will eventually lose the memory of their initial condition, the correlation time should decay at infinity. However, the forcing in an ideal fluid is much smoother than the delta-correlated forcing of the Langevin equation. The correlation function of the helical modes in ideal fluids should be smooth enough near $t = 0$ to define properly a parabolic approximation. It is still possible, however, that the parabolic approximation of the correlation function will not be able to give a correct value for the correlation time.

8.2 Hydrodynamic application (description of a new model)

8.2.1 Sweeping effect and parabolic expression

For the Navier-Stokes equation, some known results already exist on the dependence of the correlation time on the wavenumber. In the inertial range of Kolmogorov turbulence, the sweeping effect theory [18, 95] predicts that the correlation time should depend on the root mean square velocity at the forcing scale, U_{rms}. Since the energy of the forcing scale is much greater than the energy in all the other scales, the total energy of the system is almost entirely composed of the energy of the forcing scale. If the viscous term in neglected in the inertial range, the velocity modes follow an evolution equation dominated by the transport of velocity mode, U, in the forcing scale: $\partial_t u_{\boldsymbol{k}} \simeq ikU u_{\boldsymbol{k}}$. This transport lead to a de-correlation of the large scale modes than can be characterized using dimensional analysis.Using the energy and the wavenumber as only parameters, the only time-scale that can be built is

$$\tau_k^E \propto \frac{1}{U_{rms} k} \propto \frac{1}{k\sqrt{E}} \,. \tag{8.10}$$

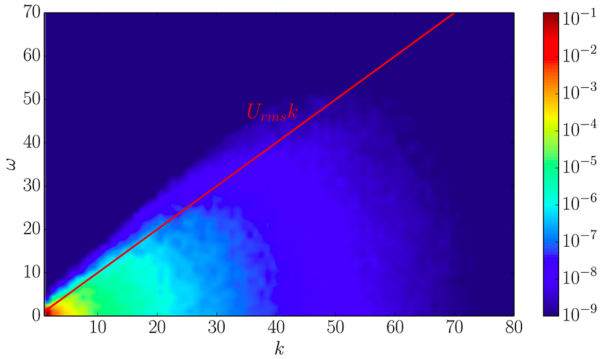

Figure 8.1 – Spatio-temporal spectrum $E(k, \omega)$ of a numerical simulation of isotropic and homogeneous turbulence. The solid red curve corresponds to $\omega = kU_{rms} = k\sqrt{E}$. Figure extracted from Clark di Leoni, Cobelli, and Mininni (2017) [96].

The sweeping effect prediction has been confirmed in numeric simulations by the spatio-temporal analysis of turbulent flows done in [96]. Fig. 8.1 represents the results of Clark di Leoni *et al.* using the spatio-temporal spectrum of the energy of an isotropic

and homogeneous turbulent flow in the $k-\omega$ Fourier space. ω represents the temporal variable in Fourier space, it is not related in any way to the vorticity. To understand the sweeping effect in the spatio-temporal spectrum, ω can be viewed as the inverse of a time. At fixed wavenumber, the energy spectrum should be non-negligible in the domain where $\omega \leq k\sqrt{E}$. More details are given on the spatio-temporal spectrum in sec. 8.3.

In the case of the truncated Euler equation, when the flow does not have any helicity, it is more difficult to define a dominant velocity since the energy is evenly spread out on every mode. The correlation time of the solution of the Euler equation could have a different behavior. Supposing that the correlation function $\Gamma_{\boldsymbol{k}}$ is smooth enough, the correlation time τ_k of solutions of the truncated Euler equation can be computed using the parabolic expansion

$$\Gamma_{\boldsymbol{k}}(t) = \frac{\overline{\boldsymbol{u}_{\boldsymbol{k}}^*(s)\boldsymbol{u}_{\boldsymbol{k}}(s+t)}}{\overline{|\boldsymbol{u}_{\boldsymbol{k}}(s)|^2}} = \frac{\overline{\boldsymbol{u}_{\boldsymbol{k}}^*(s)\boldsymbol{u}_{\boldsymbol{k}}(s)}}{\overline{|\boldsymbol{u}_{\boldsymbol{k}}(s)|^2}} + \frac{t^2}{2}\frac{\overline{\boldsymbol{u}_{\boldsymbol{k}}^*(s)\partial_t^2\boldsymbol{u}_{\boldsymbol{k}}(s)}}{\overline{|\boldsymbol{u}_{\boldsymbol{k}}(s)|^2}} + \mathcal{O}(t^4)\,. \tag{8.11}$$

Integrating by parts, the term $\overline{\boldsymbol{u}_{\boldsymbol{k}}^*(s)\partial_t^2\boldsymbol{u}_{\boldsymbol{k}}(s)}$ can be rewritten as $\overline{|\partial_t\boldsymbol{u}_{\boldsymbol{k}}(s)|^2}$. Assuming that the tuncated Euler equation is ergodic, averages over time can be replaced by ensemble averages defined in eq. (7.24). The correlation can then be expressed as

$$\Gamma_{\boldsymbol{k}}(t) = 1 - \frac{1}{2}\left(\frac{t}{\tau_{\boldsymbol{k}}}\right)^2 + \mathcal{O}(t^4) \quad \text{where} \quad \tau_{\boldsymbol{k}} = \sqrt{\frac{\langle|\boldsymbol{u}_{\boldsymbol{k}}|^2\rangle_{ens}}{\langle|\partial_t\boldsymbol{u}_{\boldsymbol{k}}|^2\rangle_{ens}}}\,. \tag{8.12}$$

The expression of the square average of the velocity mode $\langle|\boldsymbol{u}_{\boldsymbol{k}}|^2\rangle_{ens}$ is given by the absolute equilibrium statistics and the square average of time derivative of the velocity mode $\langle|\partial_t\boldsymbol{u}_{\boldsymbol{k}}|^2\rangle_{ens}$ can be computed using the temporal evolution equation of the fluid seen in eq. (2.17).

8.2.2 Correlation of velocity modes (description of new procedure)

The direct method to compute $\langle\partial_t\boldsymbol{u}(\boldsymbol{k},t)\rangle_{ens}$ consists in writing the truncated Euler equation in Fourier space with a quadratic operator that takes into account the incompressibility condition as presented in eq. (2.4). The average correlation between two modes can also be expressed with the incompressibility projection operator as

$$\langle u_\alpha^*(\boldsymbol{p})u_\beta(\boldsymbol{q})\rangle_{ens} = P_{\alpha\beta}(\boldsymbol{p})\delta(\boldsymbol{p}+\boldsymbol{q})\,\langle e_{\boldsymbol{p}}\rangle_{ens}\,. \tag{8.13}$$

The average correlation of the temporal derivative of the velocity can be computed with a method similar to that derived in p. $47-52$ of [94] in the case of non-helical flows using

$$\langle\partial_t u_\alpha^*(\boldsymbol{k})\partial_t u_\delta(\boldsymbol{k})\rangle_{ens} = \frac{1}{2}\sum_{\boldsymbol{k}+\boldsymbol{p}+\boldsymbol{q}=0}\mathcal{P}_{\alpha\beta\gamma}(\boldsymbol{k})\mathcal{P}_{\delta\mu\nu}(-\boldsymbol{k})P_{\gamma\nu}(\boldsymbol{q})P_{\beta\mu}(\boldsymbol{p})\,\langle e_{\boldsymbol{q}}\rangle_{ens}\,\langle e_{\boldsymbol{p}}\rangle_{ens}\,. \tag{8.14}$$

The derivation can be carried out by converting the discrete sums into an integral using the equivalence

$$\sum_{\boldsymbol{k}+\boldsymbol{p}+\boldsymbol{q}=0} \quad\Longleftrightarrow\quad \left(\frac{1}{{k_M}^3}\right)^2\int_{p\leq k_M}\int_{q\leq k_M}\delta(\boldsymbol{k}+\boldsymbol{p}+\boldsymbol{q})d^3\boldsymbol{p}d^3\boldsymbol{q}\,. \tag{8.15}$$

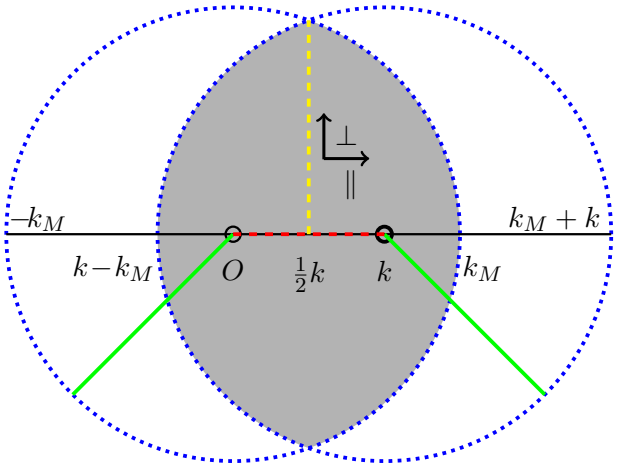

Figure 8.2 – Diagram of a cut of the integration domain. The dark surface corresponds to the integration domain. The dotted lines correspond to the limits of the circle of radius k_M and of center 0 or k. The thick full line corresponds to radii of the previously described circle. The dark dashed line corresponds to the distance between the center of the two circles. The bright dashed line corresponds to the maximal length possible for $q_\perp$.

For the moment, the truncation condition, $\boldsymbol{u}(k > k_M) = 0$, has not been applied to the velocity fields. The velocity appears in the equation within the expression of the average energy with two indices $\boldsymbol{p}$ and $\boldsymbol{q}$, therefore the summation must be done at $p \leq k_M$ and $q \leq k_M$. The domain prescribed by these conditions corresponds to the intersection of two spheres of radii k_M and center $\boldsymbol{p}$ and $\boldsymbol{q}$. The triadic condition, $\boldsymbol{k} + \boldsymbol{p} + \boldsymbol{q} = 0$, also implies that the summation over $\boldsymbol{p}$ and $\boldsymbol{q}$ can be done over $\boldsymbol{q}$ at fixed $\boldsymbol{p} = \boldsymbol{k} - \boldsymbol{q}$. The domain of summation is represented in fig. 8.2. This domain is invariant by rotation along the axis defined by $\boldsymbol{k}$ in fig. 8.2. This direction links the center of the two spheres. The coefficients of the sum also satisfy the rotation invariance of the domain. The summation can thus be performed with the variables $q_\perp$ and $q_\parallel$ where $q_\perp$ is the projection of the wavevector along the plane orthogonal to $\boldsymbol{k}$ and $q_\parallel$ is the projection of the wavevector along the axis of rotation. The sum can then be written as

$$\sum_{\boldsymbol{k}+\boldsymbol{p}+\boldsymbol{q}=0} \quad \Longleftrightarrow \quad \int_{-(1-\frac{1}{2}m)}^{1-\frac{1}{2}m} dq_\parallel \int_0^{1-\left(|q_\parallel|+\frac{1}{2}m\right)^2} \pi dq_\perp^2 \quad \text{where} \quad m = \frac{k}{k_M}\,. \tag{8.16}$$

At this point, pursuing the derivation with pencil and paper does not bring much physical intuition to the description of the evolution of the correlation. Mathematica [97] is however capable of giving plots with significant physical information. Fig. 8.3 represents the correlation time at constant energy computed using Mathematica for different Kraichnan numbers $1 - \mathcal{K}r \in \{10^{-1}, 10^{-2}, 10^{-3}, 10^{-4}, 10^{-5}, 10^{-6}, 10^{-7}, 10^{-8}\}$. In the large scales, the graphs show that the correlation time follows a k^{-1}-scaling law. In the small scale, the graphs show a rapid increase of the correlation time as wavenumbers approach the maximal wavenumber. This sharp peak in the small scales is related to the divergence of the energy when the Kraichnan number goes to one.

In large scales, the correlation time follows the k^{-1}-power law characteristic of an energy-based correlation time described in eq. (8.10). However, as the Kraichnan number goes to one, another scaling law appears in the correlation time which is consistent with a $k^{-\frac{1}{2}}$-power law. As shown in sec. 2.3, ideal fluids conserve two quantities: energy and helicity. When the Kraichnan number goes to one, the helicity becomes maximal. Using helicity, H, and the wavenumber, k, as only parameters, the only time-scale that can be built is

$$\tau_k^H \propto \frac{1}{\sqrt{kH}}\,. \tag{8.17}$$

The new scaling only concerns intermediate wavenumbers, $1-\mathcal{K}r \ll k/k_M \ll 1$, which follow a $k^{-\frac{1}{2}}$-scaling law. As the Kraichnan number approaches one, the intermediate domain widens and the scaling appears on a wider range of wavenumbers. The critical wavenumber where the transition between the $k^{-\frac{1}{2}}$- and k^{-1}-power law is reported in the center panel of fig. 8.6.

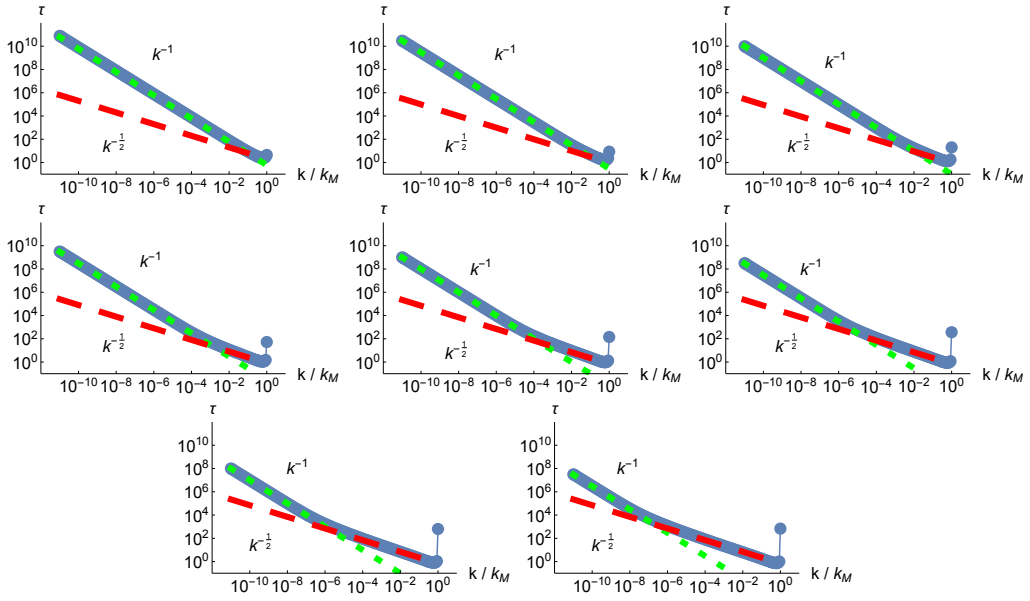

Figure 8.3 – Correlation time as a function of the wavenumber computed using the parabolic hypothesis for $1-\mathcal{K}r \in \{10^{-1}, 10^{-2}, 10^{-3}, 10^{-4}, 10^{-5}, 10^{-6}, 10^{-7}, 10^{-8}\}$ presented from left to right and top to bottom. The full curve represents the results computed using Mathematica, the dashed curve represents the $k^{-\frac{1}{2}}$-scaling and the dotted line represents the k^{-1}-scaling.

The derivation of the correlation time using the projection operator is able to give the correlation of the velocity for highly helical flows. However, it is not able to access the properties of the helical component of the velocity. In order to quantify these properties, the correct framework is the Craya-Herring helical decomposition given in eq. (2.20).

A few properties of the Craya-Herring tensor can help simplify the derivation. First, the Craya-Herring tensor $C_{\boldsymbol{kpq}}^{s_k s_p s_q}$ is symmetric on its last two variables. Second, it is equal to zero when $(s_{\boldsymbol{p}}, \boldsymbol{p})$ and $(s_{\boldsymbol{q}}, \boldsymbol{q})$ are equal. More formally, the properties can be

written as

$$C_{\boldsymbol{kpq}}^{s_{\boldsymbol{k}}s_{\boldsymbol{p}}s_{\boldsymbol{q}}} = C_{\boldsymbol{kqp}}^{s_{\boldsymbol{k}}s_{\boldsymbol{q}}s_{\boldsymbol{p}}} \quad \text{and} \quad C_{\boldsymbol{kpp}}^{s_{\boldsymbol{k}}s_{\boldsymbol{p}}s_{\boldsymbol{p}}} = 0\,. \tag{8.18}$$

With the Craya-Herring decomposition, the average correlation of the temporal derivative of the velocity can be derived with less computation since all the components are independent. The derivation leads to

$$\left\langle |\partial_t \bar{u}_{\boldsymbol{k}}^{s_{\boldsymbol{k}}}|^2 \right\rangle_{ens} = \left\langle \sum_{\substack{\boldsymbol{k}+\boldsymbol{p}_1+\boldsymbol{q}_1=0 \\ s_{\boldsymbol{p}_1}\,,\,s_{\boldsymbol{q}_1}}} \sum_{\substack{\boldsymbol{k}+\boldsymbol{p}_2+\boldsymbol{q}_2=0 \\ s_{\boldsymbol{p}_2}\,,\,s_{\boldsymbol{q}_2}}} C_{\boldsymbol{kp}_1\boldsymbol{q}_1}^{s_{\boldsymbol{k}}s_{\boldsymbol{p}_1}s_{\boldsymbol{q}_1}} u_{\boldsymbol{p}_1}^{s_{\boldsymbol{p}_1}} u_{\boldsymbol{q}_1}^{s_{\boldsymbol{q}_1}} \left[C_{\boldsymbol{kp}_2\boldsymbol{q}_2}^{s_{\boldsymbol{k}}s_{\boldsymbol{p}_2}s_{\boldsymbol{q}_2}} u_{\boldsymbol{q}_2}^{s_{\boldsymbol{p}_2}} u_{\boldsymbol{q}_2}^{s_{\boldsymbol{p}_2}} \right]^* \right\rangle_{ens} \tag{8.19}$$

$$= \sum_{\substack{\boldsymbol{k}+\boldsymbol{p}+\boldsymbol{q}=0 \\ s_{\boldsymbol{p}}\,,\,s_{\boldsymbol{q}}}} C_{\boldsymbol{kpq}}^{s_{\boldsymbol{k}}s_{\boldsymbol{p}}s_{\boldsymbol{q}}} \left[C_{\boldsymbol{kpq}}^{s_{\boldsymbol{k}}s_{\boldsymbol{p}}s_{\boldsymbol{q}}} + C_{\boldsymbol{kqp}}^{s_{\boldsymbol{k}}s_{\boldsymbol{q}}s_{\boldsymbol{p}}} \right]^* \left\langle |u_{\boldsymbol{p}}^{s_{\boldsymbol{p}}}|^2 \right\rangle_{ens} \left\langle |u_{\boldsymbol{q}}^{s_{\boldsymbol{q}}}|^2 \right\rangle_{ens} \tag{8.20}$$

$$= 2 \sum_{\substack{\boldsymbol{k}+\boldsymbol{p}+\boldsymbol{q}=0 \\ s_{\boldsymbol{p}}\,,\,s_{\boldsymbol{q}}}} \left| C_{\boldsymbol{kpq}}^{s_{\boldsymbol{k}}s_{\boldsymbol{p}}s_{\boldsymbol{q}}} \right|^2 \left\langle e_{\boldsymbol{p}}^{s_{\boldsymbol{p}}} \right\rangle_{ens} \left\langle e_{\boldsymbol{q}}^{s_{\boldsymbol{q}}} \right\rangle_{ens} . \tag{8.21}$$

To understand how the different triads interact, the sum over $s_{\boldsymbol{p}}$ and $s_{\boldsymbol{q}}$ can be separated depending on the sign of the components using

$$\mathcal{S}_m^{s_{\boldsymbol{k}}s_1s_2} = \sum_{\substack{\boldsymbol{k}+\boldsymbol{p}+\boldsymbol{q}=0 \\ s_{\boldsymbol{p}}=s_1\,,\,s_{\boldsymbol{q}}=s_2}} 2 \left| C_{\boldsymbol{kpq}}^{s_{\boldsymbol{k}}s_{\boldsymbol{p}}s_{\boldsymbol{q}}} \right|^2 \left\langle e_{\boldsymbol{p}}^{s_{\boldsymbol{p}}} \right\rangle_{ens} \left\langle e_{\boldsymbol{q}}^{s_{\boldsymbol{q}}} \right\rangle_{ens} \quad \text{and} \quad \mathcal{T}_m^{s_{\boldsymbol{k}}s_1s_2} = \sqrt{\frac{\left\langle e_{mk_M}^{s_{\boldsymbol{k}}} \right\rangle_{ens}}{\mathcal{S}_m^{s_{\boldsymbol{k}}s_1s_2}}}\,, \tag{8.22}$$

where $\mathcal{T}_m^{s_{\boldsymbol{k}}s_1s_2}$ is the time-scale associated to $\mathcal{S}_m^{s_{\boldsymbol{k}}s_1s_2}$. To simplify the expressions, we will also set $\mathcal{S}^{s_1s_2} = \mathcal{S}_m^{+s_1s_2} + \mathcal{S}_m^{-s_1s_2}$

Similarly to the direct method, the sum with the truncation constraint can be carried out on the intersection of the two spheres presented in fig. 8.2 and the discrete sum can be transformed into an integral using eq. (8.16). This final integral can be computed using Mathmatica for the different helical triadic interactions as shown in fig. 8.4 for highly helical flows. Instead of computing all the different possible triads in the sum, the graphs show computations where the triads with different helical signs are separated. The left panel of fig. 8.4 shows the three possible sums: i) $\mathcal{S}^{++}$ plotted with discs, ii) $\mathcal{S}^{+-}$ plotted with triangles and iii) $\mathcal{S}^{--}$ plotted with squares. The $\mathcal{S}^{-+}$ is not shown because it has exactly the same value as $\mathcal{S}^{+-}$.

These helical triadic sums can be related to a correlation time via the time-scale defined in eq. (8.22). When $\mathcal{K}r \to 1$, the $\mathcal{S}^{++}$ sum dominates the other terms and has a k^1-scaling at large wavenumbers consistent with a helicity-based sweeping effect, and a k^2-scaling at small wavenumbers consistent with an energy-based sweeping effect. All the other terms follow a k^2-scaling.

The center plot of fig. 8.4 shows the evolution of the $\mathcal{S}^{++}$ for different values of Kraichnan numbers. As the Kraichnan number goes to one, the domain where the sum follows a k^2-scaling widens. The right plot of fig. 8.4 shows the evolution of the correlation time, $\mathcal{T}^{++}$, built using the sum $\mathcal{S}^{++}$. Its evolution is consistent with what has been shown on the evolution of the correlation time of the full velocity field presented in the left panel of fig. 8.3.

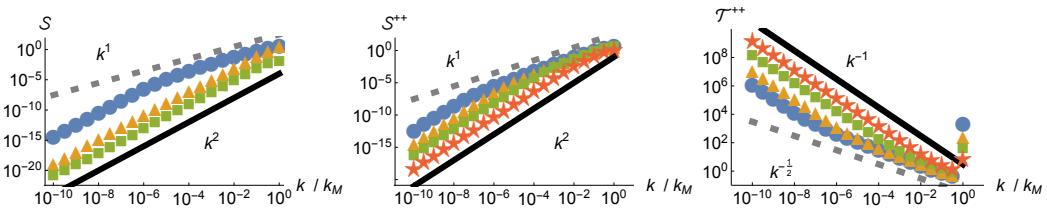

Figure 8.4 – Triadic interaction as a function of the wavenumber and associated correlation time. Left) At $\mathcal{K}r = 1 - 10^{-6}$, plots of $\mathcal{S}^{--}$ with squares, $\mathcal{S}^{+-}$ with triangle, $\mathcal{S}^{++}$ with discs, k^1 with a dashed line, k^2 with a full line. Center) $\mathcal{S}^{++}$ plotted at $\mathcal{K}r = 1 - 10^{-8}$ with discs, at $\mathcal{K}r = 1 - 10^{-6}$ with triangles, at $\mathcal{K}r = 1 - 10^{-2}$ with squares, at $\mathcal{K}r = 1 - 10^{-2}$ with stars, k^1 with a dashed line, k^2 with a full line. Right) $\mathcal{T}^{++}$ plotted at $\mathcal{K}r = 1 - 10^{-8}$ with discs, at $\mathcal{K}r = 1 - 10^{-6}$ with triangles, at $\mathcal{K}r = 1 - 10^{-2}$ with squares, at $\mathcal{K}r = 1 - 10^{-2}$ with stars, $k^{-\frac{1}{2}}$ with a dashed line, k^{-1} with a full line.

8.2.3 Asymptotic expression

In this section, we derive analytically the Eulerian correlation time of the velocity field when $k \ll k_M$ in two limits: i) $\mathcal{K}r = 0$ and ii)$\mathcal{K}r \to 1$. In order to compute the average of the correlation of the temporal derivative of the velocity, the following expression has to be computed

$$\left\langle |\partial_t \bar{u}_{\boldsymbol{k}}^{s_{\boldsymbol{k}}}|^2 \right\rangle_{ens} = 2\pi {k_M}^2 \sum_{s_{\boldsymbol{p}},\, s_{\boldsymbol{q}}} I_m^{s_{\boldsymbol{k}} s_{\boldsymbol{p}} s_{\boldsymbol{q}}}\,, \tag{8.23}$$

$$I_m^{s_{\boldsymbol{k}} s_{\boldsymbol{p}} s_{\boldsymbol{q}}} = \int_{-(1-\frac{1}{2}m)}^{1-\frac{1}{2}m} dq_{\parallel} \int_0^{1-\left(|q_{\parallel}|+\frac{1}{2}m\right)^2} dq_{\perp}^2 \left| C^{s_{\boldsymbol{k}} s_{\boldsymbol{p}} s_{\boldsymbol{q}}}(m, q_{\perp}, q_{\parallel}) \right|^2 \left\langle e_{Q_+}^{s_{\boldsymbol{p}}} \right\rangle_{ens} \left\langle e_{Q_-}^{s_{\boldsymbol{q}}} \right\rangle_{ens}\,, \tag{8.24}$$

$$\left| C^{s_{\boldsymbol{k}} s_{\boldsymbol{p}} s_{\boldsymbol{q}}}(m, q_{\perp}, q_{\parallel}) \right|^2 = \frac{m^2 q_{\perp}^2}{8 Q_+^2 Q_-^2} \left(2q_{\parallel} + s_{\boldsymbol{k}} s_{\boldsymbol{p}} \left(\tfrac{s_{\boldsymbol{p}}+s_{\boldsymbol{q}}}{2}(Q_- - Q_+) - \tfrac{s_{\boldsymbol{p}}-s_{\boldsymbol{q}}}{2}(Q_- + Q_+) \right) \right)^2, \tag{8.25}$$

$$Q = \sqrt{q_{\perp}^2 + q_{\parallel}^2} \quad , \quad Q_+ = \sqrt{q_{\perp}^2 + \left(q_{\parallel} + \tfrac{m}{2}\right)^2} \quad \text{and} \quad Q_- = \sqrt{q_{\perp}^2 + \left(q_{\parallel} - \tfrac{m}{2}\right)^2}. \tag{8.26}$$

The ${k_M}^2$ coefficient comes from the re-scaling of the term $s_p p - s_q q$ in the Craya-Herring tensor. When $q_{\parallel}$ is of order one and $m \ll 1$, the $Q_{\pm}$ terms can be simplified using $Q_- \simeq Q_+ \simeq Q$. Setting $\cos(\theta) = \frac{q_{\parallel}}{Q}$, the expression of the triad tensor can be rewritten as

$$\left| C^{\pm++}(m, q_{\perp}, q_{\parallel}) \right|^2 = \left| C^{\pm--}(m, q_{\perp}, q_{\parallel}) \right|^2 = \tfrac{m^2}{2} \left(\frac{q_{\perp}}{Q} \frac{q_{\parallel}}{Q} \right)^2 = \tfrac{m^2}{2} \mathcal{A}_1(\cos\theta) \tag{8.27}$$

$$\left| C^{+-+}(m, q_{\perp}, q_{\parallel}) \right|^2 = \left| C^{+-+}(m, q_{\perp}, q_{\parallel}) \right|^2 = \tfrac{m^2}{2} \left(\frac{q_{\perp}}{Q} \frac{q_{\parallel} - Q}{Q} \right)^2 = \tfrac{m^2}{2} \mathcal{A}_2(\cos\theta) \tag{8.28}$$

$$\left| C^{-+-}(m, q_{\perp}, q_{\parallel}) \right|^2 = \left| C^{--+}(m, q_{\perp}, q_{\parallel}) \right|^2 = \tfrac{m^2}{2} \left(\frac{q_{\perp}}{Q} \frac{q_{\parallel} + Q}{Q} \right)^2 = \tfrac{m^2}{2} \mathcal{A}_3(\cos\theta) \tag{8.29}$$

$$\mathcal{A}_1(X) = (1-X^2)X^2\,, \quad \mathcal{A}_2(X) = (1+X)(1-X)^3\,, \quad \mathcal{A}_3(X) = (1-X)(1+X)^3\,. \tag{8.30}$$

In the case of the *plus-plus* and *minus-minus* triadic interactions, the angular functions are identical since the curl is a pseudo-vector operator. It can also be noticed that $\mathcal{A}_2(\cos\theta) = \mathcal{A}_3(\cos(\theta+\pi))$, which is not surprising since, when it occurs, the vector $\boldsymbol{q}$ changes hemisphere. The angular functions $\mathcal{A}_1(\cos\theta)$ and $\mathcal{A}_2(\cos\theta)$ are represented in fig. 8.5.

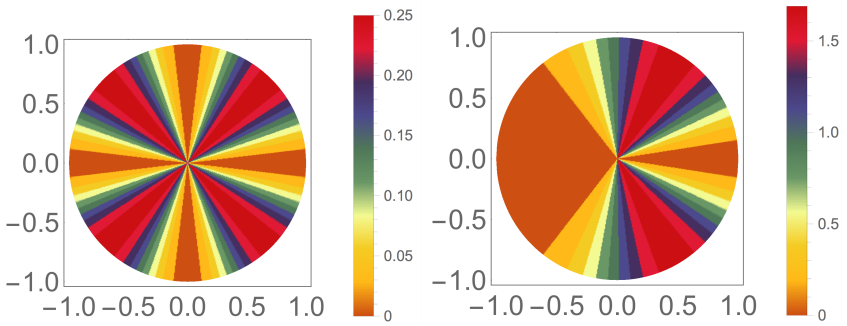

Figure 8.5 – Color-plot of the angular function. Left) $\mathcal{A}_1(\cos\theta)$. Right) $\mathcal{A}_2(\cos\theta)$.

With this new formulation, the correlation of the temporal derivative of velocity can be computed analytically when $\mathcal{K}r = 0$ and in the limit where $m \ll 1$. When $\mathcal{K}r = 0$, the average energy per helical component is $\langle e_{\boldsymbol{q}}^{s_{\boldsymbol{q}}} \rangle_{ens} = \alpha^{-1}$ and the average correlation of the temporal derivative of the velocity can be written as

$$\left\langle |\partial_t \bar{u}_{\boldsymbol{k}}^{s_{\boldsymbol{k}}}|^2 \right\rangle_{ens} = 2{k_M}^2 \int_0^\pi \sin(\theta) d\theta \int_0^1 Q^2 dQ \alpha^{-2} \tfrac{m^2}{2} \left[4\mathcal{A}_1 + 2\mathcal{A}_2 + 2\mathcal{A}_3\right](\cos\theta) \quad (8.31)$$

$$= \left(\tfrac{mk_M}{\alpha}\right)^2 \left[\int_0^1 d\tfrac{Q^3}{3}\right] \left[4\int_{-1}^1 (1-X^2)X^2 + (1+X)(1-X)^3 dX\right] = \tfrac{112}{45}\left(\tfrac{mk_M}{\alpha}\right)^2 . \quad (8.32)$$

The total energy of the system is given by $\mathbb{E} = \frac{4\pi}{3} C_N 2\alpha^{-1}$ where C_N is a constant that depends on the resolution N. Therefore, at $\mathcal{K}r = 0$ for $m \ll 1$, the parabolic correlation time can be written as

$$\tau_{\boldsymbol{k}}^{s_{\boldsymbol{k}}} = \sqrt{\frac{\langle e_{\boldsymbol{q}}^{s_{\boldsymbol{q}}} \rangle_{ens}}{\langle |\partial_t \bar{u}_{\boldsymbol{k}}^{s_{\boldsymbol{k}}}|^2 \rangle_{ens}}} = \sqrt{\frac{\alpha^{-1}}{\frac{112}{45}\left(\frac{mk_M}{\alpha}\right)^2}} = \sqrt{\frac{45\alpha}{112}} \frac{1}{k} = \sqrt{\frac{15\pi\left(\frac{N}{2}\right)^3}{14}} \frac{1}{k\sqrt{\mathbb{E}}} . \quad (8.33)$$

The correlation time follows the energy-based sweeping effect scaling law.

When the Kraichnan number is different from zero, the Craya-Herring tensor remains the same. However, the energy statistics are modified and depend on $\mathcal{K}r$, Q_+ and Q_-

$$\left\langle e_{Q_\pm}^{s_{\boldsymbol{p}}} \right\rangle_{ens} = \frac{\alpha^{-1}}{1 - s_{\boldsymbol{p}} \mathcal{K}r Q_\pm} . \quad (8.34)$$

The derivation is more difficult. It can still be carried out when the approximation $Q_+ = Q_- = Q$ does not encounter any singularity. In the case of *minus-minus* triadic interactions, the average correlation of the temporal derivative of velocity can be

written as

$$\mathcal{S}^{--} = 2\left(\frac{mk_M}{\alpha}\right)^2 \left[\int_0^\pi \mathcal{A}_1(\theta)\sin(\cos\theta)d\theta\right]\left[\int_0^1 Q^2(1+\mathcal{K}rQ)^{-2}dQ\right] \tag{8.35}$$

$$= 2\left(\frac{mk_M}{\alpha}\right)^2 \frac{4}{15}\frac{\frac{\mathcal{K}r(\mathcal{K}r+2)}{\mathcal{K}r+1}-2\ln(\mathcal{K}r+1)}{\mathcal{K}r^3}\,, \tag{8.36}$$

where $\mathcal{S}^{--}$ denotes the sum of *minus-minus* triadic interactions.

The same computation cannot be done for the other interactions because the average energy per mode diverges near the bounds of the integral on $q_\perp$ and $q_\parallel$. This divergence prevents us from simply neglecting m in front of one of the bounds of the integral. Computing the *plus-plus* interaction requires to use the exact formulation of the triadic interaction given in eq. (8.23-8.26). The *plus-plus* interaction can then be written as

$$\mathcal{S}^{++} = 2\pi\left(\frac{mk_M}{\alpha}\right)^2 \mathcal{I} \tag{8.37}$$

$$\text{where}\quad \mathcal{I} = \int_{-(1-\frac{1}{2}m)}^{1-\frac{1}{2}m} dq_\parallel \int_0^{1-\left(|q_\parallel|+\frac{1}{2}m\right)^2} dq_\perp^2\,\psi(q_\parallel, q_\perp, \mathcal{K}r)\,, \tag{8.38}$$

$$\text{with}\quad \psi(q_\parallel, q_\perp, \mathcal{K}r) = \frac{q_\perp^2\left(\left(q_\parallel+\frac{Q_--Q_+}{2}\right)^2+\left(q_\parallel-\frac{Q_--Q_+}{2}\right)^2\right)}{2Q_-^2Q_+^2\left(1-\mathcal{K}rQ_-\right)\left(1-\mathcal{K}rQ_+\right)}\,. \tag{8.39}$$

The function ψ is even on its two first variable: $\psi(q_\parallel, q_\perp, \mathcal{K}r) = \psi(q_\parallel, -q_\perp, \mathcal{K}r)$ and $\psi(q_\parallel, q_\perp, \mathcal{K}r) = \psi(-q_\parallel, q_\perp, \mathcal{K}r)$. Therefore the computation simplifies to

$$\mathcal{I} = 4\int_0^{1-\frac{1}{2}m} dq_\parallel \int_0^{1-\left(q_\parallel+\frac{1}{2}m\right)^2} dq_\perp^2\,\psi(q_\parallel, q_\perp, \mathcal{K}r) \tag{8.40}$$

When $\mathcal{K}r \to 1$ and $m \to 0$, the integral $\mathcal{I}$ is dominated by the vicinity of the maximum of the function ψ. To pursue the computation, we will introduce the small parameter $\epsilon = 1-\mathcal{K}r$ and the variable $S = 1-(q_\parallel^2+q_\perp^2)$ and $S' = 1-(q_\perp^2+(q_\parallel+\frac{m}{2})^2)$. When $\epsilon \ll 1$ and $m \ll 1$, the mass of the integral is located on the edge of the integration domain, that is for $S \ll 1$. With this approximation, we get

$$Q_\pm = \sqrt{q_\perp^2+(q_\parallel \pm \frac{m}{2})^2} \simeq \sqrt{q_\perp^2+q_\parallel^2 \pm q_\parallel m} \tag{8.41}$$

$$\simeq \sqrt{1-S\pm q_\parallel m} \simeq 1+\frac{-S\pm q_\parallel m}{2} \tag{8.42}$$

To get the next approximation, $q_\parallel$ is considered of order one and ϵ, m and S are neglected in front of one. The ψ function has the following expansions

$$\psi(q_\parallel, 1-q_\parallel^2-S, 1-\epsilon) \simeq \frac{(1-q_\parallel^2)q_\parallel^2}{\left(\epsilon+\frac{S+q_\parallel m}{2}\right)\left(\epsilon+\frac{S-q_\parallel m}{2}\right)}\,, \tag{8.43}$$

$$\psi(q_\parallel, 1-q_\parallel^2-S', 1-\epsilon) \simeq \frac{(1-q_\parallel^2)q_\parallel^2}{\left(\epsilon+\frac{S'+2q_\parallel m}{2}\right)\left(\epsilon+\frac{S'}{2}\right)}\,. \tag{8.44}$$

The computation of integral $\mathcal{I}$ can be carried

$$\mathcal{I} \simeq \mathcal{J} = 4 \int_0^{1-\frac{1}{2}m} dq_\parallel \int_{mq_\parallel}^{1-q_\parallel^2} dS \psi(q_\parallel, 1-q_\parallel^2-S, 1-\epsilon) \tag{8.45}$$

The integral $\mathcal{J}$ can be computed analytically in the two asymptotic regimes, when $m \ll \epsilon$ or when $\epsilon \ll m$. If $m \ll \epsilon$, we get

$$\begin{aligned}
\mathcal{J} \underset{m\ll\epsilon}{=} \mathcal{J}_\epsilon &= 4 \int_0^{1-\frac{1}{2}m} dq_\parallel \int_{mq_\parallel}^{1-q_\parallel^2} dS \frac{(1-q_\parallel^2)q_\parallel^2}{\left(\epsilon+\frac{S}{2}\right)\left(\epsilon+\frac{S}{2}\right)} && (8.46)\\
&= 4 \int_0^{1-\frac{1}{2}m} dq_\parallel (1-q_\parallel^2)q_\parallel^2 \int_{mq_\parallel}^{1-q_\parallel^2} dS \frac{4}{(2\epsilon+S)^2} && (8.47)\\
&= 4 \int_0^{1-\frac{1}{2}m} dq_\parallel (1-q_\parallel^2)q_\parallel^2 4 \left[-(2\epsilon+S)^{-1}\right]_{mq_\parallel}^{1-q_\parallel^2} && (8.48)\\
&\simeq 16 \int_0^1 dq_\parallel (1-q_\parallel^2)q_\parallel^2 \left[-(1-q_\parallel^2)^{-1} + \frac{1}{2\epsilon}\right] && (8.49)\\
&= 16\left(-\frac{1}{3} + \frac{2}{15}\frac{1}{2\epsilon}\right) \simeq \frac{16}{15}\frac{1}{\epsilon} && (8.50)
\end{aligned}$$

If $\epsilon \ll m$, we get

$$\begin{aligned}
\mathcal{J} \underset{\epsilon\ll m}{=} \mathcal{J}_m &= 4 \int_0^{1-\frac{1}{2}m} dq_\parallel \int_0^{1-q_\parallel^2} dS' \frac{(1-q_\parallel^2)q_\parallel^2}{\left(\frac{S'+2q_\parallel m}{2}\right)\left(\epsilon+\frac{S'}{2}\right)} && (8.51)\\
&= 4 \int_0^{1-\frac{1}{2}m} dq_\parallel (1-q_\parallel^2)q_\parallel^2 \int_0^{1-q_\parallel^2} dS' \frac{4}{\left(S'+2q_\parallel m\right)(2\epsilon+S')} && (8.52)\\
&= 4 \int_0^{1-\frac{1}{2}m} dq_\parallel (1-q_\parallel^2)q_\parallel^2 4 \left[\frac{\ln\left(\frac{S'+2\epsilon}{S'+2q_\parallel m}\right)}{2q_\parallel m - 2\epsilon}\right]_0^{1-q_\parallel^2} && (8.53)\\
&\simeq 4 \int_0^1 dq_\parallel (1-q_\parallel^2)q_\parallel^2 4 \frac{\ln\left(\frac{1-q_\parallel^2}{1-q_\parallel^2}\right) - \ln\left(\frac{2\epsilon}{2q_\parallel m}\right)}{2q_\parallel m} && (8.54)\\
&= \frac{8}{m} \int_0^1 dq_\parallel (1-q_\parallel^2)q_\parallel \left(\ln(q_\parallel) - \ln\left(\frac{\epsilon}{m}\right)\right) && (8.55)\\
&= -\frac{8}{m}\left(\frac{3}{16} + \frac{1}{4}\ln\left(\frac{\epsilon}{m}\right)\right) \simeq -\frac{2}{m}\ln\epsilon && (8.56)
\end{aligned}$$

The critical wavenumber at which the correlation time changes power law can be computed using the intersection of the two regimes

$$\begin{aligned}
\mathcal{J}_\epsilon = \mathcal{J}_m \quad &\Longleftrightarrow \quad \frac{16}{15}\frac{1}{\epsilon} = -\frac{2}{m}\ln\epsilon \quad \Longleftrightarrow \quad m = -\frac{15}{8}\epsilon\ln\epsilon && (8.57)\\
\text{thus} \quad &\frac{k_c}{k_M} = -A(1-\mathcal{K}r)\ln(1-\mathcal{K}r) \quad \text{with} \quad A = \frac{15}{8}\,. && (8.58)
\end{aligned}$$

The integral $\mathcal{I}$ can therefore be approximated by the harmonic average of the two regimes

$$\mathcal{I} \simeq \frac{-2\ln\epsilon}{m - A\epsilon\ln\epsilon} \quad \text{with} \quad A = \frac{15}{8}\,. \tag{8.59}$$

Consequently, when $\mathcal{K}r \to 1$ and $k/k_M \to 0$, it is possible to compute an asymptotic expression of the correlation time with the Craya-Herring helical decomposition [26, 27]. In this limit, most of the energy is concentrated in the positive helical components of the modes near k_M. The interactions of these modes are dominant in the temporal evolution of the velocity and give a theoretical prediction for the correlation time

$$\mathcal{T}^{++}(\boldsymbol{k}, s_{\boldsymbol{k}}) = \sqrt{\frac{\langle|\boldsymbol{u}_{\boldsymbol{k}}^{s_{\boldsymbol{k}}}|^2\rangle_{ens}}{\langle|\partial_t \boldsymbol{u}_{\boldsymbol{k}}^{s_{\boldsymbol{k}}}|^2\rangle_{ens}}} \underset{k/k_M\to 0}{\overset{\mathcal{K}r\to 1}{=}} \sqrt{\frac{\alpha\left(\frac{k}{k_M} - A(1-\mathcal{K}r)\ln(1-\mathcal{K}r)\right)}{2\pi k^2\left(1-(s_{\boldsymbol{k}}\mathcal{K}r)\frac{k}{k_M}\right)(-2\ln(1-\mathcal{K}r))}} \tag{8.60}$$

$$\text{with} \quad A = \frac{15}{8} \quad \text{and} \quad \alpha = \frac{\operatorname{argtanh}(\mathcal{K}r) - \mathcal{K}r}{\mathcal{K}r^3\mathbb{E}}\,. \tag{8.61}$$

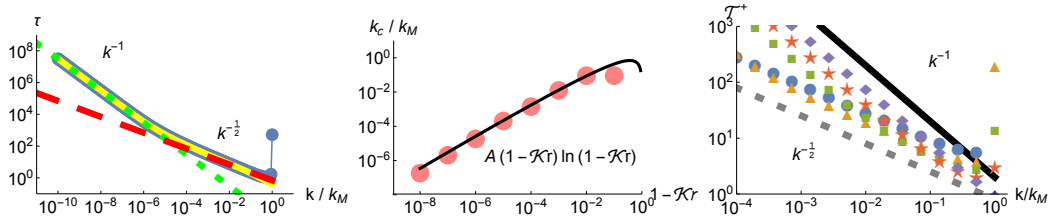

Figure 8.6 – Left) Correlation time as a function of the wavenumber for $1 - \mathcal{K}r = 10^{-6}$. The semi-analytic results are represented with the full line with dots in dark for the positive helical components and in bright for the negative helical components. The $k^{-1/2}$-scaling law is represented with the dashed line. The k^{-1}-scaling law is represented with the dotted line. Center) Critical wavenumber as a function of $1-\mathcal{K}r$, the semi-analytic results are represented with dots and the $A(1-\mathcal{K}r)\ln(1-\mathcal{K}r)$-scaling law is represented with the full line. Right) Evolution of the correlation time as the Kraichnan number increases at fixed energy for the positive helical component, for $\mathcal{K}r \in \{0; 1-10^{-1}; 1-10^{-2}; 1-10^{-4}; 1-10^{-8}\}$, represented by diamonds, stars, squares, triangles and discs respectively. The dotted line represents the $k^{-\frac{1}{2}}$-scaling and the full line represents the k^{-1}-scaling.

The left panel of fig. 8.6 represents the evolution of the correlation time computed using the parabolic hypothesis for a Kraichnan number near one : $\mathcal{K}r = 1 - 10^{-6}$. The correlation time of the positive and negative helical components of the velocity are represented. The correlation of the velocity is not shown but in the highly helical limit $\mathcal{K}r \to 1$, most of the energy is located in the positive helical component of velocity, consequently the velocity modes have the same correlation time as their positive helical components. The center panel of fig. 8.6 represents the evolution of the critical wavenumber, *i.e.* where the correlation time changes scaling law from k^{-1} to $k^{-\frac{1}{2}}$. The fit on the graph indicates that the critical wavenumber follows closely the $A(1-\mathcal{K}r)\ln(1-\mathcal{K}r)$ prediction. The right panel of fig. 8.6 represents the evolution of the correlation time at fixed total energy $\mathbb{E}$ for different Kraichnan numbers. As

the Kraichnan number goes to one, the correlation time in the small scales increases and the correlation in the large scales decreases. Increasing helicity slows down the dynamic of the small scale modes and makes the large scale dynamic quicker. Even though helicity does not appear explicitly in eq. (8.61), a $k^{-\frac{1}{2}}$-scaling appears when $1-\mathcal{K}r \ll k/k_M \ll 1$. This scaling is similar to the helicity-based correlation time and appears at Kraichnan numbers characteristic of highly helical flows.

8.3 Spatio-temporal measurements (description of a new procedure)

In order to measure the correlation function and compute the correlation time, we developed a method similar to that used to produce spatio-temporal spectrum in the profilometry experiments described in [98, 99, 96]. Fig. 8.7 represents the experimental setup of the gravito-capillary wave experiment done by Cobelli *et al.* in [98]. Fig. 8.8 represents the experimental setup of the thin plates wave experiment done by Miquel *et al.* in [99]. In profilometry experiments, a sample image is projected on surface with a video-projector which is recorded by a camera. Analyzing the deformation of the surface, the profile of the height of the surface can be reconstructed. With a temporal record of the height of the surface, the spatio-temporal spectrum of the system can be computed using Fourier transform in space and in time.

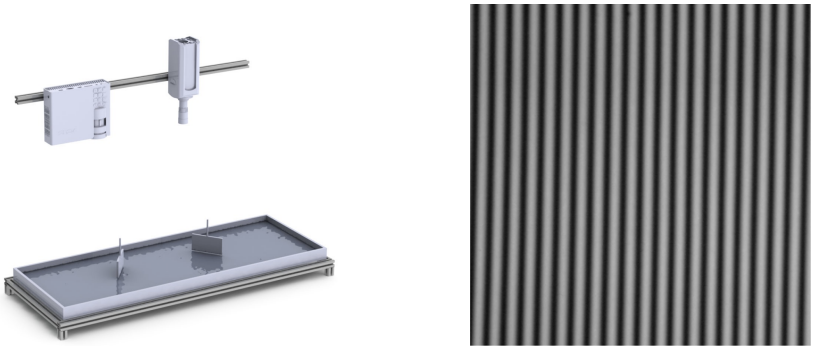

Figure 8.7 – Setup of the profilometry of the gravito-capillary wave experiments of Cobelli *et al.* (2009) and Leoni *et al.* (2015). Left) Scheme of the experimental setup. Right) Sample image of the fringes projected onto the liquid surface as registered by a camera. The figures are extracted from [98, 96].

Fig. 8.9 represents in color-plot the spatio-temporal spectrum computed from the experiments on thin plates waves and gravito-capillary waves. The purple line in the left panel of fig.8.9 and the red line in the right panel of fig.8.9 are characteristic of the dispersion relation of the system. Indeed, let us consider, for instance, the one-dimensional D'Alembert wave-equation on a passive scalar ϕ

$$0 = \partial_{tt}^2\phi - c^2\partial_{xx}^2\phi \quad \Longleftrightarrow \quad 0 = (\omega^2 - c^2k^2)\phi_{k\omega}, \tag{8.62}$$

where c, ω, k and $\phi_{k\omega}$ denote the celerity of the wave, the angular frequency, the wavenumber and the $k-\omega$ Fourier component of the passive scalar. On the one hand, if $\omega^2 \neq c^2k^2$, the Fourier component $\phi_{k\omega}$ must be equal to zero. On the other hand,

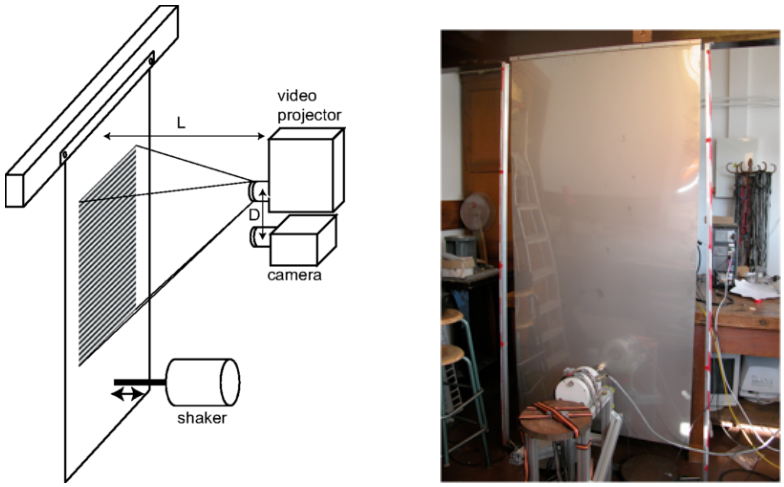

Figure 8.8 – Setup of the plate profilometry in the thin plates wave experiment of Miquel *et al.* (2014). The figures are extracted from [99].

if $\omega^2 = c^2k^2$, the Fourier component $\phi_{k\omega}$ can be different from zero. This property can be visualized on spatio-temporal spectral. The non-zero parts of the spectrum correspond to regions of parameters where the dispersion relation is satisfied and the Fourier component can be different from zero. In the other regions, the dispersion relation is not satisfied.

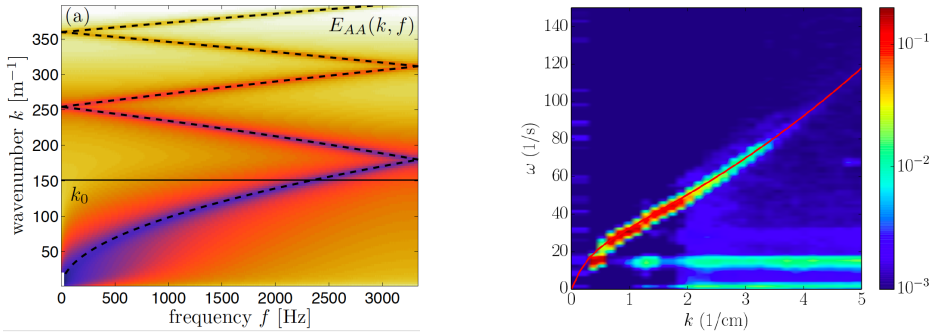

Figure 8.9 – Experimental spatio-temporal spectrum. Left) Experimental spatio-temporal spectrum from the experiment of Miquel *et al.* (2014). Right) Experimental spatio-temporal spectrum from the gravito-capillary wave experiment of Leoni *et al.* (2014). The figures are extracted from [99] and [96] respectively.

The computation of the spatio-temporal spectrum can be used to compute the power spectrum in DNS in fluid mechanics. Similarly to computation of correlation function for the stochastic Langevin equation at eq. (8.9), the power spectrum can be used to compute the correlation function via the Wiener-Khinchin theorem.

In order to produce spatio-temporal spectrum, the velocity field must be outputted from the code at a regular time-step to form a data-set in the $\boldsymbol{k} - t$ space. However, keeping in memory the entire N^3 data-set, N being the resolution, is too demanding in computational memory. To reduce the volume of the data-set without loosing the properties of the different modes, only the planes at $k_x \in \{0; 1\}$, $k_y \in \{0; 1\}$ and

$k_z \in \{0; 1\}$ are outputted for the Taylor-Green symmetric TYGRE code and $k_x = 0$, $k_y = 0$ and $k_z = 0$ for the $[0; 2\pi]^3$-periodic GHOST code. The velocity time series are then multiplied by an apodization function [100] before being Fourier-transformed to form data-set in the $\boldsymbol{k} - \omega$ space. The apodization procedure is meant to smooth the discontinuities at the beginning and end of the time series of the data in order to limit Gibbs sampling effect when carrying out the temporal Fourier transform.

The power spectrum $s(\boldsymbol{k}, \omega)$ can then be computed by taking the modulus square of the velocity and summing over the different Cartesian directions. The isotropic power spectrum $S(k, \omega)$ is then computed by summing the power spectrum over the modes of same wavenumber with a binning of spacing one in wavenumber using the formula $\lfloor k + \frac{1}{2} \rfloor$ to find the bin number. The reconstruction of the spectrum using only three planes can only be done because the flow is isotropic. The correlation function $\Gamma(k, t)$ is computed using Wiener-Khinchin theorem by doing a Fourier transform of the isotropic power spectrum and normalizing the function. Finally, the correlation time can be computed by doing a fit of the correlation function in a well-resolved domain not too close to the maximum. We chose to measure the correlation time using the time when the correlation function reaches half-height, $\tau_{\frac{1}{2}}$, and using the Poisson distribution normalization for the correlation time $\tau = \tau_{\frac{1}{2}} / \ln(2)$. The same algorithm can be used to find the correlation function of the positive and negative helical modes of the velocity field using eq. (2.19). The steps of the procedure are summed up in the algorithm presented in fig. 8.10.

Require: $\boldsymbol{u}(\boldsymbol{k}, n\Delta t)$, n, Δt,

1: $\boldsymbol{u}(\boldsymbol{k}, \omega) = \mathcal{F}[\boldsymbol{u}(\boldsymbol{k}, n\Delta t) apodization(n, \Delta t)](\omega)$
2: $s(\boldsymbol{k}, \omega) = \sum_i |\boldsymbol{u}_i(\boldsymbol{k}, \omega)|^2$
3: $S(k, \omega) = \sum_{\boldsymbol{k}} \mathbb{1}(k - \frac{1}{2} < |\boldsymbol{k}| \leq k + \frac{1}{2}) s(\boldsymbol{k}, \omega)$
4: $\gamma(k, t) = \mathcal{F}^{-1}[S(k, \omega)](t)$
5: $\Gamma(k, t) = \gamma(k, t)/\gamma(k, 0)$
6: $\tau(k) = Solve[t, \Gamma(k, t), 1/2]$

Figure 8.10 – Algorithm to compute the correlation time. $\mathcal{F}$ denotes the discrete Fourier transform, $\mathcal{F}^{-1}$ denotes the discrete inverse Fourier transform, $\mathbb{1}$ denotes the characteristic function satisfying $\mathbb{1}(bool) = 1$ if *bool* is *true* and 0 otherwise, $apodization(n, \Delta t)$ denotes an apodization function and $Solve[t, \Gamma(k, t), 1/2]$ denotes a function that finds the smallest positive t satisfying $\Gamma(k, t) = 1/2$. The reconstruction of the spectrum using only three planes can only be done because the flow is isotropic.

In order to get a better grasp of the procedure, fig. 8.11 presents spatio-temporal color-plots of the power spectrum $S(k, \omega)$ on the left panel and the correlation function $\Gamma(k, t)$ on the right panel for Taylor-Green symmetric DNS of the truncated Euler equation. In the large scales, the power spectrum function is localized near zero and the correlation function spans on a large range of time. The small scales have a totally opposite trend. The opposite behaviors of the power spectrum and the correlation function can be explained with standard Fourier transform properties. On the other hand, the change of trends between the large scales and the small scales is explained by the sweeping effect [95]. In order to quantify more precisely the sweeping effect, the

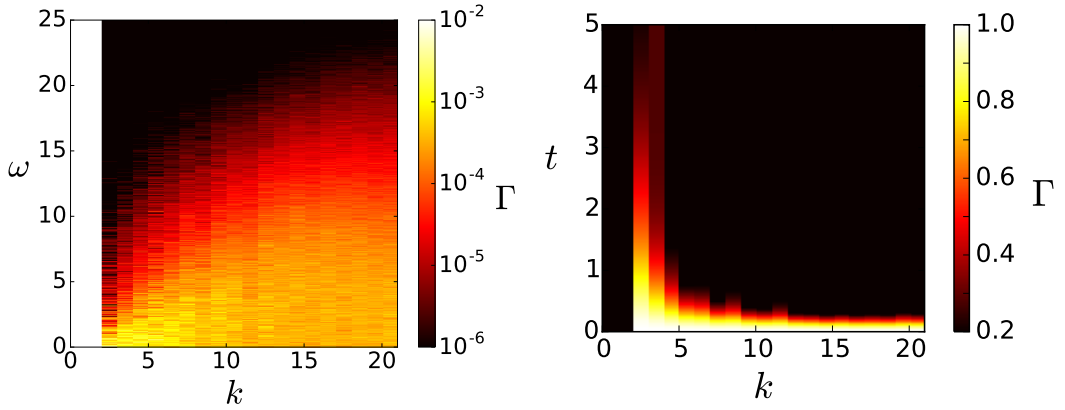

Figure 8.11 – Spatio-temporal spectrum of Taylor-Green symmetric DNS of the truncated Euler equation. Left) Power spectrum $S(k,\omega)$. Right) Correlation function $\Gamma(k,\omega)$.

correlation function has to be computed and the correlation time has to be extracted.

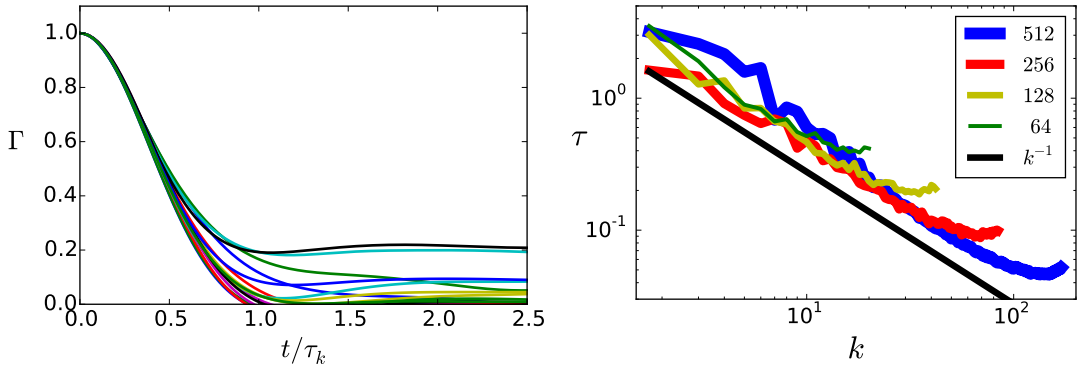

Figure 8.12 – Temporal correlation properties of Taylor-Green symmetric DNS of the truncated Euler equation. Left) Correlation function as a function of time in unit of correlation time. Right) Correlation time as a function of wavenumber.

The correlation function of different velocity modes are shown in the left panel of fig. 8.12. The time of each correlation function has been re-scaled by the correlation time measured using the time where the correlation function reaches half-height. As shown in the left panel of fig. 8.12, the correlation functions superpose on a curve for times satisfying $0 \leq t \leq \tau_k/2$. The agreement of the curves is not as clear for $\tau_k/2 < t < \tau_k$ and is off for $\tau_k \leq t$. However, the results coming from the domain where the curves collapse are already important. First, this collapse at small time confirms the use of the parabolic hypothesis made in eq. (8.12). Second, the good agreement of the curve until τ_k also confirms the use of the time at half-height as a proxy to measure the correlation time plotted on the right panel of fig. 8.12. The right panel of fig. 8.12 shows that the correlation follows a k^{-1}-scaling law characteristic of sweeping effect with an energy-based correlation time.

Chapter 9

Helicity effects on large scale correlation time in turbulence (*submitted*)

This chapter presents new results.

Solutions of the Navier-Stokes equation at scales larger than the forcing scale as well as solutions of the truncated Euler equation have been conjectured into thermalize to absolute equilibrium statistics. Using direct numeric simulations (DNS) on Taylor-Green flows and general-periodic flows, we present results on their probability density function, energy spectrum, auto-correlation function and correlation time. With the hypothesis that the correlation time of the auto-correlation function is given by its short-time parabolic approximation, we are able to propose an analytic expression which describes the correlation time for the truncated Euler equation. In the case of highly helical flows, this model is able to predict a new scaling law for the correlation time based on helicity. This scaling law is also observed in DNS. We report that large scale modes in forced Taylor-Green symmetric flows follow the same properties as solutions of the truncated Euler equation. General-periodic helical flows also have similarities between the solutions of the two equations but their largest scales can deviate from absolute equilibrium theory.

9.1 Introduction

Since Kolmogorov's theory on turbulence in 1941 [4, 3], numerical and experiemental studies [5, 6] have reproduced the energy spectrum power law predicted by the theory: $E(k) \propto \epsilon^{2/3} k^{-5/3}$ where k and ϵ denote the wavenumber and the energy dissipation respectively. Most investigations focused on the inertial range, *i.e.* for wavenumbers satisfying $k_f < k < k_d$ where k_f and k_d denote the forcing wavenumber and the viscous dissipation wavenumber respectively. To maximize the range of the inertial range, most experiments and direct numeric simulations (DNS) forced the flow at the largest scale of the system. Recently, Dallas *et al.* [101] performed turbulent DNS with enough resolution to model flows with a scale separation between the forcing scale $\ell_f \propto 1/k_f$ and the domain scale L (from now on referred to as the *large scales*). In their study,

Dallas *et al.* were able to identify the power laws of the energy and helicity spectrum in the large scales for statistically stationary solutions.

In the inertial range, the dynamic of the system is often described using the image of the Richardson cascade [3] where large scales transfer energy to smaller scales by breaking big eddies into smaller eddies. This description cannot be used to describe the large scale dynamic. Indeed, large scales do not have a direct flux of energy coming from the forcing scale contrary to the inertial range. Some arguments [3] suggest that in the large scales, a statistical steady state is reached when the eddy noise caused by the turbulent scales balances viscosity. In [10, 3], Forster *et al.* derived a model using renormalization theory which indicates that large scale modes should follow the dynamic of absolute equilibrium solutions of the truncated Euler equation (TEE) [11]. Starting from the TEE and using the fluctuation-dissipation theorem, Kraichan and Chen [12] showed that the dynamic of the absolution equilibrium solutions of the TEE should themselves resemble the large scale modes of viscous flows. Contrary to viscous flows, the absolute equilibrium theory was developed for incompressible inviscid flows following the TEE

$$\partial_t \boldsymbol{u} + \mathbb{P}_{k_M}[\boldsymbol{u}\cdot\boldsymbol{\nabla}\boldsymbol{u} + \boldsymbol{\nabla}P] = 0 \quad \text{and} \quad \boldsymbol{\nabla}\cdot\boldsymbol{u} = 0 \quad \text{and} \quad P = p/\rho\,, \tag{9.1}$$

where $\boldsymbol{u}$, P and k_M denote the velocity field, the pressure field and the truncation wavenumber respectively. The operator $\mathbb{P}_{k_M}$ enforces a spherical truncation in the TEE. It acts in Fourier space as a small scale filter. The modes whose wavenumbers satisfy $|\boldsymbol{k}| \leq k_M$, are unaffected by the projection whereas the amplitudes of the other modes are all set to zero. Despite keeping the amplitude of the truncated modes to zero, the projection conserves the total energy and helicity of the flows [102]. Some temporal properties of this system have been studied numerically in [103, 104]. Eq. (9.1) needs to be contrasted with the full Navier-Stokes equation (NSE) governing the evolution of viscous flows and given by

$$\partial_t \boldsymbol{u} + (\boldsymbol{u}\cdot\boldsymbol{\nabla})\boldsymbol{u} = -\boldsymbol{\nabla}P + \nu\Delta\boldsymbol{u} + \boldsymbol{F} \quad \text{with} \quad \boldsymbol{\nabla}\cdot\boldsymbol{u} = 0\,, \tag{9.2}$$

where $\boldsymbol{u}$, P, $\boldsymbol{F}$ and ν denote the velocity field, the pressure field, the forcing field and the viscosity respectively. Note that unlike the TEE, in the NSE, energy needs to be supplied to compensate viscous dissipation in order to have non-zero steady states.

DNS of the TEE performed in [103, 104] checked the absolute equilibrium prediction of the energy and helicity spectrum predicted in [11]. Large scale modes of solutions of the NSE have been also reported [101] to have spectra in agreement with the absolute equilibrium theory. The equivalence between the temporal dynamic of the large scale modes of solution of the NSE and the absolute equilibrium solutions of the TEE has not yet been investigated. And the equivalence of the temporal dynamic of the two systems is the bedrock of the theory whereas the spectrum is a consequence. Other mechanisms can generate energy and helicity spectrum, which results in an equivalence between the large scale modes of solution of the NSE and the absolute equilibrium solutions of the TEE. Energy can be transported to the large scales with other means than eddy noise. For instance, the study of the linear instabilities of helical flows forced at small scales [86] has shown that the dynamic of the large scale modes can be coupled to the forcing mode. This coupling could create differences

between the temporal evolution of the large scale modes of the solutions of the NSE and that of absolute equilibrium solutions of the TEE. The correlation time of the system is a good measurement to asses the temporal dynamic of large scale modes. In pseudo-spectral DNS, the Eulerian correlation time of the modes of the velocity field is the best suited to describe the temporal dynamic of system. Numerical solutions have already been used to analyze the temporal evolution of statistical equilibrium in the statistically stationary regime without helicity in [94] and in the transitory regime with helicity in [104]. But the characterization of the correlation time has not yet been studied.

Our aim in this study is to give analytic and numeric results concerning the correlation time of incompressible flows solutions of the TEE and the NSE in the large scales. We will start by presenting an analytic prediction of the correlation time for the TEE taking into account the conservation of energy and helicity. This prediction assumes: i) that the helical components of the velocity field are independent Gaussian variables and ii) that the correlation time can be computed using a short time parabolic approximation of the correlation function. Using DNS solution of the TEE with and without helicity, we will validate these assumptions by presenting the energy spectrum, the probability density function (PDF) and the correlation times of absolute equilibrium solution of the TEE. We will also show that, when the energy is not concentrated in the large scales, the correlation time always follows a time-scale based on total energy whereas it can follow time-scale based on helicity when the energy is concentrated in the large scales. Finally, we will present the energy spectrum, PDF and correlation time of DNS solutions of the NSE with helical ABC forcing [15] and non-helical Taylor-Green (TG) forcing. We will show that the modes in the large scales follow Gaussian statistics, that the statistical equilibrium statistics and energy-based correlation time can be observed for TG forcing but that ABC forced flows show trends deviating from absolute equilibrium statistics.

9.2 Results (new results)

9.2.1 Absolute equilibrium and Thermalization theory

9.2.1.1 Energy and helicity spectra

The derivation of absolute equilibrium statistics for helical flows was carried out by Kraichnan [90, 11] in an analogy to canonical ensembles in statistical thermodynamics [88]. Similarly to the micro-canonical ensemble, the TEE conserves the total energy, E. In addition, the TEE also conserves the total helicity, H, which is another global quadratic quantity in velocity

$$E = \frac{1}{L^3}\int |\boldsymbol{u}|^2 d\boldsymbol{r} \quad , \quad H = \frac{1}{L^3}\int \boldsymbol{u}\cdot\boldsymbol{\omega} d\boldsymbol{r} \tag{9.3}$$

$$\text{where} \quad L^3 = \int d\boldsymbol{r} \quad \text{and} \quad \boldsymbol{\omega} = \boldsymbol{\nabla}\times\boldsymbol{u}\,. \tag{9.4}$$

Note that, in the definition of the energy, the pre-factor $\frac{1}{2}$ has been omitted to simplify the expression of the statistics in the rest of the document. In analogy with the

thermodynamic canonical ensemble, in a statistically steady state, absolute equilibrium solutions of the TEE will correspond to a flow in a state $\boldsymbol{u}$ with probability $\mathcal{P}(\boldsymbol{u})$ that follows the Boltzmann-Gibbs distribution

$$\mathcal{P}(\boldsymbol{u}) = \frac{1}{Z} e^{-\mathcal{C}(\mathbf{u})}. \tag{9.5}$$

The functional $\mathcal{C}(\mathbf{u})$ is a linear combination of the energy E and the helicity H of the flow

$$\mathcal{C}(\mathbf{u}) = \alpha E + \beta H = \alpha \left(E - \mathcal{K}r \frac{H}{k_M} \right) \quad \text{and} \quad \mathcal{K}r = -\frac{\beta k_M}{\alpha} \tag{9.6}$$

where α and β are the two parameters introduced by Kraichnan in analogy to the micro-canonical ensemble. These parameters unequivocally define a class of absolute equilibrium solutions of the TEE with a fixed energy E and helicity H. $\mathcal{K}r$ is the only dimensionless number that can be built using α, β and k_M. It will be referred to as the Kraichnan number. The Kraichnan number indicates the degree of helicity of the flow. When $\mathcal{K}r$=0, the flow does not have helicity, whereas when $|\mathcal{K}r| = 1$ the flow is maximally helical. As a consequence of the definition of $\mathcal{C}(\mathbf{u})$, velocity modes are independent Gaussian variables. The partition function Z used as normalization in eq. (9.5) is defined by

$$Z = \int \mathcal{D}\boldsymbol{u} e^{-\mathcal{C}(\boldsymbol{u})}. \tag{9.7}$$

Similarly to statistical thermodynamics, Boltzmann-Gibbs weights can be used to compute statistical averages over the space of incompressible flows. The average of a generic observable $f(\boldsymbol{u})$ is then given by

$$\langle f(\boldsymbol{u}) \rangle = \frac{1}{Z} \int \mathcal{D}\boldsymbol{u} f(\boldsymbol{u}) e^{-\mathcal{C}(\boldsymbol{u})} \tag{9.8}$$

In the case of the TEE, the truncation in wavenumber implies that the functional integral can be done over a finite number of Fourier modes $\tilde{\boldsymbol{u}}_{\boldsymbol{k}}$ that satisfy the incompressibility condition $\boldsymbol{k} \cdot \tilde{\boldsymbol{u}}_{\boldsymbol{k}} = 0$. This last condition can be simplified by using the Craya-Herring [26, 27] helical decomposition. Each Fourier mode $\tilde{\boldsymbol{u}}_{\boldsymbol{k}}$ is written as the sum of two modes of opposite helicity: $\tilde{\boldsymbol{u}}_{\boldsymbol{k}} = \tilde{\boldsymbol{u}}^{+}_{\boldsymbol{k}} + \tilde{\boldsymbol{u}}^{-}_{\boldsymbol{k}}$, where

$$\tilde{\boldsymbol{u}}^{\pm}_{\boldsymbol{k}} = \frac{1}{2} \left[\tilde{\boldsymbol{u}}_{\boldsymbol{k}} \pm \frac{\tilde{\boldsymbol{\omega}}_{\boldsymbol{k}}}{k} \right] \tag{9.9}$$

with $\tilde{\boldsymbol{\omega}}_{\boldsymbol{k}} = i\boldsymbol{k} \times \tilde{\boldsymbol{u}}_{\boldsymbol{k}}$. This leads to two independent complex amplitudes $\tilde{\boldsymbol{u}}^{\pm}_{\boldsymbol{k}}$ for each Fourier mode of an incompressible flow.

Using this statistical average of eq. (9.8), the average energy and helicity of the modes of the flow can be derived analytically. Since the PDF of every mode of the velocity field follows a Gaussian distribution, the average energy $\langle e_{\boldsymbol{k}} \rangle = \langle |\tilde{\boldsymbol{u}}_{\boldsymbol{k}}|^2 \rangle$ and average helicity $\langle h_{\boldsymbol{k}} \rangle = \langle \tilde{\boldsymbol{u}}_{-\boldsymbol{k}} \cdot \tilde{\boldsymbol{\omega}}_{\boldsymbol{k}} \rangle$ of each mode are given by

$$\langle e_{\boldsymbol{k}} \rangle = \frac{2\alpha^{-1}}{1 - \left(\mathcal{K}r \frac{k}{k_M} \right)^2} \quad \text{and} \quad \langle h_{\boldsymbol{k}} \rangle = \frac{\beta}{\alpha} \frac{2\alpha^{-1} k^2}{1 - \left(\mathcal{K}r \frac{k}{k_M} \right)^2} = \frac{\beta}{\alpha} k^2 \langle e_{\boldsymbol{k}} \rangle. \tag{9.10}$$

When $\mathcal{K}r \to 1$, the energy is confined in the modes in the smallest scales of wavenumber near k_M. The absolute equilibrium distribution can be expressed using the Craya-Herring [26, 27] helical decomposition for the energies $\langle e^{\pm}_{\boldsymbol{k}} \rangle = \langle \left| \tilde{\boldsymbol{u}}^{\pm}_{\boldsymbol{k}} \right|^2 \rangle$ and helicities $\langle h^{\pm}_{\boldsymbol{k}} \rangle = \pm k \langle e^{\pm}_{\boldsymbol{k}} \rangle$

$$\langle e^{\pm}_{\boldsymbol{k}} \rangle = \frac{\alpha^{-1}}{1 - (\pm)\mathcal{K}r \frac{k}{k_M}} \quad \text{and} \quad \langle h^{\pm}_{\boldsymbol{k}} \rangle = \frac{\pm \alpha^{-1} k}{1 - (\pm)\mathcal{K}r \frac{k}{k_M}} \,. \tag{9.11}$$

When $\mathcal{K}r \to 1$, the energy is confined in the small scale modes and more precisely in their positive helical component.

9.2.1.2 Correlation times of absolute equilibrium solutions

Absolute equilibrium statistics are able to predict the ensemble average of the energy and helicity per mode. However they do not characterize the temporal properties of the system. The computation of statistical equilibrium only requires the knowledge of the conserved quantities of the TEE and not the equation itself. To describe with more depth the properties of the solutions of the TEE or the NSE in the thermalization domain, the temporal properties of the flows must be analyzed.

In [103], Cichowlas studied the correlation time of absolute equilibrium solutions of the TEE without helicity. It was shown that the correlation time (defined more precisely below: eq.(9.16)) should follow a time-scale based on the energy E of the flow

$$\tau^E_{\boldsymbol{k}} \propto k^{-1} E^{-1/2} \tag{9.12}$$

where $\tau^E_{\boldsymbol{k}}$ is the correlation time of the velocity mode of wavevector $\boldsymbol{k}$ and is based on the energy.

In the present work, we extend this result for flows with an arbitrary quantity of helicity and show that a new power law emerges when the flow is strongly helical. This new power law is based on the helicity H of the flow

$$\tau^H_{\boldsymbol{k}} \propto k^{-1/2} H^{-1/2} \,, \tag{9.13}$$

where $\tau^H_{\boldsymbol{k}}$ is based on the helicity. To be valid, this new power law requires highly helical flows and wavenumbers in the range $k_c \ll k \ll k_M$ where $k_c \propto k_M(1-|\mathcal{K}r|)\ln(1-|\mathcal{K}r|)$, while the non-helical scaling law of eq. (9.12) is valid for $k \ll k_c$. In what follows, we give a sketch of the derivation of eq. (9.12) and (9.13) while the full derivation is presented in appx. 9.4.1.

The parabolic correlation time $\tau_{\boldsymbol{k}}$ is built using the short time approximation of the correlation function. The temporal correlation function $\Gamma_{\boldsymbol{k}}(t)$ of a mode can be expressed as

$$\Gamma_{\boldsymbol{k}}(t) = \frac{\overline{\boldsymbol{u}^*_{\boldsymbol{k}}(s)\boldsymbol{u}_{\boldsymbol{k}}(s+t)}}{\overline{|\boldsymbol{u}_{\boldsymbol{k}}(s)|^2}} \quad \text{where} \quad \overline{f(s)} = \lim_{T\to\infty} \frac{1}{2T} \int_{-T}^{T} f(s) ds \,. \tag{9.14}$$

The correlation function satisfies the relations $\Gamma_{\boldsymbol{k}}(0) = 1$ and $\Gamma_{\boldsymbol{k}}(t) = \Gamma_{\boldsymbol{k}}(-t)$. If the system looses memory as time elapses, the correlation function also satisfies $\Gamma_{\boldsymbol{k}}(\infty) = 0$. The rule of thumb is that the correlation function assesses how fast a mode de-correlates

from its initial value. Using the Taylor expansion of the correlation function near $t = 0$, the correlation function can be written as

$$\Gamma_{\boldsymbol{k}}(t) = 1 - \frac{1}{2}t^2\tau_{\boldsymbol{k}}^{-2} + \dots \quad \text{with} \quad \tau_{\boldsymbol{k}}^{-2} = -\frac{\overline{\boldsymbol{u}_{\boldsymbol{k}}^*(s)\partial_t^2\boldsymbol{u}_{\boldsymbol{k}}(s+t)}|_{t=0}}{\overline{|\boldsymbol{u}_{\boldsymbol{k}}(s)|^2}}\,, \tag{9.15}$$

where $\tau_{\boldsymbol{k}}$ corresponds to the correlation time. The term $-\overline{\boldsymbol{u}_{\boldsymbol{k}}^*(s)\partial_t^2\boldsymbol{u}_{\boldsymbol{k}}(s+t)}|_{t=0}$ can be rewritten as $\overline{|\partial_t\boldsymbol{u}_{\boldsymbol{k}}(s+t)|^2}_{t=0}$ using an integration by parts. Assuming that the truncated euler dynamical system is ergodic, the averages over time can be replaced by the statistical averages defined in eq. (9.8). The correlation time can then be expressed as

$$\tau_{\boldsymbol{k}} = \sqrt{\frac{\langle|\boldsymbol{u}_{\boldsymbol{k}}|^2\rangle}{\langle|\partial_t\boldsymbol{u}_{\boldsymbol{k}}|^2\rangle}}\,. \tag{9.16}$$

The expression of $\langle|\boldsymbol{u}_{\boldsymbol{k}}|^2\rangle$ is given by the absolute equilibrium statistics. On the other hand, the expression of $\langle|\partial_t\boldsymbol{u}_{\boldsymbol{k}}|^2\rangle$ can be computed using the temporal evolution equation of the mode given by eq. (9.1) in the case of the TEE. The property that the modes of the velocity field are independent Gaussian variables is used to compute the thermodynamic averages.

In the limit where $\mathcal{K}r \to 1$ and $k/k_M \to 0$, it is possible to compute an asymptotic expression of the correlation time with the Craya-Herring helical decomposition [26, 27] (see appx. 9.4.1). In this limit, most of the energy is concentrated in the positive helical components of the modes near k_M. The interactions of these modes are the dominant terms in the temporal evolution equation and give a theoretical prediction for the correlation time

$$\tau_{\boldsymbol{k}} \simeq \sqrt{\frac{\langle|\boldsymbol{u}_{\boldsymbol{k}}^+|^2\rangle}{\langle|\partial_t\boldsymbol{u}_{\boldsymbol{k}}^+|^2\rangle}} \underset{\substack{\mathcal{K}r\to 1\\ k/k_M\to 0}}{=} \sqrt{\frac{A(1-\mathcal{K}r) - \frac{k}{k_M\ln(1-\mathcal{K}r)}}{4\pi\alpha^{-1}k^2(1 - s_{\boldsymbol{k}}\mathcal{K}r\frac{k}{k_M})}} \tag{9.17}$$

$$\text{with} \quad A = \frac{15}{8} \quad \text{and} \quad \alpha = \frac{\tanh^{-1}(\mathcal{K}r) - \mathcal{K}r}{E_{tot}\mathcal{K}r^3}\,. \tag{9.18}$$

The left panel of fig. 9.1 represents the correlation time τ_k as a function of k for a Kraichnan number near one: $\mathcal{K}r = 1 - 10^{-6}$. Both power laws k^{-1} and $k^{-1/2}$ are represented. The k^{-1}-power law is valid in the largest wavenumbers: $k \ll k_c$, while the $k^{-1/2}$-power law is valid for an intermediate range of wavenumber: $k_c \ll k \ll k_M$. The center panel of fig. 9.1 represents the dependence of the transition wavenumber k_c with $1 - \mathcal{K}r$. The value of the transition wavenumber was estimated using the intersection of the two power laws. The dark curve on the graph indicates that the critical wavenumber follows closely the $A(1 - \mathcal{K}r)\ln(1 - \mathcal{K}r)$ prediction. The right panel of fig. 9.1 represents the evolution of the correlation time at different Kraichnan numbers for fixed total energy E_{tot}. As $\mathcal{K}r \to 1$, the correlation time in the small scales increases and the correlation time in the large scales decreases. For absolute equilibrium solutions of the TEE, increasing the helicity slows down the dynamic of the small scales and makes the dynamic of the large scales more rapid. Even though the helicity does not appear explicitly in eq. (9.18), the correlation time has a $k^{-\frac{1}{2}}$-scaling for intermediate wavenumbers when $1 - \mathcal{K}r \ll k/k_M \ll 1$. This scaling is

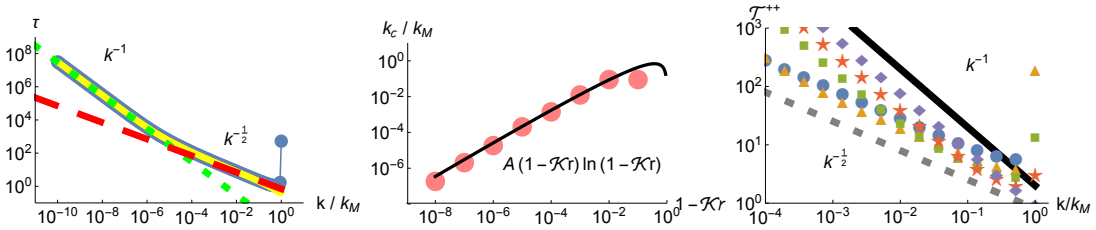

Figure 9.1 – Left) Correlation time as a function of the wavenumber for $1-\mathcal{K}r = 10^{-6}$. The results are represented with the full line with dark dots for the positive helical components and in bright dots for the negative helical components. The $k^{-1/2}$-scaling law is represented with the dashed line. The k^{-1}-scaling law is represented with the dotted line. Center) Transition wavenumber as a function of $1-\mathcal{K}r$, the semi-analytic prediction is represented with dots and the $A(1-\mathcal{K}r)\ln(1-\mathcal{K}r)$ scaling law is represented with the full line. Right) Dependence of the correlation time for the positive helical component. The Kraichnan number is increased at fixed energy: $\mathcal{K}r \in \{0; 1-10^{-1}; 1-10^{-2}; 1-10^{-4}; 1-10^{-8}\}$, represented by diamonds, stars, squares, triangles and discs respectively. The dotted line represents the $k^{-\frac{1}{2}}$-scaling law and the full line represents the k^{-1}-scaling law.

similar to the helicity-based correlation time (see eq. (9.13)) and appears for a range of Kraichnan numbers corresponding to highly helical flows.

9.2.2 Truncated Euler DNS

In the previous subsection, we discussed some predictions on the properties of the PDF, the standard derivation and the correlation time of solutions of the TEE. We will now check their validity in general-periodic flows with and without TG symmetries [105]. The DNS with TG symmetries are performed using the pseudo-spectral code TYGRES [106] and those without TG symmetries were performed using the pseudo-spectral code GHOST [52, 53]. The major advantage of studying flows with TG symmetries is that the symmetries can be used to gain a factor 32 both in storage and execution time. However, flows with TG symmetries have a total helicity equal to zero and consequently always have a Kraichnan number equal to zero. In order to study helical flows, DNS have to be performed in the general-periodic domain without TG symmetry. This last configuration will be referred to as general-periodic flow in opposition to TG symmetric flows.

9.2.2.1 No helicity: inviscid Taylor-Green flows

The first flows used to probe the statistical properties of the TEE have TG symmetries that impose the total helicity to be equal to zero. As a consequence of TG symmetries [107], the Fourier expansion of the flow can be expressed with the following simplified expression

$$\begin{bmatrix} u^x_{\boldsymbol{r}} \\ u^y_{\boldsymbol{r}} \\ u^z_{\boldsymbol{r}} \end{bmatrix} = \sum_{k_x=0}^{\infty}\sum_{k_y=0}^{\infty}\sum_{k_z=0}^{\infty} \begin{bmatrix} u^x_{\boldsymbol{k}} \times \sin k_x x \ \cos k_y y \ \cos k_z z \\ u^y_{\boldsymbol{k}} \times \cos k_x x \ \sin k_y y \ \cos k_z z \\ u^z_{\boldsymbol{k}} \times \cos k_x x \ \cos k_y y \ \sin k_z z \end{bmatrix}, \tag{9.19}$$

where $\boldsymbol{u_k} \in \mathbb{R}^3$ if k_x, k_y, k_z are all odd or all even integers and $\boldsymbol{u_k} = 0$ otherwise. All the properties of the Fourier coefficients related to TG symmetries can be found in the

appendix of [107]. Specific properties useful to understand the number of independent variables of TG symmetric flows are presented in appx.9.4.2.

Incompressible random flows with TG symmetries were used to initialize the simulations. Since TG symmetric flow do not have helicity ($H = 0$ and $\mathcal{K}r = 0$), thermalization theory predicts that they should follow

$$\langle e_{\boldsymbol{k}} \rangle = 2\alpha^{-1} \quad \text{thus} \quad E(k) = 8\pi k^2 \alpha^{-1} \quad \text{and} \quad \tau_{\boldsymbol{k}} \underset{k/k_M \to 0}{=} \sqrt{\frac{45\alpha}{112}} \frac{1}{k} \,. \tag{9.20}$$

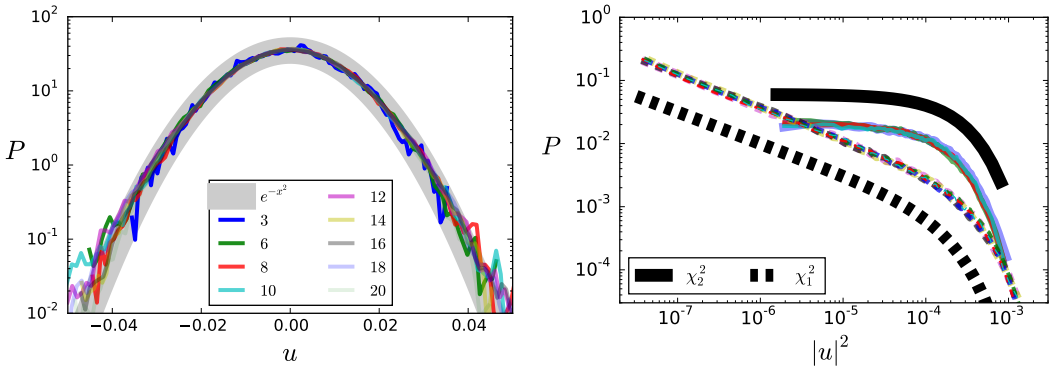

Figure 9.2 – Left) PDF of the amplitude of the velocity of modes with one degree of freedom of Taylor-Green symmetric DNS in semi-logarithmic scale. Right) PDF of energy of the modes of Taylor-Green symmetric DNS of the truncated Euler equation in logarithmic scale: (thick) theoretical predictions, (thin dashed) one degree of freedom, (thin full) two degrees of freedom.

The first hypothesis in the absolute equilibrium theory is that the components of velocity are independent Gaussian variables. As detailed in appx.9.4.2, in TG flows, the even modes with one of their components equal to zero – *i.e.* of the form $(0, k_y, k_z)$, $(k_x, 0, k_z)$ or $(k_x, k_y, 0)$ – and the xy-diagonal modes – *i.e.* of the form $(k_\perp, k_\perp, k_\parallel)$ – both only have one degree of freedom corresponding to their real amplitude. All other TG modes have two degrees of freedom. To test this assumption, temporal series of the modes are recorded and analyzed to extract the PDF. PDFs of modes with one degree of freedom are presented in the left panel of the fig. 9.2 at different wavenumbers. On the semi-logarithmic scale, the distributions of the modes follow the parabolic trend characteristic of Gaussian distribution. The fluctuations at the tail of the distribution are larger for small wavenumbers, which gives an indication that the large scales may have a larger correlation time. The right panel of fig. 9.2 represents the distribution of energy of the different velocity modes. By definition, the energy is the sum of the square of the velocity components. If the components of velocity are independent Gaussian variables, the distribution of energy must follow a χ^2_g-distribution [93]

$$\chi^2_g(X) = \frac{1}{2^{\frac{g}{2}}\Gamma(\frac{g}{2})} X^{\frac{g}{2}-1} e^{-\frac{X}{2}} \,. \tag{9.21}$$

where X denotes a generic random variable following a χ^2_g-distribution with g the number of independent Gaussian variables (see appx.9.4.3). The TG modes with one degree of freedom – $(0, k_y, k_z)$, $(k_x, 0, k_z)$, $(k_x, k_y, 0)$ and $(k_\perp, k_\perp, k_\parallel)$ – should have

an energy distribution following a χ^2_1-law. All other modes should have an energy distribution following a χ^2_2-law. If the energy follows a χ^2-distribution, it does not imply that the velocity has a Gaussian statistics, it is only a characteristic of the sum of Gaussian distributions. However, we will only check the Gaussian statistics of modes with one degree of freedom and look at the energy distribution of the other modes.

PDFs of the helical components of velocity have already been reported in [108] following the experiences on the scattering of ultra-sound by vorcity tubes [109] based on the theory established in [110]. However, the independence between the helical components of velocity has not been yet quantified.

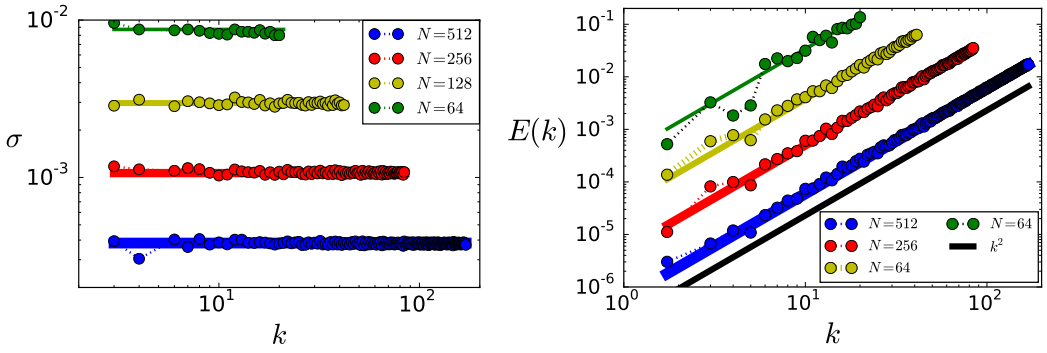

Figure 9.3 – Left) Average standard deviation of the velocity of Taylor-Green symmetric DNS of the truncated Euler equation for different resolutions. Right) Energy spectrum of Taylor-Green symmetric DNS of the truncated Euler equation at different resolutions $N = \{64, 128, 256, 512\}$ for a fixed energy.

To check the equipartition of the energy, the standard deviation of modes can be computed with their temporal series or the energy of all the modes within a shell of constant wavenumbers can be summed. The first method can be performed with the temporal series used to plot the PDF of the modes in fig. 9.2. Using this time average, the standard deviation, $\sigma^2 = \langle e_k \rangle$, is represented in the left panel of fig. 9.3. The second method, with the shell-summed energy at a fixed time, is presented in the right panel of fig. 9.3. If the system satisfies energy equipartition and is ergodic, the amount of energy per shell should be proportional to the surface of the shell, $4\pi k^2$. The k^2-power law followed by the energy spectrum in the right panel of fig. 9.3 is therefore consistent with the equipartition of energy and ergodicity.

9.2.2.2 Correlation time computation

The temporal statistics of the modes depend on the evolution equation and not only on the conserved quantities. Since the correlation function and consequently the correlation time are specific properties of the evolution equation, their measurement characterizes the temporal evolution of the system. In order to compute the correlation function and assess the correlation time, we developed a method similar to that used to produce spatio-temporal spectrum in wave experiments [98, 99, 96]. This method in presented in appx. 9.4.4.

Fig. 9.4 presents in the left panel the spatio-temporal color-plot of the power spec-

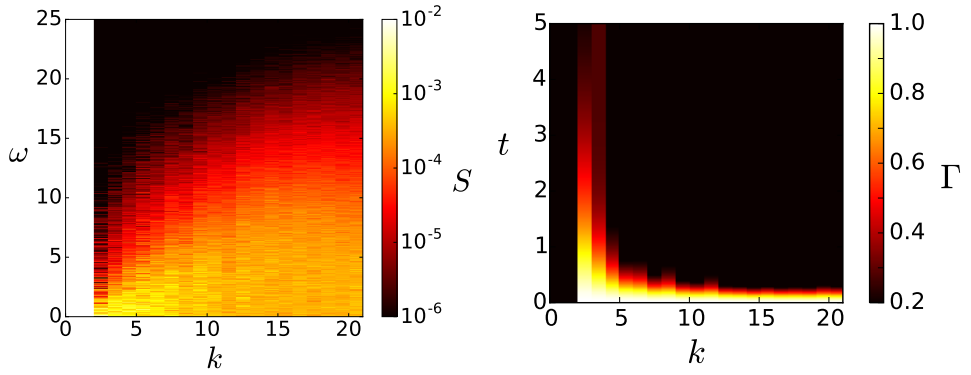

Figure 9.4 – Spatio-temporal spectrum of Taylor-Green symmetric DNS of the truncated Euler equation. The numeric data is represented with dots and the theoretical prediction with full lines. Left) Power spectrum $S(k,\omega)$. Right) Correlation function $\Gamma(k,\omega)$.

trum $s(k,\omega)$ and in the right panel the correlation function $\Gamma(k,t)$. In the large scales, the power spectrum function is localized near zero and the correlation function spans on a large time-range. The small scales have the opposite behavior. This inversion of trend between the power spectrum and the correlation function can be explained with standard Fourier-transform properties.

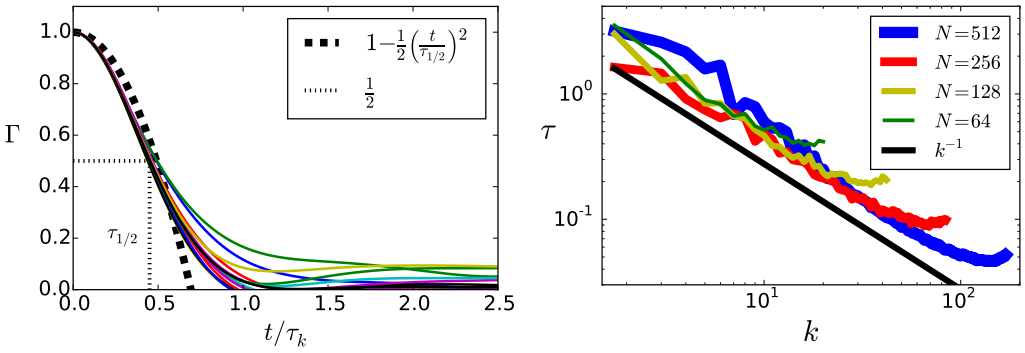

Figure 9.5 – Temporal correlation properties of Taylor-Green symmetric DNS of the truncated Euler equation. Left) Correlation function as a function of time. Right) Correlation time as a function of wavenumber.

The correlation function for different velocity modes are shown in the left panel of fig. 9.5. The time of each correlation function has been re-scaled by the correlation time measured. As shown in the left panel of fig. 9.5, the correlation functions collapse on the same curve for times in the range $0 \leq t \leq \tau_k/2$. Since long time-series are required for the correlation function to convergence in the long time, the agreement of the curves is not as clear when $\tau_k/2 < t$.

The consequences coming the collapse of the correlation functions on the $[0;\tau_k/2]$ time-range are already important. First, this collapse at small time confirms that the parabolic assumption made in eq. (9.16) is valid for absolute equilibrium solutions of the TEE. Second, the good agreement of the curve until $\tau_k/2$ also confirms that the half-height time is a good proxy to measure the correlation time. The right panel

of fig. 9.5 represents the correlation time of an absolute equilibrium solution of the TEE. It shows that the correlation time follows a k^{-1}-scaling law characteristic of an energy-based correlation time. The thermodynamic model developed in the previous section is therefore in excellent agreement with the measurements carried out with TG symmetric DNS.

9.2.2.3 Inviscid flows with helicity

The next set of DNS of the TEE were carried out using the pseudo-spectral code GHOST [52, 53]. In these DNS, every mode has four real degrees of freedom. Indeed, the Craya-Herring helical decomposition [26, 27] states that every Fourier mode of velocity can be separated into a positive and a negative helical component as expressed in eq. (9.11). The two helical components are modulated by their complex amplitude. Since there is no additional restriction on the amplitude of the mode, velocity modes have four real degrees of freedom.

In order to fix the helicity of the flow, Kraichnan's statistics eq. (9.10) are used to generate the initial velocity field. All flows are initialized with a constant energy, the only parameter left to vary is the Kraichan number $\mathcal{K}r = -k_M\beta/\alpha$. This parameter is not present for the TG flows and leads to major differences in the global aspect of the PDF of the modes. For the same mode, the helical components of helical flows have different energies.

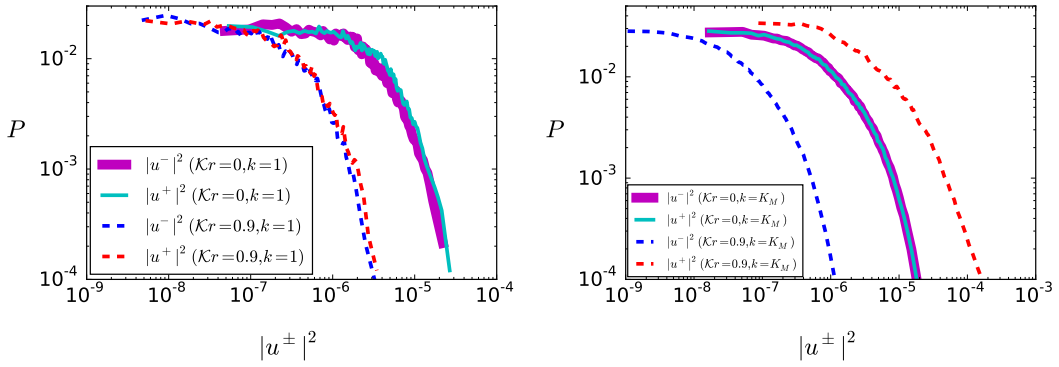

Figure 9.6 – Separation of the PDFs due to helicity in solutions of the truncated Euler equation. The PDFs have been rescaled to plateau at the same level near zero in order to compare the width of the tail of the distribution at large values. At $k = 1$ for a fixed energy, the distributions are the same because helicity does not have an important impact on the large scale modes. At $k = k_M$, the distributions of probability have an off-set for $\mathcal{K}r = 0.9$ because helicity greatly affects the distribution of energy in the small scales.

Fig. 9.6 presents the PDF of the helical components of the velocity of two flows with different Kraichnan numbers. The first flow has a Kraichnan number of zero and consequently does not have any helicity. The second flow has a Kraichnan number of 0.9 and is highly helical. For every wavenumber and every Kraichnan number, the energy of the positive and negative helical components of the velocity follows a χ^2_2-distribution. The χ^2_2-distribution is characteristic of the sum of the square of two independent Gaussian variables. The hypothesis of Gaussian-distributed velocity

modes is therefore in agreement with the DNS. In the left panel of fig. 9.6, the PDFs of the positive and negative helical components at $k = 1$ collapse both in the cases where $\mathcal{K}r = 0$ and $\mathcal{K}r = 0.9$. The PDFs of the two flows do not have the same exponential cutoff. This difference in cutoff corresponds to variations of the standard deviation of the velocity field with $\mathcal{K}r$ which is consistent with eq. (9.10). In the right panel of fig. 9.6, the PDFs of the positive and negative helical modes at $k = k_M$ collapse for the non-helical flow at $\mathcal{K}r = 0$ but do not collapse for the highly helical flow at $\mathcal{K}r = 0.9$. The separation of the PDFs at $\mathcal{K}r = 0.9$ is consistent with the statistics presented in eq. (9.11). All the characteristics of the energy distribution of the DNS are in good agreement with the properties predicted by the absolute equilibrium theory.

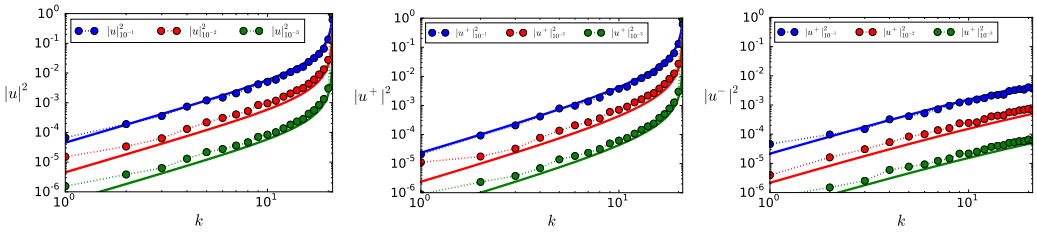

Figure 9.7 – Energy spectrum for different Kraichnan numbers $\mathcal{K}r \in \{1 - 10^{-2}; 1 - 10^{-3}; 1 - 10^{-4}\}$ for general-periodic solutions of the truncated Euler equation. The numeric data is represented with dots and the theoretical prediction with full lines. Left) Energy spectrum associated to the total velocity. Center) Energy spectrum associated to the positive helical component of the velocity. Right) Energy spectrum associated to the negative helical component of the velocity. On both panels, the full lines are associated with the energy of the total velocity; the dotted lines are associated with the energy of the positive helical component of the velocity; and the dashed lines are associated with the energy of the negative helical component of velocity.

Fig. 9.7 represents the energy spectrum of the highly helical flows $\mathcal{K}r = \{1 - 10^{-2}; 1 - 10^{-3}; 1 - 10^{-4}\}$. The results in the left panel come from DNS and those in the right panel are from the absolute equilibrium theory [11]. Theoretical and numerical results match, which confirms the validity of absolute equilibrium theory.

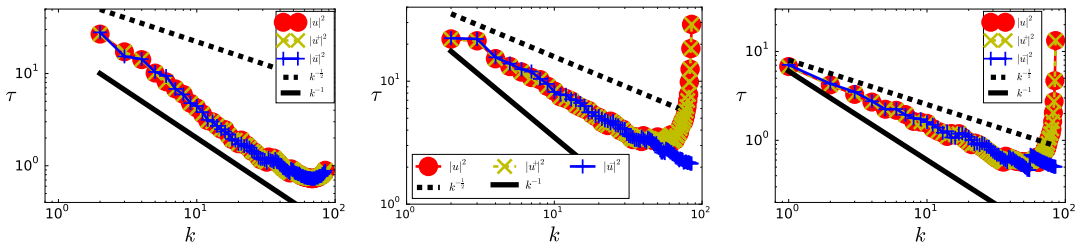

Figure 9.8 – Correlation time of DNS of general-periodic solutions of the truncated Euler equation. Left) Non-helical flow $\mathcal{K}r = 0$. Center) Slightly helical flow $\mathcal{K}r = 0.85$. Right) Highly helical flow $\mathcal{K}r = 0.9$.

The last property that will be checked concerns the evolution of the correlation time as the flow becomes highly helical ($\mathcal{K}r \to 1$). The thermalization theory, presented in sec. 9.2.1, predicts that, as the system becomes highly helical, the energy-based

correlation time (τ_k^E in eq. (9.12)) should transition to a helicity-based correlation time (τ_k^H in eq. (9.13)) in intermediate scales $(1-\mathcal{K}r) \ll k/k_M \ll 1$. With the current computational power, it is difficult to show the same number of orders of magnitude as in fig. 9.1. Consequently, the results presented in fig. 9.7 are not able to show both scaling laws on the same graph. The left panel of fig. 9.8 presents the correlation time of a non-helical flow at $\mathcal{K}r = 0$ while the right panel of fig. 9.8 presents the correlation time of a highly helical flow at $\mathcal{K}r = 0.9$. The correlation time of the non-helical flow exhibits a k^{-1}-scaling law characteristic of an energy-based correlation time, while the correlation time of the highly helical flow is closer to a $k^{-\frac{1}{2}}$-scaling law characteristic of a helicity-based. Additionally, in the right panel of fig. 9.8, the correlation time peaks in the small scales, which is characteristic of the localization of the energy near k_M of helical flows. In the highly helical case, the difference between the positive and negative helical components of the velocity can also be observed in the small scales. While both helical components collapse in the non-helical case, they are different in the small scales in the highly helical case. All these observations are in agreement with the correlation time predicted by the thermalization theory. DNS were also performed at higher Kraichnan numbers and showed a persistence of the helicity-based correlation time.

Even though the transition of the scaling law is hard to observe in the DNS carried out, results indicate that the transition of correlation time regime occurs for Kraichnan numbers in the range $0.8 \leq \mathcal{K}r \leq 0.9$. The center panel of fig. 9.8 shows that for slightly helical flows with $\mathcal{K}r = 0.85$, the correlation follows a power law with an exponent between -1 and $-\frac{1}{2}$. A clear visualization of the transition is demanding in computational power, since it occurs on nearly one order of magnitude in the left panel of fig. 9.1.

9.2.3 Navier-Stokes DNS

Because DNS of the NSE must have a converged spectrum in scales smaller than the forcing scale, their properties cannot be assessed with scale separations as important as those of DNS of the TEE. Using the same codes as in the previous subsection, we will show how the PDF, the standard deviation and the correlation time scale in the large scales for solutions of the NSE using DNS. We will also compare the results with the observation made on DNS of the TEE.

9.2.3.1 No helicity: Taylor-Green flows

TG flows are studied with different forcing wavenumbers $k_f \in \{11\sqrt{3}; 35\sqrt{3}; 59\sqrt{3}\}$. The forcing was imposed on the flow by fixing to 0.125 the amplitude of the odd modes $[k_f, k_f, k_f]/\sqrt{3}$. The other parameter of the system is the viscosity ν which was also adjusted to reach a turbulent regime. To compare the properties of flows at different forcing wavenumbers, the Reynolds number $Re = U/(\nu k_f)$ was set at a fixed value. In order to compute the Reynolds number, we checked that the total energy of the flow was dominated by the forcing mode and set the amplitude of the forcing mode to 0.125. The viscosity was then set using the forcing scale $\nu = Rek_f/U$.

Fig. 9.9 represents some properties of the PDF of velocity modes with one degree

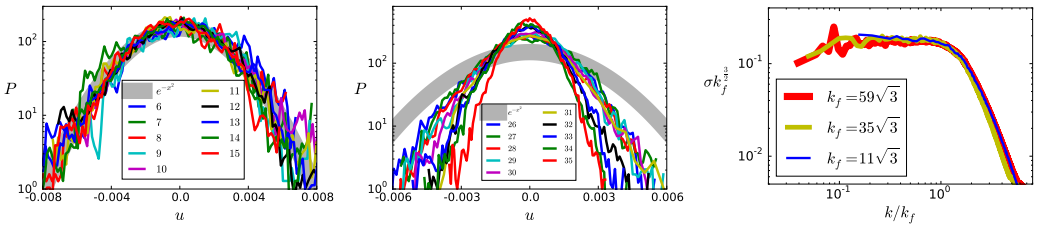

Figure 9.9 – PDF of modes of Taylor-Green symmetric DNS of the forced Navier-Stokes equation with a forcing wavenumber at $k_f = 11\sqrt{3}$. Left) PDF of even modes with one degree of freedom above the forcing scale. Center) PDF of even modes with one degree of freedom below the forcing scale. Right) Standard deviation of the velocity modes.

of freedom in the six planes $k_x \in \{0; 1\}$, $k_y \in \{0; 1\}$ or $k_z \in \{0; 1\}$. These PDFs have a clear Gaussian behavior as highlighted by their parabolic shape on the semi-logarithmic plot in the left and center panel of fig. 9.9. The data sets in the left panel, representing modes, collapse on the same curve, which indicates that their standard deviation is identical. The center panel represents modes smaller than the forcing wavenumber. In this panel, the PDF becomes narrower as the wavenumber increases. These two trends are also observed in the right panel of fig. 9.9, where the standard deviation of the PDFs are represented for different forcing scales. In the right panel of fig. 9.9, the standard deviations, σ, are compensated by a factor $k_f^{3/2}$ to take into account that the total energy is spread out on more modes as the forcing wavenumber increases. The wavenumber is also rescaled by the forcing wavenumber in order to compare the results. Using this scaling, the data sets at different resolutions collapse on the same curve. At large scales, the compensated standard deviation plateaus, indicating an analogue of the equipartition in energy of absolute equilibrium without helicity $\mathcal{K}r = 0$. Below the forcing scale, the standard deviation rapidly decreases because of the forward cascade and viscosity.

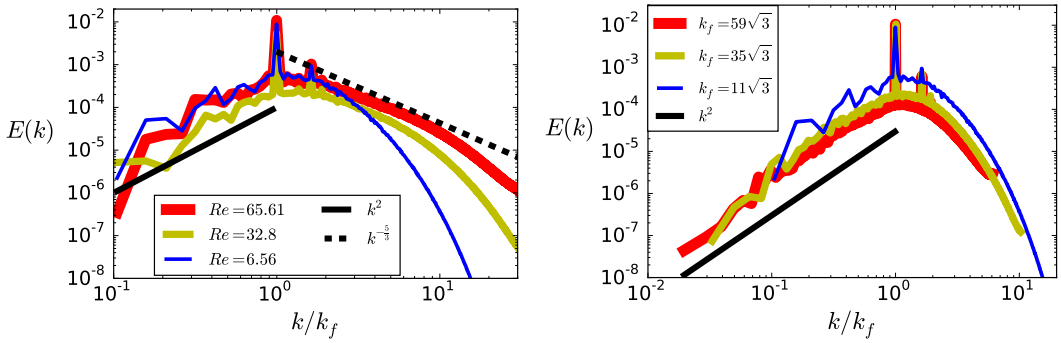

Figure 9.10 – Energy spectrum of Taylor-Green symmetric flows solutions of the forced Navier-Stokes equation. Left) Fixed forcing mode $k_f = 11\sqrt{3}$ at different Reynolds numbers $Re \in \{11\sqrt{3}; 35\sqrt{3}; 59\sqrt{3}\}$. Right) Fixed Reynolds number $Re = 6.56$ at different forcing modes $k_f \in \{11\sqrt{3}; 35\sqrt{3}; 59\sqrt{3}\}$.

Energy equipartition in the large scale modes can directly be observed in the right panel of fig. 9.9. It can also indirectly be observed in the energy spectrum presented in

fig. 9.10. Since energy shells contain a number of modes proportional to their surface, $4\pi k^2$, systems satisfying equipartition in energy should have an energy spectrum proportional to k^2. The spectra presented on both panels of fig. 9.10 are thus consistent with equipartition in energy. In left panel of fig. 9.10, the energy spectrum is presented at different Reynolds numbers for a fixed forcing wavenumber $k_f = 11\sqrt{3}$. At the biggest Reynolds number, the energy spectrum reaches the Kolmogorov's $k^{-5/3}$-scaling in the inertial range and has also the equipartition k^2-scaling in the thermalization domain. Even though Kolmogorov's scaling is not present in the other curves with smaller Reynolds numbers, the equipartition scaling law is still observable in the large scales. The smallest Reynolds number was then used to compute the DNS of the right panel of fig.9.10 where the wavenumber varies at fixed Reynolds number. The equipartition scaling of the energy spectrum can be observed on the three forcing wavenumbers used. The curve with the largest forcing scale, $k_f = 59\sqrt{3}$, shows that the energy spectrum follows a k^2-scaling for nearly two orders of magnitude.

We now turn to the temporal correlation of the flows presented in fig. 9.11. The left panel shows the dependence in viscosity of the correlation time for flows forced at $k_f = 11\sqrt{3}$. The correlations are computed using the algorithm presented in subsec. 9.2.2.2. In the small scales, the correlation time slowly decreases as viscosity decreases whereas the correlation time rapidly stabilizes on a k^{-1}-power law in the large scales. The major peak observed in the flow does not correspond to the forcing wavevector which is not located on the planes used to compute the correlation time. This peak corresponds to a harmonic of the forcing located in one of the planes used in the correlation time procedure. At low Reynolds number, the different harmonics of the forcing can be observed as a series of sharp peaks in the correlation time. At high Reynolds number, in the large scales, the correlation time aligns on a curve, which is consistent with the energy-based correlation time k^{-1}-scaling.

The k^{-1}-scaling law of the correlation time can be observed in the right panel of fig. 9.11 which shows the correlation time for TG flows with three scale separations $k_f = \{11\sqrt{3}; 35\sqrt{3}; 59\sqrt{3}\}$. The Reynolds number used in these DNS is based on the smallest viscosity used in the left panel of fig. 9.11. The correlation times for the three scale separations collapse on the k^{-1}-power law. The data at the largest forcing wavenumber $k_f = 59\sqrt{3}$ shows a trend which strongly agrees with the energy-based correlation time k^{-1}-scaling.

9.2.3.2 Helical flows: ABC flows

In order to study the impact of helicity on the velocity modes in large scales, DNS were carried out on general-periodic flows solutions of the NSE given at eq. (9.2) with an ABC forcing [15]

$$F_x^{ABC} = F_0(C \sin k_f z + B \cos k_f y) \tag{9.22}$$

$$F_y^{ABC} = F_0(A \sin k_f x + C \cos k_f z) \tag{9.23}$$

$$F_z^{ABC} = F_0(B \sin k_f y + A \cos k_f y)\,. \tag{9.24}$$

where F_0 is the intensity of the forcing. The three dimensionless parameters A, B and C were set to one to have an anisotropic flow. The main characteristic of ABC flows

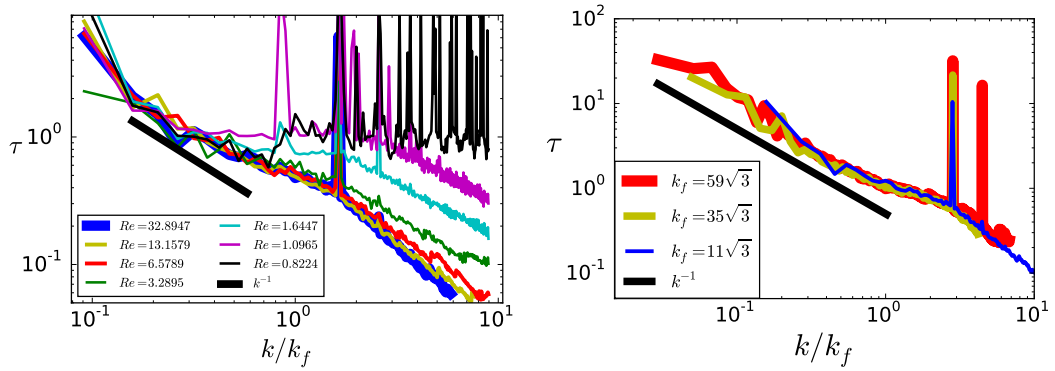

Figure 9.11 – Correlation time of Taylor-Green symmetric DNS of the forced Navier-Stokes equation. Left) Different Reynolds numbers at fixed forcing wavenumber $k_f = 11\sqrt{3}$. Right) Different forcing wavenumber $k_f \in \{11\sqrt{3}; 35\sqrt{3}; 59\sqrt{3}\}$ at fixed Reynolds number.

is their Beltrami property: $\boldsymbol{\nabla} \times F^{ABC} = k_f F^{ABC}$. This property makes them exact solutions of the TEE. All the ABC DNS presented are done at $k_f = 20$. A non-helical variant of the ABC forcing, that we will be referred to as the CBA forcing, can be built by switching the sine components of the ABC forcing to cosine components.

$$F_x^{CBA} = F_0(C\cos k_f z + B\cos k_f y) \tag{9.25}$$
$$F_y^{CBA} = F_0(A\cos k_f x + C\cos k_f z) \tag{9.26}$$
$$F_z^{CBA} = F_0(B\cos k_f y + A\cos k_f y)\,. \tag{9.27}$$

The CBA forcing has already been used as a non-helical reference of the ABC flow in [111]. At fixed coefficients, the CBA forcing has the same energy as the ABC forcing.

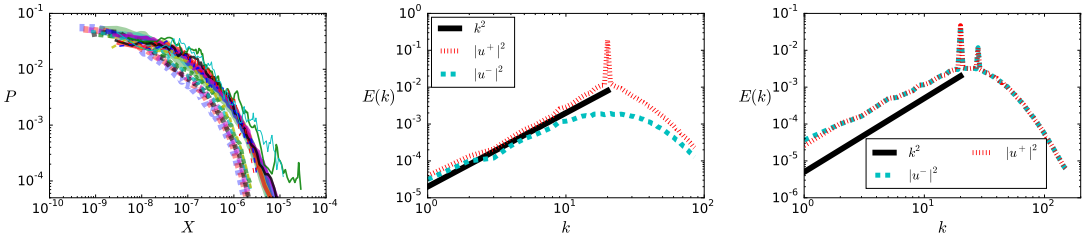

Figure 9.12 – Statistical characteristics of $[0;\pi]^3$-periodic DNS of the Navier-Stokes equation. Left) ABC forcing, PDF of modes before the forcing scale. The full lines represent the positive helical components of the velocity and the dashed lines represent the negative helical components of the velocity. Center) ABC forcing, energy spectrum of positive and negative helical components of the velocity. Right) CBA forcing, energy spectrum of positive and negative helical components of the velocity.

The PDFs of the positive and negative helical components of the modes in the large scales are presented in the left panel of fig. 9.12 for DNS of the NSE with an ABC forcing. The positive helical component of the velocity is represented with full lines and the negative helical component of velocity is represented with dashed lines. All PDFs display a plateau near zero and have an fast decay at high values. Because

general-periodic DNS do not reach the same scale separation and Reynolds number as TG symmetric DNS, the comparison with the χ^2_2-distribution is not as clear as in fig. 9.9. The PDFs of the two helical components do not have the same exponential tail as observed in absolute equilibrium solutions of the TEE. Since flows solutions of the NSE are not as helical as flows solutions of the TEE, the separation of the tail of the distributions is not as wide as in the case of absolute equilibrium solutions of the TEE. The center panel of fig. 9.12 represents the energy spectrum of the two helical components of DNS of the NSE with an ABC forcing. The positive helical component of the velocity has more energy than its negative counterpart, which is consistent with the separation of the tail of the distribution presented in right panel. Both components follow a k^2-scaling consistent with equipartition. In the large scales, the general features of the modes match the properties of absolute equilibrium solutions of the TEE. The right panel of fig. 9.12 represents the energy spectrum of the two helical components of DNS of the NSE with a CBA forcing. The energy spectrum is not as close to the k^2-scaling as the energy spectrum resulting from an ABC forcing. However, the energy spectrum of the non-helical TG symmetric flows, presented in the right panel of fig. 9.10, deviates from the k^2-scaling at the smallest scale separations. In the case of the CBA forcing, the spectrum deviates from the k^2-scaling characteristic of equipartition. However the convergence study carried out in the right panel of fig. 9.4 indicates that such a deviation can happen at small scale separations.

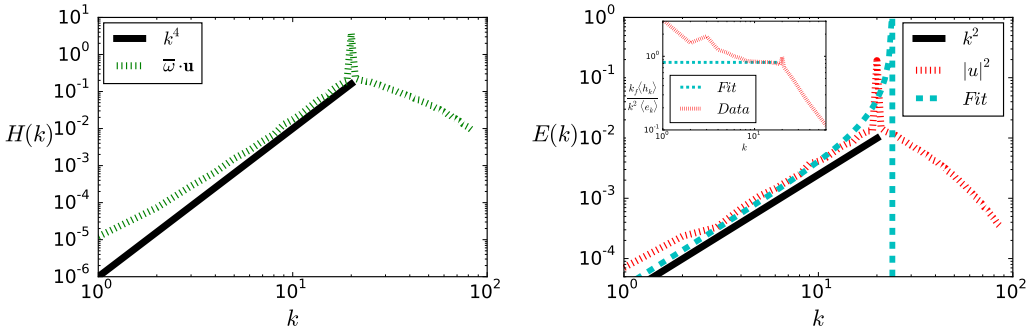

Figure 9.13 – Spectrum of $[0;\pi]^3$-periodic DNS of the Navier-Stokes equation with an ABC forcing. Left) Helicity spectrum in dotted line and the absolute equilibrium power law in full line. Right) Energy spectrum in dotted line with absolute equilibrium power law in full line and absolute equilibrium fit in dashed line. The insert represents $k_f\langle h_{\boldsymbol{k}}\rangle/(k^2\langle e_{\boldsymbol{k}}\rangle)$ and the asymptotic value used to make the absolute equilibrium fit.

The left panel of fig. 9.13 represents the helicity spectrum of a solution of the Navier-Stokes equation with an ABC forcing. In the scales slightly larger than the forcing scale, the helicity spectrum is in good agreement with the k^4-power law of the absolute equilibrium prediction. But in the largest scale, the helicity spectrum has a deviation from the k^4-power law.

To compare absolute equilibrium solutions of the TEE and the large scale modes of solutions of the NSE, we introduce an analogue of the Kraichnan number for the NSE. The equivalent of the maximal wavenumber k_M in the truncated Euler problem is assumed to be the forcing wavenumber k_f in the case of the NSE. Two expressions can be used to compute the local Kraichnan number: either $k_f\langle h_{\boldsymbol{k}}\rangle/(k^2\langle e_{\boldsymbol{k}}\rangle)$ coming

from eq. (9.10) or using eq. (9.11). Both expressions are equivalent and give the same numeric results presented in the insert of the right panel of fig. 9.13. The local Kraichnan number is not independent of the wavenumber and has an important peak in the large scales. As the wavenumber reaches the forcing wavenumber, the local Kraichnan number goes to a constant value equal to 0.83 . The result is consistent with the $|\mathcal{K}r| \leq 1$ bound of absolute equilibrium solutions. This asymptotic value is then used to plot the absolute equilibrium fit in the right panel of fig. 9.13. In the large scales, the data from the DNS is slightly above the fit, while the data is below the fit near the forcing wavenumber. The difference between the fit and the data near the forcing wavenumber can be related to the presence of the forcing. The difference found in the large scales could be related to finite size effects such as three-mode interaction with the forcing like in [86].

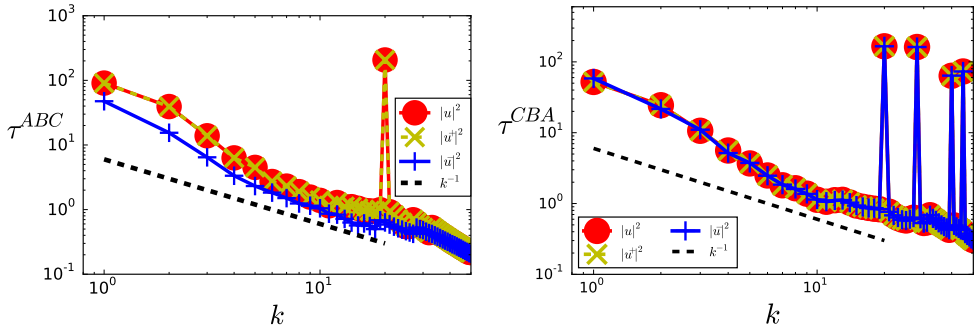

Figure 9.14 – Correlation time of $[0;\pi]^3$-periodic DNS of the Navier-Stokes equation. Left) ABC forcing. Right) CBA forcing.

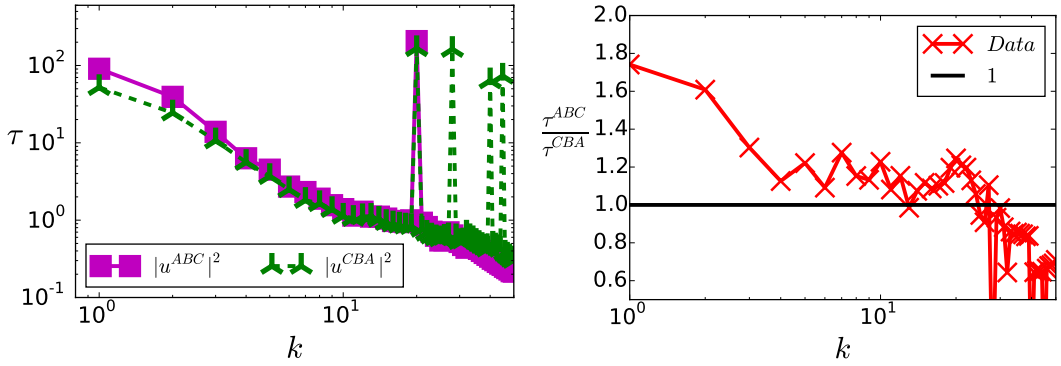

Figure 9.15 – Comparison of the correlation time of $[0;\pi]^3$-periodic DNS solutions of the Navier-Stokes equation forced with ABC and CBA forcings. Left) Energy spectrum. Right) Energy ratio.

The correlation time of DNS of the NSE with an ABC forcing increases in the large scales as shown in the left panel of fig. 9.14. In the inertial domain, the correlation time decreases as the wavenumber increases. These observations are consistent with the results coming for helical DNS of the TEE and the TG symmetric DNS of the NSE. However, the correlation time has some elements which did not appear in

helical DNS of the TEE presented in fig. 9.8. The correlation time of positive helical components of the velocity is always greater than its negative counterpart, especially in the large scales. This separation between the correlation time of the different helical components is not observed in the right panel of fig. 9.14 representing DNS of the NSE with a CBA. Contrary to the ABC forced flow, the correlation times of CBA forced flows exhibit a set of peaks in the inertial domain corresponding to harmonics of the forcing. For the ABC forcing and CBA forcing, the correlation time in the large scales deviates from the k^{-1}-power law observed in DNS of the TEE. However, for similar scale separations, the results form TG DNS also deviated from the k^{-1}-power law in the left panel of fig. 9.11. Fig. 9.15 compares the correlation times of the ABC forcing and CBA forcing. The correlation time of the two flows seems very close when observing the energy spectrum presented in the left panel. However, the ratio presented in the right panel shows that the correlation times of the helical ABC forcing are bigger than their non-helical CBA counterparts. The differences between the two correlation times reaches nearly twenty percents for all the wavenumbers smaller than the forcing wavenumber and is much more important in the two smallest shells in k.

9.3 Conclusion

In this study, we examined the temporal dynamic of absolute equilibrium solutions of the truncated Euler equation and compared them to the large scale modes of solutions of the Navier-Stokes equation.

We calculated the Eulerian parabolic auto-correlation time of velocity modes of absolute equilibrium solutions of the TEE. This calculation assumed that: i) the velocity modes are independent Gaussian variables, ii) the three-dimensional truncated Euler dynamical system is ergodic, and iii) the correlation time can be computed using a parabolic approximation of the correlation function at short times. For slightly helical flow, $|\mathcal{K}r| < 0.8$, the correlation time computed with the model follows an energy-based correlation time that decreases inversely proportionally to the wavenumber k^{-1}. On the other hand, when the flow is highly helical $|\mathcal{K}r| > 0.9$, the correlation time transition to a helicity-based correlation time $k^{-1/2}$ for intermediate wavenumbers for $(1 - \mathcal{K}r)\ln(1 - \mathcal{K}r) \ll k/k_M \ll 1$.

Using DNS of TG symmetric and general-periodic flows solutions of the TEE, we checked that their energy spectrum follows the laws predicted by the absolute equilibrium theory. We showed that the PDFs of the modes of velocity have the characteristics of Gaussian variables. We computed the Eulerian correlation function of the mode and confirmed that the short time parabolic approximation of the correlation time is valid. Finally, we identified an energy-based and helicity-based regime for the correlation time consistent with the prediction of the thermalization theory (see sec. 9.2.1).

Using non-helical TG symmetric DNS of the NSE, we showed that the velocity modes at large scales follow Gaussian distributions and that the standard deviations of the modes are consistent with equipartition. We also analyzed the correlation time and observed that the k^{-1} energy-based scaling could be observed on two decades, even for Reynolds numbers smaller than that required to observe Kolmogorov's $k^{-5/3}$-power

law in the inertial range. This is in agreement with thermal equilibrium at large scales.

To extend our analysis to helical flow, we performed DNS of general-periodic flows solutions of the NSE with helical ABC and non-helical CBA forcings at fixed wavenumber at $k_f = 20$. There is a agreement in the large scale spectrum with the thermal equilibrium prediction but the largest scales deviate significantly, being more energetic. Note that this deviation was also observed in [101].

The analysis of the correlation time of the ABC and CBA DNS showed a decrease at the large scales with the wavenumber as in thermalization theory. However, the correlation time deviates significantly from the energy-based k^{-1}-power law. Note a similar deviation is also observed in non-helical TG symmetric DNS at the smallest scale separation (see fig. 9.10).

As in thermalization theory, that predicts longer correlation times for the wavenumbers near k_M, the DNS of the helical flow also displayed longer correlation times than the non-helical flow. However, despite using a maximally helical forcing, the equivalent absolute equilibrium solution of the TEE would not generate enough helicity to have a helicity-based correlation time.

The reason that the largest scales of Navier-Stokes solutions deviate from absolute equilibrium remains an open question. Possible cause for this deviation left for other studies include: lack to universality with respect to forcing; lack of scale separation; insufficient Reynolds number ; finite-size effects *etc.*. Finally large scales instabilities may spoil the absolute equilibrium.

9.4 Appendix (description of new procedures)

9.4.1 Appendix: Correlation time – parabolic hypothesis

The derivation of the correlation time can be done using a projection operator to incompressible flows. However, this method is not able to assess the properties of the helical components of the velocity. In order to quantify these properties, the standard framework is the Craya-Herring helical basis [26, 27]. Within this decomposition, the TEE is expressed as

$$(\partial_t u_{\boldsymbol{k}}^{s_{\boldsymbol{k}}})^* = \sum_{\substack{\boldsymbol{k}+\boldsymbol{p}+\boldsymbol{q}=0 \\ s_{\boldsymbol{p}}\,,\, s_{\boldsymbol{q}}}} (s_{\boldsymbol{p}} p - s_{\boldsymbol{q}} q) \left(-\frac{1}{4} \boldsymbol{h}_{\boldsymbol{k}}^{s_{\boldsymbol{k}}} \cdot \boldsymbol{h}_{\boldsymbol{p}}^{s_{\boldsymbol{p}}} \times \boldsymbol{h}_{\boldsymbol{q}}^{s_{\boldsymbol{q}}} \right) u_{\boldsymbol{p}}^{s_{\boldsymbol{p}}} u_{\boldsymbol{q}}^{s_{\boldsymbol{q}}} \tag{9.28}$$

$$(\partial_t u_{\boldsymbol{k}}^{s_{\boldsymbol{k}}})^* = \sum_{\substack{\boldsymbol{k}+\boldsymbol{p}+\boldsymbol{q}=0 \\ s_{\boldsymbol{p}}\,,\, s_{\boldsymbol{q}}}} C_{\boldsymbol{kpq}}^{s_{\boldsymbol{k}} s_{\boldsymbol{p}} s_{\boldsymbol{q}}} u_{\boldsymbol{p}}^{s_{\boldsymbol{p}}} u_{\boldsymbol{q}}^{s_{\boldsymbol{q}}} \,, \tag{9.29}$$

where $s_{\boldsymbol{k}}$ denotes the sign of the helical component at mode $\boldsymbol{k}$, $u_{\boldsymbol{k}}^{s_{\boldsymbol{k}}}$ denotes the helical component of the velocity of sign $s_{\boldsymbol{k}}$ at mode $\boldsymbol{k}$ and $\boldsymbol{h}_{\boldsymbol{k}}^{s_{\boldsymbol{k}}}$ denotes the complex unitary helical vector of the Craya-Herring basis satisfying: $\boldsymbol{\nabla} \times \boldsymbol{h}_{\boldsymbol{k}}^{s_{\boldsymbol{k}}} = s_{\boldsymbol{k}} k \boldsymbol{h}_{\boldsymbol{k}}^{s_{\boldsymbol{k}}}$. The Craya-Herring tensor $C_{\boldsymbol{kpq}}^{s_{\boldsymbol{k}} s_{\boldsymbol{p}} s_{\boldsymbol{q}}}$ is symmetric on its last two variables: $C_{\boldsymbol{kpq}}^{s_{\boldsymbol{k}} s_{\boldsymbol{p}} s_{\boldsymbol{q}}} = C_{\boldsymbol{kqp}}^{s_{\boldsymbol{k}} s_{\boldsymbol{q}} s_{\boldsymbol{p}}}$, and also satisfies : $C_{\boldsymbol{kpp}}^{s_{\boldsymbol{k}} s_{\boldsymbol{p}} s_{\boldsymbol{p}}} = 0$. With the Craya-Herring helical decomposition, the average correlation of the temporal derivative of the velocity can be derived with the assumption that all helical components are independent Gaussian variables. The

derivation leads to

$$\langle|\partial_t \bar{u}_{\boldsymbol{k}}^{s_{\boldsymbol{k}}}|^2\rangle = \left\langle \sum_{\substack{\boldsymbol{k}+\boldsymbol{p}_1+\boldsymbol{q}_1=0 \\ s_{\boldsymbol{p}_1}\,,\,s_{\boldsymbol{q}_1}}} \sum_{\substack{\boldsymbol{k}+\boldsymbol{p}_2+\boldsymbol{q}_2=0 \\ s_{\boldsymbol{p}_2}\,,\,s_{\boldsymbol{q}_2}}} C_{\boldsymbol{k}\boldsymbol{p}_1\boldsymbol{q}_1}^{s_{\boldsymbol{k}} s_{\boldsymbol{p}_1} s_{\boldsymbol{q}_1}} u_{\boldsymbol{p}_1}^{s_{\boldsymbol{p}_1}} u_{\boldsymbol{q}_1}^{s_{\boldsymbol{q}_1}} \left[C_{\boldsymbol{k}\boldsymbol{p}_2\boldsymbol{q}_2}^{s_{\boldsymbol{k}} s_{\boldsymbol{p}_2} s_{\boldsymbol{q}_2}} u_{\boldsymbol{q}_2}^{s_{\boldsymbol{p}_2}} u_{\boldsymbol{q}_2}^{s_{\boldsymbol{p}_2}} \right]^* \right\rangle \tag{9.30}$$

$$= \sum_{s_1\,,\,s_2} \mathcal{S}^{s_1 s_2} \quad \text{where} \quad \mathcal{S}^{s_1 s_2} = \sum_{\substack{\boldsymbol{k}+\boldsymbol{p}+\boldsymbol{q}=0 \\ s_{\boldsymbol{p}}=s_1\,,\,s_{\boldsymbol{q}}=s_2}} 2 \left| C_{\boldsymbol{k}\boldsymbol{p}\boldsymbol{q}}^{s_{\boldsymbol{k}} s_{\boldsymbol{p}} s_{\boldsymbol{q}}} \right|^2 \langle e_{\boldsymbol{p}}^{s_{\boldsymbol{p}}} \rangle \langle e_{\boldsymbol{q}}^{s_{\boldsymbol{q}}} \rangle \,. \tag{9.31}$$

where $\mathcal{S}^{s_1 s_2}$ corresponds to the sum of the triadic interact of sign s_1 and s_2.

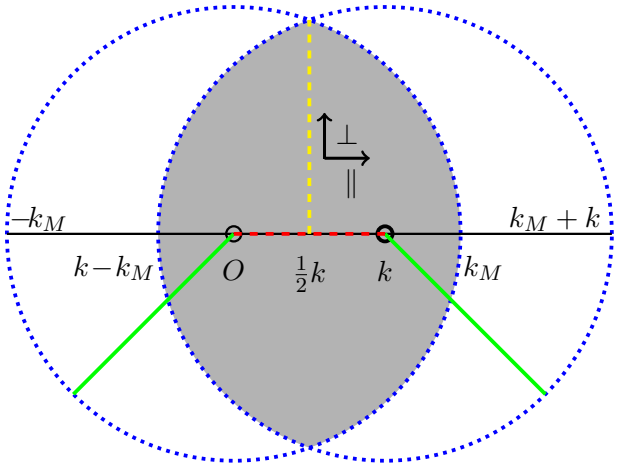

Figure 9.16 – Diagram of a cut of the integration domain. The dark surface corresponds to the integration domain. The dotted lines correspond to the limit of the circles of radius k_M and of center 0 or k. The thick full line corresponds to radii of the previously described circles. The dark dashed line corresponds to the distance between the center of the two circles. The bright dashed line corresponds to the maximal length possible for $q_\perp$.

In eq. (9.31), the truncation condition, $\boldsymbol{u}(k > k_M) = 0$, has not been applied to the velocity fields. The velocity appears in the equation within the expression of the average energy with two indices $\boldsymbol{p}$ and $\boldsymbol{q}$, therefore the summation must be done at $p \leq k_M$ and $q \leq k_M$. The domain prescribed by these conditions corresponds to the intersection of two spheres of radii k_M and center $\boldsymbol{p}$ and $\boldsymbol{q}$. The triadic condition, $\boldsymbol{k} + \boldsymbol{p} + \boldsymbol{q} = 0$, also implies that the summation over $\boldsymbol{p}$ and $\boldsymbol{q}$ can be done over $\boldsymbol{q}$ at fixed $\boldsymbol{p} = \boldsymbol{k} - \boldsymbol{q}$. The domain of summation is represented in fig. 9.16. This domain is invariant by rotation along the axis defined by $\boldsymbol{k}$ in fig. 9.16. The centers of the two spheres are also located on this direction. The coefficients of the sum in eq. (9.31) are unaffected by the rotation. The summation can thus be performed with the variables $q_\perp$ and $q_\parallel$ where $q_\perp$ is the projection of the wavevector along the plane orthogonal to $\boldsymbol{k}$ and $q_\parallel$ is the projection of the wavevector along the axis of rotation. Taking this new coordinate system, the derivation can be simplified by converting the discrete sum into an integral using the equivalence

$$\sum_{\boldsymbol{k}+\boldsymbol{p}+\boldsymbol{q}=0} \quad \Longleftrightarrow \quad \int_{-(1-\frac{1}{2}m)}^{1-\frac{1}{2}m} dq_\parallel \int_0^{1-\left(|q_\parallel|+\frac{1}{2}m\right)^2} \pi dq_\perp^2 \quad \text{where} \quad m = \frac{k}{k_M} \,. \tag{9.32}$$

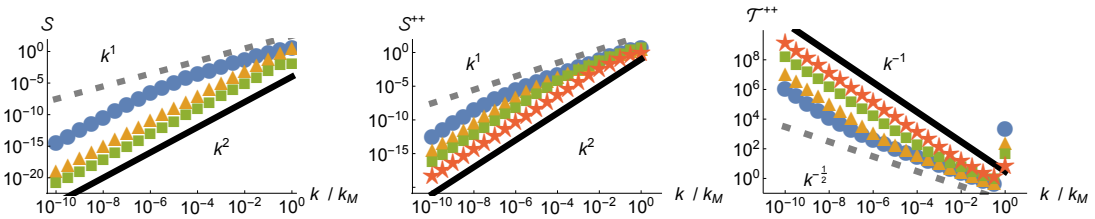

Figure 9.17 – Triadic interaction as a function of the wavenumber and associated correlation time. Left) At $\mathcal{K}r = 1 - 10^{-6}$, $\mathcal{S}^{--}$ plotted with squares, $\mathcal{S}^{+-}$ plotted with triangle, $\mathcal{S}^{++}$ plotted with discs, k^1 plotted with a dashed line, k^2 plotted with a full line. Center) $\mathcal{S}^{++}$ plotted at $\mathcal{K}r = 1 - 10^{-8}$ with discs, at $\mathcal{K}r = 1 - 10^{-6}$ with triangles, at $\mathcal{K}r = 1 - 10^{-2}$ with squares, at $\mathcal{K}r = 1 - 10^{-2}$ with stars, k^1 with a dashed line, k^2 with a full line. Right) $\mathcal{T}^{++}$ plotted at $\mathcal{K}r = 1 - 10^{-8}$ with discs, at $\mathcal{K}r = 1 - 10^{-6}$ with triangles, at $\mathcal{K}r = 1 - 10^{-2}$ with squares, at $\mathcal{K}r = 1 - 10^{-2}$ with stars, $k^{-\frac{1}{2}}$ with a dashed line, k^{-1} with a full line.

This integral can be computed exactly when $\mathcal{K}r = 0$ for $m \ll 1$. At $\mathcal{K}r = 0$, the total energy of the system is proportional to the inverse of α, $E = \frac{4\pi}{3} C_N \alpha^{-1}$, where C_N is a constant depending on the resolution. The parabolic correlation time can be expressed as

$$\tau_{\boldsymbol{k}}^{s_{\boldsymbol{k}}} = \sqrt{\frac{\langle e_{\boldsymbol{q}}^{s_{\boldsymbol{q}}} \rangle}{\langle |\partial_t \bar{u}_{\boldsymbol{k}}^{s_{\boldsymbol{k}}}|^2 \rangle}} = \sqrt{\frac{45\alpha}{112}} \frac{1}{k} = \sqrt{\frac{15\pi C_N}{14}} \frac{1}{k\sqrt{E_{tot}}} \,. \tag{9.33}$$

When $\mathcal{K}r = 0$, the correlation time follows the energy-based scaling-law.

When $\mathcal{K}r \neq 0$, the final integral can be computed using Mathematica for the different helical triadic interactions as shown in fig. 9.17 for highly helical flows. Instead of computing all the terms corresponding to all different possible triads in the sum, the graph shows the computation triad with different helical signs. The left plot of fig. 9.17 shows three possible sums: $\mathcal{S}^{++}$ plotted with discs, $\mathcal{S}^{+-}$ plotted with triangles and $\mathcal{S}^{--}$ plotted with squares. The $\mathcal{S}^{-+}$ sum has exactly the same values as the $\mathcal{S}^{+-}$ sum for symmetry reasons. The $\mathcal{S}^{++}$ sum dominates the other terms and has a k^1-scaling at large wavenumbers consistent with a helicity-based correlation time, and a k^2-scaling at small wavenumbers consistent with an energy-based correlation time. All other terms follow a k^2-scaling. The center plot of fig. 9.17 shows the evolution of the $\mathcal{S}^{++}$ for different Kraichnan numbers. As the Kraichnan number goes to one, the domain where the sum follows a k^2-scaling widens. The right plot of fig. 9.17 shows the evolution of the correlation time, $\mathcal{T}^{++}$, built using the sum $\mathcal{S}^{++}$. Its evolution is consistent with the evolution of the correlation time of the full velocity field presented in the left panel of fig. 9.1.

When the Kraichnan number goes to one, the *plus-plus* triadic interaction dominates the non-linear interaction in the TEE. Whether $m \ll \epsilon \ll 1$ or $\epsilon \ll m \ll 1$, the correlation time follows the asymptotic expression

$$\mathcal{S}^{++} = 2\pi k^2 \alpha^{-2} \frac{-2\ln\epsilon}{m - A\epsilon\ln\epsilon} \quad \text{with} \quad A = \frac{15}{8} \tag{9.34}$$

$$\text{thus} \quad \mathcal{T}^{++}(\boldsymbol{k}, s_{\boldsymbol{k}}) = \sqrt{\frac{\langle e_{\boldsymbol{k}}^{s_{\boldsymbol{k}}} \rangle}{\mathcal{S}^{++}}} = \sqrt{\frac{A(1-\mathcal{K}r) - \frac{k}{k_M \ln(1-\mathcal{K}r)}}{4\pi\alpha^{-1}k^2(1 - s_{\boldsymbol{k}}\mathcal{K}r\frac{k}{k_M})}} \,. \tag{9.35}$$

In the domain where $(1-\mathcal{K}r) \ll \frac{k}{k_M} \ll 1$, the correlation time follows a helicity-based scaling-law.

9.4.2 Appendix: Taylor Green properties

In addition to the condition listed below eq. (9.19), TG symmetries [107] impose that

$$u^y(k_x,k_y,k_z) = (-1)^{p+1}u_x(k_y,k_x,k_z) \tag{9.36}$$

$$\text{and} \quad u_z(k_x,k_y,k_z) = (-1)^{p+1}u_z(k_y,k_x,k_z)\,, \tag{9.37}$$

where p characterizes the parity of the mode: $p=1$ if k_x, k_y, k_z are all even and $p=0$ if k_x, k_y, k_z are all odd.

Since the flows studied are also incompressible, they also satisfy $\boldsymbol{\nabla}\cdot\boldsymbol{u}=0 \iff k_xu_x+k_yu_y+k_zu_z=0\,.$

In a few special cases, modes of TG symmetric flows depend on only one independent variable

- $k_x=k_y$ and $r=0$: $\boldsymbol{u}^{odd}(k_x,k_x,k_z) = (\boldsymbol{e}_x-\boldsymbol{e}_y)\psi_0(k_x,k_z)$, where ψ_0 is a real field.
- $k_x=k_y$ and $r=1$: $\boldsymbol{u}^{even}(k_x,k_x,k_z) = (k_z(\boldsymbol{e}_x+\boldsymbol{e}_y)-(k_x+k_y)\boldsymbol{e}_z)\psi_1(k_x,k_x,k_z)$, where ψ_1 is a real field.
- $k_x=0$: $\boldsymbol{u}(0,k_y,k_z) = (k_z\boldsymbol{e}_y-k_y\boldsymbol{e}_z)\psi_2(k_y,k_z)$, where ψ_2 is a real field.
- $k_y=0$: $\boldsymbol{u}(k_x,0,k_z) = (k_z\boldsymbol{e}_x-k_y\boldsymbol{e}_z)\psi_3(k_x,k_z)$, where ψ_3 is a real field.
- $k_z=0$: $\boldsymbol{u}(k_x,k_y,0) = (k_y\boldsymbol{e}_x-k_x\boldsymbol{e}_y)\psi_4(k_x,k_y)$, where ψ_4 is a real field satisfying $\psi_4(k_y,k_x)=-\psi_4(k_x,k_y)$.

The vectors $\boldsymbol{e}_\alpha$ with $\alpha\in\{x;y;z\}$ denote the directions of the Cartesian basis.

In the other cases, the TG symmetric modes of flows only depend on two independent variables – $\phi(k_x,k_y,k_z)$ and $\phi(k_y,k_x,k_z)$, where ϕ is a real field – and can be written as

$$\boldsymbol{u_k} = (k_z\boldsymbol{e}_x-k_x\boldsymbol{e}_z)\phi(k_x,k_y,k_z)+(-1)^{p+1}(k_z\boldsymbol{e}_y-k_y\boldsymbol{e}_z)\phi(k_y,k_x,k_z)\,. \tag{9.38}$$

9.4.3 Appendix: Chi-squared distribution

A Gaussian distribution of average μ and standard derivation σ has a probability density function defined by

$$G(X|\mu,\sigma) = \frac{1}{\sqrt{2\sigma^2\pi}}\,e^{-\frac{(X-\mu)^2}{2\sigma^2}}\,. \tag{9.39}$$

Chi-squared distributions are defined using g independent Gaussian variables. Let $(G_i)_{i\in[\![1;g]\!]}$ be independent, centered ($\mu=0$), reduced ($\sigma=1$) Gaussian variables. The sum of their squares, $X=\sum_{i=1}^{g}G_i^2$, is distributed according to the chi-squared distribution with g degrees of freedom denoted as χ^2_g and defined by

$$\chi^2_g(X) = \frac{1}{2^{\frac{g}{2}}\Gamma_{Euler}(\frac{g}{2})}X^{\frac{g}{2}-1}e^{-\frac{X}{2}}\,. \tag{9.40}$$

where Γ_{Euler} denotes Euler's Gamma function. The power law of the probability density function at small X gives the number of degrees of freedom of the system, and the exponential fit at large X validates the Gaussian decay of the probability density function.

$$\log \chi_g^2(X) \underset{X\to 0}{=} \left(\frac{g}{2}-1\right)\log(X) \quad \text{thus} \quad g \underset{X\to 0}{=} 2\left(\frac{\log \chi_g^2(X)}{\log(X)}+1\right) \tag{9.41}$$

9.4.4 Appendix: Computation of the correlation time

In order to produce spatio-temporal spectrum, the velocity field is outputted at a regular time interval. These outputs form a data set of the velocity field in the $\boldsymbol{k}-t$ space. However, keeping in memory the entire N^3 DNS, N being the resolution, is too demanding in computational memory. To reduce the volume of the data set without loosing the properties of the different modes, only the six planes – $k_x = \{0;1\}$, $k_y = \{0;1\}$ and $k_z = \{0;1\}$ – are outputted for the TG symmetric TYGRE code and only the three planes – $k_x = 0$, $k_y = 0$ and $k_z = 0$ – are outputted for the general-periodic GHOST code. The velocity time series are then multiplied by an apodization function [100] and Fourier-transformed to form a data set in the $\boldsymbol{k}-\omega$ space. The power spectrum $s(\boldsymbol{k},\omega)$ is then computed by taking the modulus square of the velocity and summing over the different Cartesian directions. The isotropic power spectrum $S(k,\omega)$ is computed by summing the power spectrum over the modes of same wavenumber. A binning of spacing of one is used to compute the isotropic power spectrum. The closest integer smaller than $k+\frac{1}{2}$ is used to define the bin number. The left panel of fig. 9.4 represents the power spectrum of a truncated Euler DNS computed using this method. The correlation function $\Gamma(k,t)$ is then computed using Wiener-Khinchin theorem by performing a Fourier-transform of the isotropic power spectrum and normalizing the function. The right panel of fig. 9.4 represents the correlation function of a truncated Euler DNS computed using this method.

Finally, the correlation time can be computed by doing a fit of the correlation function in a well-resolved domain as shown in the left panel of fig. 9.5. The time where the correlation function reaches half-height, $\tau_{\frac{1}{2}}$, can be evaluated numerically. We then defined the correlation time using a Poisson normalization of the half-height time $\tau = \tau_{\frac{1}{2}}/\ln(2)$. The same algorithm can be used to find the correlation function of the positive and negative helical modes of the velocity field using eq. (9.11). The steps of the procedure are summed up in the algorithm presented below.

Require: $\boldsymbol{u}(\boldsymbol{k}, n\Delta t)$, n, Δt,
1: $\boldsymbol{u}(\boldsymbol{k},\omega) = D\mathcal{F}[apo\boldsymbol{u}(\boldsymbol{k},n\Delta t)](\omega)$
2: $s(\boldsymbol{k},\omega) = \sum_i |\boldsymbol{u}_i(\boldsymbol{k},\omega)|^2$
3: $S(k,\omega) = \sum_{\boldsymbol{k}} \mathbb{1}_k s(\boldsymbol{k},\omega)$
4: $\gamma(k,t) = D\mathcal{F}^{-1}[S(k,\omega)](t)$
5: $\Gamma(k,t) = \gamma(k,t)/\gamma(k,0)$
6: $\tau(k) = Solve[t,\Gamma(k,t),1/2]$

Algorithm to compute the correlation time. $D\mathcal{F}$ denotes the discrete Fourier-transform, $D\mathcal{F}^{-1}$ denotes the discrete inverse Fourier-transform, $\mathbb{1}$ denotes the characteristic function satisfying $\mathbb{1}(bool) = 1$ if $(k-\frac{1}{2} < |\boldsymbol{k}| \leq k+\frac{1}{2})$ and 0 otherwise, $apo(n,\Delta t)$ denotes an apodization function and $Solve[t,\Gamma(k,t),1/2]$ denotes a function that finds the smallest positive t satisfying $\Gamma(k,t) = 1/2$.

Part D

Conclusion

Conclusion

This manuscript studied some aspects of flows forced in the large scales at moderate and high Reynolds numbers. It has also used the analogy between the magnetic alpha-effect and the anisotropic kinetic alpha-effect to quantify the energy located in the large scales of the instability before the threshold of the small scale instabilities and during its moderate Reynolds number development.

At moderate Reynolds number, our study has shown that the AKA-effect can be observed using Floquet analysis. It has also been shown that the AKA-effect still occurs at Reynolds numbers of order unity, which goes beyond the small Reynolds number limit in which the theory is established.

AKA-stable flows like the well-documented ABC flow and the Roberts flow have been proven to be unstable in the large scales. For the Roberts flow, the instability can be described with a simplified model considering three modes of the flow: (i) the forcing mode of wavenumber K, (ii) the large scale mode of wavenumber q and (iii) the coupling mode at wavenumber $K \pm q$. The large scale instability generated by the ABC and the Robert flow has been shown to be a second-order instability. Indeed, the growth rate of an AKA-instability is proportional to scale separation q/K, whereas the ABC and Roberts flows have an instability with a growth rate proportional to $(q/K)^2$. Because of the scaling law of the growth rate of the effect, the large scale instability of the ABC and Roberts flows can be viewed as negative eddy viscosity instabilities.

Floquet analysis has also allowed the characterization of the energy in the large scales of the instability compared with the total energy. The large scale energy to total energy ratio reported in the DNS results can be interpreted with a linear two-mode model. At low Reynolds number, the large scale energy to total energy ratio has been shown to be close to unity, which indicates that the energy is concentrated in the large scales. After the small scale instability threshold, the energy has a small projection to the large scales and the growth rate of the instability is governed by the growth rate of the small scale instability.

The same Floquet analysis method has also been used to characterize magnetic fields undergoing an alpha-effect. At low magnetic Reynolds number, it has been shown that the energy of the magnetic field is located in the large scale and the growth rate depends on the scale separation between the large scale and the forcing scale. After the small scale instability threshold, it has been shown that the energy has a small projection in the large scales and the growth rate of the instability is governed by the dynamic in the small scales. This analysis of magnetic instabilities indicates that the growth rate of the large scale instability at high magnetic Reynolds number cannot be directly related to the dynamic of the magnetic field at low magnetic Reynolds number.

Once the small scale instability occurs, the description of the large scale magnetic field must adopt an expression which takes into account the impact of the small scales.

At large Reynolds number, our study has shown that the large scale modes of a flow forced in the small scale has a dynamics close to that of solutions the truncated Euler equation as proposed in [10]. Two main criteria have been used to show the similarities between the two systems: (i) the energy spectrum, (ii) the auto-correlation time.

Concerning the truncated Euler system, our study has shown that the correlation time of the helical modes of the velocity are proportional to the inverse of the wavenumber, $\tau^E \propto 1/(k\sqrt{E})$, where E denotes the energy of the flow. This energy-based scaling law was shown to be valid when the flow is not too helical. When the flow is highly helical the auto-correlation time is proportional to the inverse of the square root of the wavenumber, $\tau^H \propto 1/(k\sqrt{H})$, where H denotes the helicity of the flow. These correlation times have been confirmed with DNS and a thermodynamic model using the parabolic approximation of the correlation function to compute the correlation time.

In the case of the forced Navier-Stokes system, our study has shown that in the large Reynolds number, the DNS of Taylor-Green symmetric flows forced in the small scales have a spectrum and a correlation time similar to that of truncated Euler system. Flows without the Taylor-Green symmetries have also been tested but the Reynolds number was not sufficiently high to observe all the properties of statistical equilibrium. However, general-periodic flows were able to highlight the impact of helicity on the correlation. Even though no change in power law could be observed because the forcing could not inject enough helicity, the helical forced flow had a correlation time bigger than the non-helical forced flow by 20% in average.

Many properties are still waiting to be characterized in the large scale modes of forced velocity fields. The way the energy is transferred to the large scales at high Reynolds numbers has still not be investigated. The transition between moderate Reynolds instabilities and high Reynolds statistically stationary solutions is still unclear. The interaction between the $k^{-\frac{3}{5}}$-Kolmogorov scaling and the large scale mode has not been quantified for the moment. Even if ABC flows are highly helical at small Reynolds number, it has not been proven that ABC forcing is the most efficient to generate a helical flow at large Reynolds number. If more helical force fields exist, it would be interesting to check if their correlation time can generate a correlation time based on helicity. On a more experimental point of view, the easiest correlation functions that can be measured are two-point correlation function. To get an experimental confirmation of the time correlation properties, the relations derived for the correlation of velocity modes should be related to two-point correlation functions.

Part E

Numerical methods

Table of Contents

Chapter 10

Elements of context: Numeric methods

The aim of this chapter is to present the pseudo-spectral numerical method used to integrate the evolution equation of fluids and introduce semi-Lagrangian schemes.

This chapter reviews elements of well-documented theories.

10.1 Pseudo-spectral methods (review)

Since the analytic results of the Navier-Stokes equation are limited, numeric methods are used to compute properties on the solutions of the equation. As described in [21], two geometries are favored to solve the Navier-Stokes equation: the entire physical space $\mathbb{R}^3$ or the $[0;2\pi]^3$-periodic box. Flows in both geometries do not have boundary-related interferences since the borders of the system are either at infinity or do not exist because of the periodicity. Even though no fluid exists in either geometries, these geometries are able to mimic what happens in the bulk of a fluid and have been able to give good predictions on the motion of fluid like the already mentioned Kolmogorov's 4/5-law. Luckily for numeric computation, modeling the $[0;2\pi]^3$-periodic box can be done with reasonable computation power. Many methods can be used to solve the Navier-Stokes equation, but spectral methods stand out of the list because they have exponential convergence compared to the algebraic convergence of finite differences, finite volumes and finite elements methods. A way to illustrate the converge rate of spectral methods [112] is to consider the solutions of the heat equation

$$\partial_t \theta = \kappa \Delta \theta \quad \text{with} \quad \theta(t=0) = \Theta \quad \text{thus} \quad \theta(t) = \sum_{\boldsymbol{k}} \Theta_{\boldsymbol{k}} e^{-\kappa k^2 t + \imath \boldsymbol{k} \boldsymbol{r}} \,, \tag{10.1}$$

where θ, $\Theta_{\boldsymbol{k}}$ and κ denote the temperature field, its Fourier coefficient at the wavevector $\boldsymbol{k}$ and the thermal diffusivity. Using a Fourier spectral method with a k_M spherical truncation, the spectral numeric solution, $\theta^{sp}(t)$, will only describe the solution for modes with wavenumber below the truncation wavenumber. The error between the spectral solution and the analytic solution will be proportional to an exponential of the truncation wavenumber

$$\|\theta^{sp} - \theta\| \propto \Theta_{k_M} e^{-\kappa (k_M + \Delta k)^2 t} \,, \tag{10.2}$$

where Δk denotes the wavenumber stepping increment. This expression of the error is valid after the relaxation of the greatest mode of the Fourier decomposition. The large modes will relax at large times, *i.e.* when $t \gg \frac{1}{\kappa k_M \Delta k}$. The type of norm used to evaluate the error is not important since numeric simulations are done with a finite resolution.

Non-spectral numeric methods have an algebraic error whose order depends on the method. For instance, the first neighbor-centered finite differences method has a second-order error

$$\mathtt{d}^2_{\mathtt{xx}}\theta_x = \frac{\theta_{x+\Delta x} - 2\theta_x + \theta_{x-\Delta x}}{(\Delta x)^2} = \partial^2_{xx}\theta_x + \frac{(\Delta x)^2}{12}\partial^4_{xx}\theta_x + \mathcal{O}\left((\Delta x)^4\right) , \tag{10.3}$$

where $\mathtt{d}^2_{\mathtt{xx}}\theta$, Δx and $\partial^2_{xx}\theta$ denote the discrete Laplacian in one dimension, the spacial stepping increment and the continuous Laplacian in one dimension respectively. The error made by the discrete method is of order two in space

$$\left\| \mathtt{d}^2_{\mathtt{xx}}\theta - \partial^2_{xx}\theta \right\| \propto (\Delta x)^2 \left\| \partial^4_{xx}\theta \right\| \quad \text{where} \quad \Delta x \sim 1/\Delta k\,. \tag{10.4}$$

At large time, spectral methods converge faster than non-spectral methods. However, they should not always be favored over other methods. When the field has strong gradients, the spectral transform generates important small scales modes. The truncated expansion strongly deviates from the initial field because an important part of the information concerning fields has been discarded. This effect is known as the Gibbs phenomenon. As a result, Godunov methods are often preferred to spectral methods when shocks arise.

Errors can also be introduced in the numeric resolution because of the discretization of the time derivative. The standard method to reduce the order of the temporal error is the Runge-Kutta algorithm [113]. As the order of the method increases, the algorithm makes more intermediate iterations within a time-step to interpolate more precisely the field at the next increment of time. Runge-Kutta method cannot integrate any time-stepping. The time-stepping increment has to satisfy the Courant-Friedrichs-Lewy (CFL) condition detailed in sec. 10.2, otherwise the algorithm is unstable.

Besides their convergence rate, spectral methods are also highly efficient at solving the Poisson equation given at eq. (1.2). Inverting a Laplacian in Fourier space is done by dividing every mode by the square of the wavenumber. However, spectral methods have one major drawback. Integrating the non-linear term corresponding to transport requires to compute a Cauchy product, which has an important numeric complexity going in $\mathcal{O}(N^2)$ compared to the $\mathcal{O}(N)$ complexity for the other operations. In order to avoid this computation, an altered version of the spectral methods called the pseudo-spectral method computes the non-linear term in the physical space. At each time-step, pseudo-spectral methods: (i) compute the non-linear term, (ii) transform the data in spectral space, (iii) compute the linear term in spectral space and (iv) transform the data back to physical space. The efficiency of the pseudo-spectral method relies on the Fast Fourier Transform algorithm [114] which is much faster than computing a Cauchy product with a $\mathcal{O}(N \ln N)$ complexity. Fig. 10.1 represents the main steps of the pseudo-spectral method. The first "for" loop at line 3 increases at every time-step. The second "for" loop at line 6 increases at every step of the Runge-Kutta method.

Require: T, Δt, ν, RK, $c_{RK}(p)$, $\boldsymbol{F}(\boldsymbol{k}, n\Delta t)$, $\boldsymbol{u}^0(\boldsymbol{r})$
1: $\boldsymbol{U}_0(\boldsymbol{r}) = \boldsymbol{u}^0(\boldsymbol{r})$
2: $\boldsymbol{U}_1(\boldsymbol{k}) = \mathcal{F}[\boldsymbol{u}(\boldsymbol{r})]$
3: **for** $1 \leq n \leq T$ **do**
4: $\quad\boldsymbol{U}_2(\boldsymbol{r}) = \boldsymbol{U}_0(\boldsymbol{r})$
5: $\quad\boldsymbol{U}_3(\boldsymbol{k}) = \boldsymbol{U}_1(\boldsymbol{k})$
6: $\quad$**for** $1 \leq p \leq RK$ **do**
7: $\quad\quad\boldsymbol{U}_4(\boldsymbol{k}) = \imath\boldsymbol{k}\times\boldsymbol{U}_3(\boldsymbol{k})$
8: $\quad\quad\boldsymbol{U}_5(\boldsymbol{r}) = \mathcal{F}^{-1}[\boldsymbol{U}_4(\boldsymbol{k})]$
9: $\quad\quad\boldsymbol{U}_6(\boldsymbol{r}) = \boldsymbol{U}_2(\boldsymbol{r})\times\boldsymbol{U}_5(\boldsymbol{r})$
10: $\quad\quad\boldsymbol{U}_7(\boldsymbol{k}) = \mathcal{F}[\boldsymbol{U}_6(\boldsymbol{r})]$
11: $\quad\quad\boldsymbol{U}_8(\boldsymbol{k}) = \boldsymbol{U}_7(\boldsymbol{k}) - (\boldsymbol{k}\cdot\boldsymbol{U}_7(\boldsymbol{k}))\boldsymbol{k}$
12: $\quad\quad\boldsymbol{U}_9(\boldsymbol{k}) = \boldsymbol{U}_1(\boldsymbol{k}) + c_{RK}(p)\Delta t\left(\boldsymbol{U}_8(\boldsymbol{k}) - \nu k^2\boldsymbol{U}_3(\boldsymbol{k}) + \boldsymbol{F}(\boldsymbol{k}, n\Delta t)\right)$
13: $\quad\quad\boldsymbol{U}_3(\boldsymbol{k}) = \boldsymbol{U}_9(\boldsymbol{k})$
14: $\quad\quad\boldsymbol{U}_2(\boldsymbol{r}) = \mathcal{F}^{-1}[\boldsymbol{U}_3(\boldsymbol{k})]$
15: $\quad$**end for**
16: $\quad\boldsymbol{U}_1(\boldsymbol{r}) = \boldsymbol{U}_3(\boldsymbol{k})$
17: $\quad\boldsymbol{U}_0(\boldsymbol{r}) = \boldsymbol{U}_2(\boldsymbol{r})$
18: $\quad\boldsymbol{u}^n(\boldsymbol{r}) = \boldsymbol{U}_0(\boldsymbol{r})$
19: **end for**

Figure 10.1 – Pseudo-spectral algorithm to solve the Navier-Stokes equation in a $[0; 2\pi]^3$-periodic box. T, Δt, ν, RK, $c_{RK}(p)$, $\boldsymbol{F}(\boldsymbol{k}, t\Delta t)$, $\boldsymbol{u}^0(\boldsymbol{r})$ denote the total number of iterations, the time increment, the viscosity, the order of the Runge-Kutta method, the coefficient of the Runge-Kutta method, the forcing field and the initial velocity field respectively. The variables starting with the character $\boldsymbol{U}$ are auxiliary vector fields.

The variables starting with the character $\boldsymbol{U}$ are auxiliary variables. Their number can be reduced to limit the memory use.

The computation of the non-linear term, line 9 in fig. 10.1, has to be carried out with caution. Fields cannot be sampled at every wavenumber, otherwise modes can overlap and the information is then distorted because of aliasing as highlighted in fig. 10.2. If the field is sampled over N wavenumbers, the plane-wave $e^{2\imath\pi\frac{P}{N}}$ of index P is the same as the plane-wave $e^{2\imath\pi\frac{p}{N}}$ of index $p = P - N$ because of the periodicity of complex exponentials. The non-linear coupling of two modes of indices P and Q forces the mode at index $P + Q$. The forced mode should not correspond to another mode whose index is smaller in absolute value. In order to suppress aliasing, the non-linear effect should not be computed for indices above $N/3$.

This numeric method is implemented in the code GHOST [53, 52] which was used to carry out the direct numeric simulations (DNS) in [86] and sec. 9. The TYGRES code was also used in the Taylor-Green symmetric DNS done in sec. 9. As shown in [105, 107] Taylor-Green symmetric flows can be decomposed into modes with only odd components or only even components. When a Taylor-Green DNS is carried out with a N^3 resolution, there are in fact only $(N/2)^3$ odd components and $(N/2)^3$ even components to compute. Computing an apparent N^3 Taylor-Green DNS can thus be

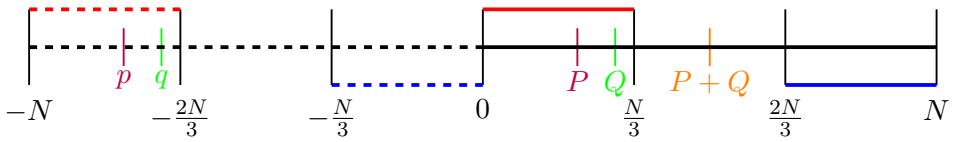

Figure 10.2 – Description of modes of a system truncated at $N/3$ to prevent aliasing. Lines of the same color represent indices describing the same plane-wave. The modes modeled in the numeric simulation are represented by full lines. The modes represented with dashed lines are related to the other modes via the periodicity of complex exponentials.

done with a $2(N/2)^3$ machine resolution. This increase of efficiency can only be done because the odd and even separation of Taylor-Green modes is compatible with the Fast Fourier Transform algorithm.

10.2 Semi-Lagrangian methods (review)

Semi-Lagrangian methods have been introduced to solve in general case the advection equation

$$D_t\Phi = \partial_t\Phi + u(x)\partial_x\Phi = 0\,. \tag{10.5}$$

where Φ and u denote a passive scalar field and the velocity of the flow. If the velocity of the flow is constant, the solutions of the problem are function of $x-ut$ respecting the boundary conditions. In the case of periodic boundary conditions, Fourier transform can be used to solve the problem using

$$\partial_t\Phi_k = -iku\Phi_k \quad \text{thus} \quad \Phi_k(t) = e^{-ikut}\Phi_k(t=0)\,. \tag{10.6}$$

However, when the velocity depends on space, computing the transport term in Fourier space is highly inefficient because it requires to compute a Cauchy product. As described in sec. 10.1, to carry out the computation faster, the pseudo-spectral method computes the non-linear term in physical space.

In order to understand the limitation of the computation of the non-linear term in physical space, let us solve the problem using finite differences for a constant positive velocity $u > 0$. The simplest finite difference stable scheme to solve the advection equation is the Upwind scheme because it uses the upwind values of the passive scalar to compute the spatial derivative. Indeed, the Upwind scheme uses the following temporal scheme

$$\Phi(x,t+\Delta t) = \Phi(x,t) - C_{CFL}\left(\Phi(x,t) - \Phi(x-\Delta x,t)\right) \quad \text{with} \quad C_{CFL} = \frac{u\Delta t}{\Delta x} \tag{10.7}$$

where Δt and Δx denote the time-step and the spatial-step respectively. The constant C_{CFL} is the Courant-Friedrichs-Lewy (CFL) number [115]. The CFL number is dimensionless and is used to determine if the flow is stable.

The stability of the Upwind scheme can be tested by applying a Fourier perturbation $\phi_k(t)e^{ikx}$ on the passive scalar. The growth factor of the perturbation after a

temporal iteration is given by

$$\xi(x, \Delta t) = \frac{\phi_k(t + \Delta t)}{\phi_k(t)} = (1 - C_{CFL}) + C_{CFL} e^{-ik\Delta x} . \tag{10.8}$$

In order to have a stable scheme, all Fourier perturbations should be damped. The growth factor must be smaller than one in modulus $|\xi(x, \Delta t)| < 1$. This stability condition is satisfied for CFL numbers less then one, $C_{CFL} < 1$. For varying velocities, the CFL number depends on the position. The stability condition can be extended by imposing the CFL number to be smaller than one everywhere, which is equivalent to replacing the velocity by its maximum in the expression of the CFL number. The stability condition can therefore be expressed as $\frac{\Delta t \max |u|}{\Delta x} < 1$.

The stability condition of a flow following the Navier-Stokes equation is related to the CFL number, but the diffusive term and the non-linearity can also perturb the numeric scheme. Doing a full numeric stability analysis of a scheme modeling the Navier-Stokes is not easy. In most numeric simulation, the time-step is chosen such that $\frac{\Delta t \max |u|}{\Delta x} < 0.5$ and convergence tests are performed to validate the stepping used.

Semi-Lagrangian schemes are able to go beyond the stability criteria by following the evolution of the passive scalar on a characteristic of the flow. The denomination of semi-Lagrangian results from the steps used to carry out the temporal evolution. The passive scalar field is first advected like a Lagrangian particle and is then reconstructed on the Eulerian grid.

The method can be illustrated using the constant velocity Upwind scheme presented in eq. (10.7). If the CFL number is greater than one, the scheme is unstable to perturbation. However, if the passive scalar is known at regular grid points, the passive scalar field can be translated using the property that the solution of the advection equation can be expressed as a function of $x - ut$. For instance, if the CFL satisfies $C_{CFL} = C_0 + C_1$ with $C_0 \in \mathbb{N}$ and $0 \leq C_1 < 1$, the evolution of the fields can be viewed as a translation of $C_0 \Delta x$ followed by an advection with a CFL number of C_1. The following semi-Lagrangian scheme is able to model the advection equation at a CFL number of $C_0 + C_1$ without becoming unstable

$$\Phi(x, t + \Delta t) = \Phi(x - C_0 \Delta x, t) - C_1 \left(\Phi(x - C_0 \Delta x, t) - \Phi(x - C_0(\Delta x + 1), t)\right) . \tag{10.9}$$

If $C_1 = 0$, the scheme returns the $\Phi(x, t+\Delta t) = \Phi(x - u\Delta t, t)$, which is an application of the expression of the solutions as a function of $x - ct$. The stability analysis performed in eq. (10.8) can be carried out on this scheme and gives the stability condition $C_1 < 1$.

In the more general case where the velocity field is not constant, the computation of the translation distance defined by $(C_0 + C_1)\Delta x$ has to be replaced by the translation of the distance traveled by the flow following the characteristic during the time interval Δt. At a given position x, this distance $\ell(x(t), t, \Delta t)$ of translation can be expressed as $\ell(x(t), t, \Delta t) = \int_0^{\Delta t} u(x(t), t) dt$. If the velocity field does not vary on the characteristic, the translation distance can be approximated by $\ell(x, t, \Delta t) \simeq \Delta t u(x(t), t,)$. Once the translation distance $\ell(x(t), t, \Delta t)$ is computed, the advection can be implemented using a reconstruction scheme like the scheme presented in eq.(10.9).

By construction, semi-Lagrangian schemes are stable, but they do not always converge to the correct solution when the time-step is too large. The stability problem

of finite difference methods has been replaced by a convergence problem in the case of semi-Lagrangian schemes. The convergence of the scheme can be related to the gradient of the velocity field since the approximation $\int_0^{\Delta t} u(x(t),t)dt \simeq \Delta t u(x(t),t)$ is valid when the velocity field has important spatial variations. The Taylor expansion of $x(\Delta t)$, as $x(0) + u(x(0),t)\Delta t$, indicates that the quantity $\Delta t \max(\partial_x u)$ should be smaller than one for the approximation to be valid. The full computation of the convergence error depends on the algorithm used to perform the temporal evolution. Similarly to the CFL condition used to implement the Navier-Stokes scheme, the safest method to check the validity of a semi-Lagrangian scheme is to carry out a convergence test. As a general feature, semi-Lagrangian methods are well-adapted to describe the evolution of passive scale in slowly varying velocity fields.

Chapter 11

Multi-stage high-order semi-Lagrangian schemes for incompressible flows in Cartesian geometries (*published* in IJNMF)

This chapter presents new results.

Efficient transport algorithms are essential to the numerical resolution of incompressible fluid flow problems. Semi-Lagrangian methods are widely used in grid-based methods to achieve this aim. The accuracy of the interpolation strategy then determines the properties of the scheme. We introduce a simple multi-stage procedure, which can easily be used to increase the order of accuracy of a code based on multilinear interpolations. This approach is an extension of a corrective algorithm introduced by Dupont & Liu (2003, 2007). This multi-stage procedure can be easily implemented in existing parallel codes using a domain decomposition strategy, as the communication pattern is identical to that of the multilinear scheme. We show how a combination of a forward and backward error correction can provide a third-order accurate scheme, thus significantly reducing diffusive effects while retaining a non-dispersive leading error term.

11.1 Introduction

Semi-Lagrangian methods offer an efficient and widely used approach to model advection-dominated problems. Initially introduced in atmospheric and weather models [116, 117], these methods are now widely used in all fields of fluid mechanics [118, 119, 120]. They have found a wide range of application in computational fluid dynamics. These methods have triggered a wide variety of schemes, including spline interpolation methods [121, 122, 123], finite element WENO algorithms [124, 125, 126] or CIP methods [127, 128]. Considerable development has also been achieved in application to hyperbolic problems (e.g. compressible hydrodynamics [129], Vlasov equation [130]) and falls out of the scope of this paper.

Semi-Lagrangian methods involve an advected field Φ, following the characteristics

backward in time. The procedure requires the estimation of field values that do not lie on the computational grid. Semi-Lagrangian methods therefore rely on an interpolation of $\Phi(t-\Delta t, \boldsymbol{x}-\boldsymbol{u}\Delta t)$, which in general is not a known quantity on the discrete grid.

Because of their local nature, low-order semi-Lagrangian methods perform remarkably well on massively parallel computers [131, 132]. Limitations occur with high-order interpolation methods. As the width of the stencil increases, the locality of the scheme is reduced and the resulting schemes require larger communications stencils. When the interpolation strategy is simple, multi-linear in the case of the CIR scheme [115], the scheme is local and the computational cost is small. If the interpolation stencil is not localized near the computational point, but near the point where the interpolated value must be reconstructed, one can show that the method is then unconditionally stable, in the case of a uniform and steady velocity field [133]. Such schemes are however prone to large inter-process communations, and are not unconditionally stable for general flows.

Dupont *et al.* [134, 135, 136] introduced two new corrective algorithms: "Forward Error Correction" (here denoted FEC) and "Backward Error Correction" (here denoted BEC). These algorithms take advantage of the reversibility of the advection equation to improve the order of most semi-Lagrangian schemes by using multiple calls of an initial advection scheme. The resulting schemes yield an enhanced accuracy. In that sense, they are built with a similar spirit to the predictor-corrector method [137] or the MacCormack scheme [138].

Here we introduce a new scheme following this methodology, and thus extend this approach to third-order accuracy.

11.2 Method (description of new procedures)

11.2.1 Multi-stage approaches

A possible strategy to increase the order of Semi-Lagrangian schemes is to use higher order interpolation formula (e.g. [139]). This has the drawback of relying on a wider stencil, which requires larger communication patterns on a distributed memory computer. Another significant issue with wider stencils is the handling of boundary conditions.

Equation (11.1) models the advection of a passive scalar Φ by a velocity field $\boldsymbol{u}$,

$$D_t\Phi \equiv \left[\partial_t + (\boldsymbol{u}\cdot\boldsymbol{\nabla})\right]\Phi = 0\,. \tag{11.1}$$

The Lagrangian derivative in eq. (11.1) is usually defined as the limit, following the characteristic, of

$$D_t\Phi = \lim_{\Delta t\to 0} \frac{\Phi(t,\boldsymbol{x}) - \Phi(t-\Delta t, \boldsymbol{x}-\boldsymbol{u}\Delta t)}{\Delta t}\,. \tag{11.2}$$

Semi-Lagrangian methods rely on this expression to discretize the advective operator $D_t\Phi$ instead of expanding the sum in a temporal term $\partial_t\Phi$ and an advective term $(\boldsymbol{u}\cdot\boldsymbol{\nabla})\Phi$, as in eq. (11.1). The semi-Lagrangian discretization of eq. (11.1) therefore introduces an interpolation operator $L_{\boldsymbol{u}}\left[\Phi^n\right] = \widetilde{\Phi}^n(\boldsymbol{x}-\boldsymbol{u}\Delta t)$, where $\widetilde{\Phi}$ denotes the interpolated value away from the grid points.

A strategy introduced by Dupont *et al.* [134] to increase the order of a semi-Lagrangian scheme, without requiring the use of high-order interpolation formula, is based on two consecutive calls to the interpolation operator, the second call involving the reversed flow. This method is known as the "Forward Error Correction" [134]. The advantages of this procedure over the above high-order schemes rely both on the accurate implementation of boundary conditions and on the limited communication stencil. The Forward Error Correction scheme is constructed as

$$\bar{\Phi} \equiv L_{-\boldsymbol{u}}\left[L_{\boldsymbol{u}}\left[\Phi^n\right]\right], \tag{11.3}$$

$$FEC\left[\Phi^n\right] \equiv L_{\boldsymbol{u}}\left[\Phi^n\right] + \left(\Phi^n - \bar{\Phi}\right)/2\,. \tag{11.4}$$

The FEC corrective algorithm has further been improved in [135, 136] using three calls to the interpolation operator for each time-step. The resulting algorithm is known as the "Backwards Error Correction" (BEC) algorithm. It is constructed using

$$BEC\left[\Phi^n\right] \equiv L_{\boldsymbol{u}}\left[\Phi^n + (\Phi^n - \bar{\Phi})/2\right]. \tag{11.5}$$

Both the FEC and the BEC algorithms suppress the leading order error term when the interpolation operator is irreversible. Both the FEC and the BEC schemes are free of numerical diffusion. However, they introduce numerical dispersive effects related to their truncation errors.

This truncation error can be advantageously used to construct a scheme free of numerical dispersion and characterized by a fourth-order derivative truncation error. This is achieved for the same computational cost as the BEC scheme. A new "Combined Error Correction" (CEC) algorithm is introduced, using a linear combination of the FEC and BEC algorithms,

$$CEC\left[\Phi\right] \equiv c_{_F} FEC\left[\Phi\right] + c_{_B} BEC\left[\Phi\right]. \tag{11.6}$$

When the CIR scheme is used as the interpolation operator, the scheme generated by the FEC algorithm is similar, in the Eulerian framework, to the one introduced in [140]. In this case, the values of the coefficients $c_{_F}$ and $c_{_B}$ in eq. (11.6) can be explicitly determined and the stability of the resulting schemes assessed. In one-dimension, their expression is

$$3\,c_{_F} = 2 - \Delta x/(|u|\Delta t) \quad \text{and} \quad c_{_B} = 1 - c_{_F}, \tag{11.7}$$

where Δt denotes the time-step and Δx the grid-step.

In one-dimension of space, the CIR scheme is strictly equivalent to the Eulerian upwind scheme. It is well known see [141, 142, 143] that this scheme is stable for Courant-Friedrichs-Lewy (CFL) numbers smaller than unity and introduces diffusive errors. The spurious diffusive effects are directly related to the truncation error of the scheme.

The generalization to d-dimension must be carried out with care. As described later, the fields can be advected one dimension at a time using a splitting technique similar to [140]. In two or three dimensions, the interpolation can be done by applying the CEC scheme on each direction separately.

11.2.2 One-dimensional algorithms

In the semi-Lagrangian formalism, the advection equation can be discretized using the CIR scheme [115]. In one-dimension, the CIR scheme has the same stencil as the Upwind scheme ([120, 137, 142]):

$$\Phi_i^{CIR} = (1-U_i)\Phi^n[i] + U_i\Phi^n[i-s_i]\,, \tag{11.8}$$

where $\Phi^n[i] = \Phi_i^n$ denotes the value of the passive scalar at time $n\,\Delta t$ and position $i\,\Delta x$, $s_i = \mathrm{sgn}(u_i)$ the sign of the velocity and $U_i = |u_i|\Delta t/\Delta x$ the reduced velocity with u_i the velocity. A Von Neumann stability analysis shows that the scheme is strictly stable for $U \leq 1$. For a constant velocity, the modified equation takes the form

$$\Big[\partial_t\Phi + u\partial_x\Phi\Big]_{CIR} = D_{CIR}\partial_x^2\Phi + ... \quad \text{with} \quad D_{CIR} = (1-U)\,\frac{|u|\Delta x}{2}\,. \tag{11.9}$$

The FEC scheme pf eq. (11.4) is a multi-stage version of the CIR scheme. The developed expression for the FEC scheme requires the first nearest neighbors for the velocity and the second nearest neighbors for the passive scalar (see Appendix A). For a constant velocity, the expression of FEC is

$$FEC[\Phi]_i = -\tfrac{1}{2}U(1-U)\Phi^n[i+1] + (1-U^2)\Phi^n[i] + \tfrac{1}{2}U(1+U)\Phi^n[i-1]\,. \tag{11.10}$$

The stability analysis of eq. (11.10) provides the following expression for the amplification factor

$$\xi_{FEC} = 1 - U^2 + U^2\cos(k\Delta x) - iU\sin(k\Delta x)\,. \tag{11.11}$$

The FEC scheme is stable for $U \leq 1$. The modified equation associated to this scheme is

$$\Big[\partial_t\Phi + u\partial_x\Phi\Big]_{FEC} = -(1-U^2)\frac{u\Delta x^2}{3!}\partial_x^3\Phi - 3(1-U^2)\frac{u^2\Delta x^2\Delta t}{4!}\partial_x^4\Phi + ... \tag{11.12}$$

The BEC scheme, presented in eq. (11.5), is a modified version of the CIR scheme using $\bar{\Phi}^n$ to correct the field before the advection step. The developed expression of the BEC scheme requires the second nearest neighbors for the velocity and third nearest neighbors for the passive scalar (see Appeendix A). To avoid using this long development, the simplified case of a constant velocity will be studied.

$$\begin{aligned} BEC[\Phi]_i = &-\frac{U}{2}(1-U)^2\Phi_{i+1}^n + \frac{(1-U)}{2}\left(3-(1-U)^2-2U^2\right)\Phi_i^n \\ &+ \frac{U}{2}\left(3-2(1-U)^2-U^2\right)\Phi_{i-1}^n - \frac{U^2}{2}(1-U)\Phi_{i-2}^n\,. \end{aligned} \tag{11.13}$$

The stability analysis in eq. (11.13) leads to the following amplification factor

$$\xi_{BEC} = 1 - 2iU\sin(\tfrac{1}{2}k\Delta x)\Big[\mathrm{e}^{-\frac{1}{2}ik\Delta x}U(1+2[1-U]\sin^2(\tfrac{1}{2}k\Delta x)) + \cos(\tfrac{1}{2}k\Delta x)(1-U)\Big]\,. \tag{11.14}$$

It can be shown analytically that the BEC scheme is stable for $U \leq 1$. In fact, the BEC scheme is still stable for a CFL number smaller than 1.5. The truncation error analysis leads to

$$\begin{aligned}\Big[\partial_t\Phi + u\partial_x\Phi\Big]_{BEC} = &-(1-U)(1-2U)\tfrac{u\Delta x^2}{3!}\partial_x^3\Phi \\ &- 9(1-U)^2\tfrac{u^2\Delta x^2\Delta t}{4!}\partial_x^4\Phi + ...\end{aligned} \tag{11.15}$$

Simulations with Heaviside, triangle and cosine distributions advected by a constant velocity were carried out for a CFL number $U > 1$. For $U \lesssim 1.5$, the BEC scheme gives finite results consistent with the stable results collected for $U < 1$. The other schemes (CIR, FEC and CEC) diverge for $U > 1$ and the BEC scheme diverges for $U \gtrsim 1.5$. This extension of stability of the BEC scheme can be understood in the following way: for $U > 1$, the interpolation is performed with points that are not the nearest value to the reconstructed point. The contribution of the second nearest neighbors in the BEC formula results in an enhanced stability of the scheme.

The FEC and BEC schemes both have modified equations with a third-order derivative truncation error. The CEC scheme, presented in eq. (11.6) and eq. (11.7) is a linear combination of these two schemes. The weights are computed to cancel the leading order of truncation error (see Appendix A) and generate a higher order scheme. Using the linearity of the stability analysis, the amplification factor is

$$\begin{aligned}\xi_{CEC} = 1 - \tfrac{2}{3}\sin(\tfrac{1}{2}k\Delta x)\Big[U\Big(3 + 2[1-U^2]\sin^2(\tfrac{1}{2}k\Delta x)\Big)\sin(\tfrac{1}{2}k\Delta x) \\ + \Big(3 + 2U[1-U^2]\sin^2(\tfrac{1}{2}k\Delta x)\Big)i\cos(\tfrac{1}{2}k\Delta x)\Big]\,.\end{aligned} \tag{11.16}$$

The CEC scheme is stable for $U \leq 1$. To leading order, the modified equation of the CEC scheme is

$$\Big[\partial_t\Phi + u\partial_x\Phi\Big]_{CEC} = -(1+U)(1-U)(2-U)\tfrac{|u|(\Delta x)^3}{4!}\partial_x^4\Phi + ... \tag{11.17}$$

The essential properties of the different schemes are reported in Tab. 11.1. The computational cost is evaluated using the number of composed interpolation operators. The complexity of the interpolation operator varies with the interpolation method used. In the case of the CIR scheme, the complexity is $\mathcal{O}(N)$ where N is the total number grid of points.

11.2.3 Results for one-dimensional problems

To assess the efficiency of the schemes introduced previously, simulations with a constant velocity were performed. A one-dimensional periodic domain is considered, and the solution is advected for 10 or 100 cycles. Fig. 11.1, 11.2 and 11.3 show the advection of three density profiles with different regularities. Because of the Fourier properties of sine functions, the first harmonic was studied thoroughly to check that it matches the properties of the modified equation.

The first set of tests was performed using an Heaviside profile $\Phi(x, t = 0) = \mathrm{sgn}\Big[\sin(2\pi x/l)\Big]$. This is a demanding test, as this profile is discontinuous at two

Scheme	Formula	Error	Stability	Nb of calls
CIR	$L_+\left[\Phi\right]$	$(1-U)\,\frac{\lvert u\rvert\Delta x}{2}\partial_x^2\Phi$	$U<1$	1
FEC	$L_+\left[\Phi\right]+\frac{1}{2}(\Phi-\bar{\Phi})$	$-(1-U^2)\frac{u\Delta x^2}{3!}\partial_x^3\Phi$ $-3(1-U^2)\frac{u^2\Delta x^2\Delta t}{4!}\partial_x^4\Phi$	$U<1$	2
BEC	$L_+\left[\Phi+\frac{1}{2}(\Phi-\bar{\Phi})\right]$	$-(1-U)(1-2U)\frac{u\Delta x^2}{3!}\partial_x^3\Phi$ $-9(1-U)^2\frac{u^2\Delta x^2\Delta t}{4!}\partial_x^4\Phi$	$U\lesssim 1.5$	3
CEC	$L_+\left[\Phi+\frac{1+U}{6U}(\Phi-\bar{\Phi})\right]$ $+\frac{1-2U}{6U}(\Phi-\bar{\Phi})$	$-(1+U)(1-U)(2-U)\frac{\lvert u\rvert(\Delta x)^3}{4!}\partial_x^4\Phi$	$U<1$	3

Table 11.1 – Comparative table of one-dimension schemes.

cross-over positions (0 and 0.5). As time elapses, the high frequencies get damped and the profile is nearly reduced to its first harmonic. In fig. 11.1, the CEC scheme is closer to the analytical solution than the other schemes by three criteria: (i) the "flatness" of its profile at the beginning of the simulation, (ii) the distance from the analytic cross-over position at all time and (iii) the phase drift of the profile at long time. These criteria may seem independent but they are all linked to the Fourier properties of the modified equation.

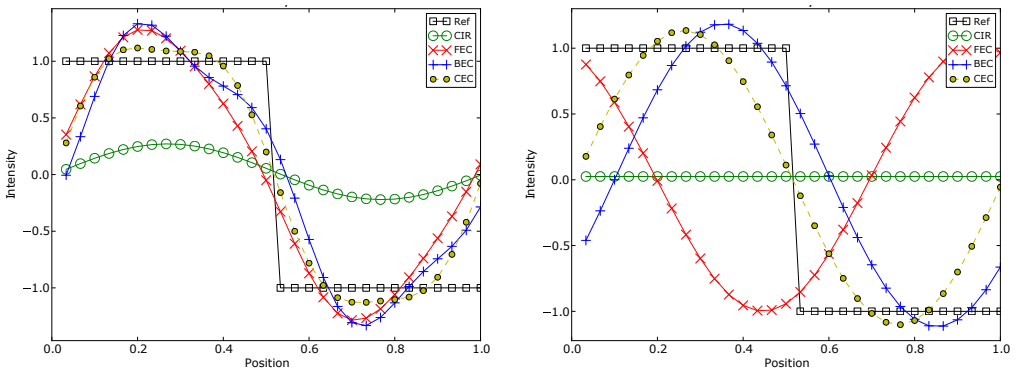

(a) 10 periods (b) 100 periods

Figure 11.1 – One-dimension advection of a Heaviside with a resolution of $N = 30$ at $CFL = 0.75$.

The second set of tests was performed using a triangular profile, $\Phi(x, t = 0) = |x/l - 0.5|$. This profile is non-differentiable at two cross-over positions (0 and 0.5). In fig. 11.2, the observations reported in the previous paragraph still hold for the triangular profile. As expected, the CEC scheme is closer to the analytic results in the case of a continuous but non-derivable profile.

The last tests were performed using the first harmonic cosine profile, $\Phi(x, t = 0) =$

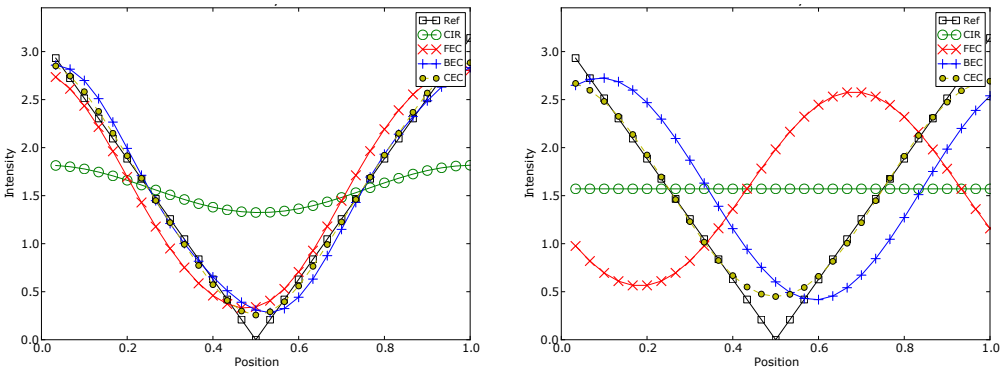

(a) 10 periods (b) 100 periods

Figure 11.2 – One-dimension advection of a triangle with a resolution of $N = 30$ at $CFL = 0.75$.

$-\cos(2\pi x/l)$. The properties of the profile will be studied in more details in fig. 11.9 and 11.10. In fig. 11.3, the CIR scheme is so diffusive that a "corrected CIR" (green diamond line)[1] is plotted. Even though the CIR scheme is near zero in fig. 11.3, the norm of its difference to the analytic profile is smaller than the FEC scheme which drifted to such an extent that it is nearly opposite to the reference profile.

As noted above, provided that the interpolation strategy involves non-neighboring points, semi-Lagrangian methods can use CFL numbers larger than one. Using a non-local interpolation stencil, we can reproduce the advection test of fig. 11.3 using a CFL number of 3.75 (see fig. 11.4).

The time-step being larger in this last case, fewer time-steps are needed for the same integration time (here respectively 10 and 100 periods), the effects of numerical dispersion and diffusion are thus weakened compared to fig. 11.3

This is achieved with a simple modification of relations eq. (11.7) to compute the weights c_F and c_B, in the form

$$3\,c_F = 2 - \frac{1}{(|u|\Delta t/\Delta x)\ \%1} \quad \text{and} \quad c_B = 1 - c_F, \tag{11.18}$$

(where %1 denotes the remainder of the division by unity), the accuracy of the CEC scheme is preserved for large CFL numbers.

11.2.4 Multi-dimensional problems

The extension of the above procedures to multi-dimensional problems requires some care. For instance, in two dimensions, the CIR scheme is

$$\begin{aligned} CIR[\Phi]_{i,j} =& (1-U^x_{i,j})(1-U^y_{i,j})\Phi^n_{i,j} + (1-U^x_{i,j})U^y_{i,j}\Phi^n_{i,j-s^y_{i,j}}\,, \\ &+ U^x_{i,j}(1-U^y_{i,j})\Phi^n_{i-s^x_{i,j},j} + U^x_{i,j}U^y_{i,j}\Phi^n_{i-s^x_{i,j},j-s^y_{i,j}}\,. \end{aligned} \tag{11.19}$$

[1] The corrected CIR values are equal to those of CIR multiplied by $\exp(D_{CIR}k^2t)$ where D_{CIR} is defined in (11.9).

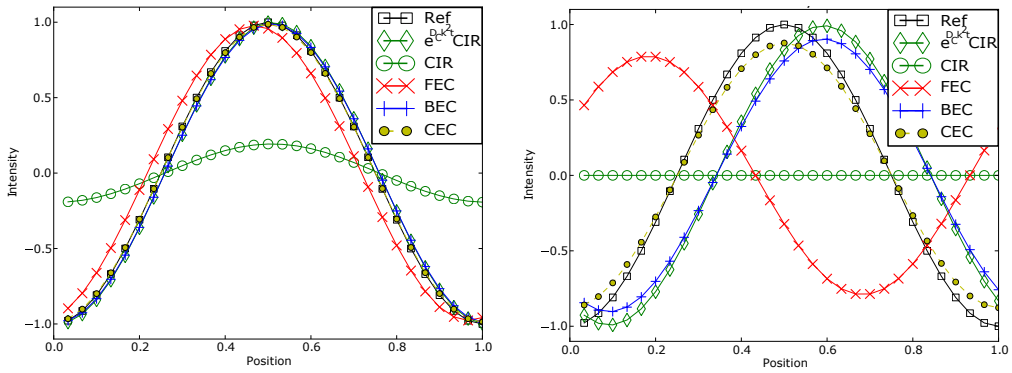

(a) 10 periods, i.e. 1200 time-steps (b) 100 periods, i.e. 12000 time-steps

Figure 11.3 – One-dimension advection of the cosine function with a resolution of $N = 30$ at $CFL = 0.75$.

The semi-Lagrangian CIR scheme uses one more value ($\Phi[i - s^x_{i,j}][j - s^y_{i,j}]$) than the Eulerian Upwind scheme. However, the CIR scheme is very similar to the directionally-split Upwind scheme

$$\Phi^{\star}_{i,j} = (1 - U^x_{i,j})\Phi^n_{i,j} + U^x_{i,j}\Phi^n[i - s^x_{i,j}][j], \tag{11.20}$$

$$\Phi^{\star\star}_{i,j} = (1 - U^y_{i,j})\Phi^{\star}_{i,j} + U^y_{i,j}\Phi^{\star}[i][j - s^y_{i,j}]. \tag{11.21}$$

In the general case in multi-dimensions, there is no expression for the c_F and c_B coefficients of the CEC scheme. It can be extended to any dimension if the scheme is directionnally-split as done in eq. (11.20) and eq. (11.21). However, if a simple splitting method is used, the approximation is reduced to first order. Special splitting methods, such as Strang splitting [144], are required to increase the order of the total scheme.

To illustrate applications of our strategy to higher dimensions, let us consider an advection problem in two dimensions of space. A squared patch is considered for the initial distribution of the passive scalar: one inside the square and zero outside, as presented in fig. 11.5(a). The order of the schemes for regularly varying velocities should be the same as the one for constant velocities. Quantitative results being difficult, only qualitative observations will be made. The following velocity field was used to test the schemes

$$u(x,y) = \frac{y}{l}\left(1 - \frac{y}{l}\right)\left(\frac{1}{2} - \frac{y}{l}\right)\left[\cos\left(2\pi\frac{y}{l}(1 - \frac{y}{l})\right) + 1\right]/(2\pi^2), \tag{11.22}$$

$$v(x,y) = -\frac{x}{l}\left(1 - \frac{x}{l}\right)\left(\frac{1}{2} - \frac{x}{l}\right)\left[\cos\left(2\pi\frac{x}{l}(1 - \frac{x}{l})\right) + 1\right]/(2\pi^2), \tag{11.23}$$

where l is the length of the box in both directions. In fig. 11.5(b), the velocity cancels out on the edges of the box and is divergence-free. With the profiles used, the patch is not transported through the walls of the box even though the simulation has periodic boundary conditions. The patch never intersects itself, which makes it easier to track. To compare the results, a fully Lagrangian method was used as a reference. The time-step of this method was twenty times smaller to have more accurate results. The solution is represented in fig. 11.5(c).

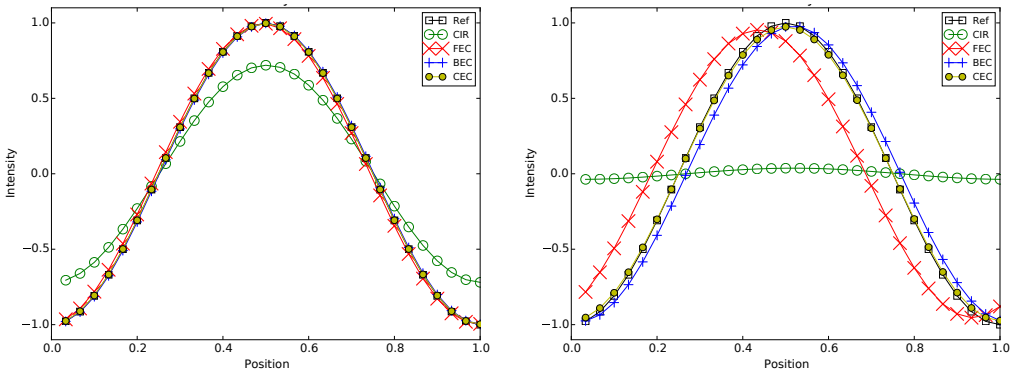

(a) 10 periods, i.e. 80 time-steps (b) 100 periods, i.e. 800 time-steps

Figure 11.4 – One-dimension advection of the cosine function with a resolution of $N = 30$ at $CFL = 3.75$.

In fig. 11.6 and 11.7, the analysis of the gap between a scheme and the reference solution should not only be guided by the intensity of the difference but also by the area impacted. The CIR scheme clearly introduces the largest computational error.

The perturbation of the distribution can also give an intuition of the leading error term in the modified equation. The quick oscillations at the tail of the patch in fig. 11.7(b) and 11.7(c) can be related to the dispersive residuals of the FEC and BEC schemes. In fig. 11.7(d), the CEC solution is the closest to the reference solution obtained by the pure Lagrangian method. The error is of small amplitude and only impacts the edges of the patch.

11.2.5 Application to thermal convection

In this section, the comparison between the different advection schemes is extended to a physically more relevant case: thermal convection in a layer of fluid heated from below. This canonical example is also known as the Rayleigh-Bénard setup. The schemes will not only be used on passive scalars that do not influence the velocity, but on the velocity itself and the temperature, which, in the Rayleigh-Bénard instability,

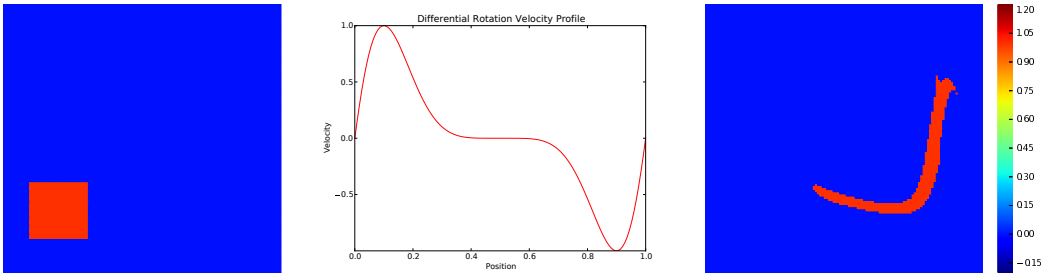

(a) Initial patch distribution (b) $u(0, y)$ and $v(x, 0)$ profile (c) Pure Lagrangian advection

Figure 11.5 – Initial condition, velocity profile and final distribution for the two-dimensional advection test case.

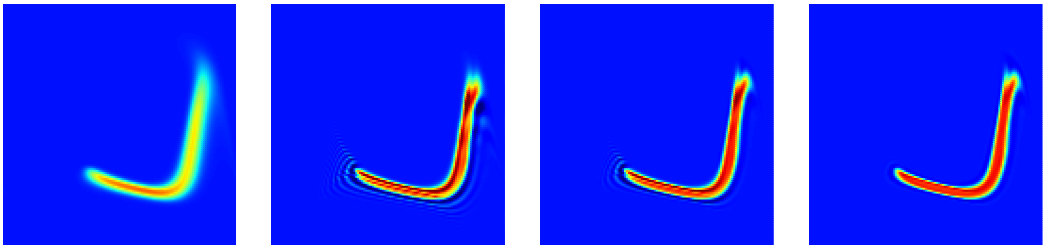

(a) *CIR* advection (b) *FEC* advection (c) *BEC* advection (d) *CEC* advection

Figure 11.6 – Two-dimensional patch advection using the different schemes.

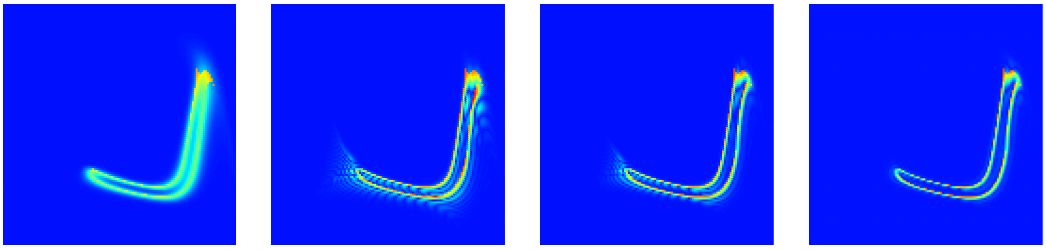

(a) *CIR* error. (b) *FEC* error. (c) *BEC* error. (d) *CEC* error.

Figure 11.7 – Errors as measured by the difference of the numerical solutions to the reference solution obtained with pure Lagrangian advection.

modifies the velocity actively.

The system of equations describing the evolution of the velocity $\boldsymbol{u}$ and the temperature T of the fluid is solved on a two-dimensional Cartesian domain of aspect ratio $\chi = L_z/L_x = 0.5$, bounded by solid and impermeable walls. The bottom and top plates are maintained at fixed temperatures T_0 and $T_0 - \Delta T$, respectively, whereas the vertical walls are assumed to be insulating (no heat flux through the vertical boundaries). Gravity is assumed to be uniform and vertical $\boldsymbol{g} = -g\boldsymbol{e}_z$.

To retain the essential physics with a minimum complexity, the Boussinesq approximation is used to describe the fluid within the cell and assume that variations of all physical properties other than density can be ignored. Variations in density are also neglected "except in so far as they modify the action of gravity" [145]. The density ρ is assumed to be constant everywhere in the governing equations except in the buoyancy force where it is assumed to vary linearly with temperature, $\rho(T) = \rho_0(1 - \alpha(T - T_0))$, where α is the thermal expansion coefficient of the fluid.

The system admits the stationary diffusive solution: $\boldsymbol{u}^\star = 0$, $T^\star = T_0 - z\,\Delta T/L_z$, and $\boldsymbol{\nabla} P^\star = -g\rho(T^\star)\,\boldsymbol{e}_z$. Subtracting the stationary solution, choosing L_z, L_z^2/κ, and ΔT as units of length, time, and temperature, respectively, and using the temperature perturbation $\theta = T - T^\star$, the system can be written [146] as

$$\partial_t \boldsymbol{u} + (\boldsymbol{u}\cdot\boldsymbol{\nabla})\,\boldsymbol{u} = -\boldsymbol{\nabla}\Pi + \mathrm{RaPr}\,\theta\,\boldsymbol{e}_z + \mathrm{Pr}\,\Delta\boldsymbol{u}\,, \tag{11.24}$$

$$\partial_t \theta + (\boldsymbol{u}\cdot\boldsymbol{\nabla})\,\theta = w + \Delta\theta\,, \tag{11.25}$$

$$\boldsymbol{\nabla}\cdot\boldsymbol{u} = 0\,, \tag{11.26}$$

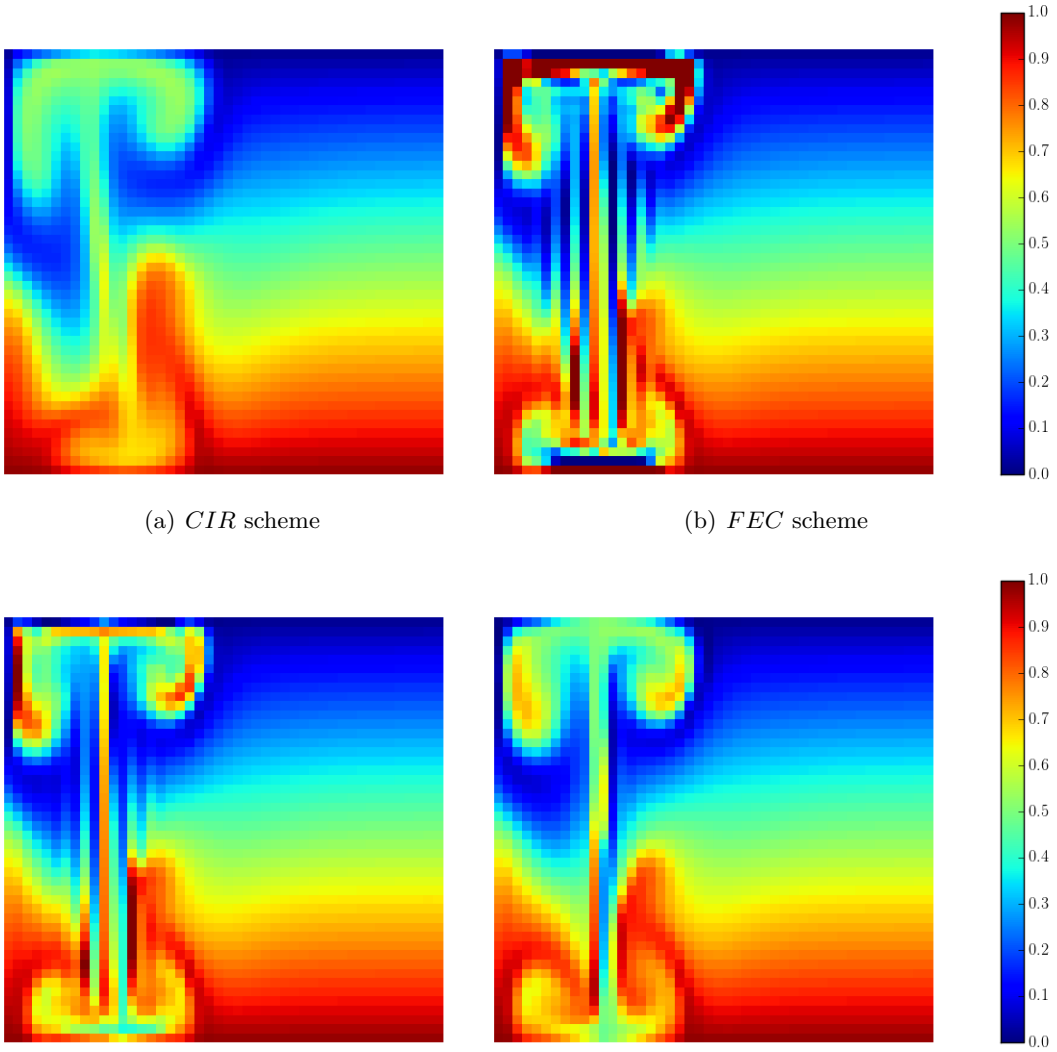

(a) *CIR* scheme (b) *FEC* scheme

(c) *BEC* scheme (d) *CEC* scheme

Figure 11.8 – Rayleigh-Bénard evolution of a localized thermal perturbation. The numerical resolution $N = 50^2$ is intentionally modest, in order to highlight numerical errors.

with $w \equiv \boldsymbol{u} \cdot \boldsymbol{e}_z$ the vertical velocity. The non-dimensional control parameters are the Rayleigh number, defined by $\mathrm{Ra} = \alpha g \Delta T L_z^3/(\kappa\nu)$ and which measures the convective driving, and the Prandtl number, defined as the ratio of viscous to thermal diffusion, $\mathrm{Pr} = \nu/\kappa$, with ν the kinematic viscosity and κ the thermal diffusivity.

Equations (11.24) and (11.25) are discretized on a uniform grid using finite volume formula of order two in space and order one in time, with all the terms being treated explicitly. To enforce the solenoidal constraint (11.26), the pressure-correction scheme [147, 148] is used. This splitting method is composed of two steps. In the first step, a preliminary velocity field $\boldsymbol{u}^\star$ is computed by neglecting the pressure term in Navier-Stokes equation. Since this preliminary velocity field is generally not divergence-free,

it is then corrected in a second step by a projection on the space of solenoidal vector fields. Given the temperature and velocity distributions at time-step n, the velocity $\boldsymbol{u}^{n+1}$ is computed by solving

$$\begin{aligned} \boldsymbol{u}^{(1)} &= L\left[\boldsymbol{u}^n, \boldsymbol{u}^n\right] , && (11.27)\\ \boldsymbol{u}^{(2)} &= \boldsymbol{u}^{(1)} + \Delta t \left(\mathrm{RaPr}\, \theta^n \boldsymbol{e}_z + [\Delta \boldsymbol{u}]^n\right) , && (11.28)\\ \Delta \phi^n &= \boldsymbol{\nabla} \cdot \boldsymbol{u}^{(2)} , && (11.29)\\ \boldsymbol{u}^{n+1} &= \boldsymbol{u}^{(2)} - \boldsymbol{\nabla} \phi^n . && (11.30) \end{aligned}$$

In eq. (11.29), the algorithm requires to solve at each time-step a Poisson equation for the pressure. The necessary impermeability conditions for the field ϕ are found by multiplying (11.30) by the normal vector $\boldsymbol{n}$. Together with the velocity boundary condition, they lead to $\boldsymbol{n} \cdot \boldsymbol{\nabla} \phi^n = 0$. The boundary conditions for the velocity field are no-slip, *i.e.* $\boldsymbol{u} = 0$, while the temperature satisfies $\theta(z = 0) = \theta(z = 1) = 0$ on the horizontal boundaries, and $\partial_x \theta = 0$ on the vertical boundaries. Boundary conditions are imposed on the intermediate velocity field $\boldsymbol{u}^\star$ by introducing ghost points outside of the domain. In consequence, the tangential component of the actual velocity field $\boldsymbol{u}$ will not exactly satisfy the boundary conditions (the error being controlled by the time-step).

In order to develop the instability (the Rayleigh number being sufficiently large and the Prandtl number set to unity), the simulations were always started with $\boldsymbol{u} = 0$ and with a small temperature perturbation. This temperature perturbation consisted of a hot spot ($\theta = 0.1$) next to a cold spot ($\theta = -0.1$). This perturbation, localized close to the lower left corner, generates a rising and a sinking plume. The different simulations were compared when the rising plume has reached the top boundary (after roughly a thousand iterations).

A very low resolution, $N = 50^2$, was deliberately chosen in order to highlight the numerical errors associated to the different schemes. Snapshots of the total temperature $T = T^\star + \theta$ associated with the thermal plume are compared on figure 11.8. In fig. 11.8(b) and 11.8(c), strong ripples appear in the wake of the plumes. They are not physically relevant and are characteristics of dispersive schemes. The comparison of the plumes in fig. 11.8(a) and fig. 11.8(d) clearly highlights that the CEC scheme is less diffusive than the CIR scheme for practical physical applications. The CEC scheme offers an improved scheme, with significantly reduced diffusive effects, and free of the strong dispersion characterizing the FEC and BEC schemes.

11.3 Conclusion

Using the simplest semi-Lagrangian CIR scheme introduced by Courant-Isaacson-Rees, it has been demonstrated that a simple multi-stage approach can increase the order of the scheme from first to third order. The resulting scheme is, at leading order, non-dispersive. This procedure was shown to yield significant improvement on a thermal convection problem. It can easily be used to increase the order of existing codes on parallel computers, as the communication stencil is unaltered by the multi-stage approach. The communications among parallel processes are then restricted to the strict miminum (one layer of cell at each domain boundary).

The CEC algorithm, introduced here, only requires a modest increase in the computational cost and can easily be implement in existing codes. Moreover, its implementation is not limited to regular Cartesian finite differences schemes. It can be generalized to other geometries and scheme types by following two simple steps: (i) deriving the modified advection equation for the FEC and BEC schemes and (ii) combining both schemes to cancel out their leading order error.

11.4 Appendix (description of new procedures)

11.4.1 Appendix: Developed expressions of the corrective schemes

The expressions relevant to eq. (11.10) and eq. (11.13) can be developed as

$$\begin{aligned} 2\,FEC[\Phi]_i = &- U_i(1-U_i)\Phi^n_{i+s_i} + (2-U_iU_i)\Phi^n_i \\ &- U_iU_{i+s_i}\Phi^n[i+s_i-s\,(i+s_i)] + U_i(1+U_{i-s_i})\Phi^n_{i-s_i}\,, \end{aligned} \tag{11.31}$$

$$\begin{aligned} 2\,BEC[\Phi]_i = &\,(f\Phi^n)\,[i+s\,(i)] + (f\Phi^n)\,[i] + (f\Phi^n)\,[i-s\,(i)+s\,(i-s\,(i))] + \\ &(f\Phi^n)\,[i+s\,(i)-s\,(i+s\,(i))] + (f\Phi^n)\,[i-s\,(i)] + \\ &(f\Phi^n)\,[i-s\,(i)+s\,(i+s\,(i))-s\,(i-s\,(i)+s\,(i-s\,(i)))] + \\ &(f\Phi^n)\,[i-s\,(i)-s\,(i-s\,(i))]\,, \end{aligned} \tag{11.32}$$

where

$$f[i+s\,(i)] = -(1-U_i)U_i(1-U_{i+s(i)})\,, \tag{11.33}$$

$$f[i] = (1-U_i)\big[3-(1-U_i)^2\big]\,, \tag{11.34}$$

$$f[i-s\,(i)+s\,(i-s\,(i))] = -U_iU_{i-s(i)}(1-U_{i-s(i)+s(i-s(i))})\,, \tag{11.35}$$

$$f[i+s\,(i)-s\,(i+s\,(i))] = -(1-U_i)U_iU_{i+s(i)}\,, \tag{11.36}$$

$$f[i-s\,(i)] = U_i\big[3-\Big(1-U_{i-s(i)}\Big)^2\big] - (1-U_i)((1-U_i)U_i)\,, \tag{11.37}$$

$$f[i-s\,(i)+s\,(i+s\,(i))-s\,(i-s\,(i)+s\,(i-s\,(i)))] = -U_iU_{i-s(i)}U_{i-s(i)+s(i-s(i))}\,, \tag{11.38}$$

$$f[i-s\,(i)-s\,(i-s\,(i))] = -U_i(1-U_{i-s(i)})U_{i-s(i)}\,. \tag{11.39}$$

11.4.2 Appendix: Analysis of the modified advection equation

The modified equation steming from the discretization of the advection equation has in one-dimension the general form

$$\partial_t\Phi + u\,\partial_x\Phi = \sum_\alpha C_\alpha\partial^\alpha_x\Phi\,, \tag{11.40}$$

where the C_α prefactors come from the truncation error in the case of numeric schemes. If the CFL stability condition is met, i.e. $\Delta t \propto u^{-1}\Delta x$, with $\Delta x \propto N^{-1}$, we have

$$C_\alpha \propto N^{-\alpha+1}\,. \tag{11.41}$$

Going into Fourier space for spacial dimensions and Fourier-Laplace space for time,

$$\Phi(x,t) = \int \mathrm{d}k\, \mathrm{e}^{\Omega(k)t-ikx}\hat{\Phi}(k,\Omega(k)) \quad \text{where} \quad \Omega(k) = -\sigma(k) + i\omega(k)\,. \tag{11.42}$$

Thus, the dispersion relation is

$$\Omega(k) = (ik)u + \sum_{\alpha}(-ik)^{\alpha}C_{\alpha}\,. \tag{11.43}$$

Using the decomposition introduced in eq. (11.42), the decay rate and the phase drift can be expressed as

$$\sigma(k) = \sum_{p}\left(k^2\right)^{2p+2}\left(C_{4p+2} - \left(k^2\right)^{2p}C_{4p}\right)\,, \tag{11.44}$$

$$\omega(k) = k\Big(u - \sum_{p}\left((k^2)^{2p}C_{4p+1} - (k^2)^{2p+1}C_{4p+3}\right)\Big)\,. \tag{11.45}$$

The equation has strictly stable solutions if and only if $\sigma(k) > 0$. Because of its dependence on the resolution, the sequence of C_{2p} is often equivalent to its first term different from zero. The stability reduces to the criterion $C_{\alpha} > 0$ if $\alpha = 4p+2$ and $C_{\alpha} < 0$ if $\alpha = 4p$. Using the equation on ω, the phase drift can be extracted

$$\phi(k) = \omega(k) - ku = -k\sum_{p}\Big((k^2)^{2p}C_{4p+1} - (k^2)^{2p+1}C_{4p+3}\Big)\,. \tag{11.46}$$

It is important to note that the procedure introduced in the FEC scheme cannot be repeated recursively. In order to highlight this point let us note that for pure advection, reversing time is equivalent to reversing the velocity

$$\partial_{-t}\Phi + u\partial_x\Phi = 0 \quad \Leftrightarrow \quad \partial_t\Phi + (-u)\partial_x\Phi = 0 \quad \Leftrightarrow \quad \partial_t\Phi + u\partial_{-x}\Phi = 0\,. \tag{11.47}$$

Going into Fourier space for the spacial dimension

$$\Phi(x,t) = \int \mathrm{d}k\, \mathrm{e}^{-ikx}\tilde{\Phi}(k,t)\,, \tag{11.48}$$

the modified advection equation can be written as

$$\partial_t\left(\ln\tilde{\Phi}\right)(k,t) = u(ik) + \sum_{\alpha}C_{\alpha}(-ik)^{\alpha}\,. \tag{11.49}$$

Reversing the sign of the coordinate, $x \to -x$, is equivalent to reversing the wavevector, $k \to -k$ (c.c. for a real field). In order to ensure time reversibility, the following relation should be satisfied

$$\partial_t\left(\ln\tilde{\Phi}\right)(k,t) = \partial_t\left(\ln\tilde{\Phi}\right)(-k,-t) = -\partial_t\left(\ln\tilde{\Phi}\right)(-k,t)\,. \tag{11.50}$$

This last relation shows that only terms of odd derivative are reversible. The error on $\bar{\Phi}$ highlights this observation. It can be evaluated using

$$\left(\ln\bar{\tilde{\Phi}}\right)(k,t) = \left(\ln\tilde{\Phi}\right)(k,t) + 2\Delta t\sum_{p}C_{2p}(ik)^{2p}. \tag{11.51}$$

Only terms of even order derivative modify the field and can be detected with this procedure. This property should also be true for the C_α coefficients when the velocity is reversed. In the case of the CIR scheme, the coefficients depend on the sign of the velocity. In the case of the non-ideal advection equation (11.40), reverting time leads to

$$\partial_t \Phi + (-u)\partial_x \Phi = \sum_p \Big(C_{2p+1}(-u)\partial_x^{2p+1}\Phi - C_{2p}(-u)\partial_x^{2p}\Phi \Big) . \tag{11.52}$$

Once more, only terms of odd order derivative are reversible.

The decay rate (fig. 11.9) and the phase drift (fig. 11.10) were measured for different resolutions. The results are plotted as a function of the resolution on a binary log scale (lb). Fig. 11.9(a) and 11.10(a) represent the decay rate and the phase drift, respectively. As shown in eq. (11.41), the prefactors of the derivative terms of the error are proportional to an integer power of the resolution, $C_\alpha \propto N^{-\alpha+1}$. The values of α are in good agreement with the error term of the modified equation. Using the theoretical value of $\alpha^{(1)}$ and $\alpha^{(2)}$, the values are rescaled to $\phi_{res} = \phi \times N^{\alpha^{(1)}-1}$ and $\sigma_{res} = \sigma \times N^{\alpha^{(2)}-1}$. Fig. 11.9(b) and 11.10(b) show that the rescaled values are nearly constant as predicted by the theory.

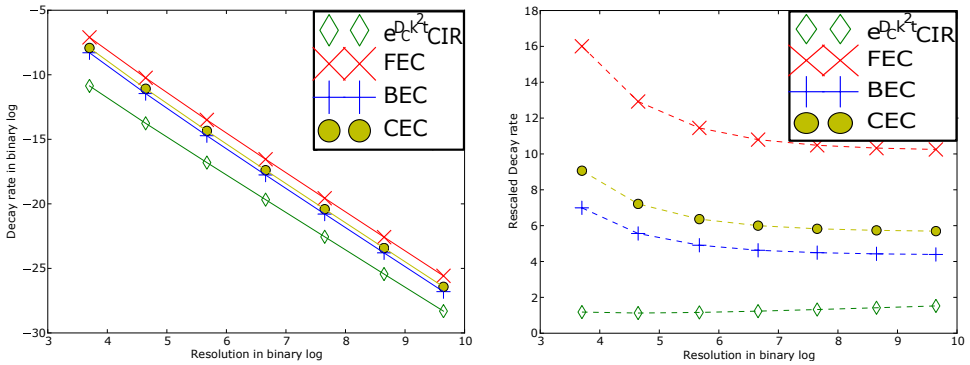

(a) Decay rate (b) Rescaled decay rate

Figure 11.9 – Evolution of the decay rate with the resolution in one-dimension.

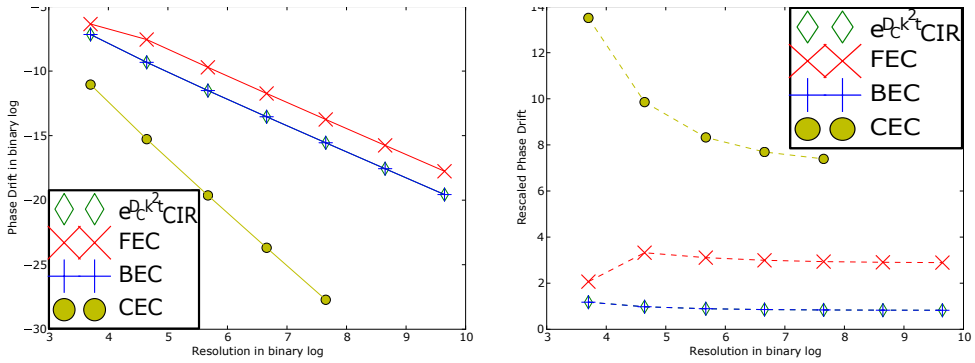

(a) Phase drift (b) Rescaled phase drift

Figure 11.10 – Evolution of the phase drift with the resolution in ofmension.

Chapter 12

A systematic method to enforce conservativity on semi-Lagrangian schemes (*submitted*)

This chapter presents new results.

Semi-Lagrangian schemes have proven to be very efficient to model advection problems. However most semi-Lagrangian schemes are not conservative. Here, a systematic method is introduced in order to enforce the conservative property on a semi-Lagrangian advection scheme. This method is shown to generate conservative schemes with the same linear stability range and the same order of accuracy as the initial advection scheme from which they are derived. We used a criterion based on the column-balance property of the schemes to assess their conservativity property. We show that this approach can be used with large CFL numbers and third-order schemes.

12.1 Introduction

Semi-Lagrangian methods have been demonstrated to be efficient schemes to model advection-dominated problems. These methods are intensively used to solve atmospheric and weather problems [116, 118], internal geophysics problems [120] or plasma simulations [149, 150, 130]. However, when conservative properties are sought, the method of discretisation usually relies on a finite volume discretisation. Conservativity is then ensured by canceling fluxes, defined on the computational cell boundaries [151, 152].

Semi-Lagrangian methods, on the contrary, are in general not conservative. Some earlier works have tried to address this issue and derive a conservative semi-Lagrangian scheme. For example, [127, 128] introduced a modified version of a non-conservative semi-Lagrangian scheme [153] to enforce conservativity. Their approach provides a conservative formulation at the cost of introducing a scheme in which the coefficients depends on the values of the advected field. An alternative strategy, which uses a semi-Lagrangian reconstruction to estimate fluxes on the faces, was introduced by [150] in the finite volume spirit to model the Vlasov equation. This strategy was adapted to compressible flows in [125]. In both of the above approaches, the formulations are

well-adapted to one-dimensional problems, but their generalization to higher spatial dimensions without using a splitting strategy is challenging.

A general method to enforce conservativity on a semi-Lagrangian scheme was introduced in Lentine *et al.* [129]. Noting that the contribution of a given cell to the update in time of the total field does not add up to unity, they introduced an *ad hoc* modification of the coefficients which allows to ensure conservativity at the cost of reducing the order of the scheme.

We propose a systematic method to enforce conservativity on a numerical scheme. Our method follows ideas introduced in the method of support operators developed by Shashkov [154], or the summation-by-part method of Carpenter *et al.* [155, 156]. It can easily be applied to semi-Lagrangian schemes. A close equivalence can be found with the flux interpretation in the sense of finite volume schemes. Let us start by considering the continuity equation, for a quantity Φ subject to a velocity field $\boldsymbol{u}$

$$\partial_t \Phi = -\boldsymbol{\nabla} \cdot (\Phi \boldsymbol{u}) \equiv \mathcal{C}(\boldsymbol{U})[\Phi] \,, \tag{12.1}$$

where $\mathcal{C}(\boldsymbol{U})$ denotes the continuity operator. If the flow is incompressible, $\boldsymbol{\nabla} \cdot \boldsymbol{u} = 0$, the continuity equation reduces to the advection equation:

$$\partial_t \Phi = -\Phi(\boldsymbol{\nabla} \cdot \boldsymbol{u}) - (\boldsymbol{u} \cdot \boldsymbol{\nabla})\Phi = -(\boldsymbol{u} \cdot \boldsymbol{\nabla})\Phi \equiv \mathcal{D}(\boldsymbol{U})[\Phi] \,, \tag{12.2}$$

where $\mathcal{D}(\boldsymbol{U})$ denotes the advection operator.

Instead of considering eq. (12.2) as a simplified version of eq. (12.1), under the solenoidal constraint, the two equations can be viewed as two independent equations. Introducing the canonical scalar product of two continuous fields Ψ and Φ, $(\Psi\,,\,\Phi) = \int \Psi\Phi \,\mathrm{d}\tau$, the continuity and advection operators are then adjoint operator up to a change of the velocity sign:

$$\int \Psi \left[(\boldsymbol{u} \cdot \boldsymbol{\nabla})\Phi\right] \,\mathrm{d}\tau = \oint \Psi\Phi\boldsymbol{u} \cdot \boldsymbol{n} \,\mathrm{d}s + \int \left[\boldsymbol{\nabla} \cdot (-\boldsymbol{u}\Psi)\right] \Phi \,\mathrm{d}\tau \,. \tag{12.3}$$

If the boundary term vanishes, the operators follow $(\Psi\,,\,\mathcal{D}(\boldsymbol{U})\Phi) = (\mathcal{C}(-\boldsymbol{U})\Psi\,,\,\Phi)$. Such relations have been intensively used in the support operator formalism [154]. Introducing the $\star$ to denote the adjoint operator, we get $\mathcal{D}(\boldsymbol{U})^\star = \mathcal{C}(-\boldsymbol{U})$. This adjoint property can be used to enforce conservativity on an arbitrary advection scheme.

12.2 Method (description of new procedure)

12.2.1 Column-balance criterion & adjoint operator

Using a linear finite difference scheme explicit on time, the advection equation is given by $\Phi_i^{n+1} = \Phi_i^n + D_{i,j}\Phi_j^n$, where $D_{i,j}$ denotes the discrete linear operator associated to eq. (12.2). For the discrete operator to be homogeneous, the coefficients $D_{i,j}$ must only depend on the reduced velocity $U_i = u_i \Delta t/\Delta x$.

In a similar way, finite difference schemes modeling eq. (12.1), which corresponds to the continuity condition, can be written as

$$\Phi_i^{n+1} = \Phi_i^n + C_{i,j}\Phi_j^n \tag{12.4}$$

where $C_{i,j}$ denotes the conservative transport matrix. The evolution of the total mass, M, is then given by

$$M^{n+1} - M^n = \sum_{i,j} C_{i,j}\Phi_j^n = \sum_i \Phi_i^n (\sum_j {}^{\mathrm{t}}C_{i,j}) \,. \tag{12.5}$$

It follows that the scheme is conservative if and only if the $C_{i,j}$ operator is column-balanced, *i.e.* for all i, $\sum_j C_{j,i} = 0$. In order to link this formalism to finite volume schemes, the column-balanced conservative matrix can be compared to the flux method. On a regular Cartesian grid, flux are defined at the boundary between two vertices. The equation modeling the flux method is:

$$\Phi_i^{n+1} = \Phi_i^n + F_{i-1/2} - F_{i+1/2} \,, \tag{12.6}$$

where Φ_i^{n+1} denotes the values of field Φ at the index i and $F_{i+1/2}$ the flux of field Φ computed at index $i+1/2$. Choosing $F_{i+1/2} = C_{i+1,i}\Phi_i - C_{i,i+1}\Phi_{i+1}$, both methods are strictly equivalent.

The adjoint relation will now be used to show how a generic advection scheme can be modified to enforce the conservativity property. Once the problem is discrete, the adjoint property leads to $C(U) = {}^{\mathrm{t}}D(-U)$. It is a property of the transpose that $C(U)$ and $D(-U)$ have the same eigenvalues. Both operators are thus stable for the same set of parameters. It also implies that the error of the $C(U)$ scheme is the transpose of the error of the $D(-U)$ scheme, therefore the two operators have the same consistency order. In addition, if $D(-U)$ is monotone, $C(U)$ is also monotone. Using the Lax-Richtmyer equivalence theorem [157], the consistent and stable $C(U)$ scheme converges to the continuity equation.

The above remarks do not ensure that the $C(U)$ scheme conserves the total mass. However, assuming that the advective scheme satisfies $\forall i \,,\ \sum_j D_{i,j}(-U) = 0$, it follows that $\forall j,\ \sum_i C_{i,j}(U) = 0$. The $C_{i,j}(U)$ operator is thus column-balanced and conserves the total mass.

It is important to stress that we only introduce a modification of the spatial operator. The conservative property of $C_{i,j}(U)$ will thus be valid both for multi-step and multi-stage time-steppings. Consider for example a Crank-Nicholson time-stepping scheme [158, 120], the fields at each time-steps are related via

$$\left(\delta - \frac{\Delta t}{2} D(U^{n+1})\right)_{i,j} \Phi_j^{n+1} = \left(\delta + \frac{\Delta t}{2} D(U^n)\right)_{i,j} \Phi_j^n \,, \tag{12.7}$$

where $\delta_{i,j}$ denotes the Kronecker delta ($\delta_{i,j} = 1$ if $i = j$ and $\delta_{i,j} = 0$ if $i \neq j$). The Crank-Nicholson advection operator (CN) can be rewritten

$$CN_{i,j}(U) = -\delta_{i,j} + \left[\left(\delta - \frac{\Delta t}{2} D(U^{n+1})\right)^{-1} \left(\delta + \frac{\Delta t}{2} D(U^n)\right)\right]_{i,j} . \tag{12.8}$$

The corresponding conservative operator (CCN) is then

$$CCN_{i,j}(U) = -\delta_{i,j} + \left[\left(\delta + \frac{\Delta t}{2} {}^{\mathrm{t}}D(-U^n)\right) \left(\delta - \frac{\Delta t}{2} {}^{\mathrm{t}}D(-U^{n+1})\right)^{-1}\right]_{i,j} . \tag{12.9}$$

12.2.2 Conservative semi-Lagrangian scheme in one dimension

Let us now turn to semi-Lagrangian schemes. The conservative method can be used to generate conservative scheme from a semi-Lagrangian algorithm. In one dimension, the CIR scheme [115], which is equivalent to the upwind scheme, will be used to show how a conservative CIR ($CCIR$) scheme can be built. The resulting $CCIR$ scheme will then be tested on a simple numerical simulation.

In order to be stable, advection algorithm must transport information in the direction of the flow. The CIR scheme satisfies this condition by adapting its stencil according to the direction of the velocity following the characteristic. For advection equation in one dimension (e.g. [159]), the CIR scheme is:

$$\Phi_i^{n+1} = \Phi_i^n + CIR_{i,j}\Phi_j^n = \Phi_i^n + (U_i^+\Phi_{i-1} - |U_i|\Phi_i^n - U_i^-\Phi_{i+1}^n)\,, \tag{12.10}$$

with $U_i^+ = \max(U_i, 0)$ and $U_i^- = \min(U_i, 0)$. To leading order, this scheme yields the diffusive error term

$$[\partial_t\Phi + u\partial_x(\Phi)]_{CIR} \simeq \frac{\Delta x}{2}\,|u|\partial_x\left[(1 - \boldsymbol{u}a)\,\partial_x\Phi\right]\,. \tag{12.11}$$

The scheme is consistent with the advection equation, but it is not conservative. The conservative counterpart of the CIR scheme can be built by changing the sign of the velocity and transposing the $CIR_{i,j}$ matrix. The expression of the $CCIR$ scheme is:

$$\Phi_i^{n+1} = \Phi_i^n + CCIR_{i,j}\Phi_j^n = \Phi_i^n + (U_{i-1}^+\Phi_{i-1}^n - |U_i|\Phi_i^n - U_{i-1}^-\Phi_{i+1}^n)\,. \tag{12.12}$$

The $CCIR$ scheme is conservative because it is column-balanced by construction. Similarly to the CIR scheme, the $CCIR$ scheme has a diffusive error. As expected, the $CCIR$ error term is the adjoint of the CIR error term:

$$[\partial_t\Phi + \partial_x(u\Phi)]_{CCIR} \simeq \frac{\Delta x}{2}\,\partial_x\left[(1 - \boldsymbol{u}a)\,\partial_x(|u|\Phi)\right]\,. \tag{12.13}$$

The $CCIR$ scheme was tested using a velocity profile $u(t;x) = \sin(2\pi x)$ and a uniform passive scalar $\Phi(t=0;x) = 1$. It conserved the total mass, M/M_0, near unity up to machine precision. This is not the case of the CIR scheme for varying velocities:

$$\Phi_i^{n+1} = \Phi_i^n + \tfrac{U_{i-1}}{U_i}(U_i^+\Phi_{i-1}^n) - (|U_i|\Phi_{i-1}^n) + \tfrac{U_{i+1}}{U_i}(U_i^-\Phi_{i-1}^n)\,. \tag{12.14}$$

In the same manner, the second-order (dispersive) Lax-Wendroff scheme (LW), which takes the form:

$$\begin{aligned}\Phi_i^{n+1} = &\left(\tfrac{U^+}{U}\tfrac{U(1+U)}{2}\right)_i\Phi_{i-1}^n + \left(\tfrac{U^+}{U}(1-U^2)\right)_i\Phi_i^n - \left(\tfrac{U^+}{U}\tfrac{U(1-U)}{2}\right)_i\Phi_{i+1}^n \\ &+ \left(\tfrac{U^-}{U}\tfrac{U(1+U)}{2}\right)_i\Phi_{i+1}^n + \left(\tfrac{U^-}{U}(1-U^2)\right)_i\Phi_i^n - \left(\tfrac{U^-}{U}\tfrac{U(1-U)}{2}\right)_i\Phi_{i-1}^n\,,\end{aligned} \tag{12.15}$$

can be transformed into a conservative LW scheme (CLW), of the form,

$$\begin{aligned}\Phi_i^{n+1} = &\left(\tfrac{U^+}{U}\tfrac{U(1+U)}{2}\Phi^n\right)_{i-1} + \left(\tfrac{U^+}{U}(1-U^2)\Phi^n\right)_i - \left(\tfrac{U^+}{U}\tfrac{U(1-U)}{2}\Phi^n\right)_{i+1} \\ &+ \left(\tfrac{U^-}{U}\tfrac{U(1+U)}{2}\Phi^n\right)_{i+1} + \left(\tfrac{U^-}{U}(1-U^2)\Phi^n\right)_i - \left(\tfrac{U^-}{U}\tfrac{U(1-U)}{2}\Phi^n\right)_{i-1}\,.\end{aligned} \tag{12.16}$$

In the same way, the third-order (hyperdiffusive) semi-Lagrangian Dahlquist and Björck scheme (DB) (e.g. [120, 160]):

$$\begin{aligned}\Phi_i^{n+1} = &-\left(\frac{U^+}{U}\frac{U(1-U^2)}{6}\right)_i \Phi_{i-2}^n + \left(\frac{U^+}{U}\frac{U(1+U)(2-U)}{2}\right)_i \Phi_{i-1}^n \\ &+\left(\frac{U^+}{U}\frac{(1-U^2)(2-U)}{2}\right)_i \Phi_i^n - \left(\frac{U^+}{U}\frac{U(1-U)(2-U)}{6}\right)_i \Phi_{i+1}^n \\ &-\left(\frac{U^-}{U}\frac{U(1-U^2)}{6}\right)_i \Phi_{i+2}^n + \left(\frac{U^-}{U}\frac{U(1+U)(2-U)}{2}\right)_i \Phi_{i+1}^n \\ &+\left(\frac{U^-}{U}\frac{(1-U^2)(2-U)}{2}\right)_i \Phi_i^n - \left(\frac{U^-}{U}\frac{U(1-U)(2-U)}{6}\right)_i \Phi_{i-1}^n ,\end{aligned} \tag{12.17}$$

has the following conservative counterpart (CDB):

$$\begin{aligned}\Phi_i^{n+1} = &-\left(\frac{U^+}{U}\frac{U(1-U^2)}{6}\Phi^n\right)_{i-2} + \left(\frac{U^+}{U}\frac{U(1+U)(2-U)}{2}\Phi^n\right)_{i-1} \\ &+\left(\frac{U^+}{U}\frac{(1-U^2)(2-U)}{2}\Phi^n\right)_i - \left(\frac{U^+}{U}\frac{U(1-U)(2-U)}{6}\Phi^n\right)_{i+1} \\ &-\left(\frac{U^-}{U}\frac{U(1-U^2)}{6}\Phi^n\right)_{i+2} + \left(\frac{U^-}{U}\frac{U(1+U)(2-U)}{2}\Phi^n\right)_{i+1} \\ &+\left(\frac{U^-}{U}\frac{(1-U^2)(2-U)}{2}\Phi^n\right)_i - \left(\frac{U^-}{U}\frac{U(1-U)(2-U)}{6}\Phi^n\right)_{i-1} .\end{aligned} \tag{12.18}$$

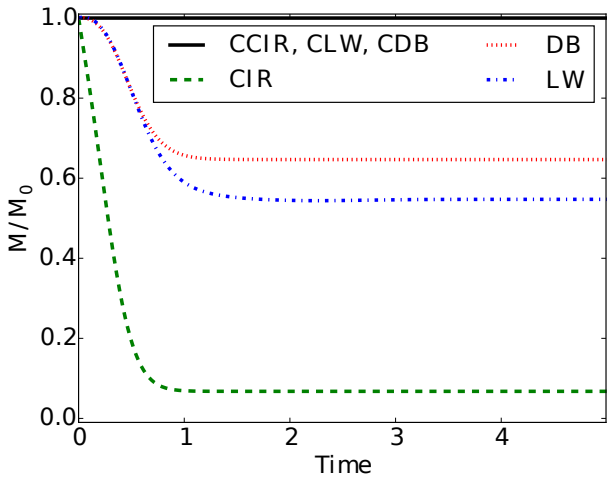

Figure 12.1 – Comparison of the total mass evolution for the 1D transport problem with $u = \sin(x)$ and $\Phi(t = 0) = 1$ for conservative and non-conservative semi-Lagrangian schemes of various orders (the CFL number is here fixed to 0.75).

These schemes are compared in fig. 12.1-12.3. First, we consider the evolution of the total mass in a simple test case of a periodic flow of the form $u = \sin(x)$ with a constant initial distribution of mass $\Phi(t = 0; x) = 1$. This is illustrated in fig. 12.1. The conservative property of the $CCIR$, CLW and CDB schemes is highlighted by the plot of the total mass which remains constant equal to its initial value. Fig. 12.2 shows standard tests of advection in a periodic domain of a Heaviside, piece-wise affine and cosine functions. The diffusive or dispersive behaviors generated by the order error term are confirmed. The order can be quantified with more details by considering

the error on the amplitude and the phase of the cosine profile (*e.g.* [161]). Fig. 12.3 illustrates that the order of the original scheme is maintained for its conservative counterpart.

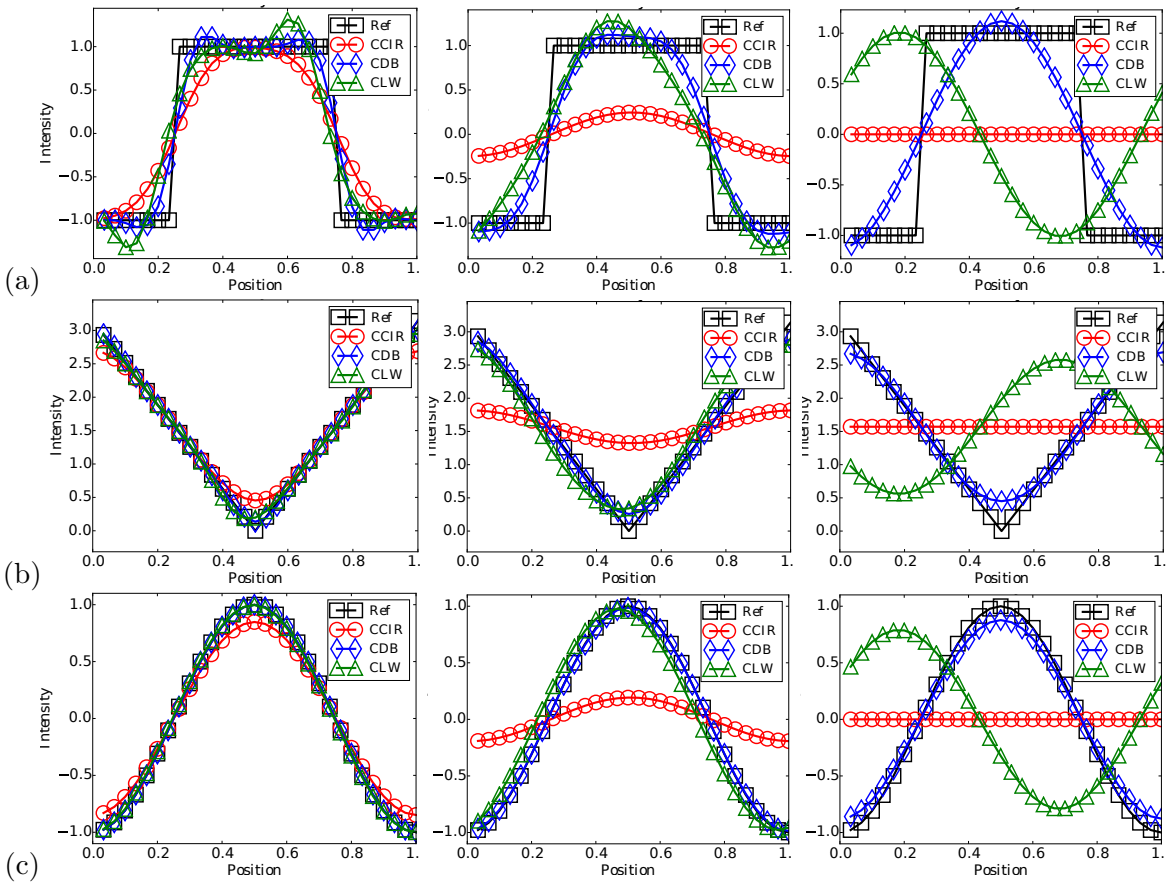

Figure 12.2 – Advection in a periodic domain with periodic boundary conditions. The advection velocity is constant and the initial profile takes the form of a Heaviside (a), a piece-wise affine (b), a cosine (c) function. Graphs from left to right correspond to 1, 10 and 100 periods of the flow respectively.

In order to generalize theses scheme to CFL numbers greater than unity, the interpolation point has to be shifted by a integer number of grid spaces, using

$$\widetilde{U}_i = [(u_i \Delta t)/\Delta x] \,\%1 \quad , \quad j = i - u_i \Delta t/\Delta x + \widetilde{U}_i \,, \tag{12.19}$$

$$\text{where} \quad \widetilde{U}_i^+ = \max(\widetilde{U}_i,\, 0) \quad , \quad \widetilde{U}_i^- = \min(\widetilde{U}_i,\, 0)\,. \tag{12.20}$$

For example, the conservative CIR scheme then becomes

$$\Phi_i^{n+1} = \Phi_j^n + \left[(\widetilde{U}^+ \Phi^n)_{j-1} - (|\widetilde{U}| \Phi^n)_j - (\widetilde{U}^- \Phi^n)_{j+1} \right] . \tag{12.21}$$

Similar expressions follow for the other schemes. The density profiles of the simulation using CFL numbers above unity are presented in fig.12.4 in the case of an initial cosine profile.

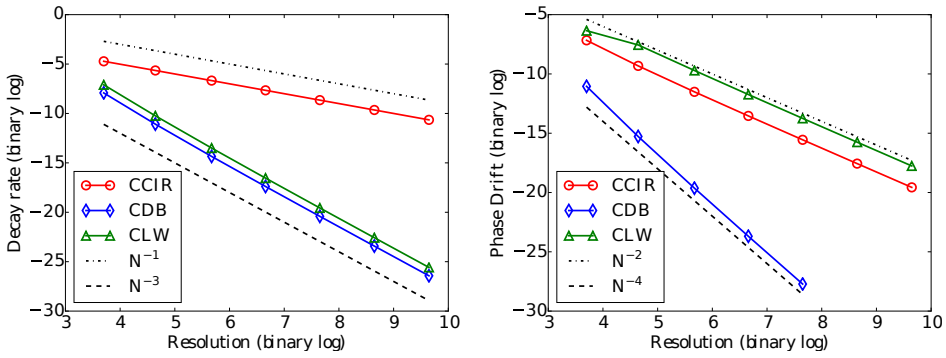

(a) Growth-rate (b) Phase-drift

Figure 12.3 – Decay rate (loss in amplitude) and phase shift per unit of time for the test cases presented in fig. 12.2 at time $t = 5$. The nature of the leading order error term (diffusive or dispersive) is clearly highlighted.

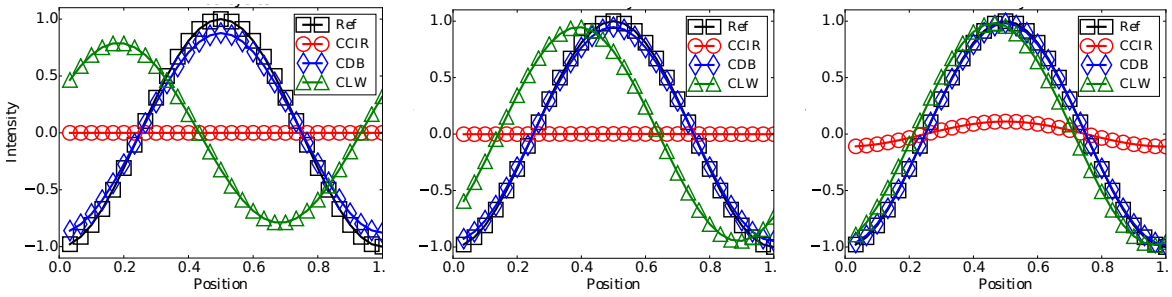

(a) CFL= 0.75 (b) CFL= 2.5 (c) CFL= 7.5

Figure 12.4 – Advection of a cosine function over 100 periods of the flow with a CFL number of 0.75 (a), 2.5 (b), and 7.5 (c).

12.2.3 Extension in higher dimensions

The standard reconstruction used with the CIR scheme is a bilinear reconstruction. It takes the form:

$$\begin{aligned}\Phi_{i,j}^{n+1} =& [(1-Ua)(1-|V|)\Phi^n]_{i,j}[Ua(1-|V|)]_{i,j}\Phi_{\alpha,j}^n \\ &+ [(1-Ua)|V|]_{i,j}\Phi_{i,\beta}^n + [Ua|V|]_{i,j}\Phi_{\alpha,\beta}^n\,,\end{aligned} \tag{12.22}$$

where $V_i = v_i\Delta t/\Delta x$, $\alpha = i - sign(u_{i,j})$ and $\beta = j - sign(v_{i,j})$.

The above stencil can be interpreted using the geometric construction presented in fig. 12.5(a). Semi-Lagrangian schemes require to reconstruct the field at the backward-advected points $\mathbf{x}_{i,j} - \mathbf{u}_{i,j}\Delta t$. Considering a CFL number smaller than unity, the reconstruction point necessarily lies in one of the cells surrounding $\mathbf{x}_{i,j}$. This point naturally splits the cell in four parts. The weight of each node in the bilinear interpolation eq. (12.22) corresponds to the ratio of the surface of the rectangle opposite to this node normalised by the total surface of the computational cell. This graphical interpretation of eq. (12.22) is illustrated on fig. 12.5(a) the backward displacement $-\mathbf{u}_{i,j}\Delta t$ being indicated with a dashed line.

Let us now turn to the conservative scheme, the two-dimensional version of the $CCIR$ scheme can be expressed as:

$$\begin{aligned}\Phi_{i,j}^{n+1} &= [|U^+||V^+|\Phi^n]_{i-1,j-1} + [|U^+|(1-|V|)\Phi^n]_{i-1,j} + [|U^+||V^-|\Phi^n]_{i-1,j+1} \\ &+ [(1-|U|)|V^+|\Phi^n]_{i,j-1} + [(1-|U|)(1-|V|)\Phi^n]_{i,j} + [(1-|U|)|V^-|\Phi^n]_{i,j+1} \\ &+ [|U^-||V^+|\Phi^n]_{i+1,j-1} + [|U^-|(1-|V|)\Phi^n]_{i+1,j} + [|U^-||V^-|\Phi^n]_{i+1,j+1}\,. \end{aligned} \quad (12.23)$$

It is enlighting to interpret this formula geometrically. The weights now correspond to the forward displacement $\mathbf{u}_{i,j}\Delta t$, indicated with a solid line on fig. 12.5(b). Again the weight of each term is given by the relative surface of the rectangle opposite to the advected vertex, normalized by the total surface of the computational cell. The key distinction is however that the computed weight corresponds to the contribution of $\Phi_{i,j}$ to the time evolution of its neighbors. This contrasts with the CIR scheme, for which the computed weights correspond to the contribution of each neighbor to the evolution of $\Phi_{i,j}$.

In fig. 12.5, mass conservation appears as a direct consequence of the fact that the sum of each sub-rectangle amounts to the total cell as highlighted by expression (12.23). Let us stress that this approach results in a conservative non-split semi-Lagrangian formulation.

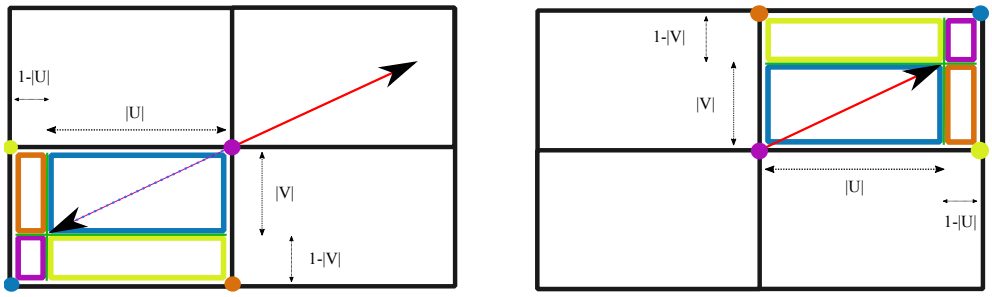

(a) Advection sketch (b) Continuity sketch

Figure 12.5 – Illustration of the reconstruction strategy and computational weights for the standard CIR scheme (a) and its conservative $CCIR$ counterpart (b). The red arrow corresponds to the forward advection. The color of a rectangle indicates its contribution to the evolution of a given point with the same color (see text).

A few observations can be made on this stencil. First, this rather simple geometric interpretation can be generalized to higher dimensions. Second, the two-dimensional $CCIR$ stencil of eq. (12.23) is identical to the split formula corresponding to the composition of two one-dimensional $CCIR$ stencils, $CCIR_{xy} = CCIR_x \circ CCIR_y = CCIR_y \circ CCIR_x$. Such is not the case for the CIR stencil. This commuting property can be used to generalize the higher-order conservative schemes from section 12.2.2 to higher dimensions of space.

To illustrate the conservative property of the $CCIR$ scheme in two dimensions of space, it was tested using an incompressible velocity profile of the form $u(t;x,y) = -\sin(\pi x)\cos(2\pi y)$, $v(t;x,y) = \cos(\pi x)\sin(2\pi y)$. The initial passive scalar field takes the form of a uniform patch $\Phi(t=0;x,y) = 1$ if $|x-0.5| \leq 0.15$ and $|y-0.3| \leq 0.15$, and 0 elsewhere (see fig. 12.6.a).

Since the flow is incompressible, the advection and continuity equation are equivalent. We thus compare the three schemes discussed in section 12.2.2 and their conservative counterparts. In fig. 12.6(b), the evolution of relative total mass of the CIR, LW and DB schemes is represented. As expected, the conservative schemes have a relative mass equal to unity, up to machine precision for the same set of parameters.

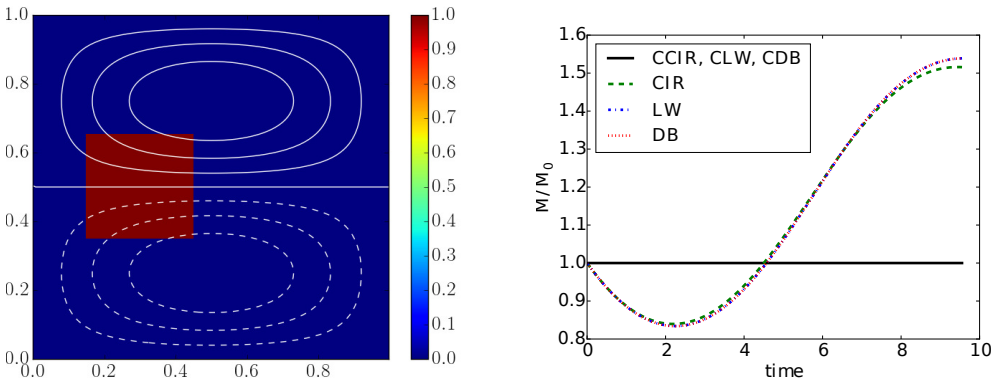

(a) Initial density profile

(b) Mass evolution with time

Figure 12.6 – Two-dimensional transport of a density distribution initially uniform within a square (a). The total mass evolution with time up to $t = 10$ with a resolution of 128^3 for conservative and non-conservative semi-Lagrangian schemes of first, second and third order (b) reflects the conservative nature of the schemes.

In fig. 12.7, color-plots of the density profile are given for all schemes at $t = 10$. The evolution of mass in the plan of symmetry is different for all schemes. The accumulation of mass near the stagnation point is clearly visible with the conservative schemes of odd orders, see figs. 12.7(d) and 12.7(f). Dispersive effects in fig. 12.7(e), which do not vanish in the symmetry plane, are still too strong to allow for this feature to emerge.

The explicit scheme introduced in eq. (12.23) corresponds to a first-order time integration. We should stress however that the modified reconstruction strategy introduced to enforced conservativity only concerns the spatial operator. The conservative property is thus retrained for higher order or multi-level time-stepping algorithms as shown in eqs.(12.8) and (12.9).

In fig. 12.8, convergence effects can clearly be identified by comparing results obtained with the $CCIR$ scheme (conservative, first order) with a fine grid (1024^2), to the ones obtained with a coarser grid (128^2) or with the CDB scheme (conservative, third order). At low resolution, owing to the effects of the numerical diffusion, the density on fig. 12.8(a) appears to be spread across three independent lobes. Increasing the resolution, or using a higher-order scheme, reveals the fine filaments of mass connecting these lobes.

Varying the resolution, the convergence of the density profile is tested for the conservative diffusive monotone $CCIR$ scheme at CFL= 1.6 in fig. 12.9. As the resolution increases at constant CFL, the numeric error decreases and the density profile becomes closer to the analytic solution. At high resolution, the grid is finer, the simulation is therefore more precise and catches the details of the structure near the symmetry axis.

At a resolution of 256^2, the $CCIR$ is able to get accurately the profile for CFL num-

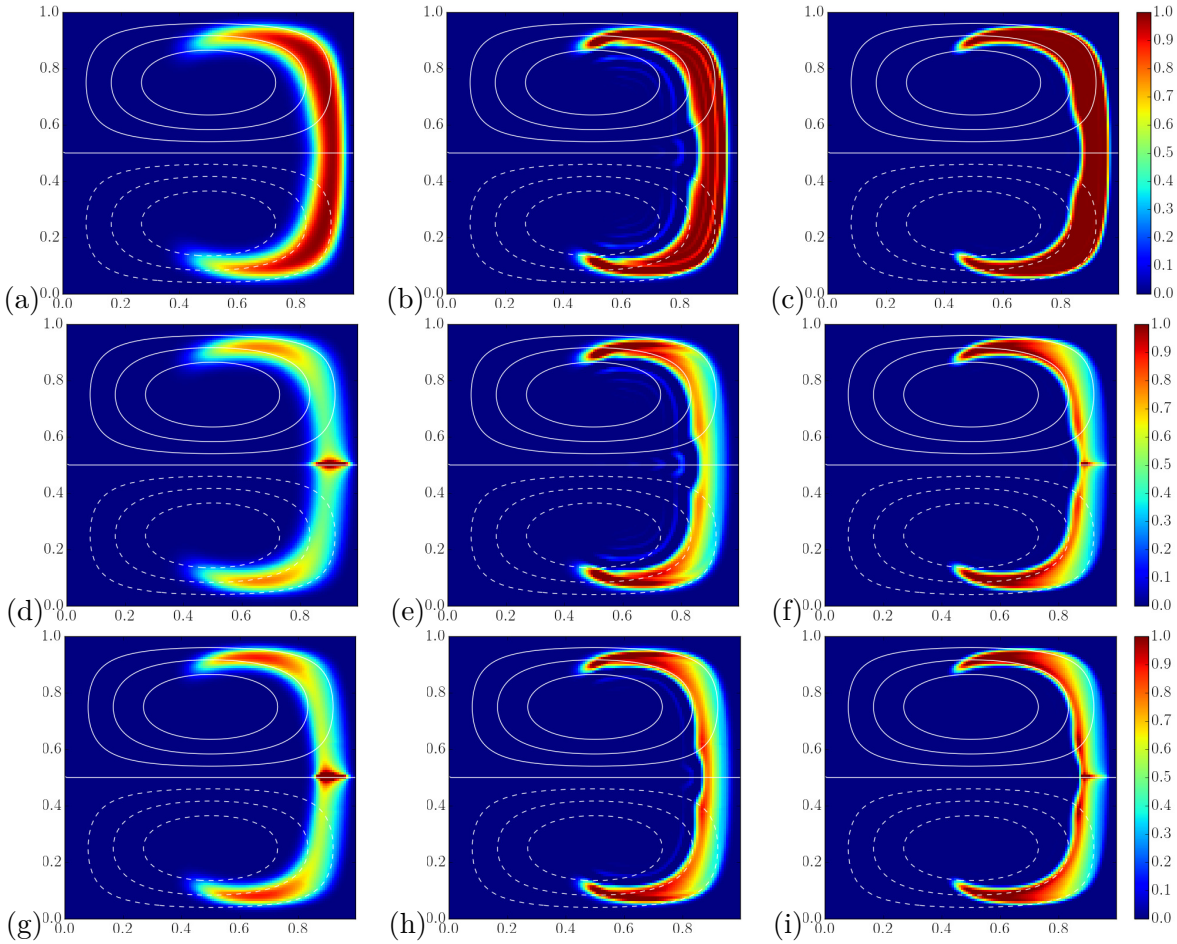

Figure 12.7 – A comparison of the non-conservative scheme at CFL= 0.8 (a,b,c) with the conservative scheme at CFL= 0.8 (d,e,f) and at CFL= 1.6 (g,h,i). The simulations were carried out at a resolution of 128^2 for an integration time of $t = 10$.

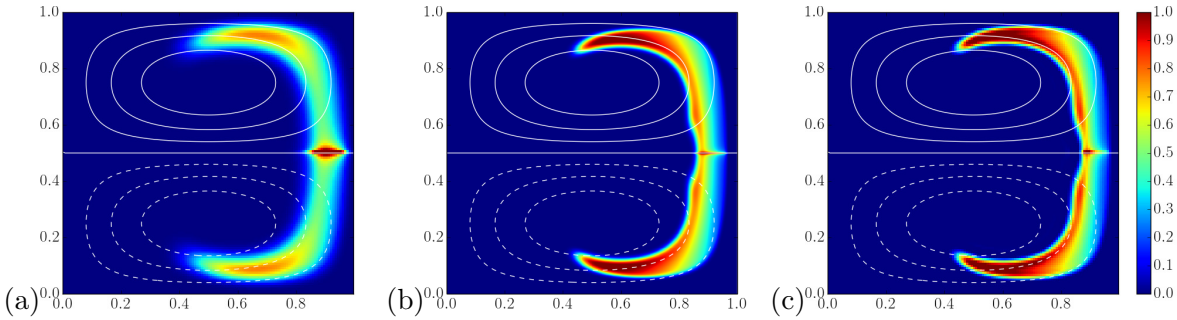

Figure 12.8 – Comparison of the first-order conservative $CCIR$ scheme with the third-order conservative CDB scheme at CFL= 0.8. Plots (a) and (b) compare simulations of resolution 128^2 and 1024^2 respectively for the $CCIR$ scheme; plot (c) presents the same setup solved with the CDB scheme at a resolution of 128^2.

bers above unity. Fig. 12.10 shows the profile computed for CFL up to 8. Comparing

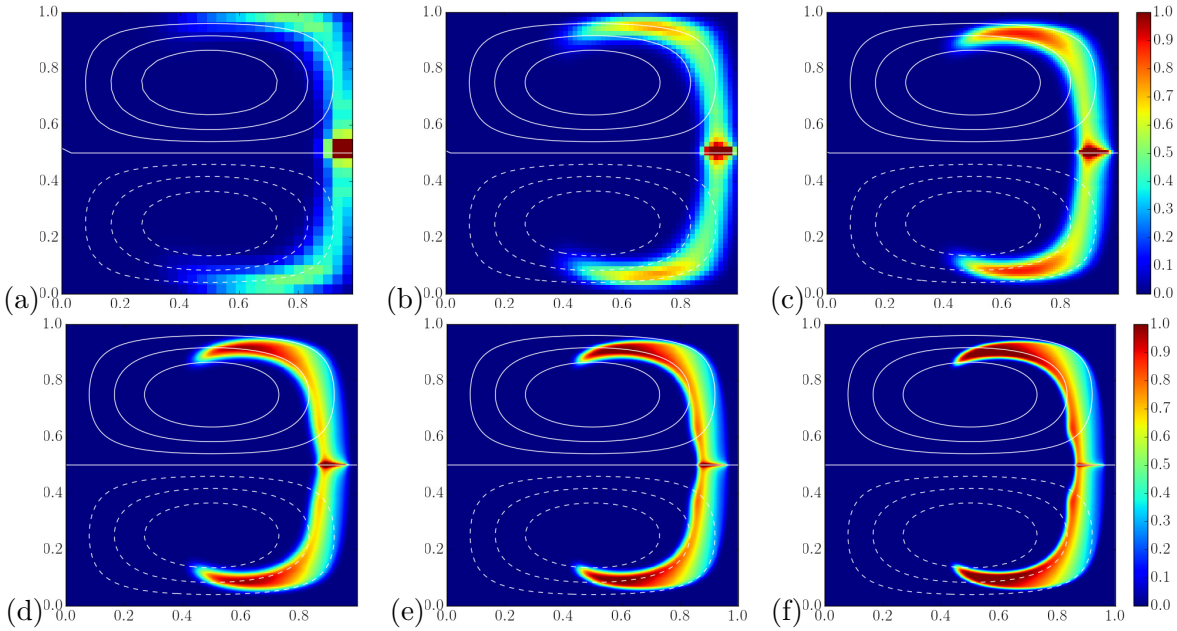

Figure 12.9 – Convergence study for the first-order conservative $CCIR$ at CFL= 1.6 with resolutions: $(a) : 32^2$, $(b) : 64^2$, $(c) : 128^2$, $(d) : 256^2$, $(e) : 512^2$, $(f) : 1024^2$.

the profiles on figs. 12.9 and 12.10 with the profile of the 1024^2 resolution simulation at CFL= 0.8 of fig. 12.8(b), the conservative schemes are able to model the flow for CFL> 1 with great accuracy. The good agreement between the simulations is not restricted to the profile, it also extents to the total mass which is conserved up to machine precision.

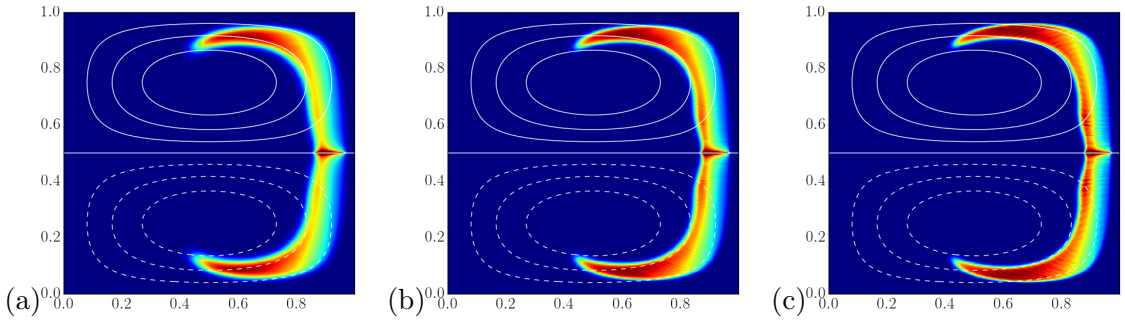

Figure 12.10 – Comparison the profile of simulations using the first-order $CCIR$ scheme at a resolution of 256^2 for different CFL: $(a) : 1.6$, $(b) : 4.0$, $(c) : 8.0$.

Semi-Lagrangian algorithms are composed of two main steps [162, 163, 150]: the computation of the characteristic curves, and the reconstruction step. The present work focused on making the reconstruction step conservative. All the simulations carried out used the $2D$-generalization of eq. (12.19)-(12.20). Even though the trajectories were computed with a law order method, the algorithm can be adapted to more sophisticated methods. To do so, the trajectory in each point can be reconstructed using high order characteristics (*e.g.* [150]) and the resulting displacement should be

decomposed as the sum of: (i) a vector whose components are equal to an integer number of grid-steps, and (ii) a remainder vector whose components are smaller than the grid-step.

12.3 Perspectives

We have introduced a systematic approach to derive a conservative scheme without the need for a finite volume discretisation. The method has been successfully applied to semi-Lagrangian schemes, which are notorious for being very efficient, but usually not conservative. Using this method, we were able to built a third-order conservative semi-Lagrangian scheme based on the scheme introduced by Dahlquist and Björck.

The approach presented here is similar in the spirit to that introduced by Verstappen *et al.* in [164] to derive energy-preserving schemes. They also used an adjoint formulation to derive the discrete scheme. As their concern is the conservation of energy, they insist of the skew symmetry property of the operator. We are here rather concerned with mass conservation and therefore focus on the column-balanced property of the scheme.

Our approach also bears similarities with ideas introduced by Shashkov in the support operators method [154] or by Carpenter [155, 156]. It however differs from the support operator method, in that we propose an algorithm (via the discretisation of the adjoint equation) to systematically transform a non-conservative advection scheme into a continuity preserving operator.

12.4 Appendix (convergence study)

In order to illustrate the order of convergence of the conservative schemes introduced in section 12.2.2 in 2D, we perform a numerical study with varying resolution. The initial distribution takes the form $\cos(x+y)$ and the flow is uniform with $u_x = u_y = 1$. The results are illustrated in fig. 12.11.

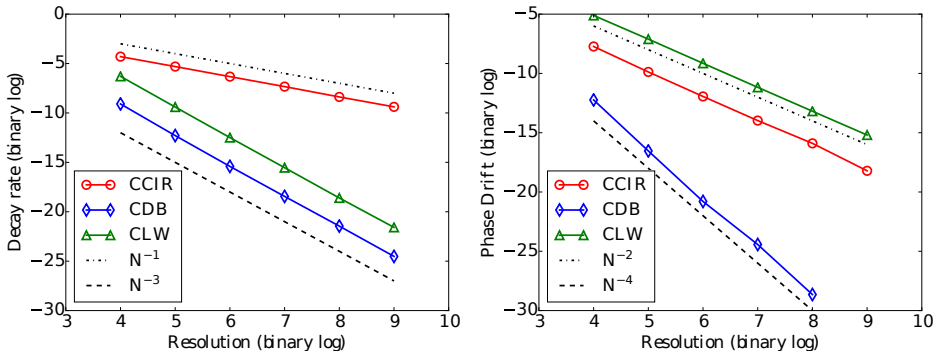

(a) Growth-rate (b) Phase-drift

Figure 12.11 – Decay rate (loss in amplitude) and phase shift per unit of time for a 2D test case, the initial distribution takes the form $\cos(x+y)$ and the flow is uniform with $u_x = u_y = 1$.

Part F

References

Acknowledgments

I would like to thank all those who helped me scientifically during these past three years. Marc-Étienne and $A\lambda\acute{\epsilon}\xi\alpha\nu\delta\rho o\varsigma$, thank you for answering my questions and asking more questions. Ludovic, thank you for your good humor and your good advice. Emmanuel, thank you for the work done at the end of my master degree. Pablo and Stéphan, thank you for helping set my research on the right direction. Ismaël and Raphaël, thank you for having shared your insight and your tricks. François and Christophe, thank you for having animated the lunch break with your discussion. Benoit, Guillaume, Florence, Kannabiran, Melissa and Mickaël, thank you all. You gave life to the workplace where we worked. I would also like to thank the LRA for allowing me to work within their office. Finally, I would like to thank Constance and the long list of family members and friends who supported me personally during these past three years.

This work was granted access to the HPC resources of MesoPSL financed by the Region Ile de France and the project Equip@Meso (reference ANR-10-EQPX-29-01) of the programme Investissements d'Avenir supervised by the Agence Nationale pour la Recherche and the HPC resources of GENCI-TGCC-CURIE & GENCI-CINES-JADE (Project No. x20162a7620) where the present numerical simulations were performed.

List of Figures

Bibliography

[1] H. A. Rose et P. L. Sulem, "Fully developed turbulence and statistical mechanics," Journal de Physique **39**, 441–484 (1978). 0.1, 0.1, 1.1, 1

[2] L. F. Richardson, *Weather Prediction by Numerical Process* (Cambridge University Press, 2007). 0.1, 1

[3] U. Frisch, *Turbulence : The Legacy of A. N. Kolmogorov* (Cambridge University Press, 1995). 0.1, 0.1, 0.5, 1, 1, 1.5, 2, 5.1, 9.1

[4] A. N. Kolmogorov, "The local structure of turbulence in incompressible viscous fluid for very large Reynolds numbers," dans "Dokl. Akad. Nauk SSSR," , vol. 30 (JSTOR, 1941), vol. 30, p. 301–305. 0.1, 1, 9.1

[5] F. H. Champagne, "The fine-scale structure of the turbulent velocity field," Journal of Fluid Mechanics **86**, 67–108 (1978). 0.1, 1, 9.1

[6] Y. Kaneda, T. Ishihara, M. Yokokawa, K. Itakura, et A. Uno, "Energy dissipation rate and energy spectrum in high resolution direct numerical simulations of turbulence in a periodic box," Physics of Fluids **15**, L21–L24 (2003). 0.1, A, 1, 1, 9.1

[7] A. S. Monin, "The Theory of Locally Isotropic Turbulence," Soviet Physics Doklady **4**, 271 (1959). 0.1, 1

[8] T. d. Karman et L. Howarth, "On the Statistical Theory of Isotropic Turbulence," Proceedings of the Royal Society of London A: Mathematical, Physical and Engineering Sciences **164**, 192–215 (1938). 0.1, 1

[9] K. R. Sreenivasan, S. I. Vainshtein, R. Bhiladvala, I. San Gil, S. Chen, et N. Cao, "Asymmetry of Velocity Increments in Fully Developed Turbulence and the Scaling of Low-Order Moments," Physical Review Letters **77**, 1488–1491 (1996). 0.1, 1

[10] D. Forster, D. R. Nelson, et M. J. Stephen, "Large-distance and long-time properties of a randomly stirred fluid," Physical Review A **16**, 732–749 (1977). A, 1, 9.1, D

[11] R. H. Kraichnan, "Helical turbulence and absolute equilibrium," JFM **59**, 745–752 (1973). A, A, 0.3.1, 1, 1, 7, 7.3, 9.1, 9.1, 9.2.1.1, 9.2.2.3

[12] R. H. Kraichnan et S. Chen, "Is there a statistical mechanics of turbulence?" Physica D: Nonlinear Phenomena **37**, 160–172 (1989). A, 1, 9.1

[13] U. Frisch, Z. S. She, et P. L. Sulem, "Large-scale flow driven by the anisotropic kinetic alpha effect," Physica D: Nonlinear Phenomena **28**, 382–392 (1987). A, 0.2.1, 0.2.4, 1, 3.2, 3.2, 5.1, 5.2.3, 5.3.1

[14] U. Frisch, H. Scholl, Z. S. She, et P. L. Sulem, "A new large-scale instability in three-dimensional incompressible flows lacking parity-invariance," Fluid Dynamics Research **3**, 295–298 (1988). A, 0.2.1, 1, 3.2, 5.1

[15] T. Dombre, U. Frisch, J. M. Greene, M. Henon, A. Mehr, et A. M. Soward, "Chaotic streamlines in the ABC flows," Journal of Fluid Mechanics **167**, 353–391 (1986). A, 0.2.3, 0.2.4, 1, 5.3.5, 9.1, 9.2.3.2

[16] M. Steenbeck, F. Krause, et K.-H. Rädler, "Berechnung der mittleren Lorentz-Feldstarke fur ein elektrisch leitendes Medium in turbulenter, durch Coriolis-Krafte beeinflusster Bewegung," Zeitschrift fur Naturforschung A **21**, 369–376 (1966). A, 0.2.1, 1, 3.1, 5.1, 6.1

[17] S. Childress, "A class of solutions of the magnetohydrodynamic dynamo problem," The Application of Modern Physics to the Earth and Planetary Interiors p. 629–648 (1969). A, 0.2.1, 1, 3.1, 6.1

[18] H. Tennekes, "Eulerian and Lagrangian time microscales in isotropic turbulence," Journal of Fluid Mechanics **67**, 561–567 (1975). A, 1, 8.2.1

[19] R. H. Kraichnan, "Eddy Viscosity in Two and Three Dimensions," Journal of the Atmospheric Sciences **33**, 1521–1536 (1976). A, 1, 5.1

[20] R. Rubinstein et Y. Zhou, "Effects of helicity on Lagrangian and Eulerian time correlations in turbulence," Physics of Fluids **11**, 2288–2290 (1999). A, 1

[21] C. L. Fefferman, "Existence and smoothness of the Navier-Stokes equation," The millennium prize problems p. 57–67 (2006). 1, 10.1

[22] P. G. Saffman, "The large-scale structure of homogeneous turbulence," Journal of Fluid Mechanics **27**, 581–593 (1967). 1

[23] G. K. Batchelor, "The role of big eddies in homogeneous turbulence," dans "Proceedings of the Royal Society of London A: Mathematical, Physical and Engineering Sciences," , vol. 195 (The Royal Society, 1949), vol. 195, p. 513–532. 1

[24] H. K. Moffatt, *Field Generation in Electrically Conducting Fluids* (Cambridge University Press, Cambridge, London, New York, Melbourne, 1978). 2, 5.1, 6.1

[25] H. K. Moffatt, "The degree of knottedness of tangled vortex lines," Journal of Fluid Mechanics **35**, 117–129 (1969). 2.3

[26] A. Craya, "Contribution a l'analyse de la turbulence associee a des vitesses moyennes," Thesis, Universite de Grenoble (1957). 2.3, 8.2.3, 9.2.1.1, 9.2.1.1, 9.2.1.2, 9.2.2.3, 9.4.1

[27] J. Herring, "Approach of axisymmetric turbulence to isotropy," The Physics of Fluids **17**, 859–872 (1974). 2.3, 8.2.3, 9.2.1.1, 9.2.1.1, 9.2.1.2, 9.2.2.3, 9.4.1

[28] F. Waleffe, "The nature of triad interactions in homogeneous turbulence," Physics of Fluids A: Fluid Dynamics **4**, 350–363 (1992). 2.3

[29] G. O. Roberts, "Spatially Periodic Dynamos," Philosophical Transactions of the Royal Society of London A: Mathematical, Physical and Engineering Sciences **266**, 535–558 (1970). 3.1, 5.3.2

[30] V. Shumaylova, R. J. Teed, et M. R. E. Proctor, "Large- to small-scale dynamo in domains of large aspect ratio: kinematic regime," Monthly Notices of the Royal Astronomical Society **466**, 3513–3518 (2017). 3.3

[31] G. Floquet, "Sur les equations differentielles lineaires a coefficients periodiques," Annales scientifiques de l'Ecole normale superieure **12**, 47–88 (1883). 4, 4.1, 5.1, 5.2.2, 6.2

[32] F. Bloch, "Uber die quantenmechanik der elektronen in kristallgittern," Zeitschrift fur Physik **52**, 555–600 (1929). 4, 5.1, 6.2

[33] G. D. Recktenwald, "The stability of parametrically excited systems : coexistence and trigonometrification," Thesis, Cornell University (2006). 4, 4.1, 4.1

[34] J. Yang, *Basic Floquet Theory* (University of Vermont, Burlington, Vermont, 2011). URL : http://www.emba.uvm.edu/~jxyang/teaching/Floquet_theory_Ward.pdf. 4, 4.1

[35] N. W. Ashcroft et N. D. Mermin, *Solid state physics* (Saunders College, 1976). 4, 4.2

[36] E. T. Whittaker et G. N. Watson, *A course of modern analysis* (Cambridge university press, 1996). 4.1

[37] E. W. Weisstein, *Mathieu Function* (MathWorld - A Wolfram Web Resource, 2017). URL : http://mathworld.wolfram.com/MathieuFunction.html. 4.1

[38] U. Frisch, "Fully developed turbulence and intermittency," dans "Turbulence and Predictability in Geophysical Fluid Dynamics and Climate Dynamics," (Elsevier, Amsterdam, North-Holland, 1985), p. 71–88. 5.1

[39] S. G. G. Prasath, S. Fauve, et M. Brachet, "Dynamo action by turbulence in absolute equilibrium," EPL (Europhysics Letters) **106**, 29002 (2014). URL : http://stacks.iop.org/0295-5075/106/i=2/a=29002. 5.1

[40] T. Lee, "On some statistical properties of hydrodynamical and magneto-hydrodynamical fields," Quart Appl Math **10**, 69–74 (1952). 5.1

[41] S. Orszag, "Analytical theories of turbulence," J. Fluid Mech. **41** (1970). 5.1

[42] R. H. Kraichnan, "Helical turbulence and absolute equilibrium," J. Fluid Mech **59**, 745–752 (1973). 5.1

[43] G. Krstulovic, P. D. Mininni, M. E. Brachet, et A. Pouquet, "Cascades, thermalization, and eddy viscosity in helical galerkin truncated euler flows," Phys. Rev. E **79**, 056304 (2009). URL : http://link.aps.org/doi/10.1103/PhysRevE.79.056304. 5.1

[44] V. Dallas, S. Fauve, et A. Alexakis, "Statistical equilibria of large scales in dissipative hydrodynamic turbulence," Phys. Rev. Lett. **115**, 204501 (2015). URL : http://link.aps.org/doi/10.1103/PhysRevLett.115.204501. 5.1

[45] B. Dubrulle et U. Frisch, "Eddy viscosity of parity-invariant flow," Physical Review A **43**, 5355–5364 (1991). 5.1, 5.2.3

[46] A. Wirth, S. Gama, et U. Frisch, "Eddy viscosity of three-dimensional flow," Journal of Fluid Mechanics **288**, 249–264 (1995). 5.1, 5.2.3

[47] A. Libin et G. Sivashinsky, "Long wavelength instability of the ABC-flows," Quarterly of Applied Mathematics **48**, 611–623 (1990). 5.2.3

[48] O. Podvigina et A. Pouquet, "On the non-linear stability of the 1:1:1 ABC flow," Physica D: Nonlinear Phenomena **75**, 471–508 (1994). 5.3.3.3, 5.3.5

[49] M. R. E. Proctor, P. C. Matthews, et A. M. Rucklidge, *Solar and Planetary Dynamos* (Cambridge University Press, 1992). 5.3.3.3

[50] C. Marchioro, "An example of absence of turbulence for any reynolds number," Communications in mathematical Physics **105**, 99–106 (1986). 5.3.3.3

[51] S. E. Jones et A. D. Gilbert, "Dynamo action in the ABC flows using symmetries," Geophysical & Astrophysical Fluid Dynamics **108**, 83–116 (2014). 5.3.5

[52] P. D. Mininni, A. Alexakis, et A. Pouquet, "Nonlocal interactions in hydrodynamic turbulence at high Reynolds numbers: The slow emergence of scaling laws," Physical review E **77**, 036306 (2008). 5.3.5, 5.5, 9.2.2, 9.2.2.3, 10.1

[53] P. D. Mininni, D. Rosenberg, R. Reddy, et A. Pouquet, "A hybrid MPI–OpenMP scheme for scalable parallel pseudospectral computations for fluid turbulence," Parallel Computing **37**, 316–326 (2011). 5.3.5, 5.5, 6.2, 9.2.2, 9.2.2.3, 10.1

[54] P. Charbonneau, "Solar Dynamo Theory," Annual Review of Astronomy and Astrophysics **52**, 251–290 (2014). 6.1

[55] M. Rieutord, "The solar dynamo," Comptes Rendus Physique **9**, 757–765 (2008). 6.1

[56] N. Weiss et M. Thompson, "The solar dynamo," dans "The Origin and Dynamics of Solar Magnetism," (Springer, 2008), p. 53–66. 6.1

[57] E. N. Parker, "Hydromagnetic dynamo models." The Astrophysical Journal **122**, 293 (1955). 6.1

[58] F. Krause et K. Rädler, "Mean-field magnetohydrodynamics and dynamo theory, 1980," Pergamon (1980). 6.1

[59] A. Lanotte, A. Noullez, M. Vergassola, et A. Wirth, "Large-scale dynamo produced by negative magnetic eddy diffusivities," Geophysical and Astrophysical Fluid Dynamics **91**, 131–146 (1999). 6.1

[60] A. Brun, M. Browning, M. Dikpati, H. Hotta, et A. Strugarek, "Recent advances on solar global magnetism and variability," Space Science Reviews **196**, 101–136 (2015). 6.1

[61] M. Dikpati et P. A. Gilman, "Simulating and predicting solar cycles using a flux-transport dynamo," The Astrophysical Journal **649**, 498 (2006). 6.1

[62] A. R. Choudhuri, P. Chatterjee, et J. Jiang, "Predicting solar cycle 24 with a solar dynamo model," Physical review letters **98**, 131103 (2007). 6.1

[63] M. Schrinner, K.-H. Rädler, D. Schmitt, M. Rheinhardt, et U. Christensen, "Mean-field view on rotating magnetoconvection and a geodynamo model," Astronomische Nachrichten **326**, 245–249 (2005). 6.1

[64] G. A. Glatzmaier, "Numerical simulations of stellar convective dynamos. ii-field propagation in the convection zone," The Astrophysical Journal **291**, 300–307 (1985). 6.1

[65] P. Gilman, "Dynamically consistent nonlinear dynamos driven by convection in a rotating spherical shell. ii-dynamos with cycles and strong feedbacks," The Astrophysical Journal Supplement Series **53**, 243–268 (1983). 6.1

[66] A. S. Brun, M. S. Miesch, et J. Toomre, "Global-scale turbulent convection and magnetic dynamo action in the solar envelope," The Astrophysical Journal **614**, 1073 (2004). 6.1

[67] M. K. Browning, M. S. Miesch, A. S. Brun, et J. Toomre, "Dynamo action in the solar convection zone and tachocline: pumping and organization of toroidal fields," The Astrophysical Journal Letters **648**, L157 (2006). 6.1

[68] M. Ghizaru, P. Charbonneau, et P. K. Smolarkiewicz, "Magnetic cycles in global large-eddy simulations of solar convection," The Astrophysical Journal Letters **715**, L133 (2010). 6.1

[69] M. S. Miesch et J. Toomre, "Turbulence, magnetism, and shear in stellar interiors," Annual Review of Fluid Mechanics **41**, 317–345 (2009). 6.1

[70] M. Schrinner, K.-H. Rädler, D. Schmitt, M. Rheinhardt, et U. R. Christensen, "Mean-field concept and direct numerical simulations of rotating magnetoconvection and the geodynamo," Geophysical & Astro Fluid Dynamics **101**, 81–116 (2007). 6.1

[71] M. Rheinhardt et A. Brandenburg, "Test-field method for mean-field coefficients with MHD background," Astronomy and Astrophysics **520**, A28 (2010). 6.1

[72] S. Sur, A. Brandenburg, et K. Subramanian, "Kinematic α-effect in isotropic turbulence simulations," Monthly Notices of the Royal Astronomical Society **385**, L15–L19 (2008). 6.1

[73] A. Brandenburg, K.-H. Rädler, et M. Schrinner, "Scale dependence of alpha effect and turbulent diffusivity," Astronomy & Astrophysics **482**, 739–746 (2008). 6.1

[74] S. Boldyrev, F. Cattaneo, et R. Rosner, "Magnetic-Field Generation in Helical Turbulence," Physical Review Letters **95**, 255001 (2005). 6.2

[75] A. Courvoisier, D. W. Hughes, et S. M. Tobias, "α Effect in a Family of Chaotic Flows," Physical Review Letters **96**, 034503 (2006). 6.2

[76] D. W. Hughes, "The mean electromotive force at high magnetic reynolds numbers," Plasma Physics and Controlled Fusion **50**, 124021 (2008). 6.2

[77] F. Cattaneo et D. W. Hughes, "Problems with kinematic mean field electrodynamics at high magnetic reynolds numbers," Monthly Notices of the Royal Astronomical Society **395**, L48–L51 (2009). 6.2

[78] F. Cattaneo et S. Tobias, "On large-scale dynamo action at high magnetic reynolds number," The Astrophysical Journal **789**, 70 (2014). 6.2

[79] Y. Ponty et F. Plunian, "Transition from large-scale to small-scale dynamo," Physical review letters **106**, 154502 (2011). 6.2

[80] D. Galloway et U. Frisch, "A numerical investigation of magnetic field generation in a flow with chaotic streamlines," Geophysical and Astrophysical Fluid Dynamics **29**, 13–18 (1984). 6.2, 6.2

[81] D. Galloway et U. Frisch, "Dynamo action in a family of flows with chaotic streamlines," Geophysical and Astrophysical Fluid Dynamics **36**, 53–83 (1986). 6.2, 6.2

[82] B. Galanti, P.-L. Sulem, et A. Pouquet, "Linear and non-linear dynamos associated with abc flows," Geophysical & Astrophysical Fluid Dynamics **66**, 183–208 (1992). 6.2, 6.2

[83] A. Alexakis, "Searching for the fastest dynamo: Laminar ABC flows," Phys. Rev. E **84**, 026321 (2011). 6.2, 6.2

[84] I. Bouya et E. Dormy, "Revisiting the ABC flow dynamo," Physics of Fluids **25**, 037103–037103 (2013). 6.2, 6.2

[85] S. E. Jones et A. D. Gilbert, "Dynamo action in the ABC flows using symmetries," Geophysical and Astrophysical Fluid Dynamics **108**, 83–116 (2014). 6.2, 6.2, 6.2

[86] A. Cameron, A. Alexakis, et M.-E. Brachet, "Large-scale instabilities of helical flows," Physical Review Fluids **1**, 063601 (2016). 6.2, 9.1, 9.2.3.2, 10.1

[87] L. D. Landau et E. M. Lifshitz, *Mechanics* (Butterworth-Heinemann, Oxford u.a., 1976). 7

[88] L. D. Landau et E. M. Lifshitz, *Statistical Physics* (Butterworth-Heinemann, Burlington, 1980). 7, 9.2.1.1

[89] S. A. Orszag, *Lectures on the statistical theory of turbulence* (Flow Research Incorporated, 1974). 7

[90] T. D. Lee, "On some statistical properties of hydrodynamical and magneto-hydrodynamical fields," Quarterly of Applied Mathematics **10**, 69–74 (1952). 7, 9.2.1.1

[91] H. Lamb, *Hydrodynamics* (Cambridge university press, 1932). 7.3

[92] C. Cartes, M. D. Bustamante, et M. E. Brachet, "Generalized Eulerian-Lagrangian description of Navier-Stokes dynamics," Physics of Fluids **19**, 077101 (2007). 7.3

[93] E. W. Weisstein, *Chi-Squared distribution* (Math\-World - A Wol\-fram Web Resource, 2017). URL : http://mathworld.wolfram.com/Chi-SquaredDistribution.html. 7.3, 9.2.2.1

[94] C. Cichowlas, "Truncated Euler equation : from complex singularities dynamics to turbulent relaxation." Thesis, Universite Pierre et Marie Curie - Paris VI (2005). 8, 8.2.2, 9.1

[95] S. Chen et R. H. Kraichnan, "Sweeping decorrelation in isotropic turbulence," Physics of Fluids A: Fluid Dynamics **1**, 2019–2024 (1989). 8.2.1, 8.3

[96] P. C. d. Leoni, P. J. Cobelli, et P. D. Mininni, "The spatio-temporal spectrum of turbulent flows," The European Physical Journal E **38**, 136 (2015). 8.1, 8.2.1, 8.3, 8.7, 8.9, 9.2.2.2

[97] I. Wolfram Research, *Mathematica Version 10.0* (Wolfram Research, Inc., Champaign, Illinois, 2014). 8.2.2

[98] P. J. Cobelli, A. Maurel, V. Pagneux, et P. Petitjeans, "Global measurement of water waves by Fourier transform profilometry," Experiments in Fluids **46**, 1037 (2009). 8.3, 8.7, 9.2.2.2

[99] B. Miquel, A. Alexakis, et N. Mordant, "Role of dissipation in flexural wave turbulence: From experimental spectrum to Kolmogorov-Zakharov spectrum," Physical Review E **89**, 062925 (2014). 8.3, 8.8, 8.9, 9.2.2.2

[100] E. W. Weisstein, *Apodization Function* (MathWorld - A Wolfram Web Resource, 2017). URL : http://mathworld.wolfram.com/ApodizationFunction.html. 8.3, 9.4.4

[101] V. Dallas, S. Fauve, et A. Alexakis, "Statistical Equilibria of Large Scales in Dissipative Hydrodynamic Turbulence," Physical Review Letters **115**, 204501 (2015). 9.1, 9.1, 9.3

[102] L. Biferale, S. Musacchio, et F. Toschi, "Split energy–helicity cascades in three-dimensional homogeneous and isotropic turbulence," Journal of Fluid Mechanics **730**, 309–327 (2013). 9.1

[103] C. Cichowlas, P. Bonaïti, F. Debbasch, et M. Brachet, "Effective Dissipation and Turbulence in Spectrally Truncated Euler Flows," Physical Review Letters **95**, 264502 (2005). 9.1, 9.1, 9.2.1.2

[104] G. Krstulovic, P. D. Mininni, M. E. Brachet, et A. Pouquet, "Cascades, thermalization, and eddy viscosity in helical Galerkin truncated Euler flows," Physical Review E **79**, 056304 (2009). 9.1, 9.1

[105] M. E. Brachet, D. I. Meiron, S. A. Orszag, B. G. Nickel, R. H. Morf, et U. Frisch, "Small-scale structure of the Taylor-Green vortex," Journal of Fluid Mechanics **130**, 411–452 (1983). 9.2.2, 10.1

[106] A. Pouquet, E. Lee, M. E. Brachet, P. D. Mininni, et D. Rosenberg, "The dynamics of unforced turbulence at high Reynolds number for Taylor–Green vortices generalized to MHD," Geophysical & Astrophysical Fluid Dynamics **104**, 115–134 (2010). 9.2.2

[107] C. Nore, M. Abid, et M. E. Brachet, "Decaying Kolmogorov turbulence in a model of superflow," Physics of Fluids **9**, 2644–2669 (1997). 9.2.2.1, 9.2.2.1, 9.4.2, 10.1

[108] C. Brun et A. Pumir, "Statistics of Fourier modes in a turbulent flow," Physical Review E **63**, 056313 (2001). 9.2.2.1

[109] C. Baudet, S. Ciliberto, et J. F. Pinton, "Spectral analysis of the von karman flow using ultrasound scattering," Physical Review Letters **67**, 193–195 (1991). 9.2.2.1

[110] F. Lund et C. Rojas, "Ultrasound as a probe of turbulence," Physica D: Nonlinear Phenomena **37**, 508–514 (1989). 9.2.2.1

[111] A. Cameron et A. Alexakis, "Fate of Alpha Dynamos at Large Rm," Physical Review Letters **117**, 205101 (2016). 9.2.3.2

[112] P. S. Marcus, "Description and philosophy of spectral methods," dans "Proceedings of Astrophysical Radiation Hydrodynamics," (Springer-Verlag, 1986), p. 359–386. 10.1

[113] E. W. Weisstein, *Runge-Kutta Method* (MathWorld - A Wolfram Web Resource, 2017). URL : http://mathworld.wolfram.com/Runge-KuttaMethod.html. 10.1

[114] J. W. Cooley et J. W. Tukey, "An Algorithm for the Machine Calculation of Complex Fourier Series," Mathematics of Computation **19**, 297–301 (1965). 10.1

[115] R. Courant, E. Isaacson, et M. Rees, "On the solution of nonlinear hyperbolic differential equations by finite differences," Comm. Pure Appl. Math. **5**, 243–255 (1952). 10.2, 11.1, 11.2.2, 12.2.2

[116] A. Robert, "A stable numerical integration scheme for the primitive meteorological equations," Atmosphere-Ocean **19**, 35–46 (1981). 11.1, 12.1

[117] A. Robert, "A semi-Lagrangian and semi-implicit numerical integration scheme for the primitive meteorological equations," J. Meteor. Soc. Japan **60**, 319–325 (1982). 11.1

[118] A. Staniforth et J. Côté, "Semi-Lagrangian Integration Schemes for Atmospheric Models—A Review," Mon. Wea. Rev. **119**, 2206–2223 (1991). 11.1, 12.1

[119] A. Oliveira et A. M. Baptista, "A comparison of integration and interpolation Eulerian-Lagrangian methods," Int. J. Numer. Meth. Fluids **21**, 183–204 (1995). 11.1

[120] D. R. Durran, *Numerical methods for wave equations in geophysical fluid dynamics*, 32 (Springer, 1999). 11.1, 11.2.2, 12.1, 12.2.1, 12.2.2

[121] G. Knorr et M. Mond, "The representation of shock-like solutions in an Eulerian mesh," Journal of Computational Physics **38**, 212–226 (1980). 11.1

[122] M. M. Shoucri, "Numerical calculations of discontinuities by shape preserving splines," Journal of Computational Physics **49**, 334–341 (1983). 11.1

[123] M. Zerroukat, N. Wood, et A. Staniforth, "Application of the parabolic spline method (PSM) to a multi-dimensional conservative semi-Lagrangian transport scheme (SLICE)," Journal of Computational Physics **225**, 935–948 (2007). 11.1

[124] X.-D. Liu, S. Osher, et T. Chan, "Weighted Essentially Non-oscillatory Schemes," Journal of Computational Physics **115**, 200–212 (1994). 11.1

[125] J.-M. Qiu et C.-W. Shu, "Conservative high order semi-Lagrangian finite difference WENO methods for advection in incompressible flow," Journal of Computational Physics **230**, 863–889 (2011). 11.1, 12.1

[126] C.-S. Huang, T. Arbogast, et J. Qiu, "An Eulerian–Lagrangian WENO finite volume scheme for advection problems," Journal of Computational Physics **231**, 4028–4052 (2012). 11.1

[127] T. Nakamura, R. Tanaka, T. Yabe, et K. Takizawa, "Exactly Conservative Semi-Lagrangian Scheme for Multi-dimensional Hyperbolic Equations with Directional Splitting Technique," Journal of Computational Physics **174**, 171–207 (2001). 11.1, 12.1

[128] F. Xiao et T. Yabe, "Completely Conservative and Oscillationless Semi-Lagrangian Schemes for Advection Transportation," Journal of Computational Physics **170**, 498–522 (2001). 11.1, 12.1

[129] M. Lentine, J. T. Grétarsson, et R. Fedkiw, "An unconditionally stable fully conservative semi-Lagrangian method," Journal of computational physics **230**, 2857–2879 (2011). 11.1, 12.1

[130] E. Sonnendrücker, J. Roche, P. Bertrand, et A. Ghizzo, "The semi-Lagrangian method for the numerical resolution of the Vlasov equation," Journal of computational physics **149**, 201–220 (1999). 11.1, 12.1

[131] Y. Liu, X. Liu, et E. Wu, "Real-time 3d fluid simulation on GPU with complex obstacles," dans "12th Pacific Conference on Computer Graphics and Applications, 2004. PG 2004. Proceedings," (2004), p. 247–256. 11.1

[132] E. Wu, Y. Liu, et X. Liu, "An improved study of real-time fluid simulation on GPU," Comp. Anim. Virtual Worlds **15**, 139–146 (2004). 11.1

[133] B. P. Leonard, "Stability of explicit advection schemes. The balance point location rule," Int. J. Numer. Meth. Fluids **38**, 471–514 (2002). 11.1

[134] T. F. Dupont et Y. Liu, "Back and forth error compensation and correction methods for removing errors induced by uneven gradients of the level set function," Journal of Computational Physics **190**, 311 – 324 (2003). 11.1, 11.2.1

[135] T. F. Dupont et Y. Liu, "Back and forth error compensation and correction methods for semi-lagrangian schemes with application to level set interface computations," Mathematics of Computation **76**, pp. 647–668 (2007). 11.1, 11.2.1

[136] B. Kim, Y. Liu, I. Llamas, et J. Rossignac, "Advections with significantly reduced dissipation and diffusion," IEEE transactions on visualization and computer graphics **13**, 135–144 (2007). 11.1, 11.2.1

[137] J. C. Butcher, *Numerical methods for ordinary differential equations* (John Wiley & Sons, 2008). 11.1, 11.2.2

[138] R. MacCormack, "The Effect of Viscosity in Hypervelocity Impact Cratering," Journal of Spacecraft and Rockets **40**, 757–763 (2003). 11.1

[139] E. Celledoni, B. K. Kometa, et O. Verdier, "High Order Semi-Lagrangian Methods for the Incompressible Navier-Stokes Equations," J Sci Comput p. 1–25 (2015). 11.2.1

[140] J. E. Fromm, "A method for reducing dispersion in convective difference schemes," Journal of Computational Physics **3**, 176–189 (1968). 11.2.1, 11.2.1

[141] R. Courant, K. Friedrichs, et H. Lewy, "Uber die partiellen Differenzengleichungen der mathematischen Physik," Math. Ann. **100**, 32–74 (1928). 11.2.1

[142] C. Hirsch, *Numerical Computation of Internal and External Flows: The Fundamentals of Computational Fluid Dynamics: The Fundamentals of Computational Fluid Dynamics* (Butterworth-Heinemann, 2007). 11.2.1, 11.2.2

[143] R. J. LeVeque, *Numerical methods for conservation laws*, vol. 132 (Springer, 1992). 11.2.1

[144] G. Strang, "On the Construction and Comparison of Difference Schemes," SIAM J. Numer. Anal. **5**, 506–517 (1968). 11.2.4

[145] L. Rayleigh, "Lix. on convection currents in a horizontal layer of fluid, when the higher temperature is on the under side," Philosophical Magazine Series 6 **32**, 529–546 (1916). 11.2.5

[146] S. Chandrasekhar, *Hydrodynamic and Hydromagnetic Stability* (Dover Publications, 1961). 11.2.5

[147] A. J. Chorin, "Numerical Solution of Navier-Stokes Equations," Mathematics of Computation **22**, 745–& (1968). 11.2.5

[148] J. Guermond, P. Minev, et J. Shen, "An overview of projection methods for incompressible flows," Computer Methods in Applied Mechanics and Engineering **195**, 6011 – 6045 (2006). 11.2.5

[149] N. Besse et E. Sonnendrucker, "Semi-Lagrangian schemes for the Vlasov equation on an unstructured mesh of phase space," Journal of Computational Physics **191**, 341–376 (2003). 12.1

[150] N. Crouseilles, M. Mehrenberger, et E. Sonnendrücker, "Conservative semi-Lagrangian schemes for Vlasov equations," Journal of Computational Physics **229**, 1927–1953 (2010). 12.1, 12.2.3

[151] S. V. Patankar, *Numerical Heat Transfer and Fluid Flow* (CRC Press, 1980). 12.1

[152] R. Eymard, T. Gallouët, et R. Herbin, "Finite volume methods," dans "Handbook of Numerical Analysis," , vol. 7 (Elsevier, 2000), p. 713–1018. 12.1

[153] H. Takewaki, A. Nishiguchi, et T. Yabe, "Cubic interpolated pseudo-particle method (CIP) for solving hyperbolic-type equations," Journal of Computational Physics **61**, 261–268 (1985). 12.1

[154] M. Shashkov, *Conservative Finite-Difference Methods on General Grids* (CRC Press, 1995). 12.1, 12.1, 12.3

[155] M. H. Carpenter, J. Nordström, et D. Gottlieb, "A Stable and Conservative Interface Treatment of Arbitrary Spatial Accuracy," Journal of Computational Physics **148**, 341–365 (1999). 12.1, 12.3

[156] T. C. Fisher, M. H. Carpenter, J. Nordström, N. K. Yamaleev, et C. Swanson, "Discretely conservative finite-difference formulations for nonlinear conservation laws in split form: Theory and boundary conditions," Journal of Computational Physics **234**, 353–375 (2013). 12.1, 12.3

[157] P. D. Lax et R. D. Richtmyer, "Survey of the stability of linear finite difference equations," Communications on Pure and Applied Mathematics **9**, 267–293 (1956). 12.2.1

[158] J. Crank et P. Nicolson, "A practical method for numerical evaluation of solutions of partial differential equations of the heat-conduction type," Mathematical Proceedings of the Cambridge Philosophical Society **43**, 50–67 (1947). 12.2.1

[159] E. F. Toro, *Riemann Solvers and Numerical Methods for Fluid Dynamics* (Springer Berlin Heidelberg, Berlin, Heidelberg, 2009). 12.2.2

[160] G. Dahlquist et A. Bjorck, *Numerical Methods* (Prentice Hall, Englewood Cliffs, New York, 1974). 12.2.2

[161] A. Cameron, R. Raynaud, et E. Dormy, "Multi-stage high order semi-Lagrangian schemes for incompressible flows in Cartesian geometries," International Journal for Numerical Methods in Fluids (2016). 12.2.2

[162] J. Pudykiewicz et A. Staniforth, "Some properties and comparative performance of the semi-Lagrangian method of Robert in the solution of the advection-diffusion equation," Atmosphere-Ocean **22**, 283–308 (1984). 12.2.3

[163] P. K. Smolarkiewicz et J. A. Pudykiewicz, "A Class of Semi-Lagrangian Approximations for Fluids," Journal of the Atmospheric Sciences **49**, 2082–2096 (1992). 12.2.3

[164] R. W. C. P. Verstappen et A. E. P. Veldman, "Symmetry-preserving discretization of turbulent flow," Journal of Computational Physics **187**, 343–368 (2003). 12.3

Résumé

Ce manuscrit décrit comment les champs de vitesses solutions de l'équation de Navier-Stokes se comportent à grande échelle pour un forçage à petite échelle. Il analyse aussi le comportement à grande échelle des champs magnétiques solutions de l'équation d'induction cinématique lorsque le champ de vitesse est de petite échelle. Les résultats présentés ont été obtenus à l'aide de simulations numériques directes utilisant des algorithmes pseudo-spectraux des équations non modifiées ou avec un développement utilisant la méthode Floquet.

Dans le cadre hydrodynamique, les simulations utilisant la méthode de Floquet permettent de retrouver les résultats de l'effet AKA à bas Reynolds et de les étendre pour des Reynolds d'ordre un. Elles permettent aussi d'étudier des écoulements AKA-stable et de mettre en évidence une autre instabilité pouvant être interprétée comme un effet de viscosité négative. Dans le cadre magnétique, l'effet alpha est observé sur une gamme de séparation d'échelle dépassant par plusieurs ordres de grandeur les autres résultats connus. Il est aussi montré que le taux de croissance de l'instabilité devient indépendant de la séparation d'échelle une fois que le champ magnétique est déstabilisé dans ses petites échelles.

Le spectre d'énergie et le temps de corrélation d'équilibres absolus solutions de l'équation d'Euler tronquée sont présentés. Un nouveau régime où le temps de corrélation est régi par l'hélicité est mis en évidence. Ces résultats sont aussi comparés à ceux des modes de grandes échelles de solutions de l'équation de Navier-Stokes forcée dans les petites échelles. Ils montrent que le temps de corrélation croît avec l'hélicité.

(1674 caractères, espaces inclus)

Mots clés

Instabilité, hélicité, effet AKA, méthode de Floquet, MHD, dynamo, effet alpha, séparation d'échelle, turbulence, équation Navier-Stokes, équation d'Euler tronquée, équilibre absolu, spectre spatio-temporel, correlation temporelle, écoulement ABC, symétries de Taylor-Green

Abstract

This manuscript describes how solutions of the Navier-Stokes equations behave in the large scales when forced in the small scales. It analyzes also the large scale behavior of magnetic fields solutions of the kinetic induction equation when the velocity is in the small scales. The results were acquired with direct numeric simulation (DNS) using pseudo-spectral algorithms of the equations as well as their Floquet developments.

In the hydrodynamic case, the Floquet DNS were able to confirm the results of the AKA-effect at low Reynolds number and extend them for Reynolds number of order one. The DNS were also used to study AKA-stable flows and identify a new instability that can be interpreted as a negative viscosity effect. In the magnetic case, the alpha-effect is observed for a range of scale separations that exceed known results by several orders of magnitude. It is also shown that the growth rate of the instability becomes independent of the scale separation once the magnetic field is destabilized in its small scales.

The energy spectrum and the correlation time of absolute equilibrium solutions of the truncated Euler equation are presented. A new regime where the correlation time is governed by helicity is exhibited. These results are also compared with those coming from large scale modes of solutions of the Navier-Stokes equation forced in the small scales. They show that the correlation time increases with the helicity of the flow.

(1451 characters, spaces included)

Keywords

Instability, helicity, AKA-effect, Floquet method, MHD, dynamo, alpha-effect, scale separation, turbulence, Navier-Stokes equation, truncated Euler equation, absolute equilibrium, spatio-temporal spectrum, temporal correlation, ABC flow, Taylor-Green symmetries